SHOCK COMPRESSION OF A HETEROGENEOUS, POROUS POLYMER COMPOSITE

A Dissertation
Presented to
The Academic Faculty

by

Christopher Holmes Neel

In Partial Fulfillment
of the Requirements for the Degree
Doctor of Philosophy in the
School of Materials Science and Engineering

Georgia Institute of Technology
August 2010

SHOCK COMPRESSION OF A HETEROGENEOUS, POROUS POLYMER COMPOSITE

Approved by:

Professor Thomas Sanders,
Committee Chair
School of Materials Science and Engineering
Georgia Institute of Technology

Professor Min Zhou
School of Mechanical Engineering
Georgia Institute of Technology

Professor Naresh Thadhani, Advisor
School of Materials Science and Engineering
Georgia Institute of Technology

Dr. Richard Ames
Raytheon Missile Systems
Raytheon Company

Professor Vladimir Tsukruk
School of Materials Science and Engineering
Georgia Institute of Technology

Professor Karl Jacob
School of Polymer, Textile, & Fiber Engineering
Georgia Institute of Technology

Date Approved: April 20, 2010

This work is dedicated to the scientists and engineers who came before me, and to those who will come after me. My sincerest hope is that this work both meets the expectations of the former and contributes something of use to the latter.

ACKNOWLEDGEMENTS

Like most modern research, this work could never have been completed without the aid of many individuals.

First and foremost, I would like to express my gratitude to my advisor, Dr. Thadhani, who was always willing to help me through difficult problems and provide encouragement on occasions when I was unsure of the next step to take. I would also like to thank him for treating all of his graduate students as well as he does, and for the genuine interest he takes in our welfare.

Besides Dr. Thadhani, I would like to thank the following people for helping me when they were under no obligation to give assistance and had little to gain by doing so. Dr. Yunshu Zhang at Georgia Tech for TGA experiments on THV and associated composites. Dr. Brian Patterson at Los Alamos National Laboratories for Computer-Aided X-ray Tomography on ZrC/THV composites. Peter Marshall and Dr. Cochran at Georgia Tech for the tube furnace runs. Laura Cerully at Georgia Tech for helpful discussion on reaction thermodynamics. Lex Nunnery at Georgia Tech for the use of DSC and FTIR equipment, as well as assistance and patient guidance in attempting to dissolve THV. Dave Safranski at Georgia Tech for the use of DSC and many DSC pans. Dr. Ainiwaer Wushuer at the University of Hawaii for the diamond anvil cell Raman spectroscopy experiments. If I have omitted anyone, it is by accident and I apologize.

I would also like to thank the members of my committee for their time and guidance, and all the research staff in the MSE department who make modern research possible.

Finally, of course, I would like to thank the members of my research group who have helped me along the way, all of whom have been there every day and assisted me in numerous way, both large and small. They include: Dan Eakins, Lou Ferranti, Morgana Martin, Anthony Fredenburg, Chris Wehrenberg, Brad White, Paul Specht, Chris Miller, Brady Aydelotte, Adam Jakus, Sean Kelley, Tyler Jackson, and Jon Tooker.

TABLE OF CONTENTS

LIST OF TABLES

LIST OF FIGURES

SUMMARY

The objective of this study was to investigate the shock compression response of several composite materials composed of 25% by volume of a ceramic powder in a THV polymer matrix. There were four different ceramic powders used to make the composites: 1, 10, and 100 μm alumina (Al_2O_3) and 10 μm zirconium carbide (ZrC). Characterization of the four composite materials revealed that the ceramic particles were not homogenously distributed in the matrix. Instead, there were large ($\sim$0.5 mm) regions of pure THV, surrounded by mixed-phase regions consisting primarily of packed ceramic powder, partially infiltrated with THV but still containing some void space. In addition, it was found that the morphology of the 1 μm Al_2O_3 powder was distinctly different from that of the other Al_2O_3 powders as well as the ZrC powder, in that it was composed of small ($\sim$250 nm) particles agglomerated and partially fused to make larger $\sim$1-10 μm porous aggregates. Furthermore, the ZrC/THV composite was found to contain large amounts of contaminants. All of the composites contained some porosity, varying from 1.4% for the 100 μm Al_2O_3/THV composite, to 15.9% for the 1 μm Al_2O_3/THV composite.

The experiments were performed using the 80 mm gas gun (for shock characterization) or the .30 caliber gas gun (for high strain rate mechanical property characterization). In order to understand the behavior of the constituent materials for the composites, the shock compression response of THV was also investigated. The U_S-U_P Hugoniot of THV was similar to that reported for other fluoropolymers in the literature. For the composites, the Hugoniots displayed unexpected trends and, in general, did not match the predictions of a number of analytical models. The trends observed in the stress wave profiles (obtained in the course of the Hugoniot experiments) were compared with those reported in the literature for similar materials. Two of the alumina powders employed in the composites were investigated using static and dynamic methods to understand the compaction/compression response. In order to build confidence in the ability of the analytical models used in the literature to

predict the shock response of a polymer composite, shock compression of a homogeneous ceramic powder/polymer composite (alumina in an epoxy matrix) was also investigated. Models that agreed with experimental results for this composite were applied to the more complex THV composites. Correlating the model predictions and the experimental data lead to questions concerning the inertness of the composites and the validity of the assumed form of the Grüneisen coefficient. Possible reactions between the ceramic particles and the THV matrix were investigated. Although no reaction was discovered between Al_2O_3 and THV, evidence of a reaction was found between ZrC and THV. It was demonstrated that consideration of the reaction improves the correlation between the predictive models and the observed response. The proper form of the Grüneisen coefficient γ for polymers was also considered, and a new dependence of γ on volume was proposed based on literature data. The new form of γ improved the correlation between the predictive models and the observed response, and also aided in explaining possible reasons for the anomalous response of the PVDF stress gauges employed in the study. This study is the first time these ideas concerning the higher Grüneisen coefficient have been applied to explain a material shock response.

The results in this work on the homogeneous ceramic powder/polymer composite and on the less-porous 10 and 100 μm Al_2O_3/THV composites show that the Hugoniot of nonporous composites made of polymers and ceramic particles can be reasonably predicted by several analytical models from the literature, although for all composites, the Hugoniot stiffness is underpredicted. As the porosity of the composites increases, the underprediction increases. Although there are several possible explanations for the observed response, it is most satisfyingly explained by reconsidering how the Grüneisen coefficient γ is evaluated for polymers. By considering that γ is a measure of the anharmonicity of the system, it follows that the most anharmonic bonds primarily determine γ. Such considerations have been analyzed by previous researchers, and lead to much higher values of γ for polymers. Increasing γ has a strong effect on the Hugoniot of a porous material, and leads to significant improvements in the agreement between the experimental and predicted shock Hugoniot for all of the Al_2O_3/THV composites.

For the 10 μm "ZrC/THV" composite, a major challenge in predicting the shock compression results is identifying the starting components. It was shown that the composite is actually composed of ZrC, monoclinic ZrO_2, THV, and some other unknown contaminants. Even with this compositional uncertainty, it was shown that predictions for the composite Hugoniot agree quite well with experimental results, provided that the higher value γ was used and the crush-up behavior of the particles is accounted for. This work also presents evidence of a thermally-induced reaction in the ZrC/THV composite, and presents an alternative explanation for the observed Hugoniot based on an exothermic, shock-induced reaction model. Furthermore, this work shows that the waveforms of these porous, heterogeneous polymer composites follow previously noted trends of decreasing risetime with increasing pressure. The relationship between risetime and pressure, and therefore the wave dispersion characteristics, follow trends more closely associated with powders than with solids.

As part of the investigation into the shock-wave risetimes of the composites, this work also investigated the inherent risetime of the PVDF stress gauges used to record the pressure wave profile, using comparisons with experiments done with VISAR particle velocity gauges. A clear discrepancy in the gauge records after the initial shock wave front has passed is observed. It has been proposed in the past that this discrepancy is due to a pressure-induced phase transformation in the PVDF gauge material, although no evidence of a phase transition is observed at room temperature. However, a significant question is raised concerning the appropriate form of the Grüneisen coefficient γ for polymeric materials. Although the exact form of $\gamma(V)$ is unclear, it is reasonable to assume an exponentially-decaying form of $\gamma(V)$, where at low temperatures γ is an order of magnitude higher than the traditional values, and at high pressures, the traditional (lower) values are approached as the bonding becomes less anharmonic. When such an exponentially decaying form of $\gamma(V)$ is applied to the PVDF stress gauge material, it was shown that a pressure-induced phase transformation could be prevented in static high pressure experiments at room temperature, while still occurring in the shock compressed material.

CHAPTER I

INTRODUCTION AND MOTIVATION

Shock-wave experimentation has been around since the Manhattan Project, and in the early years most work focused on the metals and ceramics pertinent to detonation systems, target structures, and terrestrial wave propagation. With few exceptions, the shock response of polymers was neglected, and the shock response of polymer composites was completely overlooked. In the 1970's, some shock experimentation was done on polymer composites as a result of their use as an encapsulant (potting compound) in explosive systems and as a model system for development of theoretical models. More recently, there has been considerable research interest in a new class of polymer composite materials called structural energetic materials. Structural energetic materials are compounds formulated to be able to bear mechanical loads and remain chemically inert under normal loading conditions, but then react and release energy upon exposure to highly dynamic loading, such as impact[1]. These materials are typically constructed using a polymeric binder and filled with either a single type of explosive particle, or several different types of particles, where one serves as the fuel and the other as the oxidizer.

The purpose of this research is to investigate inert analogues to these reactive, structural-energetic materials. While the composites investigated in this work are not expected to be energetic, understanding the inert shock response of purely mechanical systems is an important part of understanding more complex shock phenomena involving mechanical and chemical energy, such as detonation and reaction initiation criteria. The detonation and initiation criteria can depend on a number of factors, including the magnitude of the shock wave entering the material as well as the temperatures induced in the material during the passage of the shock wave. Both of these initiation criteria (pressure and temperature created by a shock wave) may depend upon factors such as the size, shape, and density of the fill material used in the composites. Therefore, the effect of the morphology and density

of the fill material is a subject of interest, and is examined in this work.

The composites investigated in this work consist of 75% by volume THV, with the remainder filled by either 1, 10, or 100 μm Al_2O_3 or 10 μm ZrC particles. THV is a fluorinated terpolymer consisting of polymerized tetrafluoroethylene, hexafluoropropylene, and vinylidene fluoride in mass ratios of approximately 60/20/20. THV is used because fluorinated polymers have been documented in the past as suitable for energetic systems where the binder also serves as a reactant[1], and THV is much more easily processed than the more familiar PTFE, or Teflon®. The ceramic particles were chosen to represent a range of particle sizes and densities which would allow for increased understanding into the effects such variations have on the shock properties, which in turn aids in interpreting the behavior of the energetic compounds.

This work will begin with a review of relevant literature in Chapter 2. It will include the basics of shock wave science, as well as information explaining the techniques and vernacular employed throughout the remainder of the work. In Chapter 3, the characteristics of the tested materials are documented, along with practical details of the experimental setups employed. Chapter 4 will cover the experimental results and discussion concerning the shock response of the THV composites and the individual components from which the composites are made. The transient wave profiles are analyzed and the trends observed are compared and contrasted with those reported by previous researchers. The chapter concludes with a discussion of the equilibrium shock response where two competing explanations are presented, one of which involves a divergence from some longstanding assumptions made concerning the thermodynamics of shocked polymers. Chapter 5 begins by recalling some results from Chapter 4 regarding variations in the shock wave profile as recorded by different measurement techniques. Finally, conclusions are provided in Chapter 6, and several recommendations for future work are made in Chapter 7.

CHAPTER II

BACKGROUND

This chapter will begin by briefly introducing shock waves, how they can be described and predicted, and what is gained from studying them. In addition, terms and techniques used later in this work are defined and explained. More complete general information regarding the nature and description of shock waves can be found in several books[2, 3, 4, 5, 6, 7, 8, 9]. This chapter also introduces the physical basis for several shock wave diagnostic tools employed in the work. Finally, the chapter will conclude with several sections of literature reviews covering the shock response of materials similar to those examined in this work.

2.1 Introduction to Shock Wave Science

Shock waves are a special case of longitudinal, compressive mechanical waves. In the case of "normal" (non-shock) longitudinal pressure pulses, the speed at which the wave travels is roughly proportional to the square root of the modulus (the proportionality is exact if we assume incompressibility). In materials exhibiting classical linear elastic response, the modulus is constant, and so the elastic wave speed is constant- i.e. the elastic wave speed is independent of the magnitude of the pulse. In the plastic region, modulus decreases monotonically, and so as the material is subjected to higher stress (the magnitude of the plastic wave increases) the wave speed of the "plastic" wave[1] decreases. This phenomenon will cause a sharp (Heaviside-step) pressure pulse to spread out, or disperse, over time (or distance traveled) so that it becomes a small step (corresponding to the elastic limit), followed by a gradual ramp to the applied stress. Such a pressure wave is termed an elastic-plastic wave.

As the amplitude of the stress wave is increased, the analogy to classical material behavior breaks down, and the stress wave propagation speed increases with increasing stress

[1]The applicability of the concept of wave propagation to plastic deformation is under some debate. For instance, see the descriptively titled paper "On the Myth of Plastic Waves" by Horie[10].

magnitude. Once the stress wave speed exceeds the elastic wave speed, the wave is termed a "shock" wave, and its propagation speed is termed the shock velocity U_S. If the stress is gradually ramped up over a period of time, a ramp wave will result, but since the shock velocity of the maximum stress is greater than the wave velocity at any lower stress, the highest amplitude wave will gradually overtake the lower amplitude waves. Such a process of transitioning from a ramp wave to a shock wave is termed "shocking up". Although shock waves can, and have been, described in a number of ways, a common definition is the one alluded to above; i.e. "a shock wave is a compressive wave of sufficient magnitude that it overtakes the elastic wave, and so shocks up". This requirement leads to several other definitions of shock waves, such as that they are "discontinuous boundaries across which thermodynamic properties change nearly instantaneously", in time scales of picoseconds to a few nanoseconds. If one prefers to think of a shock wave in spatial terms, then it is a region with a thickness on the order of a few free path lengths of molecules, over which a thermodynamic state variable changes. Any difference in a thermodynamic variable within a material is obviously unstable, and so the boundary between the disturbed and undisturbed regions must propagate as a wave front. If the boundary travels faster than the elastic wave speed (i.e., is supersonic), then it is a shock wave. So, although we mostly think of shock waves as being created by an abrupt change in pressure, it is just as valid to consider them as created by abrupt changes in energy or density. The propagating boundary is commonly called the "shock front", and the "instantaneous" change in state variables across the shock front is commonly called a "jump".

All real materials have some shear strength, or resistance to flow. Even in liquids, the viscosity provides shear strength when the loading is very fast, as occurs in a shock wave. However, shock compression can result in the buildup of pressure in a material to sufficiently high levels that the shear strength is insignificant in comparison. This causes the material to deform as if it has no resistance to flow and it behaves "hydrodynamically", or as an ideal fluid. The assumption of negligible flow stress is called the "hydrodynamic approximation". A shock wave can carry a shear component, but it can only be as strong as the shear strength of the material- thus there are no shear or tensile shock waves. If we accept the

approximation that a shock wave is a purely compressive pulse, it must also be true that a shock wave produces a condition of one dimensional, or uni-axial, strain, since in dilatation waves the particle motion, and therefore strain, can only be parallel to the direction of wave propagation[11]. The hydrodynamic approximation also explains the interchangeability of the terms "stress" and "pressure" encountered in much shock-compression work. In an isotropic material in a shocked state that has a significant strength component, the deformation is still uniaxial, but the stress is biaxial. The strength in this situation is the shear strength τ, and is equal to half the difference between the longitudinal strength (σ_x, the direction parallel to the shock and particle velocity) and the lateral strength (σ_y, perpendicular to the shock or particle velocity), as shown in Equation (1) (the Tresca yield criterion).

$$2\,\tau = \sigma_x - \sigma_y \tag{1}$$

Furthermore, if the material has strength, it can be shown that σ_x will be greater than the hydrostatic pressure according to Equation (2). Both equations can be derived from continuum mechanics, as shown by Davison[6]. From Equation (2), it is easy to see that if $\sigma_x \gg \tau$, then $\sigma_x \approx P$, hence the common interchangeability of stress and pressure.

$$\sigma_x = P + \frac{4}{3}\,\tau \tag{2}$$

The idea of an ideal discontinuity is a concept that only makes sense in a continuum, and all real shocks must have some thickness. Within the community of scientists who study shock waves, there is still disagreement over exactly how instantaneous a shock front must be in order to qualify as a shock front. Such differences have led to the emergence of terms such as "strong shock" and "weak shock" to describe shock waves that show rise times in pressure from ambient to peak state in tens of picoseconds (currently state-of-the art in time-resolved shocks) from those that rise in tens of nanoseconds. The idealized concept of strong shocks enables the application of hydrodynamic theory for correlating changes in pressure, density, and energy across the discontinuity. A first-order approximation of

the idealized concept is often applied even in the case of weak shocks, using conservation equations described in the following section.

2.1.1 Conservation Equations and the Hugoniot

Considering the shock front, or jump, as a discontinuity in the material, equations for the conservation of mass, momentum, and energy can be derived to correlate the states across the front. Equations (3)-(5) represent the algebraic form of these conservation equations, often called the Rankine-Hugoniot Equations, or "jump conditions". The equations are developed by considering a steady state shock wave creating a state of uniaxial strain in a continuum, and by neglecting thermal conduction and radiation (an adiabatic shock). The shock front moves at velocity U_S, the particles move at velocity U_P, and the material has specific volume V (and density $\rho = 1/V$), pressure P, and internal energy E. Here the term "pressure" means the stress in the direction of wave propagation. The specific volume, pressure, and energy terms with zero subscripts represent initial values, and are often called the "centering point" of the Hugoniot. A schematic illustrating a shock wave profile (instantaneous rise to peak pressure, region of constant pressure, gradual release) is shown in Figure 2.1. More general, differential forms of these equations relax the requirement of steady-state wave propagation, and can be found in any of the references cited at the beginning of this chapter.

$$\rho_0(U_S - U_{P0}) = \rho(U_S - U_P) \tag{3}$$

$$P - P_0 = \rho_0(U_S - U_{P0})(U_P - U_{P0}) \tag{4}$$

$$\begin{aligned} PU_P - P_0U_{P0} = \frac{1}{2}\rho(U_S - U_P)U_P^2 + E\rho(U_S - U_P) \\ - \left\{\frac{1}{2}\rho_0(U_S - U_{P0})U_{P0}^2 + E_0\rho_0(U_S - U_{P0})\right\} \end{aligned} \tag{5}$$

These jump conditions, although usually derived across a sharp, instantaneous shock front, apply as long as the shock wave is steady (no longer evolving as it travels)[12, 13].

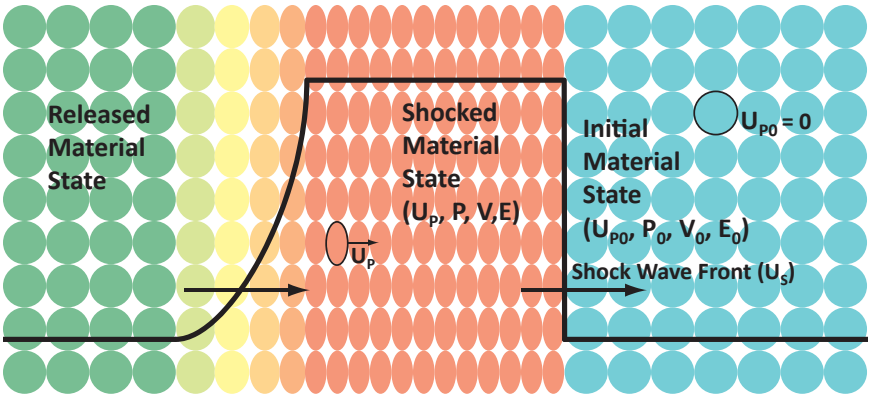

Figure 2.1: Schematic of a Shock Wave. The particle shapes illustrate the 1-D strain experienced, and the colors indicate temperature. The pressure trace is indicated by the solid black line, with the front propagating to right at a velocity of U_S. The pressure compresses the material until the arrival of the "release" wave, which relieves the pressure on the particles. In this figure, the particles are shown recovering to their original shape, although this is not usually the case. Note that the temperature, as indicated by the color, does not return to the original temperature, but remains elevated even after the pressure has returned to ambient.

This also follows from the not-uncommon view that even the sharpest shock is a mathematical construct and that even the most intense shock waves have a finite, though miniscule, risetime. This paradoxical view reflects the incomplete understanding about exactly how to differentiate between "strong shocks" and "weak shocks", especially as events that were previously considered "strong shocks" become "weak shocks" or even isentropic as experimental temporal resolution improves.

Much experimental shock wave science is concerned with the determination of the shock wave pressure required to produce a certain compression, shock wave speed, or internal energy in a given material. This data is most often displayed as a plot called a "Hugoniot", which is the loci of material states that can be produced by a shock wave. For example, Figure 2.2 shows several Hugoniot plots for poly(tetrafluoroethylene) (PTFE). The Hugoniot in P-V space centered at ambient conditions (the "principal" Hugoniot) describes the set of densities to which a shock wave can compress ambient PTFE. Hence, the Hugoniot represents the locus of states available to an initial state via a shock, rather than the path by which those states are achieved. The Hugoniot will be distinctly different from the isotherm

or the isentrope (both of which describe continuous pathways), and is sometimes more descriptively called the "shock adiabat", especially in the Soviet literature. A Hugoniot is a plot of any two of the five variables (U_S,U_P,P,V,E) generated as a result of shock compression. However, three forms of Hugoniot plots are particularly useful and widely utilized to describe the shock response of materials. These include the shock vs. particle velocity (U_S-U_P), the pressure vs. particle velocity (P-U_P), and pressure vs. specific volume (P-V) Hugoniots, all of which are shown for PTFE in Figure 2.2. The Hugoniot in U_S-U_P space is a particularly sensitive space (the measurements are differential measurements) in which many materials can be described by a linear relationship that is a material characteristic, and will be described in more detail later. The P-U_P Hugoniot is useful for predicting shock wave interactions between materials due to the continuity of pressure and velocity across an interface under compression. The utility of the P-U_P Hugoniot for this purpose will be described more fully in a later section. The P-V Hugoniot provides the most intuitive representation of shock compression, especially when comparing with isothermal and isentropic compression data, and because many energy considerations, such as the concept of temperature rise after shock compression and release, can be conveniently illustrated in P-V space as "areas under the curve". In any case, a Hugoniot plot, or simply a "Hugoniot", represents a 2-D slice (for instance, a plot in $P-V$ space) of the material's 3-D equation of state surface (a surface in $P-V-E$ space), and as such, gives important clues as to the high pressure behavior of a material.

The $P-V$ Hugoniot in Figure 2.2(a) contains a useful line called the Rayleigh line. The Rayleigh line serves to further reinforce the point that the material does not follow the path of the Hugoniot plot, but rather jumps from the initial state to the final state. The slope also contains useful information. The slope of the Rayleigh line can be shown (through the conservation equations) to be equal to $-(\rho_0 U_S)^2$. The term $\rho_0 U_S$ is called the "shock impedance" (z), which is used to convey how shock waves are affected by material interfaces, and will be discussed later in more detail. For now, simply note that the impedance is also equivalent to the slope of the jump in pressure - particle velocity space, as shown in Figure 2.2(c).

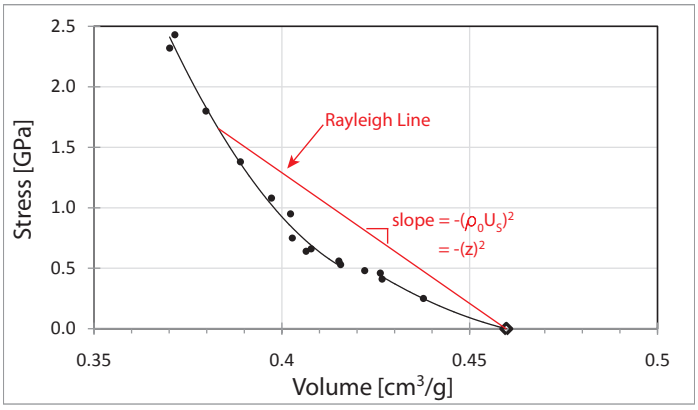

(a) Hugoniot plot in P - V space. The zero-pressure point is from density measurements at ambient conditions.

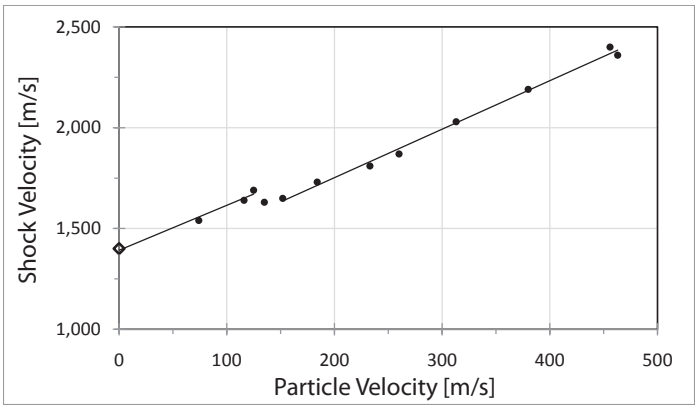

(b) Hugoniot plot in U_S - U_P space. The zero-pressure point (at $U_P = 0$) is taken from ultrasonic sound speed measurements.

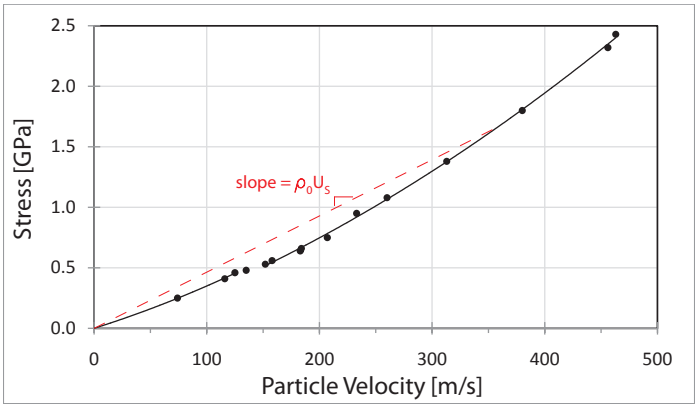

(c) Hugoniot plot in P - U_P space.

Figure 2.2: Hugoniot plots for PTFE. All of the plots contain identical information, and each can be transformed into the others by application of the conservation equations. Since these data were gathered on PTFE shocked from ambient conditions, these plots represent the primary Hugoniot. Note the evidence of the phase transition at 0.5 GPa suggested by the separate fits to the data above and below 0.5 GPa. Note that the break in the data is most noticeable in $U_S - U_P$ space. All data taken from Champion[14].

Often we perform experiments on materials that are initially at ambient conditions. Since the initial particle velocity U_{P0} is usually taken as zero, and the initial atmospheric pressure P_0 is usually negligible compared to the pressure of the shock wave, Equations (3)-(5) simplify to Equations (6)-(8).

$$\rho_0 U_S = \rho(U_S - U_P) \tag{6}$$

$$P = \rho_0 U_S U_P \tag{7}$$

$$PU_P = \frac{1}{2}\rho(U_S - U_P)U_P^2 + E\rho(U_S - U_P) - E_0\rho_0 U_S \tag{8}$$

Equation (8) can be further simplified to a more common form and represented as Equation (9).

$$E - E_0 = \frac{1}{2}P(V_0 - V) \tag{9}$$

In addition to being a useful form of the jump conditions, Equation (9) indicates that exactly one-half of the energy in the shock goes into internal energy (the remainder is kinetic). As was previously stated, a common view is that even shock waves with the steepest front have some finite rise time. Equation (9) represents the sharp-shock limit (again assuming no interaction with the environment) that applies during a gradual compression, $E - E_0 = \int P dV$.

Assuming the initial material properties are known, the three simplified algebraic equations provide relationships between five variables. Therefore, measuring any two of the unknown variables allows for the determination of a Hugoniot point. A fourth relationship allows the determination of any of the parameters with only one measured parameter. The fourth relationship is usually called the Equation of State (EOS), and its determination is often the object of shock experimentation.

2.1.2 Equation of State (EOS)

2.1.2.1 Shock EOS

Any equation relating thermodynamic variables of matter is called an equation of state. For studies of shock compression of materials, the equation of state can be obtained theoretically based on interatomic potentials or quantum-mechanical considerations, or experimentally by subjecting materials to shock waves generated by impact or explosive detonation and measuring some combination of parameters. Theoretical determination of the equation of state is currently limited to simple material systems. There are numerous forms of equations of state that can be used to describe shock waves, but for condensed materials, by far the most common is the dependence of U_S on U_P, since it has long been noted that these two variables are empirically related for almost all materials by an equation of the form:

$$U_S = C_0 + SU_P + S'U_P^2 \tag{10}$$

where C_0, S, and S' are empirical constants, all of which will be discussed in more detail below. Usually the quadratic term is negligible unless a phase transition is occurring in the sample or the sample is porous. A significant deviation from linearity in the U_S-U_P Hugoniot plot is often taken as evidence of a phase transformation or chemical reaction. Adherence of experimental data to a linear EOS has even been taken as evidence of the validity of the jump conditions in porous materials with relatively long rise times[15]. Although most materials display the linear relationship, there is no widely accepted first-principles based explanation for the linearity. Shock properties of many materials are tabulated merely by specifying C_0 and S, as these two parameters can be used to obtain Hugoniot relationships relating any two shock variables. Equation (10) is sometimes called the "shock-wave equation of state", and is most applicable at pressures sufficiently high that the hydrodynamic approximation is valid. However, at exceptionally high pressures, the linear form of Equation (10), together with Equation (6), limits the volume compression V_0/V to $S/(S-1)$, or about 3 for a typical material with $S = 1.5$ - a result that does not agree with experiments for many materials[6]. It is worth pointing out that Equation (10) is not a thermodynamic equation of state, but

the term is nevertheless often used since it relates the variables of interest.

The physical interpretation of the term C_0 is straightforward. As the magnitude of the stress approaches zero, U_S should obviously approach the elastic wave speed and U_P should approach zero. Therefore, C_0 should equal the bulk elastic wave speed $C_B = \sqrt{(\lambda + \frac{2}{3}\mu)/\rho}$, and excellent agreement (within ~1% [16]) is found in simple materials. If the material remains in the solid form, or otherwise exhibits shear strength, the U_S-U_P data obtained from shock experiments is usually expected to extrapolate to the higher, solid value of C_0, whereas, if melting has occurred, the shear modulus $\mu \to 0$, and so C_B, and therefore C_0, are slightly lower. A phase change will also obviously affect the sound speed, hence the earlier statement that a change in intercept of the $U_S - U_P$ plot is considered as evidence of a phase transformation. However, this rule breaks down with polymers, that are widely known to have C_0 values significantly higher than the values predicted by the ambient pressure bulk modulus[17]. This discrepancy, once again, is most commonly attributed to a structural change in the material arising from the inherent microstructural anisotropy in long-chain polymers.

The physical interpretation of the term S is not so straightforward, but there is some consensus that it is related to the bulk modulus. Ruoff[18] showed that S can be related to the first pressure derivative of the zero-pressure isentropic bulk modulus B'_{0s} by Equation (11), although a slight correction based on experimental evidence with a number of elemental metals was later proposed by Steinberg[19]. However, a few more complex materials exhibit negative values of S over certain pressure ranges, which calls into question the universal applicability of this relationship.

$$S = \frac{1}{4}(1 + B'_{0s}) \tag{11}$$

2.1.2.2 Mie-Grüneisen Equation of State

Many theoretical equations of state have been used to describe high pressure material behavior. A widely used form is the Mie-Grüneisen equation of state (MG-EOS). In general, it is used to relate the pressure-volume-energy (P-V-E) state of a material to that of the

same material at a reference state. It is commonly used to predict compressibility curves corresponding to one set of thermodynamic constraints from the compressibility curve of another; for instance, to estimate the isentrope or isotherm from a Hugoniot. In order to make such a transformation, some measure of the pressure due to thermal vibrations must be accounted for. This pressure is simply the isochoric analogy to the more familiar isobaric thermal expansion, and is commonly called the "thermal pressure". The thermodynamic parameter most often used is called the Grüneisen parameter γ, and is defined in Equation (12a) below, where P is pressure, ϵ is specific internal energy, and V is specific volume. Like any thermodynamic derivative, there are other, equivalent expressions for γ, but this is the most intuitive derivative form when considering γ as a thermal pressure. Also shown in Equation (12b) is an expression of γ based on commonly measured thermodynamic material properties (derived by differentiating Equation (13) with respect to temperature at constant volume), where α is the linear coefficient of thermal expansion (the 3α term can be replaced by the volumetric thermal expansion), β_T is the isothermal bulk modulus, C_V is the isochoric specific heat, and V is specific volume.

$$\gamma = V \left.\frac{dP}{d\epsilon}\right|_V \tag{12a}$$

$$\gamma = V\frac{3\alpha\beta_T}{C_V} \tag{12b}$$

Although γ depends on two state variables, it is virtually always considered to be a function of volume only, and is sometimes even considered to be constant. Because a precise form of $\gamma(V)$ is still very difficult to determine, it is commonly assumed that $\gamma(V) = \frac{\gamma_R}{V_R}V$, where the subscript R represents a reference state (usually standard temperature and pressure), allowing γ_R to be calculated from Equation (12b). Although there are more complex forms of $\gamma(V)$, this simple relationship captures the observed trend of decreasing γ with decreasing V[6]. The Mie-Grüneisen EOS is represented by Equation (13), although it is not actually the full form of the equation of state. As previously stated, it is often used to transform knowledge of a reference curve, such as a Hugoniot, into a prediction of the state

of a material compressed by a path other than the shock path. Often the approximation just discussed is invoked, so that $\gamma/V \rightarrow \gamma_0/V_0$.

$$P(V) - P_R(V) = \frac{\gamma}{V}\left(E(V) - E_R(V)\right) \tag{13}$$

2.1.3 Shock Wave Interactions

The science of general wave interactions is a developed field and entire textbooks can be found on the subject. A specific technique known as the "impedance match technique" or the "impedance matching technique" is cited as a method of determining Hugoniot states using the conditions of equal particle velocity and pressure on either side of a shocked interface, and the known shock response of at least one of the materials. The method is best described visually using P - U_P Hugoniot plots. Strictly speaking, in order to predict anything other than an unstressed material impacting another unstressed material, we must know a complete EOS for the materials. This is because when a material is reshocked, the states generated are not predicted by the primary Hugoniot, but by the Hugoniot recentered at the initial shocked state. Similarly, when a material is unloaded due to an interface with a lower impedance medium, the isentrope, not the Hugoniot, describes the relaxation process. An additional complication is the effect of the elastic region in the initial stage of loading and unloading. The exact method, using isentropes, recentered Hugoniots and elastic regions, is described by Davison[6]. It is worth reiterating here that these complications arise from using the isentrope, Hugoniot, and elastic data which are merely subsets of the complete EOS corresponding to specific loading conditions, and that if a complete EOS is used, the concern vanishes. Unfortunately, complete equations of state are seldom available for materials, and even in the most advanced simulation codes, a mathematical description of the EOS is often avoided by using tabular data obtained from experimentation.

At moderate pressures, the recentered Hugoniots and release isentropes are very close to the primary Hugoniots. In addition, the elastic region has not been observed in shock studies of polymers . Therefore, the primary Hugoniot is used as an approximation for the recentered Hugoniot as well as for the isentrope. It is also assumed that the shock response

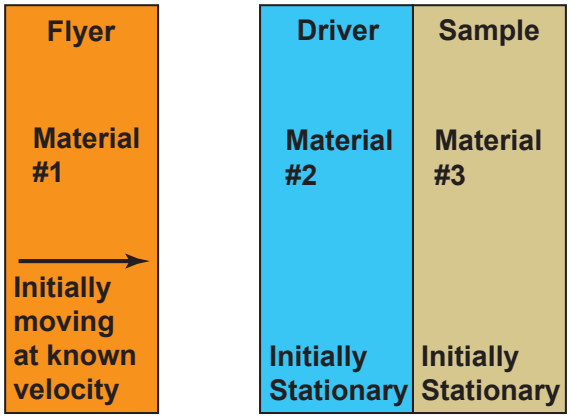

Figure 2.3: Experimental Description for Impedance Matching Technique, showing the flyer, driver, and sample material in the configuration used for the discussion of the impedance-matching technique.

of all materials can be described by Equation (10). This simplified impedance matching method is described and illustrated in detail by Cooper[20]. For an experiment such as that shown in Figure 2.3, where the flyer and driver are known materials (Hugoniots available in the literature), the initial density of the sample is obtained prior to assembly, and the impact velocity and the shock speed are measured during the experiment. For the application of the impedance matching technique the flyer will be denoted by subscript **1**, the driver by subscript **2**, and the sample by subscript **3**. The interfaces will be denoted by compound subscripts. For example, P_{2-3} is the pressure at the interface between material **2** and **3**. The flyer, at ambient pressure but moving to the right at a particle velocity equal to the impact velocity, impacts the driver and sample, which are initially stationary, at ambient pressure, and in contact with one another.

The jump conditions described previously were developed from a Lagrangian perspective, and assumed a right-going wave. If we perform a transformation of axis to a Eulerian reference (the initial particle velocity ahead of the shock front), and consider the wave to be right-going, then $U_P \rightarrow U_P - U_{P,0}$, and if it is left-going, $U_P \rightarrow -(U_P - U_{P,0}) \rightarrow (U_{P,0} - U_P)$.

For the flyer (material 1), combining Equations (7) and (10) to eliminate U_S, then substituting $U_{P,0} - U_P$ for U_P since the shock will be left-going, and setting the initial particle velocity $U_{P,0}$ equal to the impact velocity V_{imp}:

$$P_1 = \rho_{0,1}(C_{0,1} + S_1(V_{imp} - U_{P,1}))(V_{imp} - U_{P,1}) \tag{14}$$

In the driver (material **2**), the shock is right going so that $U_P = U_P - U_{P,0}$. However, the material ahead of the shock front is at rest so that U_P is unchanged. Then, if the same methodology used for Equation (14) is applied to the driver (material **2**), except that the shock wave in the driver is right-going:

$$P_2 = \rho_{0,2}(C_{0,2} + S_2 U_{P,2})U_{P,2} \tag{15}$$

At impact the flier strikes the driver, and the pressure and particle velocity must be continuous across the interface. So, if Equations (14) and (15) are set equal to one another, and $U_{P,1} = U_{P,2} = U_{P,1-2}$:

$$\rho_{0,1}(C_{0,1} + S_1(V_{imp} - U_{P,1-2}))(V_{imp} - U_{P,1-2}) = \rho_{0,2}(C_{0,2} + S_2 U_{P,1-2})U_{P,1-2} \tag{16}$$

In this equation, since V_{imp} is the impact velocity, and S, C_0, and ρ_0 are known from the literature, the only unknown is $U_{P,1-2}$, which is easily obtained as the positive root of the quadratic equation. The mathematics are vastly simplified if the flier is of the same material as the driver; in that case $U_{P,1-2} = 1/2\ V_{imp}$ and no assumptions about the EOS must be invoked.

We now turn our attention to the interface between the driver (material **2**) and the sample (material **3**) and perform a similar, but subtly different, analysis. After the shock wave travels through the driver and interacts with the sample, a wave will travel to the left through the driver. Therefore, we can use the following equation to describe the left-going Hugoniot in the driver, where the initial particle velocity is the $U_{P,1-2}$ value previously solved for:

$$P_2 = \rho_{0,2}(C_{0,2} + S_2(U_{P,1-2} - U_{P,2}))(U_{P,1-2} - U_{P,2}) \tag{17}$$

Recall that the shock speed in the sample, $U_{S,3}$, is obtained from measurements, so for the sample material, U_S is not eliminated from Equation (7). U_S is also subject to the

transformation of axis, but remains positive for a right-going wave. Therefore, the Hugoniot of the right-going wave in the sample is described by:

$$P_3 = \rho_{0,3} U_{S,3} U_{P,3} \tag{18}$$

Once again, we recall that $P_2 = P_3$ and $U_{P,2} = U_{P,3} = U_{P,2-3}$ at the interface, and obtain:

$$\rho_{0,2}(C_{0,2} + S_2(U_{P,1-2} - U_{P,2-3}))(U_{P,1-2} - U_{P,2-3}) = \rho_{0,3} U_{S,3} U_{P,2-3} \tag{19}$$

Since $U_{P,1-2}$ has already been calculated, $\rho_{0,3}$ and $U_{S,3}$ have been measured, and the rest of the term are known from the literature, $U_{P,2-3}$ is again found. Since $U_{P,2-3} = U_{P,3}$, a U_S-U_P data point is obtained for material **3** (the sample), and can be transformed into a Hugoniot point in any other space using the jump equations previously discussed in Section 2.1.1.

The method described above can be performed graphically using P - U_P Hugoniot plots for the flier and driver. The plot of the material with the left-going wave (the flyer) must be "flipped" around the ordinate (the pressure axis) and then "shifted" along the abscissa so that the particle velocity at zero pressure is the impact velocity. This is the graphical manifestation of the change in reference frame. Then, the flipped and shifted flier Hugoniot curve is overlaid on the Hugoniot curve of the driver material. The intersection of the two curves defines the pressure and particle velocity that will result from the impact. This process is illustrated in Figure 2.4(a) (See Cooper[20] for more detailed information and illustrations). In the figure, the flyer (dashed line) is either tantalum or copper impacting a stationary copper driver (solid line) at either 600 or 1000 m/s. For example, if a Ta flyer impacts Cu at 1000 m/s, the Ta Hugoniot is flipped and shifted by 1000 m/s, overlaid with the Cu Hugoniot, and the intersection point is found at point 1 (25 GPa and 575 m/s). If a Cu flyer impacts a Cu driver at 600 m/s, the intersection is found at point 2 (12 Gpa and 300 m/s), and we note that the resulting particle velocity is half the impact velocity, as mentioned previously.

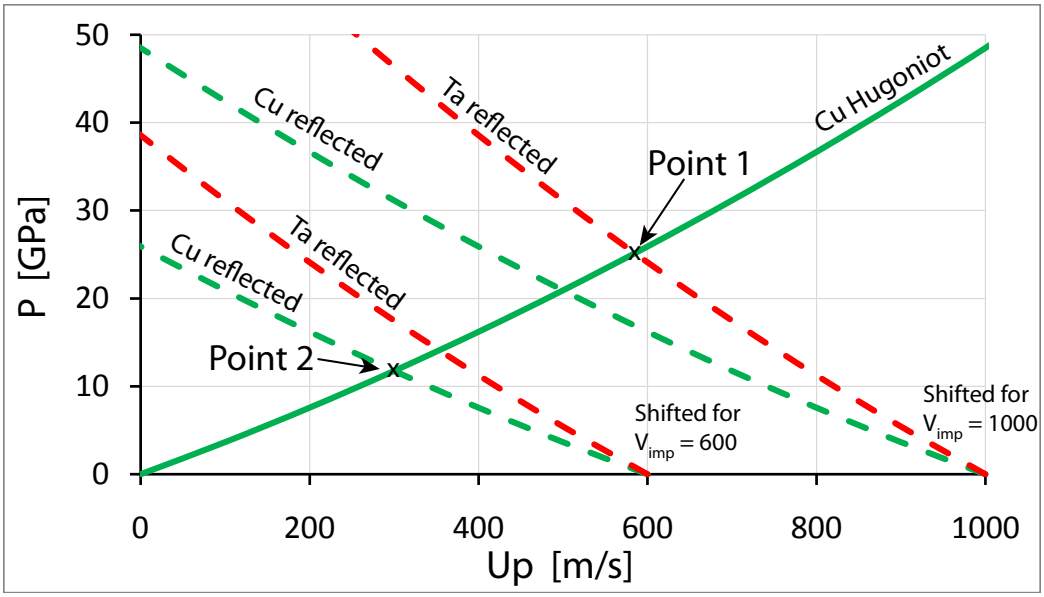

(a) Interaction between the flyer and driver. The copper Hugoniot is shown in green. "Reflected and shifted" Hugoniots for copper and tantalum are also shown, and are shifted to represent impact velocities of 600 and 1000 m/s. Point 1 is the state produced by Ta at 1000 m/s impacting Cu, and point 2 is the state produced by Cu at 600 m/s impacting Cu.

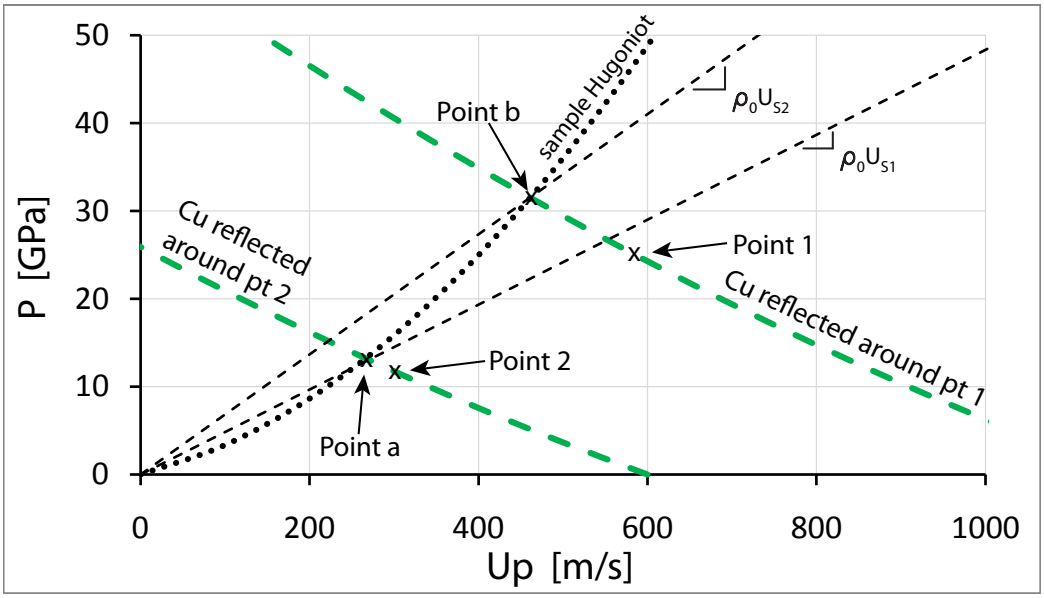

(b) Interaction between the driver and sample. The driver (Cu) Hugoniot has been reflected around points 1 and 2. These reflected curves have been intersected with lines of slope $\rho_0 U_S$ (where U_S is the value measured in the respective experiment) to find points a and b, which are points along the Hugoniot of the sample. The Hugoniot of the sample (shown as the dotten line) is then found by fitting a line of the proper form through points a and b.

Figure 2.4: Graphical impedance matching. After Meyers[2].

To then find the shock state of the unknown material using the measured shock speed U_S, we make use of the impedance concept presented earlier. Although the Hugoniot for the sample is not available, recall that the slope of the line in $P - U_P$ space is equal to the impedance z, and that $z = \rho_0 U_S$ (see Figure 2.2(c). Using this knowledge, the shocked state for the sample can be calculated as shown in Figure 2.4(b). The figure shows a scenario that would result if two experiments were performed: one with a Ta flyer at 1000 m/s impacting a Cu driver cemented to the sample, and another with a Cu flyer at 600 m/s impacting a Cu driver cemented to the sample. The Cu Hugoniot has therefore been "reflected" about points 1 and 2, as shown by the heavy dashed lines. The measured values of U_S corresponding to these two experiments are used with the measured initial density to construct straight lines of slope z, as shown by the light dashed lines. The intersection points, labeled a and b, are the shocked states in the sample material in the respective experiments. This pair of Hugoniot states is then used to find the sample Hugoniot (represented by the heavy dotted line) by a fitting algorithm, although ideally more than two experimental points are used.

2.2 Predicting the Shock Equation of State

Many schemes for predicting the shock properties of solid and porous mixtures have been proposed. Most of these require custom implementation into finite difference or finite element computer codes, as they are aimed at predicting non-equilibrium phenomena, and any prediction of the stress-wave profile will necessarily take into account constitutive relations for which straightforward analytical solutions are not available. However, if only the equilibrium Hugoniot state is desired, a number of simple methods have been developed to skirt this requirement and predict the Hugoniot of a composite based only on the Hugoniot of its constituents. These methods will be reviewed here.

2.2.1 Solid Mixtures

2.2.1.1 Simple Additivity Method

The additivity method[21, 16][2] is based on the assumption that the volume of a mixture shock-compressed to a pressure P is equal to the sum of the volume of its components shocked to that same pressure. This method provides only a rough approximation, and is exact under unrealistic shock conditions, such as when one of the materials is incompressible and thermally non-conducting. Although the idea was developed in order to determine the Hugoniot of a low-impedance material at high pressure, it can also be used to predict the Hugoniot of a mixture of two or more known components, as shown in the following equation, where α is the mass fraction of each component and n is the number of components.

$$V_{mix}(P) = \sum_{i=1}^{n} \alpha_i V_i(P) \tag{20}$$

$V(P)$ is found by manipulating the jump equations (Equations (6) - (8)) and assuming a linear shock EOS (Equation (10)) to solve for specific volume V as a function of pressure P, as shown in the equation below.

$$V = \frac{C_0^2}{2S^2P}\left\{\frac{2SPV_0(S-1)}{C_0^2} - 1 + \sqrt{\frac{4SPV_0}{C_0^2}+1}\right\} \tag{21}$$

2.2.1.2 McQueen's Method

McQueen et al.[22] proposed a method for predicting the Hugoniot of a solid mixture or composite using P-V space. The method is an extension of the additivity idea, and attempts to relieve the idealistic assumptions by correcting for the effects of shock heating. In a shock-compressed material, there is substantial shock heating (following from Equation (9) and a finite specific heat), and different components are heated by different amounts upon shock loading to any given pressure. The method attempts to account for that and yield the temperature-equilibrated response by first removing the thermal contribution to the

[2]This method has been attributed to Dremin and Karpukin by the cited authors. However, the original paper by Dremin and Karpukin is an early (1960) Soviet work in Russian and so was not verified by the author.

volume of the material by calculating the Hugoniot at absolute zero (variously termed the "zero K isotherm", "cold curve", or "zero K isentrope", since at 0 Kelvin the isotherm and isentrope merge) by solving the following differential equation for each material.

$$\left(\frac{dP}{dV}\right)_{T_0} + \frac{\gamma_0}{V_0} P_{T_0} = \frac{\gamma_0}{2V_0}\left[P_H + \left(\frac{2V_0}{\gamma_0} + V - V_0\right)\left(\frac{dP}{dV}\right)_H\right] \tag{22}$$

where

$$\left(\frac{dP}{dV}\right)_H = \frac{C^2(V_0 + SV_0 - SV)}{(-V_0 + SV_0 - SV)^3} \tag{23}$$

since the linear shock EOS has been assumed.

The zero K isotherm for the composite is constructed by summing the volume of each component, weighted by the mass fraction. The composite's zero K isotherm is then transformed into the room temperature Hugoniot using Equation (24)[23], where the value of γ for the composite is usually the mass-averaged component γ.

$$P_H = \frac{P_{T_0} - \frac{\gamma_0}{V_0}\int_{V_0}^{V} P_{T_0}\,\mathrm{d}V}{1 - \frac{\gamma_0}{2V_0}(V_0 - V)} \tag{24}$$

This method, the McQueen Rule-of-Mixtures Method, or "McQueen ROM" yields a prediction for the Hugoniot of a solid composite.

2.2.1.3 Baer Model

Baer developed a model for predicting the Hugoniot of a mixture[24, 25]. The model is based primarily around an equation for the sound speed in homogeneous flow for a mixture of two materials, A and B, given below[26], where ϕ represents the volume fraction of each mixture component at pressure. The middle term arises from $U_S = C_S + U_P$, where C_S is the sound speed at pressure.

$$\frac{1}{C_S^2} = \frac{1}{(U_S - U_P)^2} = (\phi_A\rho_A + \phi_B\rho_B)\left(\frac{\phi_A}{\rho_A C_{S,A}^2} + \frac{\phi_B}{\rho_B C_{S,B}^2}\right) \tag{25}$$

In the above equation, both components have the same particle velocity U_P, so that there are four unknowns- U_S, U_P, ϕ_A, and ϕ_B. The sound speed at pressure in material A, $C_{S,A}$, is found from $C_{S,A} = U_{S,A} - U_P$. The system is further constrained by the saturation

requirement that the mixture occupies all space, and by conservation of mass jump equation, both of which are shown below for completeness.

$$\phi_A + \phi_B = 1 \quad \text{(saturation constraint)} \tag{26}$$

$$\frac{V}{V_0} = 1 - \frac{U_P}{U_S} \quad \text{(cons. mass constraint)} \tag{27}$$

Together, Equations (25)-(27) comprise a system of three equations and four unknowns, which can be solved for any given U_P numerically. The model, like the methods mentioned previously, assumes a homogeneous distribution of materials, and therefore also assumes thermal equilibrium.

2.2.1.4 $P - \lambda$ Model

Shock compression of a non-porous mixture of two condensed phases can be considered as belonging to one of two regimes- that of intermediate stress, so that at least one of the phases has significant strength effects or is within the elastic limit, and that of high stress, such that the hydrostatic stress is well beyond the elastic limit of both materials. The additivity method and the McQueen ROM method both assume the latter condition- that both materials are stressed well beyond their elastic limit and behave hydrodynamically. However, the first condition, that of intermediate stress, also applies to the current work. A commonly used model to describe the compression behavior in this regime was introduced by Grady et al.[27]. They proposed an empirical method that has since become known as the P-λ method, where the compression response at intermediate stresses is assumed to be bounded by the elastic response and the Hugoniot. The justification for using the elastic response as a bound is that in the intermediate stress range, the material is supported by a lattice or bridgework of the stiffer material which is still elastic, and so the response of the mixture is also elastic.

The volume of the mixture at any pressure $\nu_m(P)$ can be considered to be bounded by the volume of the mixture in the pressure-equilibrated state $\nu_h(P)$ and the elastic state $\nu_e(P)$. An empirical state variable λ is introduced to account for the mass fraction of the

material in the Hugoniot (pressure-equilibrated) state, and so the volume of the mixture is given by:

$$\nu_m(P) = \lambda\nu_h(P) + (1-\lambda)\nu_e(P) \tag{28}$$

where λ is assigned the empirical form:

$$\lambda = 1 - e^{-(P/Y)^n} \tag{29}$$

where P is the pressure, Y is yield strength or crush-up strength, and n is an empirical parameter controlling the pressure interval over which the compression will occur. The exponential form of λ allows the compression to proceed along the elastic route until P approaches Y, and then gradually shift to the Hugoniot. The framework of the $P-\lambda$ model is easily adaptable to various formulations of the elastic response or Hugoniot response, or whenever the mathematical description of compressive response changes within a given pressure range. In the simplest application, where the goal is to describe an observed compression behavior, high pressure Hugoniot data is used to build the high pressure, pressure-equilibrated bounding curve (also called iso-pressure or Reuss limit), and elastic measurements are used to build the low pressure bounding curve (the iso-strain, or Voigt limit). Then a set of experimental data is used to find λ at a number of pressures, and then Y and n are determined by regression analysis of Equation (29)[28].

2.2.2 Mixture Methods Incorporating Porosity

The preceding mixture methods do not account for porosity in a material. In porous materials, the collapse of pores (or the deformation and flow of particles, depending on the type of porosity) cause very high local deformation and therefore the formation of hot spots. These hot spots cause the internal energy of the shocked material to increase tremendously, producing a significant increase in temperature. The temperature rise causes thermal pressures if the material is confined, and so the Hugoniot of a porous material will be shifted to higher volumes at any given pressure. Several methods have been established to predict the shocked state of porous materials, given the Hugoniot of solid materials.

A general assumption made for all of the following models is that the contribution of the surface energy of the particles is negligible compared to the energy generated during the shock compression due to plastic deformation and void collapse. However, this assumption has been challenged in the case of nanoparticles by Dai et al.[29]

2.2.2.1 Additivity Method

The additivity method previously discussed for mixtures is easily extended to porous materials by considering air as one of the components. The Hugoniot of air (available in the literature[30]) is incorporated as a component in Equation (20) to find the porous material's Hugoniot.

2.2.2.2 Mie-Grüneisen EOS

As previously noted, Equation (13) can be used to relate the pressure, volume, and energy of a material to the pressure and volume of the same material along a reference state such as a Hugoniot. It can also be used to relate the Hugoniot of a porous material to that of the solid material. From Equation (9), setting $E_0 = 0$,

$$E_{SH} = \frac{1}{2} P_{SH}(V_0 - V) \tag{30}$$

$$E_{PH} = \frac{1}{2} P_{PH}(V_{00} - V) \tag{31}$$

Where subscript SH refers to the solid Hugoniot, subscript PH to the porous Hugoniot, and V_0 and V_{00} respectively to the solid and porous initial specific volumes. Since V_{00} is always larger than V_0, it follows that the energy deposited by a shock of magnitude P in a distended material will always exceed that deposited by the same shock in a solid material. If these relations are substituted into Equation (13), where the solid Hugoniot is the reference and the porous Hugoniot is the unknown, then

$$P_{PH} = \frac{1 - \frac{\gamma}{2V}(V_0 - V)}{1 - \frac{\gamma}{2V}(V_{00} - V)} P_{SH} \tag{32}$$

Assuming γ/V is constant and the linear shock EOS of Equation (10), the pressure along the porous Hugoniot can be found at any volume:

$$P_{PH} = \frac{[2V - \gamma(V_0 - V)]C^2(V_0 - V)}{[2V - \gamma(V_{00} - V)][V_0 - S(V_0 - V)]^2} \tag{33}$$

where C_0 and S are the linear fits for the solid Hugoniot. Equations (32)-(33) assume that the crush-up to full density occurs at negligible pressure relative to the applied shock wave.

2.2.2.3 Wu-Jing Model

The Mie-Grüneisen EOS-based porosity model is limited in several ways. It calculates the pressure along the porous P-V Hugoniot from the pressure on the solid P-V Hugoniot using an isochoric approach. Therefore, it cannot handle volumes larger than that of the solid-the crush-up must take place at zero pressure. In addition, from Equation (32), V cannot equal $\frac{V_{00}}{2/\gamma+1}$, meaning that the compression (V_{00}/V) can never reach $2/\gamma + 1$. The Wu-Jing model[31] avoids these limitations by using an isobaric approach, where the volume is calculated from the solid P-V Hugoniot at a constant pressure. The following equation is a simplified version[29] of the central relationship of the Wu-Jing model:

$$V_{PH} = V_{SH} + \frac{(R/2)(V_{00} - V_0)}{1 - R/2} \tag{34}$$

where $R = P\gamma/K_S$, and

$$K_S = \frac{P\gamma}{2} - \left(\frac{dP}{dV}\right)_{SH}\left[V_{SH} - \frac{\gamma}{2}(V_0 - V_{SH})\right] \tag{35}$$

The simplified model is implemented in the following way: Beginning with a P-V Hugoniot for a solid material, the slope $\frac{dP}{dV}$ and γ are calculated for each P-V point. Although in the original Wu-Jing implementation a sophisticated form of γ is used, the $\gamma(V) = \frac{\gamma_0}{V_0}V$ simplication can also be employed. K_S is then calculated and used to determine R. Equation (34) is then employed to find the porous volume corresponding to each P-V point along the solid material Hugoniot.

2.2.2.4 Simons and Legner Model

Simons and Legner[32] developed a model using the Mie-Grüneisen equation, the jump conditions, and by considering that the internal energy and pressure can be separated into thermal and athermal components. They demonstrated that the model reduces to an equation of linear elasticity at low pressure, and to the shock-limit of compressibility for an ideal gas at high pressure, illustrating that it agreed with expected trends at the upper and lower limits of compression. They validated their model using literature data for several porous metals at intermediate pressures and demonstrated that the prediction was good. The model, given below, consists of a single equation relating pressure and volume.

$$V = V_0 \left[\frac{2 + \gamma \frac{V_{00}}{V_0} P K_0}{2 + (2 + \gamma) P K_0} \right] \tag{36}$$

where V_0, V_{00}, P, and K_0 are respectively the initial solid material specific volume, the initial porous material specific volume, pressure, and the bulk compressibility. The equation must be solved iteratively due to the dependence of γ on V (see Section 2.1.2.2).

2.2.2.5 Baer 3-phase Model

Baer's model can be extended to three materials, as done by Jordan et al.[25]. Similar equations to those used in the two phase model are employed, except that two artificial components (denoted by subscripts 12 and 13) are created from the three actual components. If the three components are components A, B, and C, and the actual volume fractions are denoted by ϕ, the artificial volume fractions are:

$$\alpha_{12} = \frac{\phi_A}{\phi_A + \phi_B} \tag{37}$$

and the artificial densities are:

$$\rho_{12} = \alpha_{12} \rho_A + (1 - \alpha_{12}) \rho_B \tag{38}$$

Equations (25) and (27) are rewritten, replacing ϕ_A and ϕ_B with ϕ_{12} and $1 - \phi_{12}$, as shown below:

$$\frac{1}{C_S^2} = \frac{1}{(U_S - U_P)^2} = \rho_{12}\left(\frac{\phi_{12}}{C_{S,A}^2} + \frac{1-\phi_{12}}{\rho_B C_{S,B}^2}\right) \tag{39}$$

$$\frac{V}{V_0} = 1 - \frac{U_P}{U_S} (\text{Identical to Eqn. (27)} \tag{40}$$

Given a value of U_P, equations (39) and (40) can now be solved for U_S and ϕ_{12}. This process is repeated for artificial component 13, replacing all subscript 12 terms with subscript 13 terms and replacing B with C in equations (37) - (40) and solving using the same value of U_P. Once ϕ_{12} and ϕ_{13} are obtained, the volume fractions of the actual components are recovered:

$$\phi_A = \frac{\alpha_{12} + \alpha_{13}}{\alpha_{13}(1-\alpha_{12}) + \alpha_{12}}, \quad \phi_B = \frac{(1-\alpha_{12})\alpha_{13}}{\alpha_{13}(1-\alpha_{12}) + \alpha_{12}}, \quad \phi_C = \frac{\alpha_{12}(1-\alpha_{13})}{\alpha_{13}(1-\alpha_{12}) + \alpha_{12}} \tag{41}$$

Then, the overall specific volume of the mixture is calculated by extending Equation (26) to three materials, and the other variables follow from the jump equations. This method has been summarized in the context of three generic materials, but can be used to predict the effects of porosity in a composite simply by using air as the third material.

2.2.2.6 Krueger-Vreeland Model

Krueger and Vreeland[33] developed a Hugoniot mixture model using an approach allowing for the thermal energy to be distributed unequally between the mixture components. Essentially, they relaxed an assumption made in other analytical models of thermal equilibrium. The model predicts Hugoniot states from quasi-static compression data and was validated using experimental data from the literature. Although the model predicts solid and porous single-component Hugoniots fairly well, especially considering the quasi-static input properties, and the results for porous mixtures agreed with experimental results, the model predicted only minor differences in the Hugoniot when the thermal energy was unevenly distributed. The mixture model can be implemented by numerically solving a system of four equations in five unknowns (P, U_S, U_P, V_A, and V_B) after assigning a value for one of the unknown variables. The four equations, shown below, respectively reflect the conservation

of mass, momentum, energy, and the manner in which the thermal energy is partitioned. Although the conservation of mass and momentum equation are identical to those previously discussed, they are repeated here for completeness and to provide notational consistency.

$$\rho_{00,mix} U_S = \rho_{mix} \ (U_S - U_P) \tag{42}$$

$$P = \rho_{00,mix} U_S U_P \tag{43}$$

$$P = \frac{\sigma_A P_{E,A} + \sigma_B P_{E,B} - \frac{x E_{E,A}}{V_{0,A} V_{0,B}} - -\frac{(1-x) E_{E,B}}{V_{0,A} V_{0,B}}}{\sigma_A + \sigma_B - \frac{1}{2}(\phi - \eta_A \lambda_A - \eta_B \lambda_B)} \tag{44}$$

$$P(1 - \xi/\epsilon) = P_{E,B} - (\xi/\epsilon) P_{E,A} \tag{45}$$

where for Equation (44),

$$\begin{aligned} \sigma_A &= \tfrac{x}{\gamma_{0,A} V_{0,B}}, \quad & \sigma_B &= \frac{1-x}{\gamma_{0,B} V_{0,A}} \\ \eta_A &= \tfrac{x}{V_{0,B}}, & \eta_B &= \frac{1-x}{V_{0,A}} \\ \lambda_A &= \tfrac{V_A}{V_{0,A}}, & \lambda_B &= \frac{V_B}{V_{0,B}} \\ \phi &= \tfrac{V_{00,mix}}{V_{0,A} V_{0,B}} \end{aligned} \tag{46}$$

and for Equation (45),

$$\xi \equiv \frac{E_{T,B}}{E_{T,A}} \text{ , and } \epsilon = \frac{V_{0,B} \gamma_{0,A}}{V_{0,A} \gamma_{0,B}} \tag{47}$$

In these equations, subcripts A and B correspond to properties for mixture components A and B, and the mix subscript denotes the property for the mixture. Initial porous specific volume is V_{00}, and non-porous initial specific volume is V_0. The mass fraction of component A is denoted by x. Energy (E) and pressure (P) are divided into elastic (subscript E) and thermal (subscript T) components. To solve the system, values of U_P and a partition function for the thermal energy ξ were chosen (a constant ratio is used in the model), and the

elastic pressure as a function of specific volume $P(V)$ is determined by using the Murnaghan equation[34] and published material data. The elastic energy is obtained by integrating the P(V) relationship. The pressure and energy equations based on the Murnaghan relationship are given below, where $\beta_{0,S}$ and $\beta'_{0,S}$ are the isentropic bulk modulus and the first pressure derivative of the bulk modulus.

$$P_E = \frac{\beta_{0,S}}{\beta'_{0,S}} \left[\left(\frac{V_0}{V} \right)^{\beta'_{0,S}} - 1 \right] \tag{48}$$

$$E_E = -\int_{V_0}^{V} P_E dV = \frac{\beta_0 V}{\beta'_0} \left(\frac{(V_0/V)^{\beta'_0}}{\beta'_0 - 1} + 1 \right) - \frac{\beta_0 V_0}{\beta'_0 - 1} \tag{49}$$

2.2.2.7 P - alpha Model

Similar to the case of the previously mentioned bulk mixture Hugoniot predictions, shock compression of porous materials can be considered as belonging to one of two regimes- that of intermediate stress, where pores have partially collapsed, so that some of the volume reduction is due to pore collapse but some is due to the material compressing irreversibly, and that of high stress, such that no porosity remains in the material as the material is compressed. The previously mentioned Mie-Grüneisen equation is used for the latter condition. For the intermediate stress case, many complex models have been developed to describe the compaction behavior, but the most widely used is the P-α model[35].

The P-α model separates the compaction of the pores from the compression of the material by the use of a parameter α, variously called the distention or porosity, where $\alpha = V/V_s$, and V is the specific volume of the porous material and V_s is the specific volume of the non-porous parent solid at the same pressure and internal energy. Using the initial porous specific volume V_{00} and the nonporous parent material initial specific volume V_0, the initial porosity α_0 is described by $\alpha_0 = V_{00}/V_0$. At some pressure the porosity is eliminated (the crush pressure P_c) and above that pressure the material is described by the Mie-Grüneisen equation of state or by any applicable EOS for porous materials. Below the elastic limit P_e the material is described by elastic theory. The model describes the crush-up between the two extremes, and relies on the assumption that the specific internal energy of a porous

material is the same as that for the solid material. Therefore, any constitutive equation for pressure $P = f(V_s, E)$ for a parent solid can become $P = f(V/\alpha, E)$ for the porous material. The model was later corrected by Carroll and Holt[36] to include a prefactor of $1/\alpha$, so that the general pressure equation takes the form of $P = (1/\alpha)f(V/\alpha, E)$. In practice the form of $P(V)$ usually taken is

$$P = \frac{[2V_s - \gamma(V_0 - V_s)]C^2(V_0 - V_s)}{[2V_s - \gamma(V_{00} - V_s)][V_0 - S(V_0 - V_s)]^2} \tag{50}$$

which is derived from Equation (13) using the Hugoniot as the reference, the jump conditions, and by assuming the linear shock EOS. If the prefactor is incorporated and V/α is substituted for V_s, the equation becomes

$$P = \alpha^{-1}\frac{[2\frac{V}{\alpha} - \gamma(V_0 - \frac{V}{\alpha})]C^2(V_0 - \frac{V}{\alpha})}{[2\frac{V}{\alpha} - \gamma(V_{00} - \frac{V}{\alpha})][V_0 - S(V_0 - \frac{V}{\alpha})]^2} \tag{51}$$

Any function can be used for α so long as $\alpha(P) \to 1$ as $P \to P_c$, $\alpha(P) \to \alpha_0$ as $P \to P_e$, and $\alpha_0 \geq \alpha \geq 1$. Although any form of $\alpha = g(P)$ can be used, virtually the only form reported in the literature is that proposed by Herrmann[35], a polynomial in P:

$$\alpha = \alpha_0 + \alpha_1 P + \alpha_2 P^2 + \alpha_3 P^3 + ... \tag{52}$$

This form of $\alpha(P)$ is merely an empirical fit. Herrmann proposed using a fourth order polynomial, and values for $\alpha_0, \alpha_1, \alpha_2$, and α_3 can be found in his original work[35]. However, the third order formulation has become the standard[37], in which case α simplifies to

$$\alpha = 1 + (\alpha_P - 1)\left[\frac{P_c - P}{P_c - P_e}\right]^n \tag{53}$$

where P_e is often taken as 0 (indicating that crush-up begin immediately), n is usually 2 (although occasionally n is used as a free empirical parameter[28]), and α_P is the distention at which plastic deformation occurs (often set to α_0 by the same logic that P_0 is often set to zero). To implement the model as described by Equations (51) and (53), a pressure is chosen between P_e and P_c and α is calculated from Equation (53). V is then calculated by solving Equation (51) numerically, keeping in mind that γ is a function of V. If Herrmann's

original model is being used, such that there is no α^{-1} prefactor, the model can by solved by finding $V_s(P)$ using Equation (50) (or whatever form of $P(V)$ is chosen), and then finding V from $V = \alpha V_s$. If the compression of the solid material at P_c is fairly small, $V_s(P_c) \approx V_0$, the model can be further approximated by considering $V = \alpha V_0$.

2.2.3 Reactive Mixtures

The discussions thus far in the section have concentrated on inert mixtures, but mixtures may not remain inert, and often have the potential to react under conditions created by shock loading. The reaction initiation can result solely from the high internal energy conditions present during the shocked state and proceed by normal thermal and transport processes, or by mechanical means where fuel and oxidizer are brought into intimate contact as a result of mechanical deformation, essentially bypassing the thermal transport processes and allowing reaction to proceed almost instantaneously provided there is sufficient internal energy to overcome any activation energy barrier. This section will briefly discuss these reactions and introduce a method by which the Hugoniot of a reactive mixture can be predicted.

The first case presented above, where the reaction proceeds by normal thermal energy and transport processes, is called "shock assisted". Shock assisted reactions occur over the time scale of thermal equilibrium- typically completing after unloading from the high pressure state- and therefore, they do do not affect the measured shock wave equilibrium (Hugoniot) states, nor do they affect any characteristics of the transient shock front. In the second case presented, where the reaction bypasses thermal transport kinetic limitations and has sufficient thermal energy to easily overcome activation energy barriers, the reaction is called a "shock induced" reaction. Shock induced reactions occur within the time scale of the high pressure shock front (tens of nanoseconds or less), or immediately following it, and can drastically influence the shock properties of a material[38]. Familiar explosive detonations are a special case of shock induced reactions where all reaction products are gaseous, but the shock induced reactions in the case of metal-metal, metal-oxide, and metal-polymer mixtures mainly involve condensed-phase reaction products and are treated differently.

Several methods have been developed to predict the Hugoniot of a reactive mixture undergoing a shock induced reaction. One of the most well known analytical methods for determining the Hugoniot of a reactive mixture where the products remain in a condensed state is the Ballotechnic model, first proposed by Graham[3] and further developed by Bennett and Horie[39]. Bennet and Horie derive an expression analogous to the Mie-Grüneisen equation (Equation (13)), except that the new EOS is a constant pressure adjustment, whereas the Mie-Grüneisen equation is a constant volume adjustment. The new EOS is shown below.

$$E - E_S^\star = (V - V_S^\star)\left[\left(\frac{V}{\gamma}\right)^\star \left(\frac{\beta_S}{V_S}\right)^\star - P_S^\star\right] \tag{54}$$

where β_S is the isentropic bulk modulus $-V(\delta P/\delta V)_S$, and the star superscript denotes that the quantity refers to the reference curve: the isentropic compression curve of the dense product material. Using the jump conditions, the equation for $P\delta V$ along the isentrope, and the constant pressure condition, they derived the following equation relating the reaction product Hugoniot (of a potentially porous material) to the dense product isentrope:

$$V_{RP} = \frac{V_S^\star\left[\left(\frac{V}{\gamma}\right)^\star \left(\frac{\beta_S}{V_S}\right)^\star - \frac{P_S^\star}{2}\right] + \frac{1}{2}P_S^\star V_{00} + \int_{V_o^\star}^{V_S^\star} P_S^\star dV_S^\star - (E_0^\star - E_0)}{\left(\frac{V}{\gamma}\right)^\star \left(\frac{\beta_S}{V_S}\right)^\star - \frac{1}{2}P_S^\star} \tag{55}$$

where the RP subscript refers to the volume of the reaction product. Although the model is developed to reference the dense product isentrope, in this study it is assumed that the Hugoniot is equivalent to the isentrope. The same assumption was made earlier in regard to shock wave interactions. In Equation (55) the heat of reaction comes into play through the last term in the numerator $(E_0^\star - E_0)$.

2.3 Time-resolved Diagnostics for Shock Compression Studies

Many techniques have been devised over the years to measure shock-compression variables which allow for the determination of the material's Hugoniot. These techniques typically include exploiting piezoresistive or piezoelectric properties of gauge materials to measure stress, Faraday's Law or interferometry to measure velocity, devices that make or break

electrical connections or create a flash at the moment of impact to record arrival times and thus determine the shock wave velocity, and high-speed or streak cameras to measure material position and arrival times. This list is by no means complete, but merely conveys the breadth of techniques that have been widely used over the past several decades.

The following section will describe two diagnostic systems relevant to the current work to determine the shock response. The two systems are based on very different physical principles, but both systems record continuous traces of one of the shock variables (particle velocity U_P or pressure P) with nanosecond resolution over several microseconds, and are capable of capturing profiles similar to that shown previously in the idealized schematic of Figure 2.1.

2.3.1 Interferometry Particle Velocity Measurements

Velocity interferometry has been used in shock-wave studies since at least the mid-1960s[40], shortly after the development of lasers. Although several types of interferometry have been developed and are routinely used in shock-physics work (for example, Fabry-Perot[41] and PDV[42]), the Velocity Interferometry System for Any Reflector (VISAR), developed by Barker and Hollenbach in the early 1970s, is the most popular. In the VISAR system, or indeed in any interferometry system, laser light reflected from a surface to be measured is doppler shifted as the surface moves, and the reflected light is collected and recombined with a reference beam to create a time-dependent interference signal. In the interference signal, each cycle from fully-constructive to fully-destructive interference is termed a "fringe". The number of fringes created corresponds to the change in position or velocity of the probed surface. A VISAR is slightly more complex than a more familiar Michelson interferometer because the accelerations and large velocities involved create too many fringes too quickly to count using currently available monitoring equipment. The VISAR system skirts this equipment limitation by using a time-delayed version of the collected beam as the reference, rather than using the original laser beam as a reference, as done in the Michelson interferometer. If the velocity changes very quickly, the time delay is shortened so that over each time delay, only a fraction of a fringe occurs. If the velocity changes more slowly,

the time delay can be lengthened to allow enough of a fringe to develop that it can still be accurately measured. The time delay must be chosen prior to each experiment based on an educated guess of the outcome. In this manner, each fringe in a VISAR represents a change in position *per time-delay*, or a change in velocity. Accordingly, the fringe history is recorded and integrated to generate a velocity profile for the surface. This velocity profile is a semi-direct measurement of the particle velocity[43](it is actually a series of direct measurements of particle acceleration). Additionally, there is no physical contact with the surface to be measured, so with the exception of slight adjustments to index of refraction, the measurement is completely unaffected by factors such as pressure, temperature, lateral waves, phase changes, etc. that may occur within the probed material, or other gauge artifacts commonly encountered with contact gauges (such as piezoelectric and piezoresistive gauges). An example of a VISAR trace is shown in Figure 2.5. The trace was obtained by capturing the light scattered from the back surface of an initially-stationary ARMCO iron target impacted by a tungsten-carbide projectile traveling at 615 m/s. The wave profile shown in the figure captures several characteristic features of shock waves, including the elastic precursor, transition to plastic deformation and the shock front (the "plastic wave" in the figure), as well as a shock-induced phase transformation.

2.3.2 PVDF Stress Gauges

Poly(vinylidene-fluoride), or PVDF, is a polymer intensely investigated as a stress gauge in the late 1980s and early 1990s. PVDF gauges exploit the piezoelectric properties of a particular crystalline structure of PVDF to create a self-powering dynamic pressure gauge. PVDF gauges work by maximizing the fraction and orientation of the strongly polar β phase, which has the carbon backbone extended (in the trans configuration), with all fluorine ions on one side and all hydrogen ions (protons) on the other. In addition, PVDF has at least three other polymorphs, the α, γ, and δ phases[44]. The α phase is the most common other polymorph and is the predominant phase present after melt cooling. However, crystallites of α are not polar. The δ phase can be formed by poling the α phase, and is weakly polar, but is not a significant component in the PVDF used in stress gauges. The β phase is favored

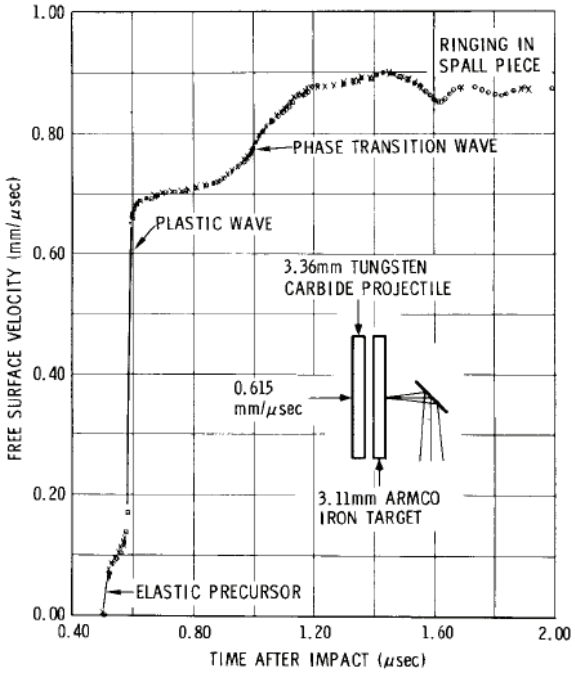

Figure 2.5: An example VISAR trace. The trace shown also serves as a "real" example of a shock wave trace and builds upon the simple schematics shown in Figures 2.1 and 2.8. The "elastic precursor" corresponds to the HEL, which will be discussed in Section 2.4. From Barker[43].

at high pressure and is formed from the melt by crystallization at pressures above about 0.1 MPa[45, 46]. Due to this relatively low pressure threshold, any phase transition that might occur during the shock compression is not visible in published Hugoniot data[47]. Although a few tangential references[48] indicate that the overall percent crystallinity is ∼50%, the relative amounts of the crystalline phases in the poled PVDF used in stress gauges is not known.

Bauer[49] developed a technique to precisely stretch and pole PVDF films so that the piezoelectric properties[50] are repeatable enough to be used as a stress gauge. Mechanical stretching coupled with the application of an electric field increase the percentage of the desirable β phase by aligning the carbon backbone chains and by orienting both the C-H and C-F dipoles[51]. Bauer's method employs biaxially stretching and polarizing the spun film[52]. The measured value of the piezoelectric coefficient d_{33} is generally 22 pC/N, which indicates a high degree of β phase material since the theoretical maximum for d_{33} is 30 pC/N[53, 50]. Typical PVDF gauges for shock stress measurements[54, 55] consist

of a 25μm thick PVDF film with Au/Pt electrodes deposited on either side by magnetron sputtering. The Pt is a bonding layer, and the Au is the main electrical conductor[56]. Reports of the electrode thickness vary slightly in the literature, from 2500Å Au on 500Å Pt[57](for a total thickness of 300nm) to a total electrode thickness of 200 nm[58]. Using Bauer's cyclic poling ramp[56], the material is permanently polarized to 9.2 $\mu C/cm^2$. Early investigators were surprised that such a polymer could be used as a shock gauge because the temperature increase can potentially cause melting and therefore the loss of the crystalline structure necessary for piezoelectricity. However, Samara and Bauer[59] showed that, at least at low pressures (up to 1 GPa), both the ferroelectric transition temperature and the melting temperature were sufficiently pressure dependent that the material could remain crystalline even after the passage of a shock wave and the resulting temperature increase. A PVDF trace from the literature is shown in Figure 2.6. The trace shown was obtained using a tungsten flier traveling at 1167 m/s impacting a stationary copper driver and Al/Fe_2O_3/ 78 $vol\%$ epoxy sample. The PVDF gauge was placed at the copper/sample interface. The figure shows both the current produced by the gauge and the corresponding stress trace, and shows a shock wave rising to $\sim$9 GPa. The pressure trace clearly shows the "ringing up" caused by the impedance mismatch between the gauge and the driver and sample materials. The technique for determining the pressure from the current will be described later in Section 3.2.

A large portion of the work characterizing the PVDF gauges in the pressure range and time scales of interest has been conducted on poly(methylmethacrylate) (PMMA) or other polymers, where the rounded stress profile and slow rise were expected and explained as viscoelastic responses (this will be discussed in more detail later). Although working with gauges embedded in PMMA, Lemar et al.[61] noted a slow, unexplained rise in charge (while working in "charge mode"[62]), when the PVDF gauge was subjected to a "flat topped" shock. In other work, the slow rise should not be present, but is visible in the researcher's data and is not commented on[63, 51, 64]. Setchell[65] reported nearly simultaneous PVDF-VISAR measurements in fused silica (the PVDF gauge and internal mirror were separated by a 1.6mm fused silica buffer). In that work, the PVDF gauge shows a more rounded

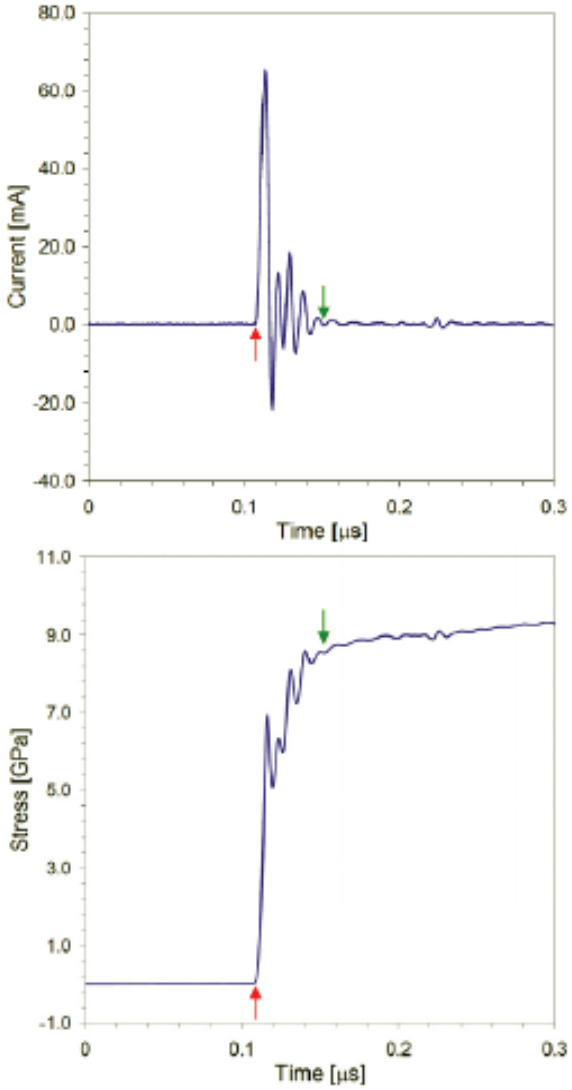

Figure 2.6: An example PVDF trace. At the top is the current produced by the gauge across a known resistance, and at the bottom is the stress trace. The arrows indicate the beginning and approximate end of the pressure rise. From Ferranti[60].

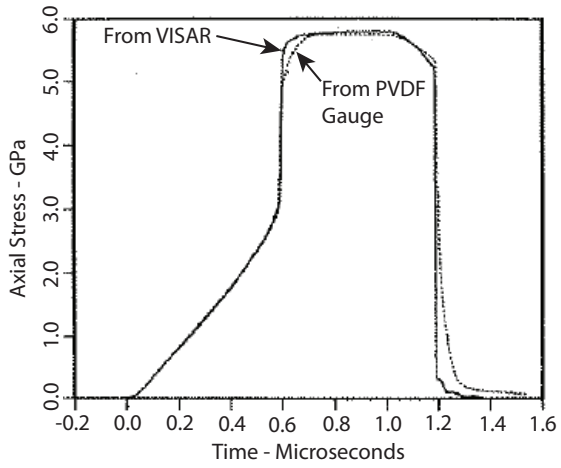

Figure 2.7: Slight variation in PVDF and VISAR traces. The traces shown are from a symmetric impact experiment, where fused silica traveling at 1010 m/s impacted a fused silica driver, sample, and backer. The PVDF gauges and VISAR mirror locations were separated by the thin sample layer. Both show the fully-developed $\sim$3 GPa ramp wave characteristic of fused silica. This is due to an anomalous shock response of fused silica at low pressures and is not discussed in this work. However, note that the VISAR trace and PVDF traces differ slightly where the shock wave transitions to the steady high pressure region. From Setchell[65].

profile, but stabilizes after about 200 nsec, as shown in Figure 2.7. Anderson and Graham identified this unexplained phenomenon as the "PVDF response"[66]. Bauer et al.[67] have attributed the anomalous charge increase to a reorientation of the the small amount of α phase into β phase. The slow rise after the initial shock is possibly absent from much early data because an early PVDF gauge data reduction program developed at Sandia, "PVDF-Auto", automatically determined where the shock was approximately stable, and then subtracted out the positive charge to "correct" the data[68]. The data generated using this approach will therefore have had any small positive slope artificially removed.

2.4 Shock Compression of Ceramics

The question of whether or not ceramic particles completely densify under shock compression is of interest in this work. Hence, the dynamic crush behavior of ceramic particles, along with a representation of dynamic strength, the Hugoniot Elastic Limit (HEL), is briefly reviewed here.

2.4.1 The Hugoniot Elastic Limit

The Hugoniot Elastic Limit, or HEL, is simply the stress at which a material undergoing shock compression no longer behaves elastically. Therefore, it represents a yield strength at the upper limit of strain rate. In the very idealized sketch of the shock wave profile previously shown in Figure 2.1, the shock front was presented as a sharp rise to peak pressure. In ceramics, an initial sharp rise to the HEL is observed, followed by either fracture or a plastic flow regime in which the pressure rises to the peak pressure state, as shown in Figure 2.8(a). The concept of the HEL is also easily visualized in a $P-V$ Hugoniot plot, as shown in Figure 2.8(b). In the elastic region (up to the HEL), the material is shown displaying linear dependence of volume on pressure, and at pressures above the HEL the more familiar compressibility curve is evident. Materials shocked to pressures below state **1** marked on the P-V Hugoniot in Figure 2.8(b) will exhibit the stepped profile shown in Figure 2.8(a). At higher pressures the shock speed will exceed the elastic precursor wavespeed and thus a distinct HEL will not be observed. In polymers and even many metals, the HEL is small enough that it is often not observed in the measured shock profiles and so is not shown in Hugoniot plots (notice that the HEL is absent in the $P-V$ Hugoniot for PTFE shown in Figure 2.2(a)). However, in ceramics it is often a significant feature of the shock compression response.

It should be noted that the HEL provides only a measure of the *initial* yield strength of a material under shock compression. It conveys no information about the post-yield behavior, which can vary substantially. Grady[69] clearly demonstrated this by comparing the particle velocity traces of silicon carbide and boron carbide, as shown in Figure 2.9. Both materials have similar HEL values, but SiC strengthens after yielding, whereas BC does not.

The HEL, ideally, would be the point at which the Hugoniot deviates from elastic theory. Elastic theory shows that in an isotropic material in one-dimensional strain, transverse stress (σ_y) is related to longitudinal stress (σ_x) by Equation (56) below, where ν is Poisson's ratio.

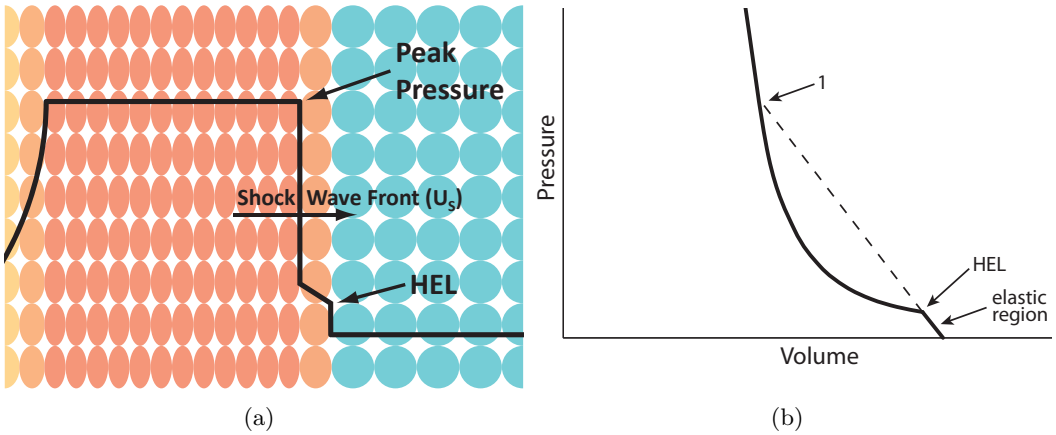

Figure 2.8: The Hugoniot Elastic Limit (HEL). (a) Schematic illustrating the Hugoniot Elastic Limit on the same idealized shock wave as shown in Figure 2.1. The dark line represents a pressure trace, and the colored shapes represent the 1-D strain state of the material. (b) Generic Hugoniot in $P - V$ space, showing the elastic region and the HEL. The dashed line is an extension of the elastic region. If the pressure in the shock wave exceeds the pressure at the intersection point labeled 1, the shock wave will overtake the elastic wave, and no HEL will be visible. Such a shock is often called "overdriven", and no HEL will be visible.

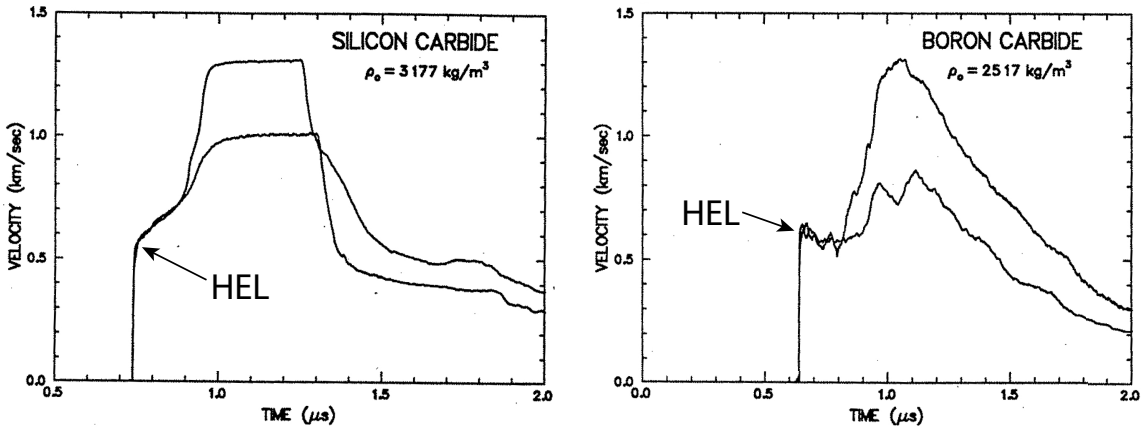

Figure 2.9: Traces from SiC and BC showing similar HEL but varying post-yield behavior. Although these traces are particle velocity vs. time, the particle velocity can be considered as the stress for these purposes. Two experimental data traces are shown for each material- one at a pressure only slightly above the HEL, and another well above the HEL. From Grady[69].

$$\sigma_y = \frac{\nu}{1-\nu}\sigma_x \tag{56}$$

Since the ideal Hugoniot is the hydrostat, the Hugoniot for a material with strength will be offset from the ideal Hugoniot. This is illustrated by Equation (2) for an elastic-perfectly plastic material (constant shear strength and elastic strain after yielding). If we combine Equations (1) and (56) to eliminate σ_y, recall that $2\,\tau$ equals the yield strength Y (from the Tresca yield criterion), and recall that the experimentally measured HEL is actually σ_x, then,

$$HEL = \frac{1-\nu}{1-2\nu}Y \tag{57}$$

For ceramics, typical values of ν are 0.1 to 0.3[69], implying that yield strengths as estimated from elastic-perfectly plastic yield theory are ∼60-90% of the measured HEL.

2.4.2 Ceramic Powder Shock Compaction

The Hugoniot data for a number of ceramic powders is available in the literature. The pressure at which the powder is completely densified (or nearly so) is called the crush strength (or crush pressure) and can be estimated in a number of ways. First, in U_S - U_P Hugoniot space, the high pressure data will be linear, as previously noted. The data will become non-linear once the pressure becomes too low to consolidate the powder, i.e., below the crush strength. From P - V data, the volume of a slightly porous material (such as a powder compact) will approach the solid volume, then begin to rise at a slope similar to (or slightly steeper than) the solid material Hugoniot, similar to what is predicted by the $P-\alpha$ model. The point at which the slope changes rapidly is the crush strength. Lastly, risetime data (from either pressure or particle velocity traces) can be used. In a plot of risetime as a function of pressure, the risetimes for a powder will initially decrease as pressure is increased before reaching a steady state[70]. The pressure at which the steady-state rise time is approached is the crush strength. Additionally, from particle velocity or stress traces, the crush pressure as well as the pressure at which crush begins can sometimes be identified. It should be noted that while the crush strength of ceramic powders is the

compressive stress at which full density is reached, the HEL corresponds to the dynamic yield strength of a solid material. Attempts at correlating the crush strength and the HEL have been made, although the crush strength may also depend on particle morphology and initial density.

The shock response of sintered porous alumina has been reported by Erlich and Curran[71]. Most of the data was at a sufficiently high pressure (20-50 GPa) that no precursor corresponding to the crush strength of the powder is observed. However, three experiments were performed below 10 GPa, one each at 20%, 35%, and 45% porosity, and the data implies a crush strength of ∼3-5 GPa for 20% porous material, and $\sim 2-4$ GPa for 35% porous material. The shock response of $\sim 0.5\mu$m sintered porous alumina has also been reported by Taniguchi et al.[41], where they report that even at pressures of 11.5 GPa the material is not completely consolidated. Bourne et al.[72] reported the HEL of solid alumina to be 6-7 GPa. The lack of agreement between these two reports on sintered alumina is typical of literature concerning shock consolidation of ceramic powder. Furthermore, the solid HEL seems to be loosely related, at best, to the consolidation pressure for sintered powder or porous material. Resnyansky and Bourne[73] report a crush strength for sand (silica) of about 1.25 GPa. Trunin[74] has generated pressure-volume compression plots for a number of different silica initial densities, and though the data is very noisy, it appears that the crush strength is below his lowest data point of ∼2 GPa. Borg et al.[37] experimented on porous silica across a range of porosities and found that the crush strength varied inversely with initial porosity, from 2.85 GPa for $V_{00}/V_0 = 2.9$ (35% TMD)to 0.2 GPa for $V_{00}/V_0 = 22$ (4.5% TMD). Malaise et al.[75] review the available dynamic data on fully dense fused silica and also perform their own tests. They conclude that the HEL is around 9 GPa, although values as low as 6 GPa have been reported. Vogler et al.[76], performing both static and dynamic experiments with tungsten carbide (WC) powder, found a dependence of static compressibility on powder particle morphology. They found that agglomerates of very small WC powders were significantly stiffer in static compression than blocky, solid particles above a threshold of about 0.5 GPa; below that threshold the compressibilities were similar. Vogler et al. also found that WC powder, loaded statically to ∼1.5 GPa, did not

fully densify, but instead went from an initial distention (V_{porous}/V_{dense}) of ∼1.8 to a final distention of ∼1.15. For the dynamic experiments on the blocky WC powder (no dynamic experiments were performed on the agglomerates), the waveform (captured using VISAR) was fully developed after traversing 1 mm of powder, and no elastic precursor was observed, although the possibility of a two-wave structure was not ruled out. Their Hugoniot results on the powder suggest incomplete compaction even at the highest pressure obtained, ∼5 GPa. In a subsequent paper, Borg[77] modelled Vogler's results using CTH and a simplified microstructure. His simulations predicted full densification at around 5 GPa, and he therefore reported that the simulations underpredicted the stiffness of the powder. Millett et al.[78] reviewed the dynamic compression of solid WC and report a HEL of ∼6.6 GPa. The rutile polymorph of titania (TiO_2) powders was investigated by Anderson et al.[70]. Although a definitive crush strength was not established, the results suggest that the crush strength is at or above 6.1 GPa, the highest pressure tested. The HEL of polycrystalline rutile TiO_2 is not found in the literature, but the work of Mashimo et al.[79] on oriented single crystals suggests it is 3-4 GPa.

With the exception of the work by Vogler[76], little work has been done on the effect of powder morphology on shock compression response for ceramics. However, there is slightly more information on the effect of powder morphology in the case of metals, with some work suggesting that shock properties are not strong functions of powder morphology[13], and other work stating that morphology plays a large role[80], especially in the partially compacted, crush-up regime. One especially applicable work by Linde[81] comparing the static and shock compaction response of porous iron, tungsten, and copper shows that these three materials can be shocked to several times the solid HEL and still display porosity in the recovered samples. Tungsten, for instance, has a HEL of ∼ 4 GPA, but still displayed porosity after being shocked to 14 GPa.

There are several reports available in the literature concerning the shock compression and recovery of ceramic powders. It should be noted that shock recovery experiments require robust fixtures which eliminate the one-dimensional shock propagation conditions

employed in making measurements of the shock parameters. Because of impedance differences between the fixture material and the ceramic powders, the powders are subjected to complex two dimensional loading conditions. Hence, the compaction conditions are often reported as calculated values (using impedance matching) or are obtained from two dimensional numerical simulations. Akashi et al.[82] performed several experiments on 10 μm SiC powder at peak pressures from 8 to 13 GPa and reported a recovered density of 98.6% TMD that did not vary with peak pressure. Akashi and Sawaoka[83, 84, 85] also compacted diamond, cubic boron nitride (cBN), and silicon nitride (SiN) powders. With the SiN powder (of 600 nm particle size), they reported a recovered specimen density of 96% TMD which was not a function of the shock pressure at peak pressures of ~20-77 GPa. With diamond powders of 250 nm to 50 μm size, the peak pressure ranged from ~77 to ~108 GPa. For the cBN powder, particle sizes from 2 to 60 μm were investigated at a peak pressure of ~77 GPa. The results for both the diamond and cBN powders indicated that porosity in the recovered specimen decreased with increasing shock pressure and with increasing particle size- i.e., larger particles were more easily densified. However, the remnant porosities were quite different- the 50 μm cBN powder compacted to 98% TMD, while the 50 μm diamond powder only compacted to 89% TMD (both powders were about 60% dense initially). The authors attributed the difference between the diamond and cBN behavior to the high strength of diamond at high temperature. They do not, however, offer an explanation for the dependence of recovered speciment porosity on pressure in cBN and diamond, but not in SiC or SiN. In later work[86], they suggest that some of the diamond was transformed into graphite, potentially complicating the results. There is some evidence in the work by Sawaoka et al. and Bergmann et al.[87, 88, 89] that oxides, which are typically ionically bonded, behave differently under shock loading than carbides, which are typically covalently bonded. In particular, Sawaoka et al.[87] reports that ionic materials showed large amounts of microstrain after being shocked, whereas covalent materials showed primarily a decrease in crystallite size.

A widely accepted correlation between material yield strength, morphology, and the pressure required to fully densify a ceramic powder remains elusive. Meyers et al.[90, 91]

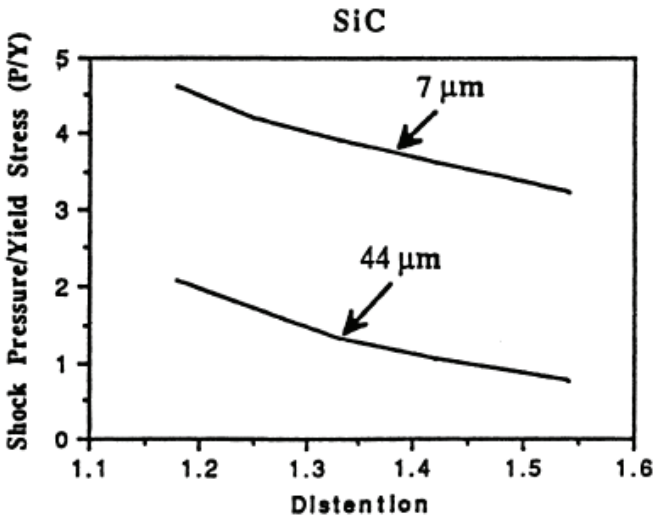

Figure 2.10: Pressure to consolidate SiC powder vs. Initial Distention and Particle Size. From Meyers et al.[91].

have developed an energy-balance relationship between the pressure required to consolidate a material (P_{Con}) and the yield strength, the inter-particle friction coefficient, and several other characteristics. They validated their model by showing that it qualitatively agreed with trends that P_{Con} increases as distention decreases and as particle size decreases for a metal, an intermetallic, and, most notably, silicon carbide. Meyers et al.[91] also correlate P_{Con} to yield strength for diamond and cubic boron-nitride, and showed that a linear relationship between yield strength σ_Y and P_{Con} holds across multiple material classes, indicating that material strength plays a dominant role in P_{Con}. The linear relationship is $P_{Con} = 1.6\sigma_Y + 4$ [GPa]. They use the dependence of the consolidation pressure on yield strength as evidence that void collapse or particle crush-up is occurring before substantial melting can occur. In addition, they present data for SiC showing that P_{Con} actually decreases with initial distention and increases with particle size, as shown in Figure 2.10. They explain the decrease in P_{Con} with initial distention as being due to the additional energy available to melt the interfaces. In the linear relationship, the yield strength σ_Y is determined from the Fischmeister-Arzt equation below[92, 93, 94], implying that a fit to quasi-static compression data can be employed.

$$P = 2.97\rho^2 \frac{\rho - \rho_0}{1 - \rho_0} \sigma_Y \tag{58}$$

From the equation, it is clear that the Fischmeister-Arzt model predicts $P_{Con} \approx 3\sigma_Y$. Although Equation (58) has been developed for spherical particles, irregularly shaped particles have been shown to converge to the spherical solution as compaction proceeds[92]. The density terms ρ and ρ_0 correspond to the final and initial density, and are expressed in terms of fraction of TMD. Although Meyers et al. employed the Fischmeister-Arzt equation, another relationship relating yield stress σ_Y to P_{Con} is also commonly encountered. Known as the Carroll-Holt model[95], it is developed by considering the collapse of a hollow sphere of incompressible elastic-plastic material. It uses the distention α introduced previously in discussion of the $P - \alpha$ model, where $\alpha = V/V_s$, and is given by:

$$P = \frac{2}{3}\sigma_Y \ln \frac{\alpha}{\alpha - 1} \tag{59}$$

These two models, the Fischmeister-Arzt model represented by Equation (58), and the Carroll-Holt model represented by Equation (59), are compared with each other in Figure 2.11. Note that the two models are similar, with two key differences: The Carrol-Holt model does not depend on initial density, and predicts a finite stress to begin the consolidation process. The Fischmeister-Arzt model, on the other hand, does depend on initial porosity (but not for the final P_{Con}) and predicts that consolidation will begin to occur at any pressure.

Very little work is available in the literature addressing the relationship between initial density and P_{Con} in a shock-consolidated material. A rare exception is a work by Kondo et al.[96] on SiC powder. In that work a commercial SiC powder is statically pressed to several initial densities in steel recovery fixtures, then impacted, recovered, and analyzed. The data displays a trend that agrees with those in Meyers et al., where decreasing initial porosity led to increased P_{Con}, and this may well be the source of the SiC trend mentioned by Meyers. However, the data also displays a curious drop in density as the pressure is increased beyond P_{Con} which is unaddressed.

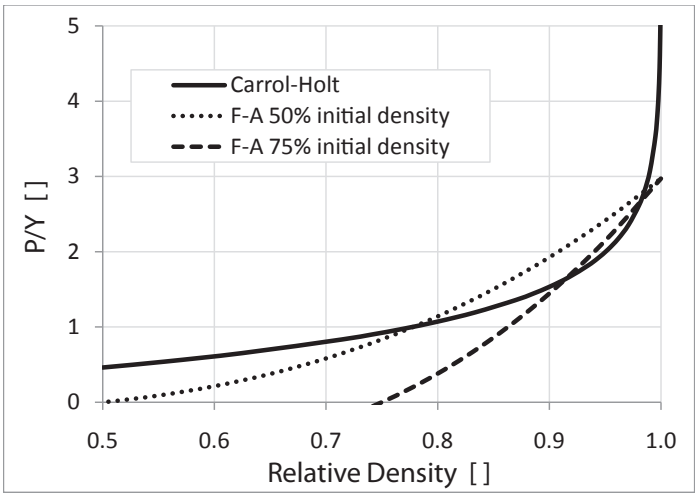

Figure 2.11: Comparison of the Fischmeister-Arzt (F-A) and Carroll-Holt strength-based compaction models. Density is relative to the solid density. Note that the Fischmeister-Arzt model depends on initial porosity, whereas the Carroll-Holt model does not.

2.5 Viscoelasticity, Dispersion, and Shock Compression Response of Polymers

Polymeric materials exhibit unique characteristics under shock compression. One characteristic is the lack of an observable HEL in stress or particle velocity traces obtained experimentally. Another is that the linear U_S - U_P Hugoniots taken at high pressures (more than ∼1 GPa) extrapolate to values of C_0 above the ambient bulk sound speed (C_B) measured ultrasonically. Carter and Marsh[17] discuss this discrepancy between sound speeds and attribute it to either the heterogeneity of polymer properties with respect to the polymer backbone, or to a complex yield mechanism that occurs over a range of stresses, which would likely include the effects of inter-chain and intra-chain anisotropy. A viscoelastic/viscoplastic response has also been used to explain the behavior, and will be discussed in more detail. This failure of the high pressure U_S - U_P data to extrapolate to the ambient sound speed is also sometimes described as curvature in the low pressure $U_S - U_P$ data.

Another characteristic observed in some polymers, and mentioned previously, is viscous behavior. This is usually referred to as viscoelasticity, although it is unclear whether or not the relaxation is actually elastic (it is also sometimes called viscoplasticity). Most investigations of the shock Hugoniots states of polymers focus on the equilibrium response rather than the early, time-dependent response. However, the transient response of a few

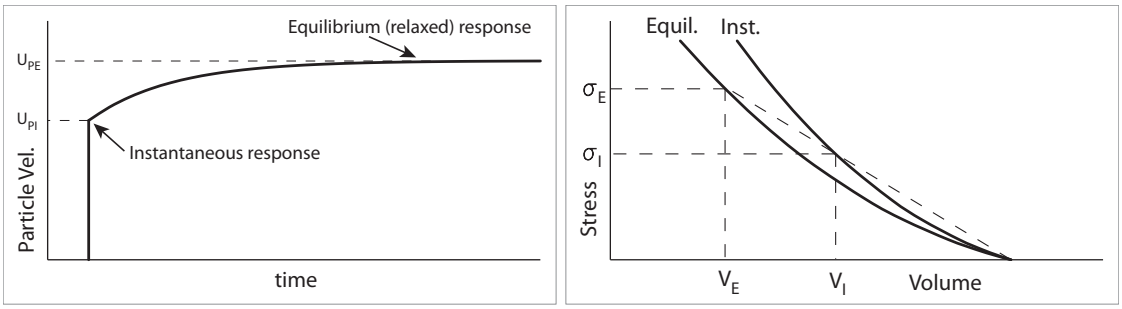

(a) Schematic of particle velocity - time trace showing typical viscoelastic response. Note the quick rise, followed by the slow relaxation to the equilibrium state.

(b) Schematic of instantaneous vs. equilibrium response curve. The straight line is a Rayleigh line, illustrating the initial "shock" to the instantaneous response curve, followed by the gradual transition from the instantaneous to the equilibrium response.

Figure 2.12: Schematic illustrating the "viscoelasticity" effect on observed shock response. Adapted from Schuler[99].

model polymers (such as PMMA) have been studied in more detail. While investigating window materials for the development of VISAR (Section 2.3), Barker and Hollenbach[97] and Schuler[98] performed parallel-plate impact measurements on PMMA up to 2.6 GPa. Using thin-film mirrors embedded in PMMA, they recorded particle velocity profiles that showed an initial shock front where the particle velocity jumped to at least two-thirds of the equilibrium value in a few nanoseconds, followed by a gradual rounding, as shown schematically in Figure 2.12(a). Schuler[98, 99] showed that the gradual rounding develops as the wave propagates until it reaches an equilibrium profile, and can be explained as a consequence of viscoelasticity. The propagation distance required to reach the equilibrium profile is a function of the shock strength (stronger shocks reach equilibrium in a lesser distance). Since then, these profiles have become the archetypal polymer viscoelastic response, and when a profile similar to that shown in Figure 2.12(a) is observed in the particle velocity or stress trace of a polymer, the polymer is said to exhibit a viscoelastic response. Although such a wave profile can be steady, the spreading of a shock front from a sharp input shock to a propagated profile such as that shown in the figure is often called viscous dispersion. This viscous behavior has been observed to disappear in some polymers as the stress is raised beyond a few GPa [100].

The preceding section introduced viscous dispersion, or shock wave dispersion due to

viscoelasticity. However, in polymer composites (or any composite), wave dispersion can also be caused by geometric dispersion from interfaces, leading to profiles which appear similar to those produced by viscous dispersion[101]. In addition, even if it is known that an observed response is due to viscous dispersion rather than geometric dispersion, it is impossible to discern between a viscous decay in the shear stress and a viscous, time-dependent compressibility of the type illustrated in Figure 2.12(b)[3] from pressure or particle velocity traces alone (such as that shown in Figure 2.12(a)). Such a decay in the shear stress was reported in PMMA by Millett and Bourne[103] using a combination of embedded lateral and longitudinal stress gauges. They observed that the lateral stress (σ_y) steadily decreased with time, and they concluded that time-dependent material strengthening based on Equation (1) (presumably the longitudinal stress σ_1 was constant, although this was not shown). They attributed this time-dependent decrease in lateral stress to the viscoelastic/viscoplastic behavior of the material. Using the calculated shear strength they also inferred a value of $\sim$0.9 GPa for the HEL of epoxy by examining when the calculated shear stress (using the shear stress immediately behind the shock front, ie, not taking into account the aforementioned decay) deviated from the relationship predicted by elastic theory (Equation (57)).

Along with PMMA, the shock compression response of epoxy has been investigated by a number of researchers. Munson and May[102] showed that the Hugoniot of epoxies of interest in ALOX (alumina particles in an epoxy matrix) formulations were independent of the hardener used (and therefore independent of the degree of crosslinking), although they only considered one resin- Epon 828. Barnes et al.[104] used an unidentified epoxy, and reported close agreement with earlier work, suggesting that the shock response of epoxy is not only independent of hardener system, but also largely independent of resin used. Ferranti[60] corroborated this by using Epon 826 resin, which has a lower molecular weight than Epon 828. Millet et al.[105] have measured the shear strength (τ) of epoxy using lateral and longitudinal stress gauges. They observed a trend similar to what they reported for PMMA- that although the longitudinal stress (σ_1) remained constant (this was explicitly

[3]Munson and May[102] cite an unpublished Sandia report by Nunziato et al. (SC-DR-70-630) for this statement. The report could not be obtained.

shown in this case) during the time of the experiment above ∼1.5 GPa, the lateral stress steadily decreased, again indicating material strengthening. In a method analogous to that used for PMMA, they also inferred a value of ∼0.5 GPa for the HEL of epoxy. In Estane^{TM}, a thermoset elastomer (a thermoset above the glass transition temperature), Bourne and Gray[106] also reported a steady decrease of lateral stress behind the shock front.

Another model polymer that has been investigated by multiple researchers is PTFE, or Teflon^{TM}. PTFE is an excellent example of a seemingly simple polymer that displays very complex behavior by undergoing a phase transformation. The Hugoniot of PTFE was shown previously in Figure 2.2, and the phase transformation is easily identified in the U_S - U_P plot. Bourne et al.[107] reviewed the past work and demonstrated that the ratio of the release wave speed U_R (the sound speed at pressure) to the shock wave speed U_S can be used to predict the threshold below which curvature in the U_S - U_P Hugoniot becomes apparent. They also explain an observed ductile-brittle transformation in PTFE as a consequence of the phase transformation. In addition to the complex shock compression response due to the phase transition, different researchers have reported different shock profiles in PTFE. For example, in the just-mentioned work of Bourne et al.[107], sharp rises to a constant particle velocity were observed, even after propagating through 7mm of material (giving the viscous waveform time to develop), whilst in other work on very similar PTFE at similar pressures (∼0.7 GPa) and using similar techniques, rounded wave profiles similar to those shown in Figure 2.12 were observed to fully develop after just ∼ 2.5 mm[108]. At much higher pressures (11.7 GPa) the viscous rounding was not present, although no intermediate-pressure experiments were performed to ascertain the point at which the viscous behavior began to disappear.

THV is a thermoplastic terpolymer of tetrafluoroetheylene, hexafluoropropylene, and vinylidene fluoride (TFE-HFP-VDF, or THV), and is available in several variants that differ in monomer ratio and/or molecular weight, including THV 500 and THV 220. The monomer ratio for THV 500 is 59:19:22 by weight[109]. Dattelbaum et al.[110] recently investigated the static and dynamic high pressure response of THV 500 in order to determine the phase stability behavior and equation of state. Evidence of a possible phase transition at 4 GPa

was reported, along with a linear equation of state in the shock velocity - particle velocity plane ($U_S = 1.60[km/s] + 2.05U_P$). THV 220 has a different monomer mix and molecular weight[111], but the exact formulation is not available in open literature.

Unlike epoxy or Estane^{TM}, THV is a thermoplastic, and so is not crosslinked. Therefore, THV may not display the increase in shear strength (decrease in longitudinal stress) behind the shock wave similar to that seen in epoxy. Bourne and Gray[106] investigated Teflon, the primary constituent of THV, as well as Kel-F-800^{TM}(poly(chlorotrifluoroethylene), or PCTFE), and reported a constant lateral stress for the duration of the 1D shock pulse, indicating no increase in shear strength as a function of time. However, decreasing lateral stress was reported by Bourne and Millett[112] for polyethylene, PVC, and PMMA, indicating that thermoplastics can also display strengthening during shock compression. No studies examining the influence of crystallinity or molecular weight on this strengthening effect have been reported.

Millett et al.[113] have investigated the shock EOS for Viton^{TM}B, a fluorinated tripolymer containing the same monomers as THV. However, little is known about the precise composition or morphology of Viton^{TM}B (it is proprietary) or exactly what trace additives may be present, other than that the fluorine composition is 68% by weight. Unfortunately, this information is insufficient to determine the fractions of the monomers or to otherwise determine exactly how Viton^{TM}B differs from THV. The EOS for Viton^{TM}B was reported to be $U_S = 1.88[km/s] + 2.37U_P$.

2.6 Shock Compression of Polymer-Particle Composites

Polymers have long been used as a binder phase in explosives and propellants, as encapsulants for explosive components, and in structural composite materials subject to dynamic loading. Therefore, the shock response of many polymer composites has been investigated. However, the explosive polymer composite systems are easily initiated by shock, and so wave profile data is complicated by reaction energies[114]. There are, however, a few exceptions where the shock compression response of inert polymer/particle composites has been investigated.

Hydroxyl-terminated polybutadiene (HTPB) is a rubber commonly used as a binder in explosives. Millett and Bourne[115] investigated an inert analogue to an explosive using sugar crystals dispersed in HTPB. They reported that the coarse (160 μm) sugar displayed a higher shock impedance than the smaller crystal sugar (16 μm). They mentioned that this result was unexpected, and attributed it to the larger crystals preventing material flow, and therefore raising the shear strength, of the composite. They also questioned whether any chemical interactions at the sugar/HTPB interface influenced the results. Millett et al.[116] then investigated soda-lime glass spheres distributed in HTPB. Again, they reported that the larger-particle composite displayed higher measured impedance, but similar hydrostatic behavior, than the small-particle impedance. They therefore concluded that the phenomenon was due to the larger particles preventing material flow (effectively increasing the shear strength) rather than a surface interaction.

Most of the shock compression studies on inert polymer-particle composites has been performed on the alumina powder/epoxy (ALOX) system due to its use as an encapsulant and as a model system. Investigating ALOX composites with 20%, 30%, and 43% alumina particles by volume with Epon 828 resin and hardener "Z"[117], Munson et al.[118, 119] performed an extensive set of impact experiments in the pressure range of 1-3 GPa with the goal of validating a model for estimating the shock response of a particle composite. They noted higher release wave speeds than expected, and hypothesized that although the epoxy should control the compression response, the high sound speed measured at pressure indicated that the alumina was playing some part in the release response. Millett et al.[120], using a setup of transverse manganin gauges identical to that used in their previously mentioned-work on epoxy[105], examined an ALOX material with different epoxy and alumina sizes from that used by Munson et al.[119], and reported a very similar Hugoniot[121], and an inferred HEL of 1.6 GPa for the composite[120], but no measurable time-decay of lateral stress, as seen in the case of pure epoxy. They attributed the lack of time-decay to a dilution effect. Setchell and Anderson[122] examined the 43% ALOX mixture used in the earlier work of Munson et al.[119] and extended the data to pressures of $\sim$10 GPa, again noting the high release

wave speeds, and also noting the slowly-rising, S-shaped shock wave profile at low pressures. They explained the "lazy S", sigmoidal profiles as being due to the matrix viscously opposing particle reorientation during the passage of the shock front, and demonstrated that changes in initial temperature (and therefore matrix viscosity) had a large effect on the shock front profile. Setchell et al.[123] have also examined the effects of different sizes, shapes (aspect ratios of 1 to ∼1.5), and loading fractions of alumina in ALOX, and found that small round particles, as well as compositions with lower alumina fraction, displayed less of the S-shaped wavefront profiles, again confirming their hypothesis that the viscous matrix opposes particle reorientation and causes the S-shaped wave profile. However, they found that size and shape of the particles had little effect on release wave speeds.

It should be noted that in polymer composites, or in any non-homogenous material (such as a porous material), the shock front at the mesoscale will not actually be a plane moving through the material, as implied in the idealized scematic in Figure 2.1. Instead, the shock front will have some thickness corresponding to the length scale of the heterogeneities. The thickness of the shock front can manifest itself as a finite time for the pressure to fully develop at a material location (a finite "rise time"), instead of the instantaneous shock front described previously. The thickness of the shock front can be measured by spatially sensitive diagnostic techniques, or indirectly by assuming that the shock wave rise time corresponds to the time for the full thickness of the shock front to pass the diagnostic device. In addition, the shock front thickness can be studied by computationally modeling the material. Recently, actual (as opposed to idealized) microstuctures have been used to generate computational models of shock waves propagating through a Ni-Al composite, and the resulting images, shown in Figure 2.13, illustrate the concept of shock front thickness due to heterogeneity.

In this work, the shock compression behavior of THV-matrix composites (75 % by volume) reinforced with 25% by volume of 1, 10, or 100 μm Al_2O_3 particles or 10 μm ZrC particles was determined via gas-gun experiments using PVDF stress gauge measurements. In addition to these basic measurements, this work will demonstrate:

1) The dispersive characteristics of the shock front display traits intermediate between

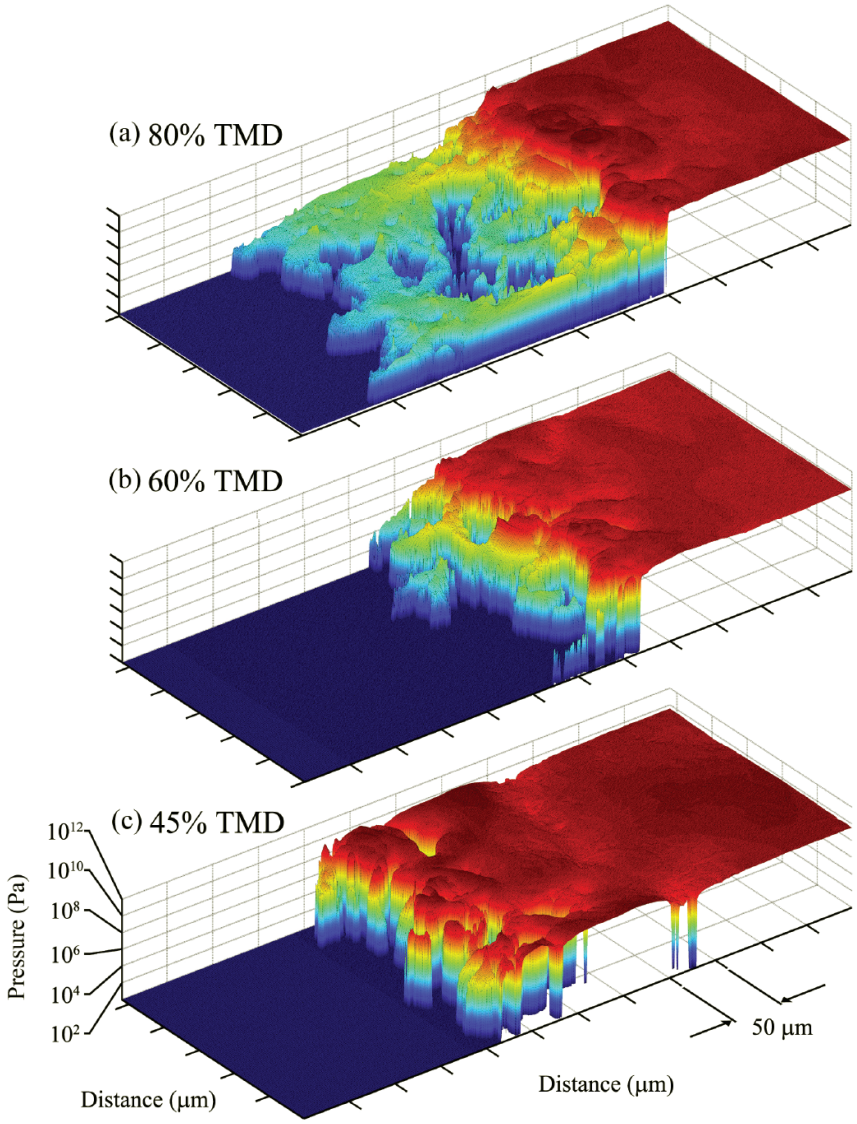

Figure 2.13: Pressure surface in Ni-Al composites of various initial porosity (given as a percent of theoretical maximum density, or TMD), illustrating the shock front thickness (and the corresponding rise time) in heterogeneous media. All three plots represent the same particle velocity in the composite media, and the shock front thicknesses were observed to be steady. From Eakins[124].

those typical of fully dense solids and powders.

2) The Hugoniot of a nonporous composite made of polymers and ceramic particles can be reasonably predicted by several analytical models from the literature, although for all composites, the Hugoniot stiffness is underpredicted. As the porosity of the composites increases, the underprediction increases.

3) The size of the particles does not contribute to the high strain rate strength or the Hugoniot response, at least within the uncertainty caused by the porosity.

4) The Grüneisen coefficient of polymers as calculated by the equations presented thus far is too low. Considering higher Grüneisen coefficients brings the predictions of the shock response into much better agreement with the experimental results, and can help explain a disagreement between PVDF stress gauges and VISAR particle velocity gauges. A new form of the Grüneisen coefficient is proposed.

CHAPTER III

EXPERIMENTAL PROCEDURE AND CHARACTERIZATION

This chapter will introduce the materials used in this work and detail the basic characterization procedures that were employed. It will also present the more-specialized experimental methods used to determine the Hugoniot, and explain the setup, assembly, and basic analysis of the data generated from the tests. The computational methods employed to explore the shock-compression behavior of the materials will also be described.

3.1 Materials and Characterization

The THV and THV composites were supplied by NSWC-Dahlgren through a contract manufacturer, ATK, as part of a project to investigate the response of the as-manufactured material. Although it would have been desirable to have more homogeneous composites (as discussed in the section on the THV composites below), the system tested in this work was part of a larger design of experiments. Optimizing the manufacturing process for the tested composites was beyond the scope of this work.

3.1.1 THV

THV was received in several forms, including small discs 50.9 mm in diameter and 4 mm thick, large discs 102 mm in diameter and 51 mm thick, and small cylinders 7.6 mm in diameter and 51 mm long. The density of the samples was nominally 2.00 g/cm^3 as measured using the immersion density technique and was consistent across the sample geometries received. The melt temperature (T_m) was $\sim 157°C$ and the glass transition temperature (T_g) was $\sim 25-30°C$, as determined by differential scanning calorimetry performed at a heating rate of 10°C/min. T_g measured by DMA was $\sim 40-42°C$, using 1 Hz oscillation frequency, 10°C/min heating rate, and a tension fixture. A mottled appearance was observed in the rod samples, as shown in Figure 3.1. This mottled appearance was not observed in the disc samples, perhaps because they were from a different lot and had a different thermal history

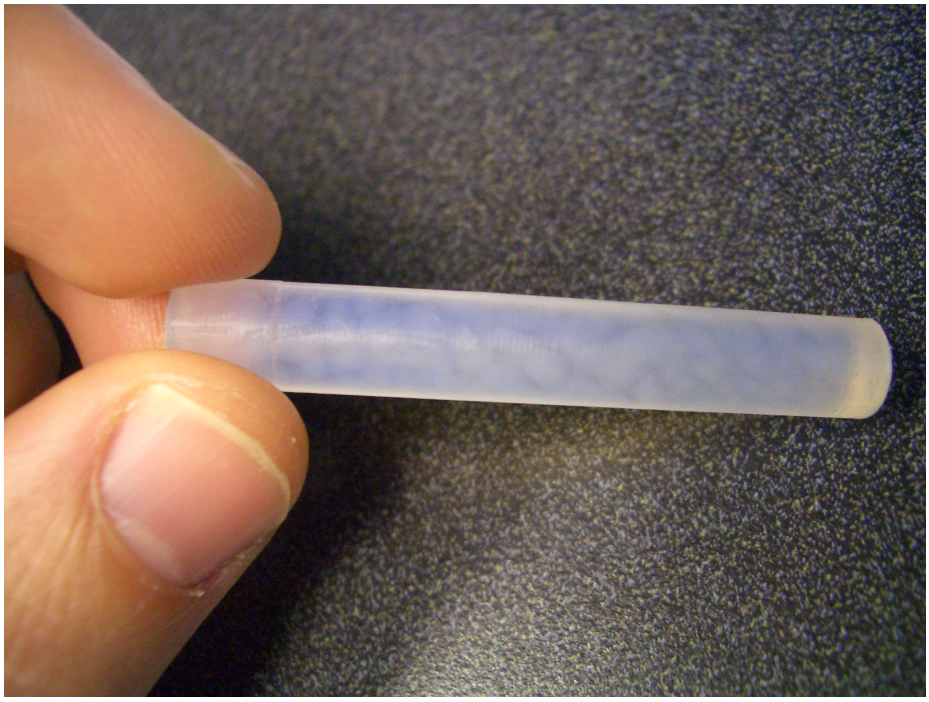

Figure 3.1: "Mottled" appearance of rod-shaped THV specimens

from the other samples[125]. The measured density, T_g, and T_m are in good agreement with the samples investigated by Dattelbaum et al.[110]. X-ray diffraction (XRD) was also performed on the THV sample. The XRD trace, shown in Figure 3.2, agrees very well with that of Emmons et al.[126].

3.1.2 THV - Ceramic Composites

Four types of ceramic particle-filled composites with THV matrix were used in this study. All materials were made by ATK for NSWC-Dahlgren. Images of the composite discs are shown in Figure 3.3.

The composites consisted of a THV matrix with 25% by volume of either 1, 10, or 100 μm alumina (Al_2O_3), or 10μm zirconium carbide (ZrC) particles. The THV was composed of 95% by weight THV 500 and 5% THV 220. This matrix is assumed to have properties essentially equivalent to THV 500, and is hereafter referred to as THV. The particles sizes stated above are nominal sizes. Actual sizes of the particles, as measured by the supplier, ATK, using laser diffraction, are given in Table 3.1. The 1 μm alumina was a fused alumina

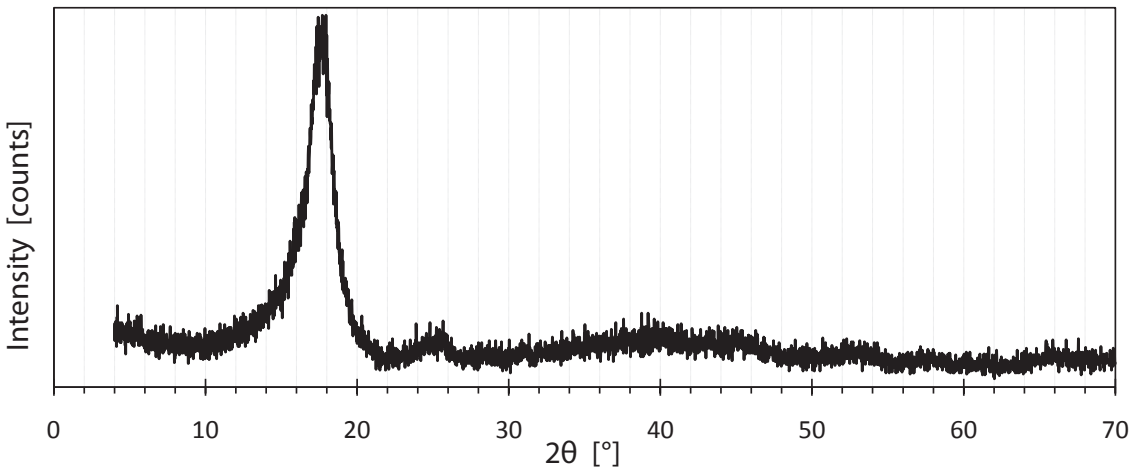

Figure 3.2: XRD trace for THV, acquired using Cu Kα_1 radiation. The peak position agrees with the study by Emmons et al.[126] using higher energy radiation.

powder (Atlantic Equipment Engineers (AEE) AL-601), whereas the 10 and 100 μm alumina were crushed powders (Unibrite White Aluminum Oxide, 600 grit and 150 grit respectively). Microstructural characterization of the Al_2O_3 composites revealed that the fused 1μm Al_2O_3 particles were not fully dense, but instead were made of small $\sim$0.25 μm alumina particles fused into porous spheres of 1-24 μm diameter, as shown in Figures 3.4(a) and 3.4(b). The other Al_2O_3 particles appear blocky as revealed by the morphologies shown in Figures 3.4(c), 3.4(d), and 3.4(e). Morphological characteristics of the ZrC powder were not provided. The composites were prepared by ATK using a hot-pressing operation at 176-180°C, but no futher information about the manufacturing process was available. The reported melting point of THV 500 is $\sim$160°C[110]). SEM images of the pressed Al_2O_3 composites are shown in in Figure 3.5. Despite the processing temperature being above the melt temperature, it can be seen that the THV does not fully penetrate into the 1 μm Al_2O_3 particles (Figure 3.5(b)). The poor degree of infiltration in the 1 μm composite, as well as the overall heterogeneity of the Al_2O_3 composites is illustrated in Figure 3.5. Figure 3.6 illustrates similar heterogeneities in the ZrC/THV composite microstructure (pure THV and mixed phase areas). In general, all composites are characterized by pure THV regions $\sim$0.5 mm in size, surrounded by mixed-phase porous regions of ceramic particles and THV. The ceramic particles appear to be in contact with one another, forming a continuous powder phase. The

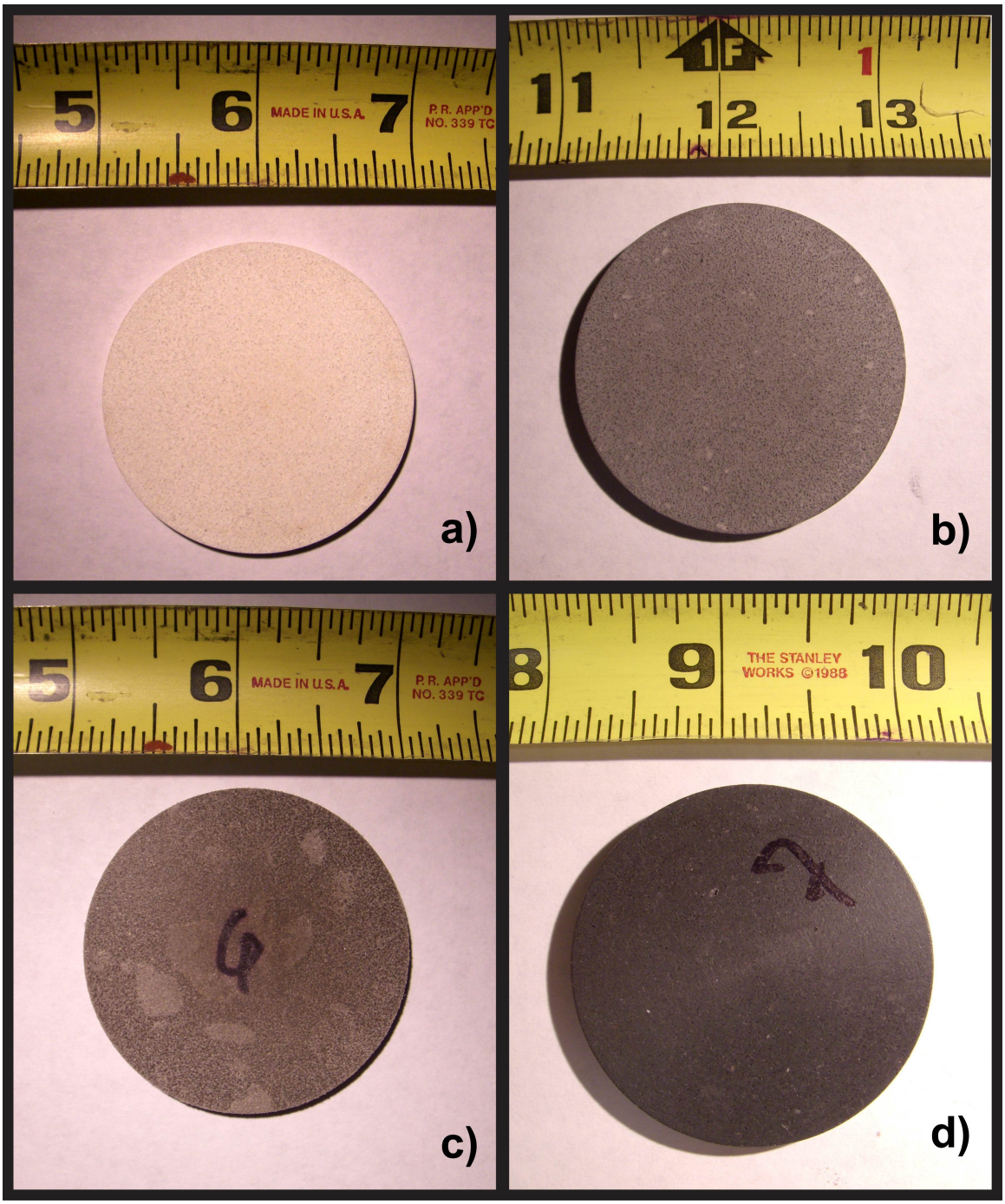

Figure 3.3: As received ceramic/THV composite discs. a) 1 μm Al_2O_3/THV composite. b) 10 μm Al_2O_3/THV composite. c) 100 μm Al_2O_3/THV composite. Note similarity of 10 and 100 μm Al_2O_3/THV composites. d)10 μm ZrC/THV composite.

Table 3.1: Particle sizes for ceramic particles

Material	Nominal Size	Avg. actual size	Size range[a]
Al_2O_3	1 [μm]	6 [μm]	2-24 [μm]
Al_2O_3	10	8	3-16
Al_2O_3	100	109	55-178
ZrC	10	_[b]	_[b]

[a] As reported by ATK, using laser diffraction. Size ranges given account for 90% of particles, ie, the tails of the distribution are truncated.

[b] ATK did not take data for the ZrC particles before mixing and pressing. Size range determined using micro X-ray computed tomography of composite. Minimum size limited by instrument resolution.

pure regions are thought to correspond to the original ground particles of THV that were not completely melted and mixed in the hot-pressing operation. Although all composites held together sufficiently well for handling, the 1μm Al_2O_3 material was crumbly and was easily broken because of the poor infiltration of the THV between particles and the cracks, as shown in Figure 3.5(a). The composites were difficult to polish because of the rubbery behavior at room temperature and the ease with which the particles pulled out, essentially limiting the minimum grit size since the particles themselves became abrasives once free of the matrix. As a result, it was not possible to polish the composites to better characterize the porosity. Measured Archimedean densities and sound speed data for the various composites are given in Table 3.2. The sound speed measurements were challenging due to attenuation of the higher frequencies and dispersion. The sound speed was also sensitive to pressure on the transducers, especially in the case of the 1 μm Al_2O_3 composite. The main frequency component of the longitudinal signal was 0.8 MHz, and that of the shear signal was 0.5 MHz. Higher frequencies were too attenuated to measure. The table also includes the densities and sound speeds of components obtained from the literature.

The composite discs were examined with XRD. The alumina composites appeared to be mixtures of alumina and THV, as shown in Figure 3.7. However, the ZrC composite's XRD trace did not match available ZrC data. Instead the trace appeared to have THV and cubic ZrC, as expected, but also included significant amounts of monoclinic zirconia (ZrO_2), along with what may be orthorhombic or tetragon zirconia and some small amount of what may be graphitic carbon, hexagonal quartz, and other impurities, as shown in Figure 3.8.

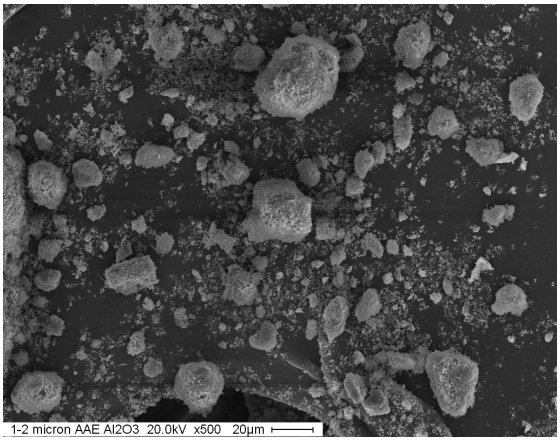

(a) 1 μm AEE Al_2O_3 powder at 500x.

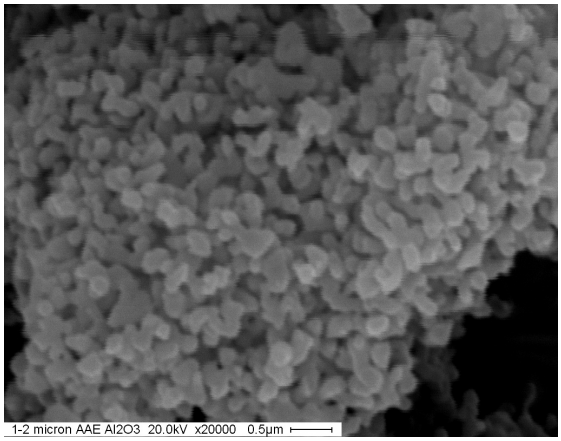

(b) 1 μm AEE Al_2O_3 at 20kx showing porosity in aggregates.

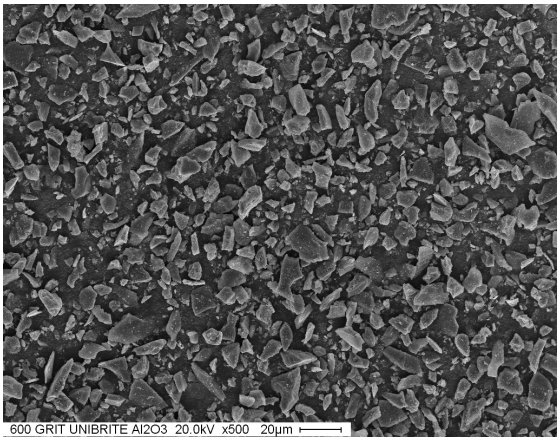

(c) 10 μm Unibrite Al_2O_3 powder at 500x.

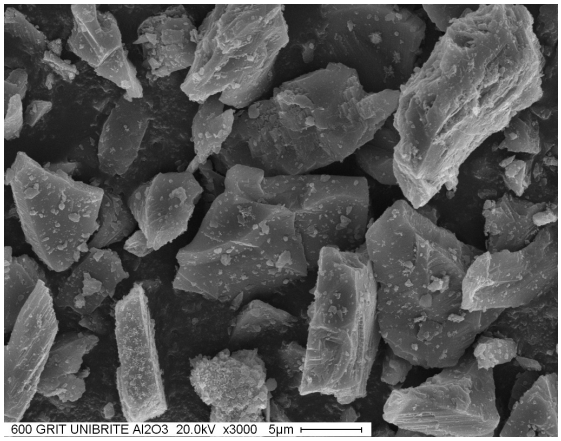

(d) 10 μm Unibrite Al_2O_3 powder at 3000x.

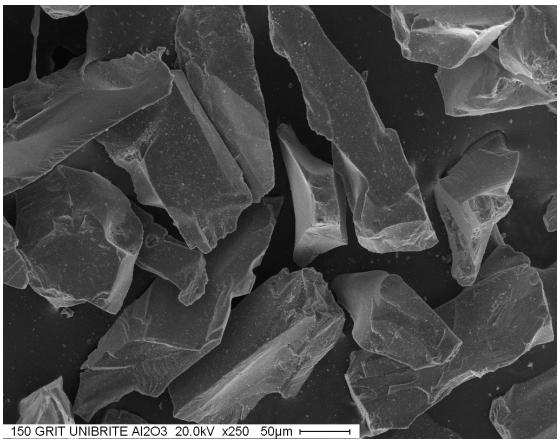

(e) 100 μm Unibrite Al_2O_3 at 250x. Note similarity between 10 and 100 μm Al_2O_3 powders.

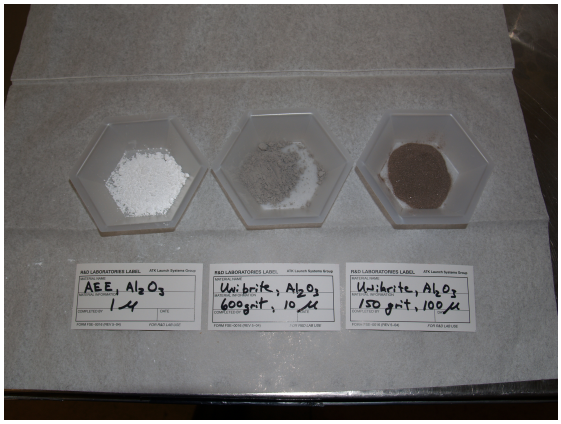

(f) Optical images of each Al_2O_3 powder before mixing. Note that only the AEE powder is white- the other two are tan, also indicating contamination.

Figure 3.4: Initial states of alumina powder as obtained from ATK. Images provided by ATK.

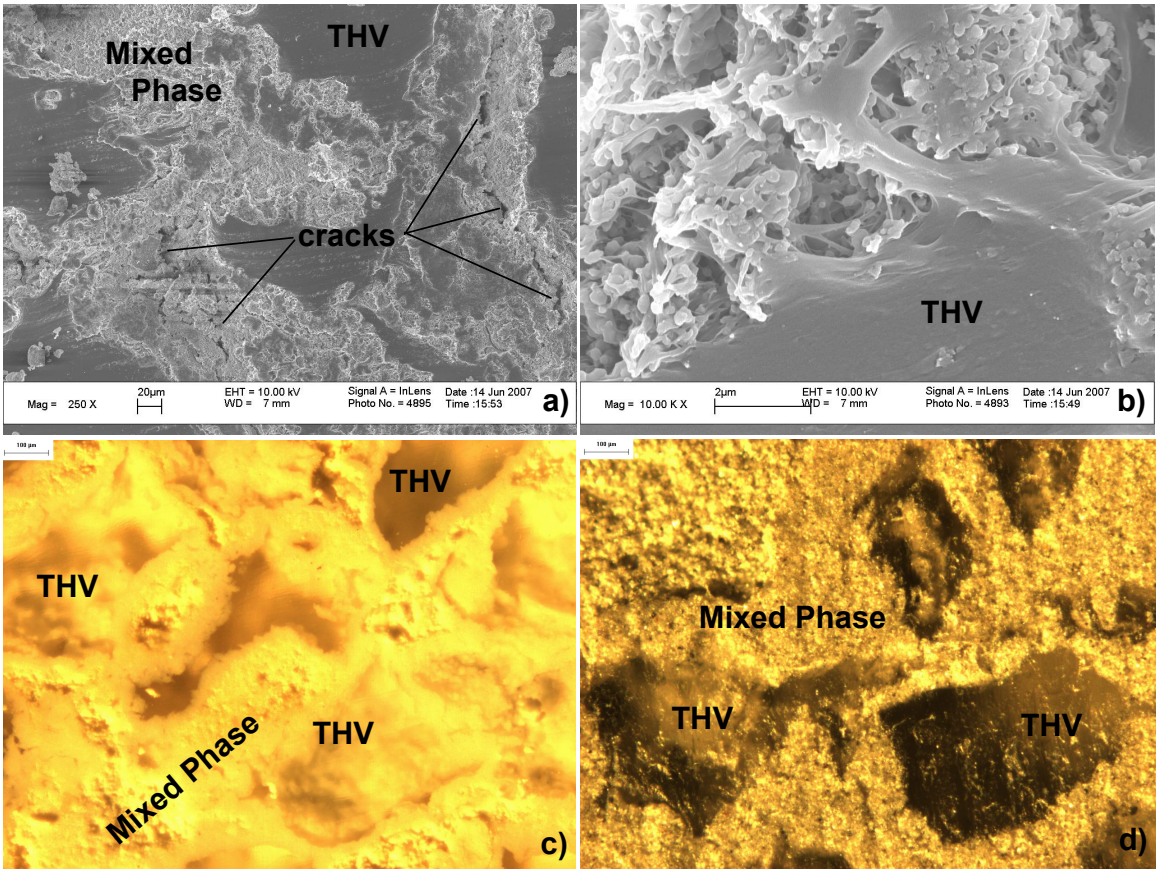

Figure 3.5: Initial states of Al_2O_3 composite materials a) 1μm Al_2O_3 / THV composite at 250x. Note regions of pure THV surrounded by regions of porous alumina and cracks in alumina-filled region. b) 1μm Al_2O_3 / THV composite at 10kx. Note poor infiltration of THV into fused alumina c) Optical image of 1μm Al_2O_3 / THV composite at 50x. The clear material is pure THV. d)10μm Al_2O_3 composite at 50x. The 10 and 100 μm composites looked very similar. They did not have the cracks separating the THV particles (as the 1 μm material did), but were still very inhomogeneous, as shown.

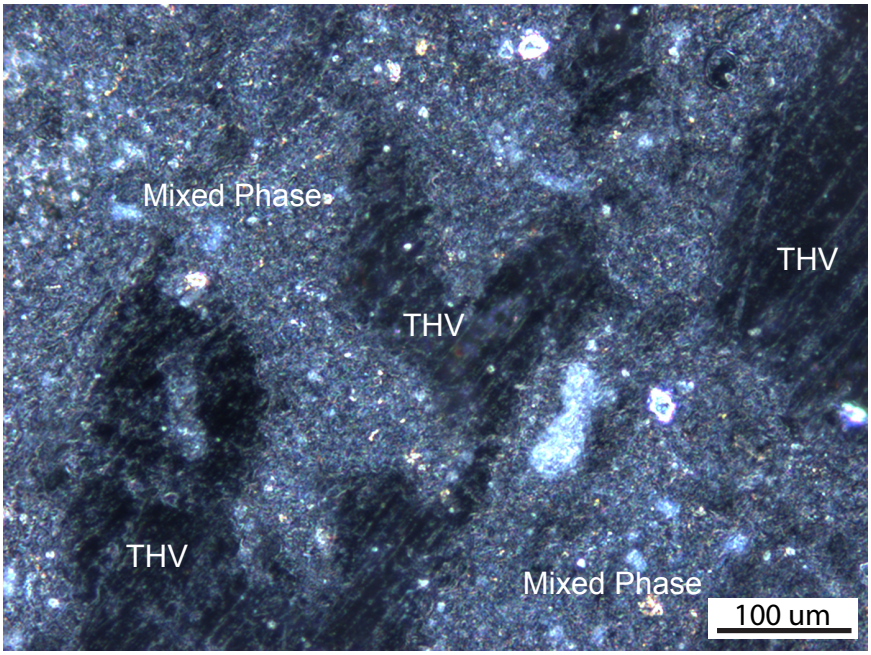

(a) 10μm ZrC / THV composite at 200x.

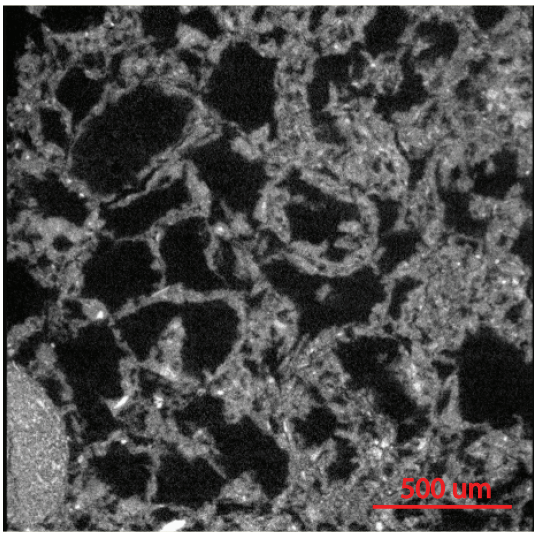

(b) 10μm ZrC / THV composite taken using computer-aided x-ray tomography. Parallel to axis of cylindrical specimen.

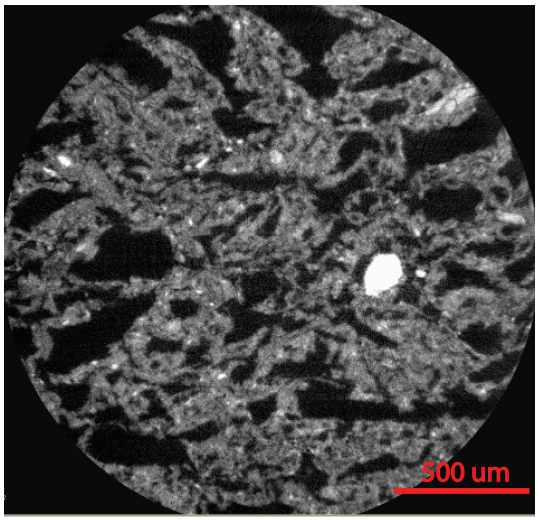

(c) 10μm ZrC / THV composite taken using computer-aided x-ray tomography. Perpendicular to axis of cylindrical specimen.

Figure 3.6: Initial states of ZrC composite materials. a) is an optical image. b) and c) are generated using computer-aided x-ray tomography. Dark regions are low density, brighter regions are high density. The white spots are large ZrC particles. Note regions of pure THV (black regions) surrounded by regions of mixed-phase, porous THV/alumina (grey regions). Both images are courtesy of Brian Patterson at Los Alamos Nat'l Lab.

Table 3.2: Density, Porosity, and Elastic Properties of Components and Composites

Material	Nom. Size [μm]	TMD [g/cm^3]	Act. Dens.[a] [g/cm^3]	Porosity[b] [%]	c_L [$\frac{mm}{\mu sec}$]	c_S [$\frac{mm}{\mu sec}$]
Al_2O_3[107]	bulk	–	3.95	–	10.66	6.28
ZrC	bulk	–	6.72	–	8.5[c]	5.6[c]
THV 500[111]	bulk	–	2.00	–	1.44	0.46
Al_2O_3/THV	1	2.49	2.09±.06	15.9±.02	1.17±.12[d]	0.67±.07[d]
Al_2O_3/THV	10	2.49	2.42±.02	2.6±.01	1.51±.07[d]	0.70±.03[d]
Al_2O_3/THV	100	2.49	2.46±.02	1.4±.01	1.30±.07[d]	0.65±.03[d]
ZrC/THV	10	3.18	2.82±.03	11.4±.01	1.33±.07[d]	0.65±.03[d]

[a]Measured by Archemedean immersion density and validated by mass and volume measurements.

[b]Calculated from theoretical max density and actual density.

[c]Values shown are from theoretical calculations of Cheng et al.[127]

[d]c_L and c_S measured using impulse loading with 2 MHz transducers. The materials were challenging to measure due to attenuation of the higher frequencies and were very dispersive. The sound speed was also sensitive to pressure on the transducers, especially on the $1\mu m$ material. The main frequency component of the longitudinal signal was 0.8 MHz, and that of the shear signal was 0.5 MHz. Higher frequencies were too attenuated to measure.

The presence of oxygen in some of the particles (and not in the THV or in other particles) was confirmed with EDS. EDS also confirmed the presence of primarily carbon, fluorine, zirconium, and oxygen, although some particles containing large amounts of aluminum, magnesium, and silicon were found. Because the pedigree of the ZrC is unknown, and because there are clearly impurities in the composite, it could not be ascertained whether the powder was actually ZrC when it was measured for mixing and was oxidized and contaminated at a later point, or whether the powder contained zirconia and impurities when it was measured and mixed. It is known that ZrC will readily oxidize to zirconia in the presence of oxygen at elevated temperatures[128], and Shimada[129] has shown that in addition to oxidizing at 380°C in air, free carbon is formed once oxidation begins and remains until it oxidizes to CO_2 at 700°C. Therefore, it appears that the ZrC may have been, at some point, sufficiently heated in the presence of oxygen to partially oxidize, but was not heated sufficiently to burn off the carbon. The presence of the free carbon may also explain the black appearance of the ZrC/THV composite (see Figure 3.3). The relative volumetric concentrations of the ZrC and ZrO_2 phases was determined by taking the area under the main peaks for each phase, as calculated using a peak fitting algorithm. The use of this method assumes that zirconium carbide and zirconium oxide have similar X-ray mass absorption

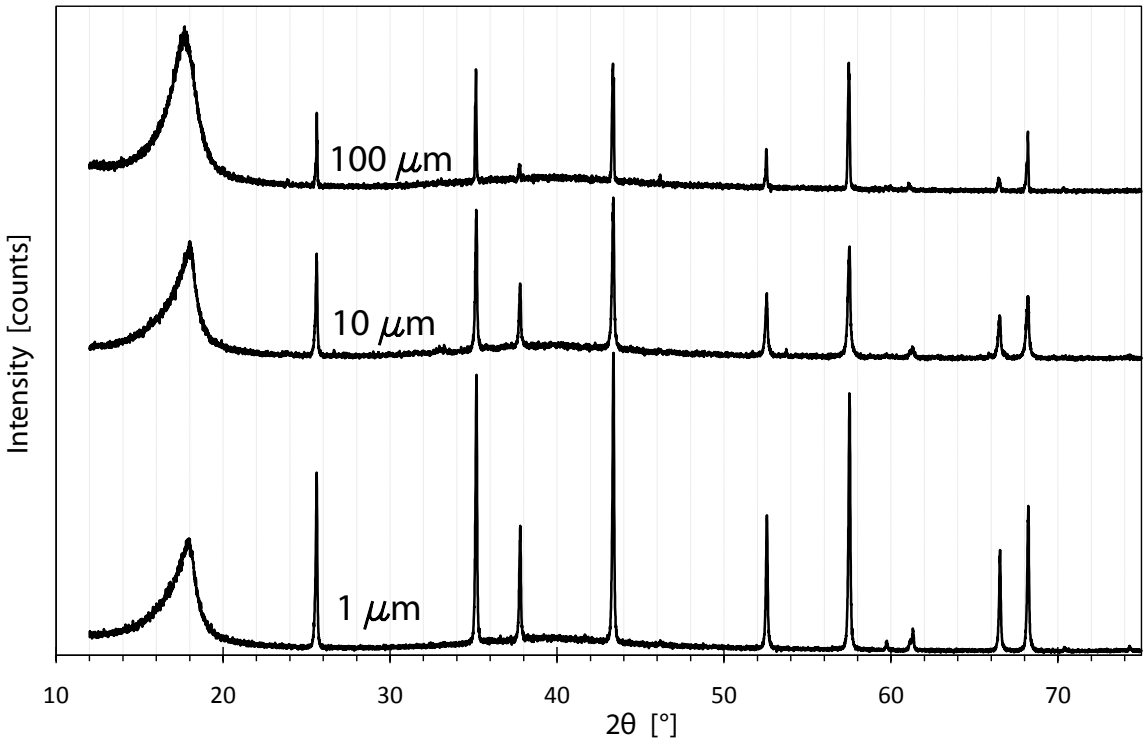

Figure 3.7: XRD Patterns for Al_2O_3/THV composites, acquired using Cu Kα_1 radiation. The broad peak at ∼17.9° and amorphous hump at ∼40° visible in all traces is due to the THV. Otherwise, the 1 μm Al_2O_3/THV composite pattern is almost identical to corundum alumina reference XRD files. The patterns for the 10 and 100 μm Al_2O_3/THV composites also have peak positions corresponding with corundum alumina, although the relative intensities do not match as well. There is only minor evidence of impurities in the traces for the 10 and 100 μm Al_2O_3/THV composites.

coefficients, and is a rough estimate. The ratio of the calculated volumetric concentrations X is $X_{ZrC}/X_{ZrO2} \approx 1.25$. Although there is clearly significant contamination in the ZrC/THV composite, and it should more correctly be called the ZrC/mZrO_2/other/THV composite, for convenience the composite is simply called the "ZrC/THV composite" in this work. Only when analysis is performed examining differences between ZrC and ZrO_2 will the distinction again be made.

3.1.3 Alumina Powder

The 1 μm AEE alumina powder and a powder similar to the 10 μm Unibrite alumina powder which were used to create the composites described above were obtained separately from the respective manufacturers. Unibrite no longer manufactures the 600 grit powder,

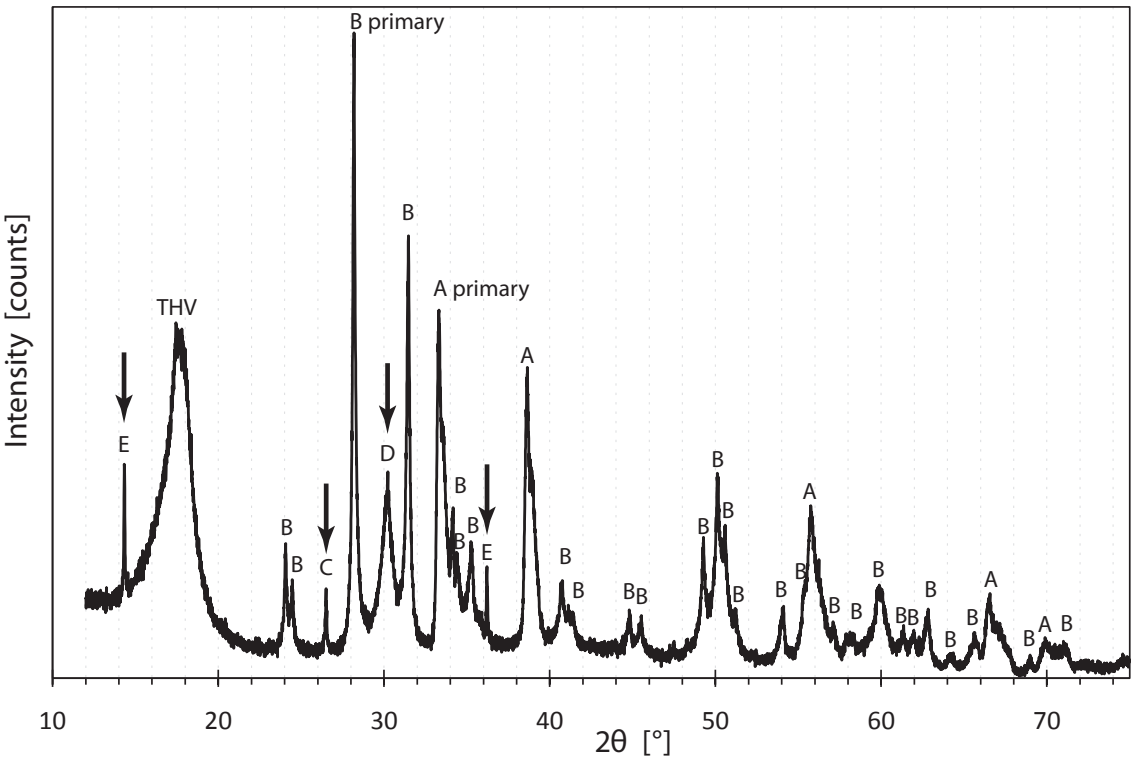

Figure 3.8: XRD pattern for ZrC/THV composite, acquired using Cu Kα_1 radiation. The peaks labeled "A" correspond to ZrC and the peaks labeled "B" correspond to monoclinic ZrO_2. The four unidentified peaks are marked with arrows, and represent impurities. "C" may indicate some carbon in the form of graphite or hexagonal (β) quartz (recall that Si was detected in the sample), and "D" may indicate either an orthorhombic or monoclinic phase of ZrO_2. The origin of the peaks labeled "E" at 14.32° and 36.21° are not clear. The broad THV peak is also visible. The two peaks labeled "primary" are the highest intensity peaks for the "A" and "B" phases used to approximately calculation the relative concentration of the two phases using peak fitting and integrating the area under the peak.

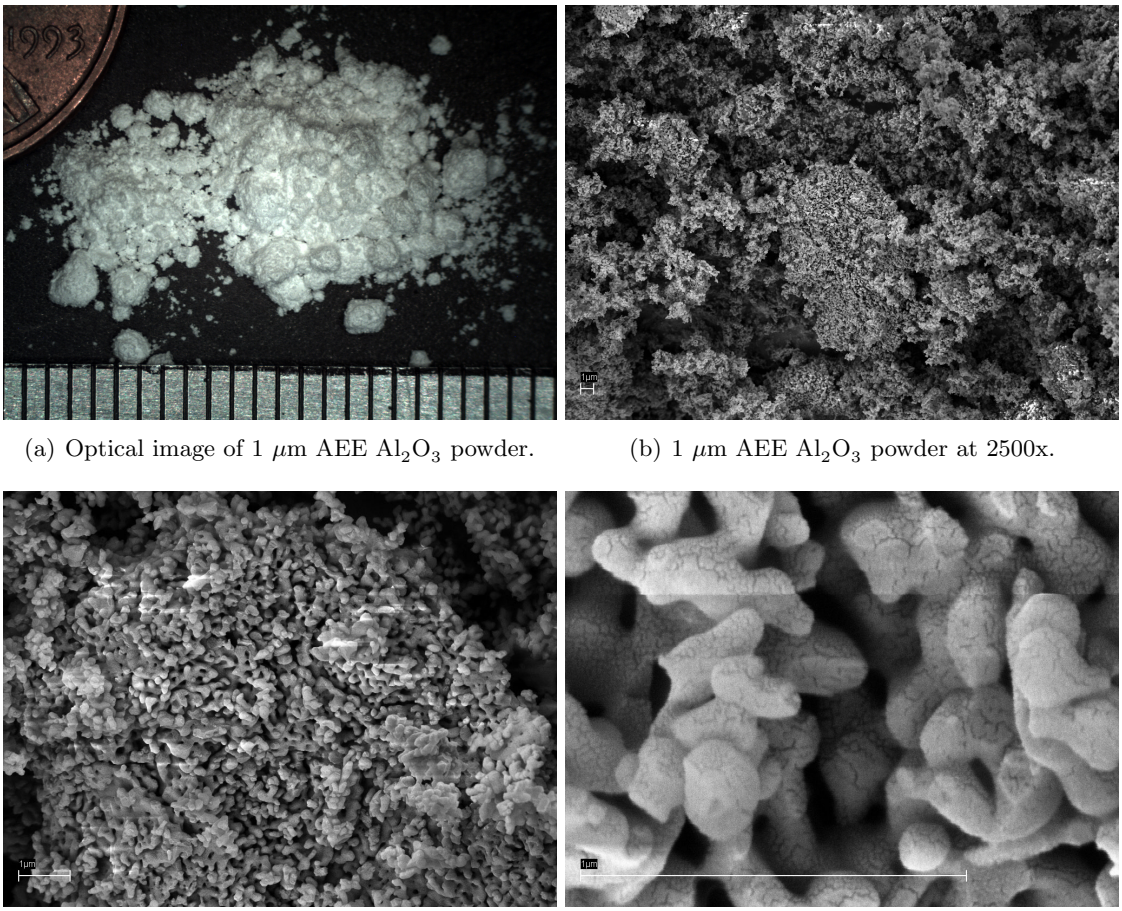

(a) Optical image of 1 μm AEE Al_2O_3 powder.

(b) 1 μm AEE Al_2O_3 powder at 2500x.

(c) 1 μm AEE Al_2O_3 powder at 10kx.

(d) 1 μm AEE Al_2O_3 powder at 75kx.

Figure 3.9: Directly obtained AEE alumina powder. On the optical image, a penny is shown for scale, in addition to the scale bar at the bottom, where each tick is 1 mm. On each SEM image, the scale bar in the lower left corresponds to 1 μm.

so slightly coarser 500 grit powder was obtained. Henceforth the 500 grit powder will also be referred to as "10 μm". Both powders appeared fine and white, although the Unibrite was more sand-like and the AEE was more apt to clump together like powdered sugar, as shown in the optical images in Figures 3.9(a) and 3.10(a). In addition to the optical images, SEM images of both powders are shown in Figures 3.9 and 3.10.

As seen from the images, the 1 μm powder obtained directly appears very similar to that obtained by DTE (see Figure 3.4). The primary difference between the AEE 1 μm Al_2O_3 and that in the composite provided by ATK is the presence of small features, either surface ridges or fissures, visible at the highest magnifications (Figures 3.9(d)). These features are

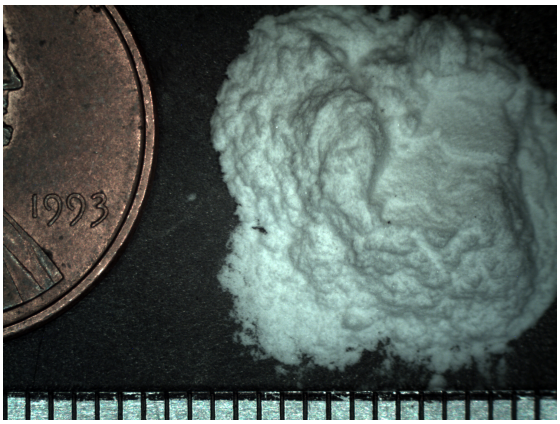

(a) Optical image of 10 μm Unibrite Al_2O_3 powder.

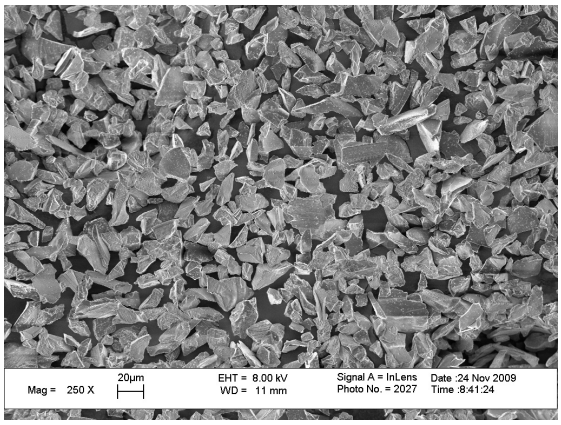

(b) 10 μm Unibrite Al_2O_3 powder at 250x.

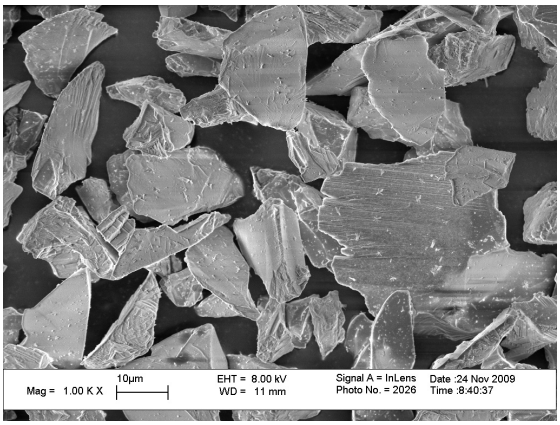

(c) 10 μm Unibrite Al_2O_3 powder at 1000x.

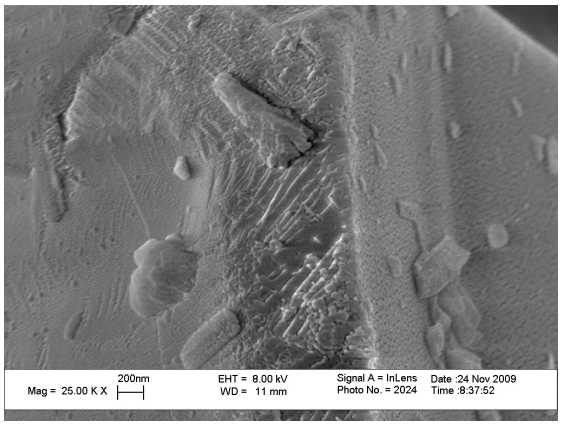

(d) 10 μm Unibrite Al_2O_3 powder at 25kx.

Figure 3.10: Directly obtained Unibrite alumina powder. On the optical image, a penny is shown for scale, in addition to the scale bar at the bottom, where each tick is 1 mm.

not visible in the images received from DTE (Figure 3.4(b)) or noted by ATK, although the lack of the features in the ATK images can probably be attributed to differences in the resolution of the microscopes.

Comparing Figures 3.10(a) and 3.4(f), the 500 grit Unibrite powder obtained has a fundamentally different color than that used by ATK (600 grit Unibrite Al_2O_3). The powder obtained directly was very white in appearance, while the color of the powder obtained by ATK was a tan color. Some differences in the morphologies can also be observed in the SEM images of Figures 3.10(c) and 3.4(d). The cause of these obvious differences is unknown. However, when compared with the porous, fused agglomerates of the 1 μm AEE powder, the two morphologies are similar, and so this material is assumed to have compaction properties

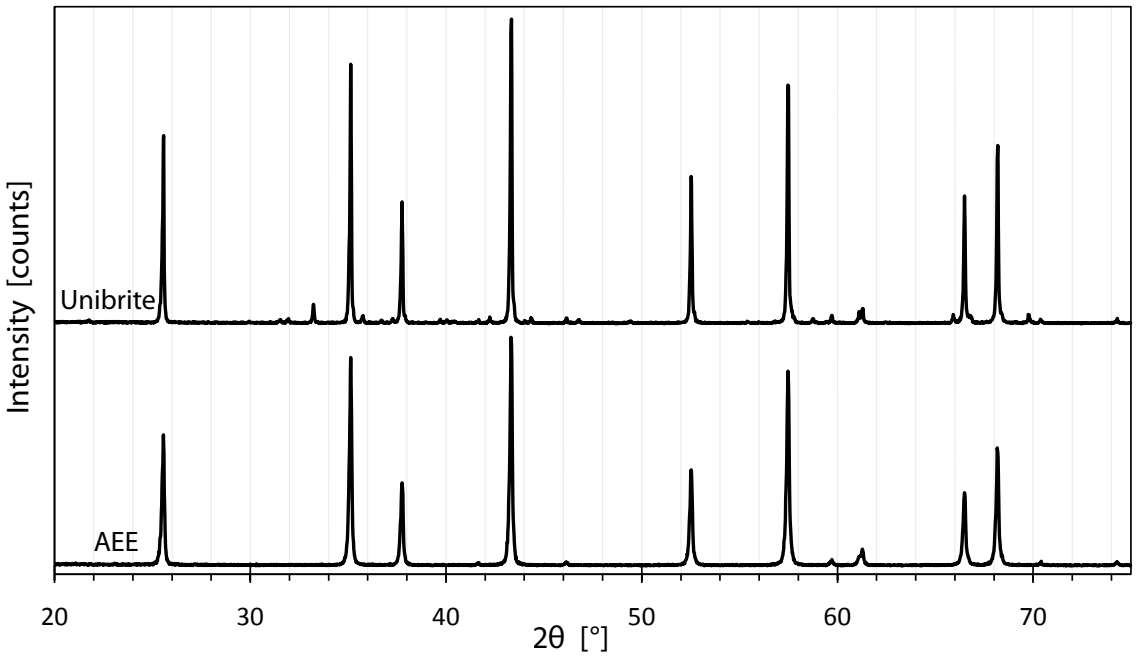

Figure 3.11: XRD Patterns for alumina powders, acquired using Cu Kα_1 radiation. The AEE pattern is virtually identical to reference XRD data for corundum Al_2O_3, while the Unibrite pattern shows evidence of minor impurities.

relatively similar to the material used by ATK to create the 10 μm Al_2O_3/THV composites.

X-ray diffraction (XRD) was performed on both the 1 μm AEE powder and on the 10 μm powder. As shown in Figure 3.11, the profiles are very similar, and agree with reference XRD data for Al_2O_3.

3.1.4 Static Powder Compression

Static compression tests were performed on a SATEC 100,000 lb capacity hydraulic materials testing frame at Georgia Tech. The system is equipped with a load cell so that force-displacement data is generated. The samples were pressed by pouring a known mass of powder into a 0.500 inch diameter, 1.5 inch tall steel die with a 1/4 inch tall steel plug in the bottom. The powder was weighed so that the initial height of the powder column (with a 20 lb preload) was ∼3 mm. The die and punch assembly was then inserted into the test frame and loaded at a rate of 3,000 lb_f per minute to a maxiumum force of 25,000 lb (corresponding to 878 MPa), which was the rated load of the die. The load was then reduced at a rate of 6,000 lb_f per minute until the sample returned to ambient pressure. In

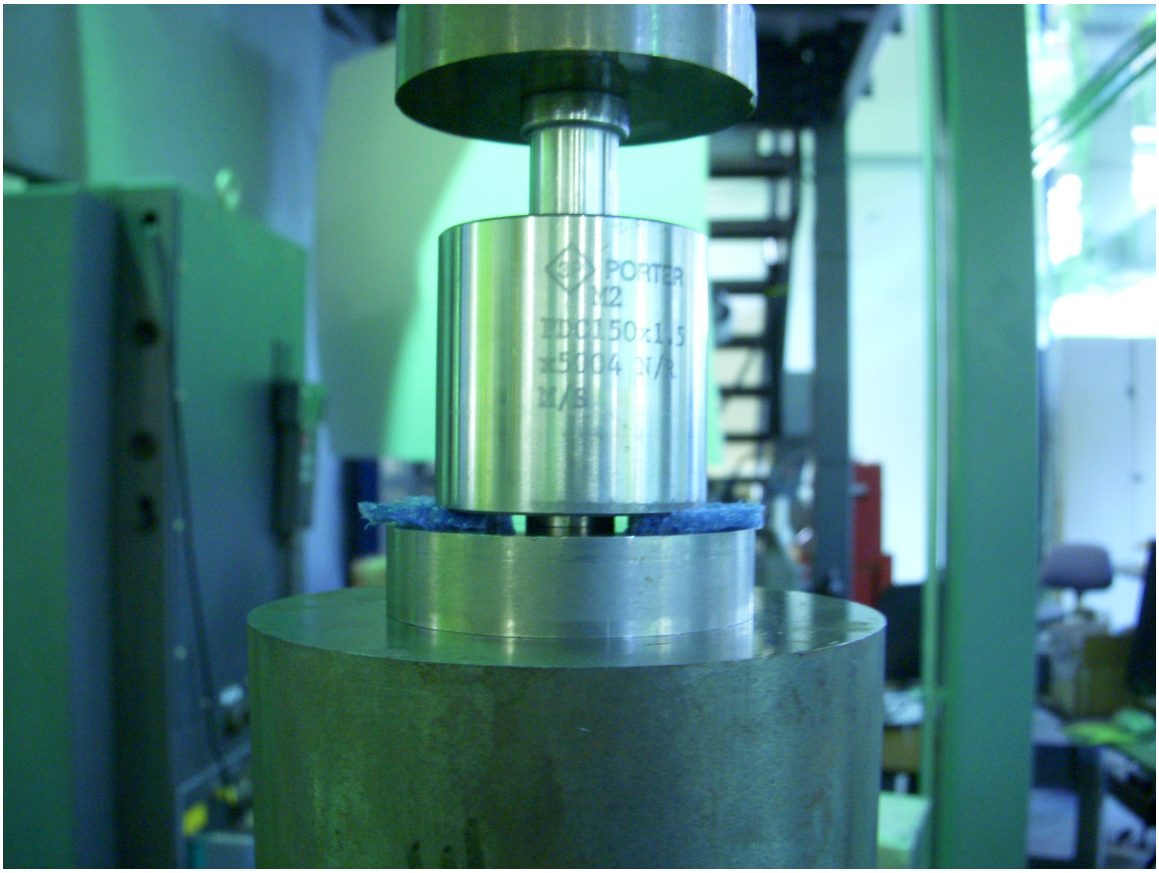

Figure 3.12: Powder Pressing Setup - Photo showing the punch and die situated between the platens of the testing machine. The plug can be seen extending below the bottom surface of the die to the bottom platen, and the foam pieces are clearly seen holding up the die. Once the loading cycle began, the pads were removed, allowing the die body to float.

order to ensure that the punch was not transferring a significant portion of the load to the die body and thereby circumventing the powder, the die body was initially supported on foam pads so that it was about 1-2 mm above the bottom platen, as shown in Figure 3.12. Once the assembly was in place and the load ramping had just begun, the foam pads were removed. This allowed the die body to move down slightly during the testing cycle as the powder compacted, without coming into contact with the bottom platen during the load cycle. Load transferred from the punch to the die body to the bottom plug was assumed to be negligible.

3.1.5 Alumina-Epoxy Composite

The alumina/epoxy (ALOX) composite fabricated for this study was composed of 43% by volume alumina, with the remainder epoxy. This loading was chosen because it represents the upper limit of the alumina that could be easily mixed into epoxy resin by early investigators[118], and has since been investigated by several researchers[105, 122, 123]. Thus, it represents a standard "fully-filled" ALOX formulation. The 40 μm disc-shaped alumina was calcined powder obtained from Saint-Gobain (PN: 7920). An SEM micrograph of the powder is shown in Figure 3.13. The epoxy system was Epon 828 resin (obtained from Miller-Stephenson) with DEA (diethanolamine, obtained from Fisher) hardener mixed in a 100:14 ratio by weight. For mixing purposes, the densities of alumina and epoxy were assumed to be 3.95 and 1.192 g/cm^3 respectively. The alumina powder was mechanically mixed into the resin in several stages, and then heated to 90°C prior to adding the hardener (at 21°C). The resulting mixture was degassed for 5 minutes and poured into a 2 inch diameter cylindrical mold that had been pre-heated to 90°C. Once in the mold, the mixture was degassed for an additional 5 minutes, and then returned to atmospheric pressure and allowed to cure at 70°C for 48 hours with the cylinder oriented vertically.

Disc-shaped samples were cut from the cylinder, and after discarding the top and bottom samples to account for slight settling of the alumina powder during cure, the remaining samples had a uniform density of 2.375 $\pm$0.001 g/cm^3. The opaque sample discs were checked for porosity by visually searching for pores on the surface (typically 0.25 - 1 mm) and by using optical microscopy. Porosity was statistically determined to be $\sim$0.02% by calculating the area of the voids intersected by a plane of polish and dividing by the total surface area of each plane[130]. A micrograph of the composite showing the particle distribution and orientation is shown in Figure 3.14.

Longitudinal and shear sound speed measured on the ALOX disks using pulse-echo transducers (4.5 and 4.0 MHz, respectively) were found to be 3210$\pm$30 m/s and 1970$\pm$70 m/s, respectively, which corresponds to a bulk sound speed of 2265$\pm$92 m/s. The longitudinal sound speed value is in good agreement with prior work on 43% ALOX[118, 131, 121, 120, 122], but the measured shear wave speed is significantly ($\sim$10-25%) higher than

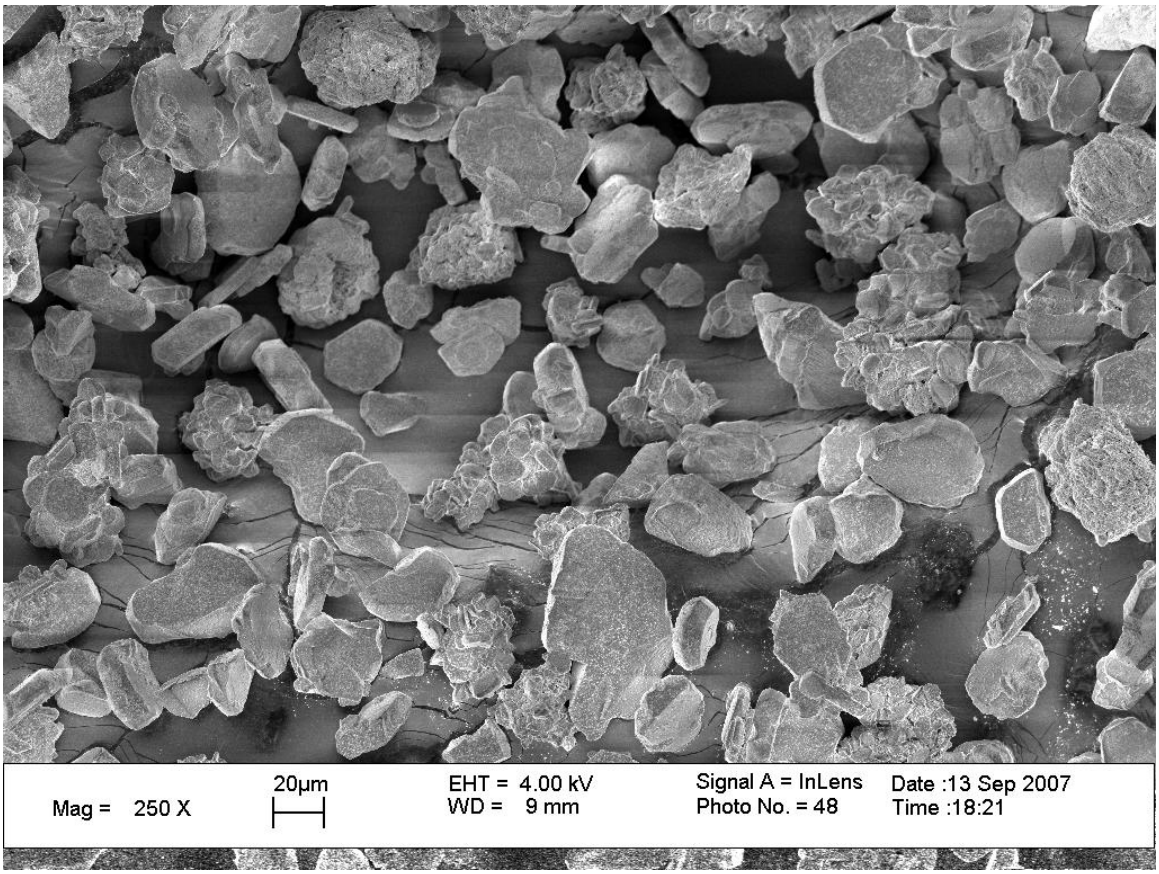

Figure 3.13: Initial state of calcined alumina powder. The particles have shape factors (diameter/thickness) of approximately 4. Note that the particles are 15-60 μm in size and are composed of both single plate-shaped particles and also relatively round clusters of smaller particles 5-10 μm particles.

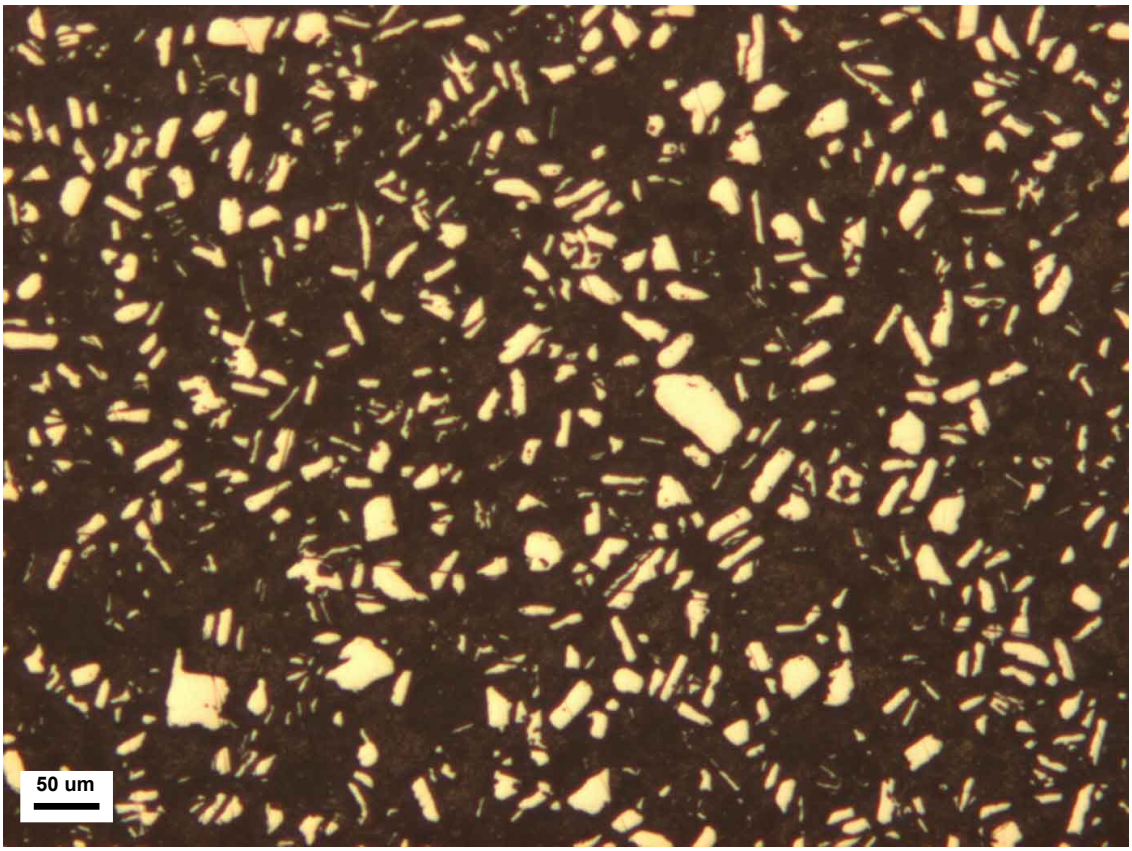

Figure 3.14: Optical micrograph of ALOX. The volume fraction appears less than 43% due to some pull-out of Al_2O_3 plates aligned with the plane of polish. The particles appear randomly oriented and distributed in the epoxy matrix. No difference between cross sections parallel to the cylinder axis and perpendicular to the cylinder axis could be found. The particles appear to be mostly surrounded by epoxy, with very little interparticle contact.

that reported in the literature. Setchell and Anderson[123] have noted that Al_2O_3 particle morphology seems to affect ultrasonic wave speed, and an examination of their data reveals that the effect is most pronounced in shear. They reported lower ultrasonic wave speeds for ALOX made with low-aspect ratio (spherical) particles than with higher aspect ratio particles (blocky aspect ratio ≈1.5). Therefore, the higher shear wave speeds may be a consequence of the high-aspect ratio particle shape employed in this investigation. The experimental data of Sutherland[131] has also shown that shear wave velocity in ALOX is more sensitive to frequency than longitudinal wave velocity, and the strong dependence of shear wave velocity on particle shape may be a related effect. Although various authors have attempted to predict such effects based on multiple scattering theory[132], there exists no widely accepted theoretical model applicable to a material with a high a concentration of scattering sites (such as 43 vol% ALOX).

3.2 Impact Experiments

This section provides an overview of several specialized test methods employed to determine the shock compression and high-strain-rate mechanical properties of the various ceramic-particle/THV composites.

3.2.1 Parallel-Plate Impact Experiments

Parallel-plate impact experiments are used to determine the shock compression behavior of materials. In particular, they can be used to find points along the Hugoniot curve and thereby determine the shock EOS. The experiments are designed such that the material at the center of the plate is inertially confined for a sufficient time (usually a few microseconds) so that the shock velocity and/or particle velocity can be measured without the influence of edge effects, i.e., the material is in a true state of one-dimensional strain.

Parallel-plate impact experiments were performed using the 80 mm diameter, 8 m long, single-stage helium gas gun at Georgia Tech. Figure 3.15 illustrates the projectile and target assembly. The projectile consisted of an aluminum sabot carrying a flyer plate (usually OFHC copper). The target assembly usually consisted of a driver disc (usually copper), a sample disc, and a backer disc (usually fused silica[133]) bonded together with a

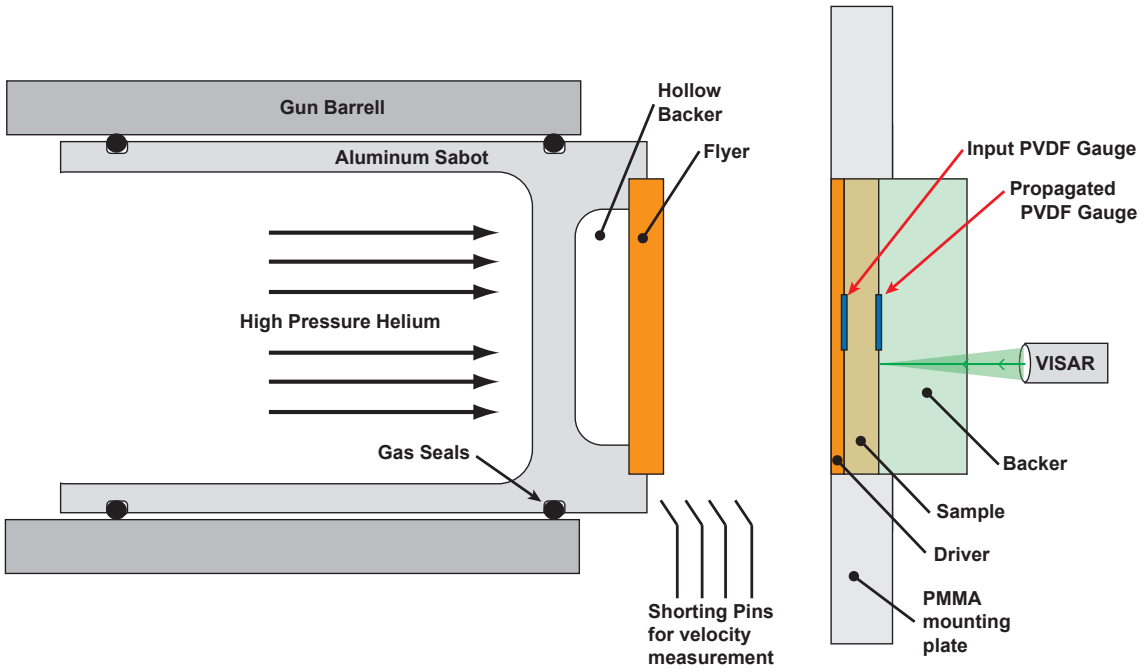

Figure 3.15: Parallel Plate Experimental Setup. Although both VISAR and PVDF gauge positions are shown, some experiments did not employ both PVDF and VISAR. The "Hollow Backer" refers to a recessed pocket cut into the Al sabot, such that the flyer is only supported on the edges.

low-viscosity epoxy (Loctite Hysol RE2038 resin and Loctite Hysol HD3475 hardener in a 4:1 ratio by weight). A picture of the experimental setup is shown in Figure 3.16.

PVDF gauges[49] were embedded between the driver and the sample to monitor the input stress profile, and between the sample and backer to monitor the propagated stress profile. The PVDF gauge package (M-25-09-PL 3x3mm from Ktech in Albuquerque, NM) consists of a 25 μm thick film of precisely stretched and poled, piezoelectric polyvinylidene fluoride film sandwiched between two thin gold/platinum traces (see Section 2.3). The piezoelectric film creates a well-characterized charge as a function of pressure. Previous researchers have noted that the orientation of the PVDF material has an effect on the stress vs. charge calibration curve[54], and so the gauges were aligned such that the positive lead was exposed to the shock front first. The PVDF gauge was used in "current mode"[62], where a current viewing resistor (CVR, obtained from T&M Research, Albuquerque, NM) is connected in parallel across the gauge leads, and the resulting voltage across the CVR is recorded by an oscilloscope. Integration of the current trace (calculated from the recorded

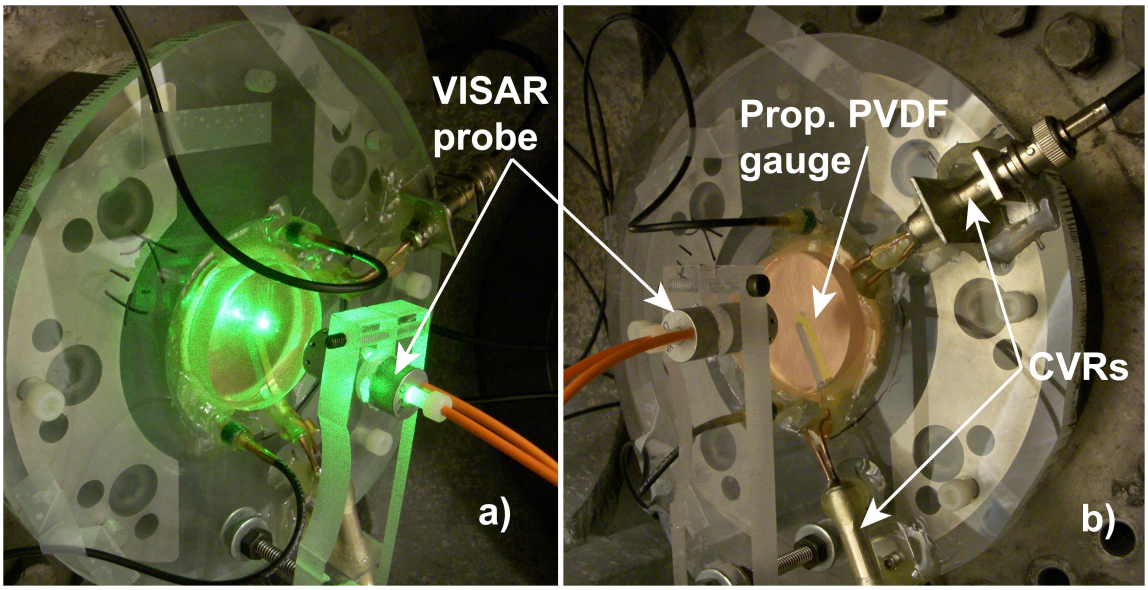

Figure 3.16: Parallel Plate Experimental Setup Images. These images, taken for Shot 0913, are representative of an experiment using both VISAR and input and propagated PVDF gauges. a) From left side with VISAR laser on. b) From right side with VISAR laser off.

voltage trace) allows a pressure profile to be calculated for each embedded gauge, as well as time-of-flight wave speed determination based on the travel of the shock wave through the sample thickness. Data analysis was performed with Plotdata software[134]. The calibration curve relating pressure to charge (or current) from the PVDF gauge is built into Plotdata. This calibration curve, previously cited as originating with Graham et al.[63], is actually an unpublished 6^{th} order polynomial developed by Jim Greenwoll[135, 136] that acceptably fit the entire range of data considered by Graham et al.[63]. The calibration curve relates stress σ [GPa] to charge density Q [$\mu C/cm^2$], and is given below in Equation (60).

$$\sigma = 0.427Q + 1.145Q^2 - 0.984Q^3 + 0.517Q^4 - 0.119Q^5 + 0.010Q^6 \tag{60}$$

In some experiments a push-pull VISAR[43, 137, 138] was used to measure the particle velocity at the interface between the sample and the backer window (see Section 2.3.1 for a brief theoretical description). Plotdata software was used to produce a velocity trace from the recorded VISAR fringe data. When VISAR was used, a 30mm focus VISAR probe (Valyn VIP #FOP-PP-300) was positioned approximately perpendicular to the target

assembly so that the beam was probing a spot near the center of the sample. The velocity of the impactor projectile (sabot-flyer assembly) was monitored by four sequentially shorting pins positioned just ahead of the target assembly. The pins allow for a velocity determination of ∼0.5%. The experiment chamber is evacuated to 100 mtorr or better prior to each experiment.

3.2.1.1 Error Calculation Procedures

The primary analysis of parallel-plate impact experiments involved the impedance matching method described in Section 2.1.3 to obtain points along the Hugoniot. The uncertainty analysis performed for these calculations is based on the sum of squares approach commonly used for small, independent, random uncertainties[139]. In the calculation, for an arbitrary function $f(m, ..., n)$ dependent on variables m through n, the uncertainty in f is given by:

$$\delta f = \sqrt{\left(\frac{\partial f}{\partial m}\delta m\right)^2 + ... + \left(\frac{\partial f}{\partial n}\delta n\right)^2} \tag{61}$$

where δ denotes the uncertainty in a variable. This was the approach taken for determining the shock speed $U_S = \frac{d}{t}$, pressure $P = \rho_o U_S U_P$, and specific volume $V = V_0 - U_P^2/P$. The explicit equations applied to these variables have been published previously by Dai et al.[29]. The uncertainties in material thickness d, travel time t, initial density ρ_0, and impact velocity V_{imp} were taken from the total range of the respective parameter's measured values.

The uncertainty in U_P is less straightforward because an explicit expression for the sample particle velocity U_P includes the compounded solutions of two quadratic functions. Therefore, a slightly modified approach was employed in this work, similar to that described by Mitchell[140], and represented by the equation

$$\delta f = \delta f(m) + ... + \delta f(n) \tag{62}$$

where the quantities on the right correspond to the change in f arising from the variation in only one input variable. Equation (62) is essentially the same idea as Equation (61),

except that the deviation is assumed sufficiently small for linearity to apply and the components are directly added, rather than added in quadrature. The direct addition represents the conservative, worst-case scenario, whereas quadrature assumes that maximum outlier conditions will not occur simultaneously. The approach taken was to vary each input to U_P by its uncertainty (both positive and negative) and monitor the effect on the calculated U_P to determine whether an increase in the input led to an increase in U_P or not. Then, by applying the condition for each input that results in a greater value for U_P, the positive uncertainty was obtained. By applying the opposite conditions, a negative uncertainty was obtained. The uncertainty with the larger absolute value was taken as the uncertainty in U_P, which was then used to find the uncertainty in P and V as described above.

3.2.2 Recovery (3-capsule) Experiments

Recovery experiments are designed to subject the sample to a shock wave and protect the sample so that it can be recovered for post-shock analysis. They constitute a complementary tool to the parallel-plate impact experiments. To ensure recovery, steel sample containers are used. The shock impedance difference between the steel and the samples causes complex loading histories within the sample, which makes direct comparison with Hugoniot measurements difficult.

Recovery experiments were performed on the 80 mm gas gun using a setup which has been previously described[141]. Briefly, the setup contains three sealed steel capsules held in a steel surround ring that are impacted by a steel flier mounted on an aluminum sabot. AISI 630 (17-4) stainless steel is used for the assembly. Radial and back momentum traps are used to optimize the loading and unloading experienced by the sample. The steel flier is carried on a 6061 aluminum sabot, such that the aluminum is in full contact with the rear of the steel driver (the "hollow backer" in Figure 3.15 is absent) so that the release wave generated at the rear of the flier is of a lesser magnitude than it would be if the rear of the flier were a free surface. The loading of the samples contained within the sealed capsules is quite complex, due to the impedance mismatch between the samples and the steel. The geometry of the capsule assembly ensures that the samples are recoverable after

the experiment by machining the capsules.

This work included a recovery experiment containing three different samples within each of the three capsules. Capsule I contained the AEE 1 μm alumina powder, and the Capsule II contained the Unibrite 10 μm powder. The powders were pressed into the capsules at 800 MPa using a Carver hydraulic press, before being sealed with threaded steel plugs hand tightened to $\sim$10 ft-lbs and sealed with Loctite 271 threadlocker. The resulting initial densities of the powders were estimated using the static compression and release curves (presented later in Section 4.4) and also by using measurements of the capsule and plug geometry before and after powder delivery, pressing, and plug insertion. The two estimates of the initial powder density agreed to within 1%.

The third capsule (Capsule III) contained the 1 μm Al_2O_3/THV composite. A cylindrical specimen approximately 12 mm in diameter and 4 mm in height was milled from a larger disc, such as that shown in Figure 3.3. This cylinder was then lightly pressed into the bottom of the steel capsule, and then the plug was inserted and sealed. The initial density was assumed to be unchanged from that of the bulk composite.

3.2.3 Rod-on-Anvil (Taylor) Impact Experiments

Rod-on-Anvil impact experiments were first used by Taylor[142] to determine an estimate of the average yield stress at high strain rates. The tests have since become known as "Taylor tests", and consist of impacting a right circular cylinder perpendicularly onto a rigid anvil. The deformed cylinder is recovered and measured, allowing for an estimate of the yield stress by a number of methods (for examples, see [143, 144, 145, 146]). The Taylor test is now used primarily as a tool for evaluating high-strain-rate constitutive models, as it subjects the sample to a wide range of stress and strain states in a convenient, radially symmetric geometry.

Hutchings[143] introduced a method for yield stress determination using an elastic-perfectly plastic model for polymeric materials. To perform the analysis, only the initial density ρ, initial length L_0, recovered length L, impact velocity V, and the critical velocity V_c at which plastic deformation first occurs must be known. To implement the model, the

fractional reduction in length k is calculated from $k = 1 - L/L_0$. Then, the following two equations must be solved to find the yield stress Y and the true yield stain ϵ_y:

$$\epsilon_y = \frac{\rho V_c^2/Y}{1 + (\rho V_c^2/Y)} \tag{63}$$

$$\sqrt{\frac{Y}{\rho V^2}} = \frac{\overline{C}_p}{\sqrt{\epsilon_y - \epsilon_y^2 \left[\frac{1}{1-\epsilon} - \frac{1-\overline{C}_p}{1-\epsilon_y}\right]}} \tag{64}$$

where in Equation (64),

$$\overline{C}_p = \sqrt{\epsilon_y/(1-\epsilon)} \tag{65}$$

and

$$\epsilon = \frac{1}{8\epsilon_y}\left\{(8\epsilon_y^2 + 4k\epsilon_y - k^2) + \sqrt{\left[(k^2 - 8\epsilon_y^2 - 4k\epsilon_y)^2 - 16\epsilon_y(4\epsilon_y^3 + 4k\epsilon_y^2 + k^2\epsilon_y - k^2)\right]}\right\} \tag{66}$$

Although explicit expressions for Y and ϵ_y cannot be obtained, the system can be solved by guessing a value for ϵ_y and then iterating between Equations (63) and (64).

Taylor experiments were performed on a single stage, 7.62 mm diameter gas gun at Georgia Tech. Compressed helium gas is used to accelerate a 7.55-7.62 mm diameter projectile down a 6' barrel onto a rigid anvil made of hardened and lapped S7 steel. Velocity is determined by interruption of two laser beams, and the samples are recovered for analysis after each experiment. In addition, an Imacon 200 high speed camera is used to capture silhouette images of the projectile during deformation. A proportional delay counter (Physics Applications model UDC-100) ensures that the camera and flash are triggered at appropriate times before impact, regardless of projectile velocity. The experiment chamber is evacuated to 100 mtorr or better prior to each experiment.

CHAPTER IV

SHOCK COMPRESSION RESPONSE OF THV-CERAMIC COMPOSITES

In order to investigate the shock compression response of the THV-ceramic particle composites, the behavior of the components was also studied separately. In this chapter both experimental and computational results concerning the THV composites will be presented. It will also include discussions pertaining to the form of the measured wave profiles, as well as investigations into several theories to explain the observed composite Hugoniot results as a function of ceramic particle type and size.

4.1 Shock Compression Response of THV

The overall objective of this research is to explore the shock compression response of the four different ceramic particle/THV composites described in Chapter 3. In order to understand the response of the composite, it was first necessary to understand the response of the constituent bulk materials. Numerous studies of the shock response of Al_2O_3 have been reported, and some data for ZrC is available. However no data for the shock response of THV was available. Therefore, the shock Hugoniot and high strain rate mechanical properties of THV were investigated.

4.1.1 THV Polymer Hugoniot

In order to determine the shock compression response and shock equation of state of THV, several parallel-plate impact experiments were performed. Table 4.1 details the materials and geometry for each experiment on pure THV. In most experiments (except 0728 and 0825), a single piece of 25 μm thick FEP-Teflon was inserted between the driver and the PVDF gauge for electrical insulation. In several experiments the PVDF gauges were electrically shielded from the sample due to suspected sample polarization[147]. In these experiments the gauge package consisted of a layer of FEP-Teflon film, the PVDF gauge,

Table 4.1: Experimental setups for Parallel Plate Experiments

Shot#	Flier	Driver	Sample	Backer[a]	Foil[b]
thicknesses for flier, driver, sample, backer, and foil given in parenthesis (mm)					
0728	Cu (5.161)	THV (0.889)	THV (2.537)	THV (0.570)	none
0904	Cu (4.944)	Cu (1.542)	THV (2.466)	f. silica (12.7)	Cu
0723	Cu (5.083)	Cu (2.477)	THV (2.680)	f. silica (12.761)	none
0825	Cu (5.088)	Cu (2.271)	THV (2.515)	f. silica (12.799)	Cu
0725	Cu (5.133)	Cu (2.723)	THV (2.598)	f. silica (12.718)	none
0827	Cu (5.116)	Cu (1.524)	THV (2.497)	f. silica (12.779)	Cu
0730	W-6Ni-4Cu (3.901)	Cu (2.644)	THV (2.540)	THV (0.574)	none

[a]Fused silica was Corning 7980 from Mark Optics.
[b]Cu foils were grounded in order to shield PVDF gauges from sample polarization.

another layer of FEP-Teflon film, and a 25 μm thick piece of Cu foil, for a total gauge package thickness of 100 μm. In experiments without copper foils, no film was inserted between the gauges and the sample, or between the 2^{nd} gauge and the backer. With the single Teflon film, the total gauge package thickness is 50 μm. Without the Teflon film (as in the second cemented interface), the total gauge package thickness is $\sim$25 μm. Shot 0825 did not employ PVDF gauges, eliminating the need for any gauge package, and so no teflon films were used. Therefore, in shot 0825, the "gauge package" is merely the epoxy layer, which was a few microns thick.

A summary of the results of the gas gun experiments performed on THV and measured/calculated parameters is shown in Table 4.2. Figure 4.1 shows an example of the PVDF gauge traces and VISAR velocity profile (obtained from Shot 0723). Shock velocity (U_S) measurements were obtained from time-of-arrival calculations by finding the time at which the respective input and propagated stress trace had risen to 50% of the steady state value, less the time of travel through the gauge packages at pressure. The pressure (P_{ig}) was measured using the first PVDF gauge (the "input gauge", between the driver and the sample). In all experiments, the pressure indicated by the PVDF gauge continued to rise for 0.5-1.0 microseconds before reaching a steady value, as shown in Figure 4.1, which is the value reported in Table 4.2. The last two columns in the table are calculated values of U_P and pressure. To calculate these values, the measured U_S values in the sample (from

Table 4.2: Gas Gun Experiments Performed on THV

Shot#	Material	Measured Values			Calculated Values[a]	
		Impact Vel. m/sec	U_S m/sec	P_{ig} GPa	U_P m/sec	P_{calc} GPa
0728	THV	472	2412	2.1	416	2.0
0904	THV	477	2412	2.4	420	2.0
0723	THV	662	2798	3.1	574	3.2
0825	THV	666	–	–	–	–
0725	THV	1024	3407	5.3	866	5.9
0827	THV	1031	3469	5.7	870	6.0
0730	THV	1072	3896	9.0	1141	8.9

[a] U_P and P_{calc} were calculated from impact velocity and U_S using impedance matching.

time-of-arrival) and the measured impact velocities were used to determine the particle velocity, U_P, using standard impedance matching techniques and the known behavior of the impactor and driver materials. Pressure was then calculated from the conservation of momentum jump equation (Eqn. (7)).

VISAR traces of the particle velocity profile were also obtained on a few experiments. The samples were not transparent, and so the surface probed by the VISAR was necessarily the sample/backer interface. The measured values of U_P from VISAR are shown in Table 4.3, and are calculated from the recorded fringe data, the known fringe constant, and the window correction for fused silica[97]. It should be noted that the VISAR probed the sample/backer interface; hence, the particle velocities and pressures shown in Table 4.3 are different from the calculated values shown in Table 4.2 (which are calculated for the driver/sample interface). However, since the shock properties of fused silica are well known[47], the pressure indicated by the VISAR probe can be compared with the pressure recorded by the second PVDF gauge as a further validation of the PVDF gauges. The recorded steady state pressure of the second PVDF gauge (at the sample/backer interface) is shown in the table for comparison. Furthermore, using impedance matching and the U_S-U_P relationship presented in Figure 4.2, the expected pressure at the sample/backer interface can be calculated, and is shown in the last column of Table 4.3. It can be seen from Table 4.3 that the pressure calculated from the VISAR trace and the fused silica window properties agrees very well with that calculated from the U_S-U_P EOS of Figure 4.9

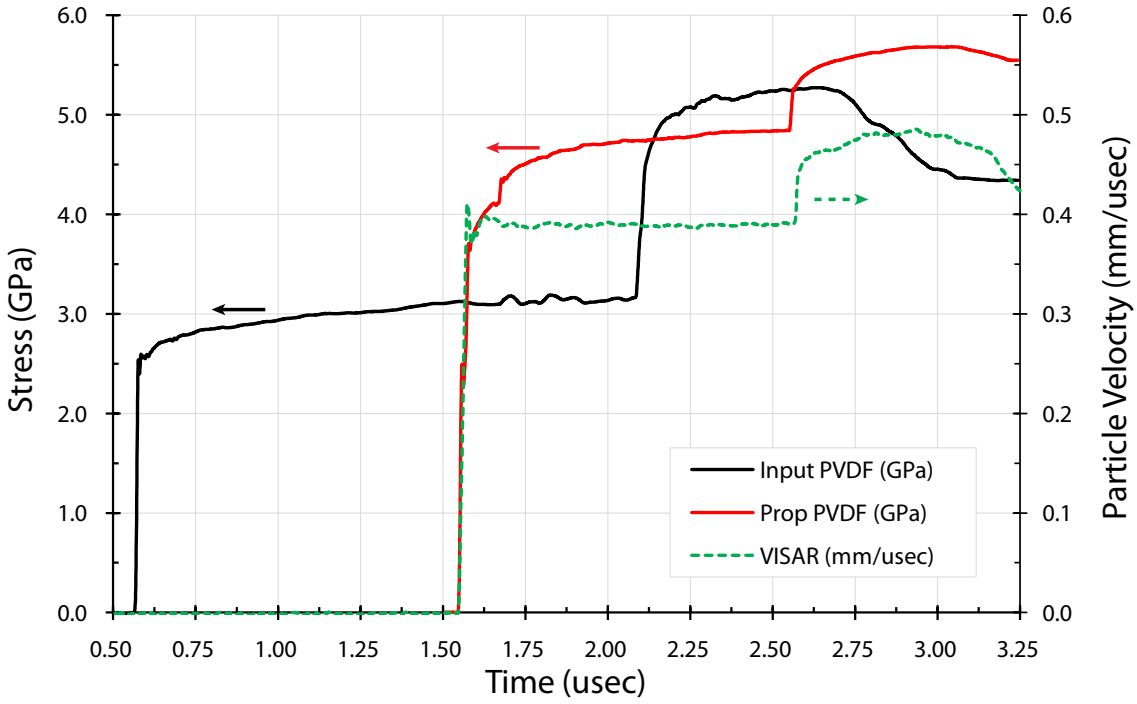

Figure 4.1: PVDF traces from THV Shot 0723. The surface probed by VISAR was the gold electrode behind the active element on the PVDF gauge. On all experiments, the VISAR trace reliably lagged the PVDF trace, even when probing the same surface, by 60-100 nsec. Here, the VISAR trace has been time shifted by -75 nsec to make it align with the propagated PVDF trace.

Table 4.3: Gas Gun Experiments Performed on THV with VISAR instrumentation

Shot#	Material	Impact Vel.	Up	P^a_{calc}	P^b_{pg}	P^c_{exp}
0723	THV	662	389	4.70	4.8	4.71
0825	THV	666	395	4.77	–[d]	4.75
0827	THV	1031	670	8.04	7.5	8.02
0904	THV	477	263	3.18	3.3	3.18

[a] P_{calc} - Pressure calculated from measured U_P and fused silica material properties.
[b] P_{pg} - Steady-state pressure measured from the 2_{nd} (propagated) PVDF gauge.
[c] P_{exp} - Expected pressure using THV EOS shown in Figure 4.9 and impedance matching.
[d] Shot 0825 did not employ PVDF gauges, so no data is available. It was meant to confirm the VISAR results from shot 0723.

and the value of U_S measured from the PVDF gauges, indicating that the presence of a PTFE film between the reflecting surface and window material does not affect the validity of the VISAR analysis. The agreement between the measured steady-state pressure from the PVDF gauges and the pressure calculated from the other two methods shows a maximum deviation of 6% (in Shot 0827).

A representative trace for the THV experiments was shown previously in Figure 4.1, which displays the stress trace from the PVDF gauges and the particle velocity trace from the VISAR probe. The figure shows a sufficiently long time record that reshock waves from the fused silica backer and release waves from the driver are visible in the traces. Also, it can easily be seen that both PVDF gauges continue to rise for 1-2 μsec. This is a typical result, and made the determination of pressure from the PVDF gauges difficult. However, the VISAR trace in Figure 4.1 does not show a continued rise. Instead, it shows a very fast rise to a peak particle velocity of approximately 389 m/sec. This phenomenon, where the PVDF gauges show a slow rise after the initial arrival of the shock wave, and the VISAR trace shows a very fast rise to constant particle velocity, is discussed at some length in Chapter 5.

Figure 4.2 shows a plot of the measured shock velocity (U_S) versus calculated particle velocity (U_P) (data from Table 4.2) illustrating the linear relationship for THV. The figure also includes data from the work of Dattelbaum et al.[110] obtained for THV using electromagnetic particle velocity gauges. It can be seen that the agreement is quite good.

Figure 4.3 shows the same data and linear trend as shown in Figure 4.2, but also includes

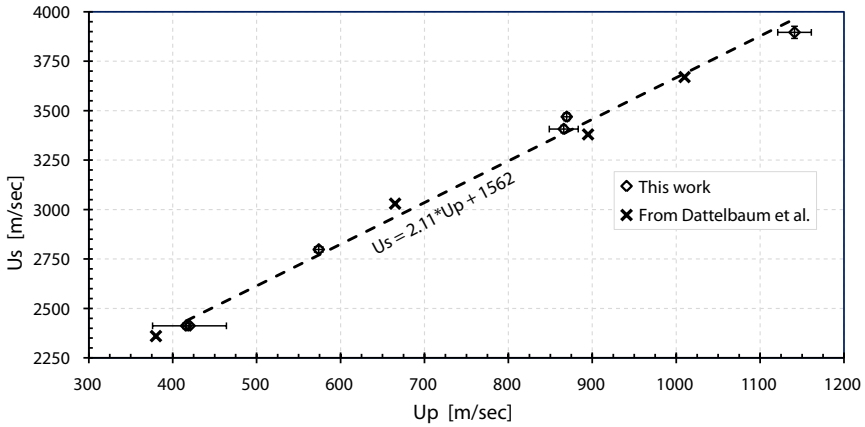

Figure 4.2: U_S-U_P data for THV, with linear fit. The linear fit shown is for the data in this work. However, it can be seen that the data of Dattelbaum et al.[110] obtained using material from a different lot and using electromagnetic particle velocity gauges agrees quite well with the results of this work using PVDF gauges to measure shock velocity and impedance matching to find the Hugoniot point.

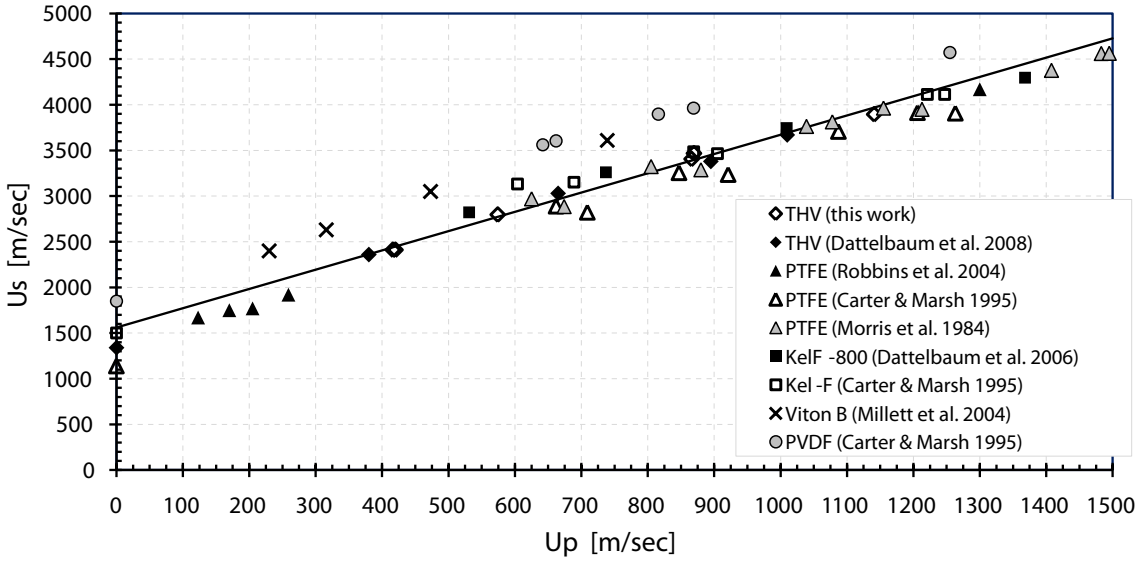

Figure 4.3: U_S-U_P data for THV and other Fluoropolymers. Note that the data for THV, PTFE, and Kel-F are very similar, while the data for Viton B and PVDF are offset by $\sim$500 m/s. The references are: Dattelbaum et al. 2008[110], Robbins et al. 2004[108], Carter and Marsh 1995[17], Morris et al. 1984[148], Dattelbaum et al. 2006[149], Millett et al. 2004[113]. Figure adapted from Dattelbaum et al.[110]

Table 4.4: THV Taylor Test Results

Shot#	Density $[kg/m^3]$	Impact Vel. $[m/s]$	Crit. Vel. $[m/s]$	Y $[MPa]$	ϵ_y	$\epsilon_{elastic}$
08-141	1986	94	71	169	.056	.142
08-138	1992	131	71	130	.072	.171
08-139	1990	180	71	88	.102	.226
08-143	1988	181	71	101	.090	.215

data from the literature on related fluorinated polymers. It is clear that THV is very similar to PTFE and Kel-F in U_S-U_P space, which implies that the Hugoniots will be similar if the initial densities are similar. Since Kel-F has an initial density only 6% greater than THV, the shock behavior for THV and Kel-F are very similar. Although from the data shown it appears that PTFE will also have a similar Hugoniot since PTFE is only 7% more dense than THV, recall that the data shown for PTFE are above the low temperature phase transition shown previously in Figure 2.2. The initial density of the new phase is higher, and so the Hugoniots are less similar than they appear in Figure 4.3. It can also be seen in the figure that the U_S - U_P data for Viton B and PVDF are $\sim$500 m/s above the data for THV, PTFE, and Kel-F. The reason for this is unknown.

4.1.2 THV Rod-on-Anvil (Taylor) Test

Taylor tests were also performed on THV to determine an averaged high-strain-rate yield strength. Table 4.4 lists the impact conditions and calculated yield strengths using the Hutchings analysis (described in Section 3.2.3) for specimens that did not fracture.

In Table 4.4, $\epsilon_{elastic}$ represents the observed elastic engineering strain, as measured by comparing the recovered specimen length l_{rec} to the length at maximum deformation l_{min} through the relation $\epsilon_{elastic} = (l_{rec} - l_{min})/l_0$, where l_0 is the initial length. The length at maximum deformation is determined from the high speed camera images. An example high-speed camera record is shown in Figure 4.4, and illustrates how the elastic strain was computed. The critical velocity is the threshold velocity below which plastic strain does not occur. The yield strength Y and yield strain ϵ_y are calculated using the Hutchings analysis discussed previously in Section (Section 3.2.3).

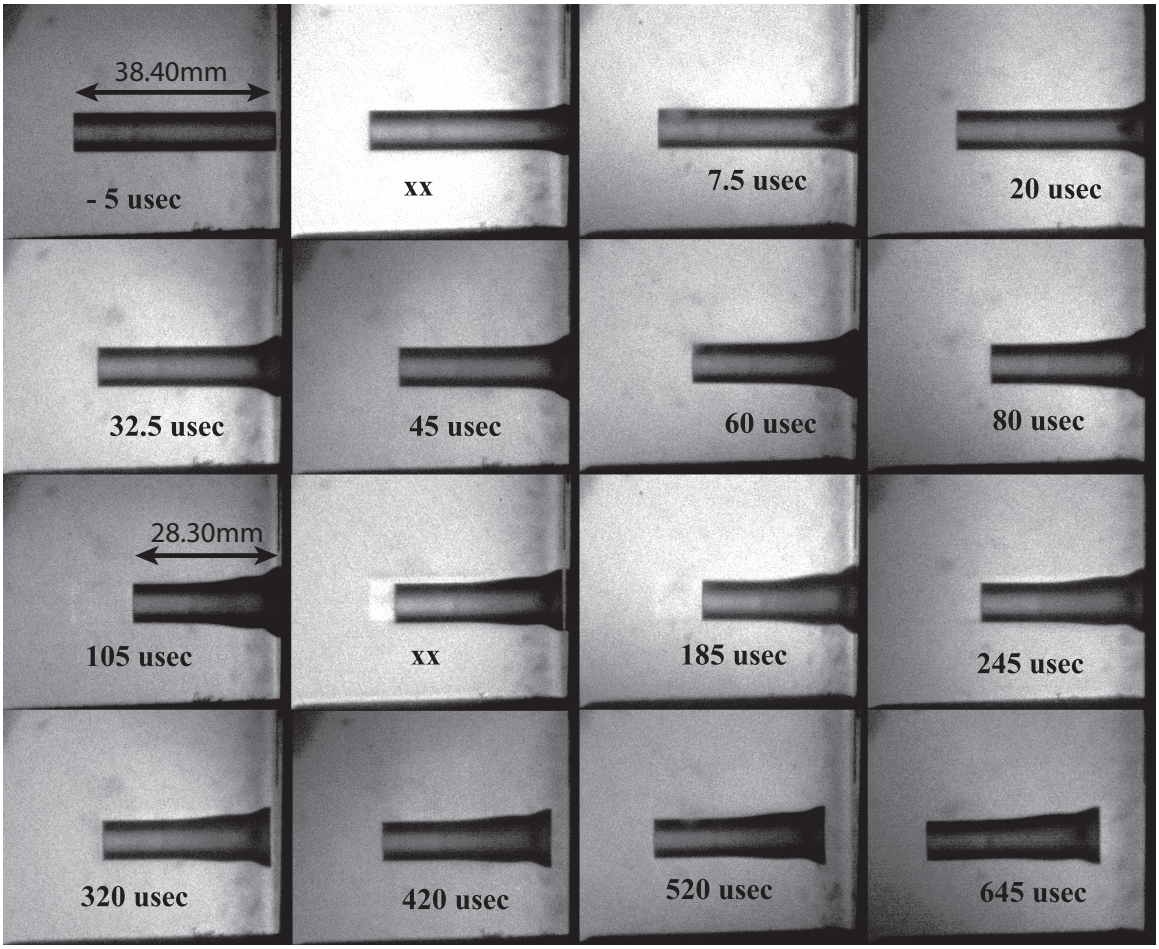

Figure 4.4: The Imacon camera record for Taylor shot 08-138. The frame timing is programmable- the times listed in the frames are the times after impact. The timing is corrupted in 2 of the 16 frames- these frames are listed with "xx" instead of the time. The sample can be seen just before impact in the first frame, and bouncing off the anvil in the last four frames. Measurements are taken using knowledge of the initial size of the specimen. In this experiment, the maximum strain occured in frame 9, at 105 μsec after impact. The original sample length (l_0) was 38.40 mm, the length at 105 μsec (l_{min}) is 28.30 mm, and the length of the recovered specimen (l_{rec}) was 34.87 mm. Therefore, the recovered (elastic) strain ($\epsilon_{elastic}$) was $(l_{rec} - l_{min})/l_0$=0.171, as indicated in Table 4.4.

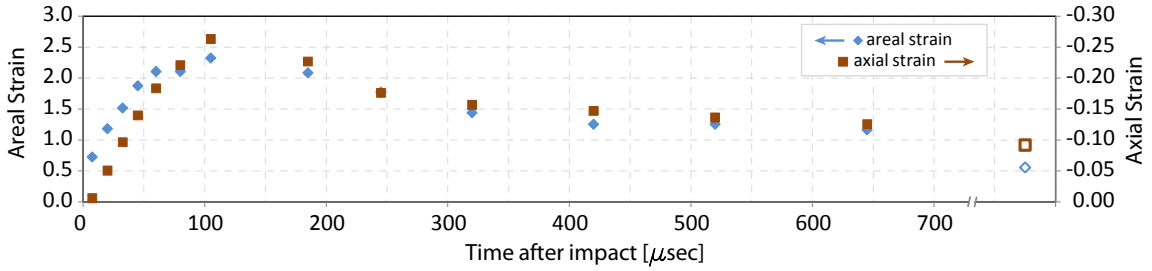

Figure 4.5: Axial and Areal strains calculated from Imacon camera record for Taylor shot 08-138. The hollow markers at the end of the time trace represent the measurements of the recovered specimen.

From the camera images, we can calculate the axial strain $(l - l_0)/l_0$ and areal strain $(a - a_0)/a_0$, where a is the area at the anvil face, at each image time. Figure 4.5 shows such a plot for shot 08-138. We can then estimate a strain rate for both axial and areal deformations. Performing this analysis on all four experiments confirms that strain rate increases with impact velocity and, for the areal strain rate, decreases with time after impact.

If the material were truly elastic-perfectly plastic, we would expect the observed elastic strain $\epsilon_{elastic}$ to equal the strain at yield ϵ_y shown in Table 4.4. However, in every case $\epsilon_{elastic}$ is $\sim$2.5 times ϵ_y, suggesting that THV is not exhibiting elastic-perfectly plastic behavior. Nevertheless, there are a few trends in the data. As impact velocity increases, strain rate increases, yield strength Y decreases, and the yield strain ϵ_y increases. This behavior is difficult to explain. The material seems to soften and become more ductile with strain rate. It is tempting to attribute this to a heating effect. We can make a rough estimate of the temperature rise using the calculated stress and strain values from Table 4.4, the specific heat from the literature, and the knowledge that in an perfectly plastic material the stress times the strain equals the specific energy added to the material by the deformation. If we use representative values for the inputs, we find that the temperature rise can be no greater than a few tens of degrees Centigrade. For instance, if W is the work put into a perfectly plastic material at a stress σ and strain ϵ, then $\rho c_P \Delta T = \sigma\epsilon$. If $\sigma = 100$ MPa, $\epsilon = 0.1$, $c_P = 1\ \frac{J}{gK}$ (from [111]), and $\rho = 2\ g/cm^3$, then $\Delta T = 5°$C. Although this is an estimate, it is likely overestimating the temperature rise, since it was demonstrated earlier that some

of the deformation energy is elastic, and so does not contribute to heating. Therefore, it is unlikely that bulk heating can explain the strain-rate softening observed. However, localized heating in highly strained regions may still cause the strain-rate softening.

4.2 Shock Compression Response of THV Composites

Once the Hugoniot and strength of the matrix material, THV, was established, the shock compression and strength properties of the composites were investigated using similar methods. This section will detail the results of parallel-plate impact experiments designed to measure the Hugoniot, as well as Taylor experiments designed to measure the high-strain rate strength of the four ceramic particle/THV composites.

4.2.1 THV Composites Hugoniot

Parallel-plate impact experiments were performed on the ceramic powder filled THV composites described previously (Section 3.1.2). Table 4.5 details the materials and geometry used for the experiments on the THV composites. The setup and analysis is very similar to that for the pure THV described previously, but differs in several details, and so is repeated here. In all experiments, a single piece of 25 μm thick FEP-Teflon was inserted between the copper driver and the PVDF gauge for electrical insulation. However, no Teflon film was inserted between the gauges and the sample, or between the 2^{nd} gauge and the fused silica window. With the Teflon film, the total gauge package thickness is $\sim$50 μm, and without it (as in the second cemented interface), the total gauge package thickness is $\sim$25 μm. In several experiments the PVDF gauges were electrically shielded (using grounded Al foil) from the sample due to suspected sample polarization[147]. In these experiments the gauge package consisted of a layer of FEP-Teflon film, the PVDF gauge, another layer of FEP-Teflon film, and a 12 μm thick piece of aluminum foil. The metallic foil was then epoxied to the sample and was grounded.

PVDF stress gauge traces were obtained for all experiments. The early portions of the input and propagated PVDF stress gauge traces for the 10 μm ZrC composite experiments are shown in Figure 4.6, which are also representative of the traces for the Al_2O_3 composites (although the trend in the Al_2O_3 composites was noisier). At low impact velocities, the

Table 4.5: Experimental setups for Impact Experiments on THV composites

Shot#	Flier	Driver	Sample	Backer[a]	Foil[b]
thicknesses for flier, driver, sample, backer, and foil given in parenthesis (mm)					
0755	Cu (2.708)	Cu (1.435)	1μm Al_2O_3/THV (3.962)	f.s. (6.386)	none
0757	Cu (3.134)	Cu (1.448)	1μm Al_2O_3/THV (4.011)	f.s. (6.368)	none
0754	Cu (2.667)	Cu (1.549)	1μm Al_2O_3/THV (4.003)	f.s. (6.35)	none
0822	Cu (3.124)	Cu (1.505)	1μm Al_2O_3/THV (4.018)	f.s. (12.751)	Al
0821	Cu (2.266)	Cu (1.513)	10μm Al_2O_3/THV (4.016)	f.s. (12.751)	Al
0748	Cu (1.529)	Cu (1.593)	10μm Al_2O_3/THV (2.489)	f.s. (6.375)	none
0752	Cu (2.736)	Cu (1.521)	10μm Al_2O_3/THV (2.515)	f.s. (6.380)	none
0746	Cu (2.685)	Cu (1.527)	10μm Al_2O_3/THV (2.504)	f.s. (6.375)	none
0802	Cu (3.127)	Cu (1.582)	100μm Al_2O_3/THV (2.553)	f.s. (6.368)	none
0759	Cu (3.134)	Cu (1.537)	100μm Al_2O_3/THV (2.578)	f.s. (6.370)	none
0803	Cu (3.124)	Cu (1.514)	100μm Al_2O_3/THV (2.578)	f.s. (6.342)	none
0916	Cu (2.680)	Cu (1.450)	10μm ZrC/THV (4.006)	f.s. (12.810)	none
0806	Cu (3.124)	Cu (1.524)	10μm ZrC/THV (2.522)	f.s. (6.363)	none
0808	Cu (3.063)	Cu (1.585)	10μm ZrC/THV (2.525)	f.s. (6.370)	none
0810	WA[c] (3.942)	Cu (1.516)	10μm ZrC/THV (3.942)	f.s. (6.35)	none

[a]Fused silica (f.s.) was Corning 7980 from Mark Optics.
[b]Foils were grounded in order to shield PVDF gauges from sample polarization.
[b]WA is Tungsten Alloy, W-6Ni-4Cu

propagated gauge traces exhibit the sigmoidal shape discussed previously in Section 2.6 and noted by prior researchers[122] with ALOX material, indicative of a dispersive material. At high peak pressures, the rise time of the propagated stress decreases considerably, and approaches the rise time of the input gauge stress wave profile for the highest impact velocity experiment. As expected, the rise times of the input gauges (∼10 nsec) are almost independent of peak pressure, since the only dispersion at the input gauge is due to angular tilt at impact and to the dispersion caused by propagating through the Cu driver. In some experiments the gauges survived long enough to view loading and unloading behavior in the composites. Figure 4.7 shows the input and propagated PVDF stress gauge traces for shot 0754 (the 1 μm Al_2O_3 composite). The figure illustrates several methods of calculating shock travel time through the sample thickness for determining the shock velocity, U_S, including 10% rise, 50% rise, and 90% rise. Due to the large variations in the shock front rise times, the time at 50% rise (less the time for the wave to propagate through the gauge package) was used to calculate the shock velocity, U_S.

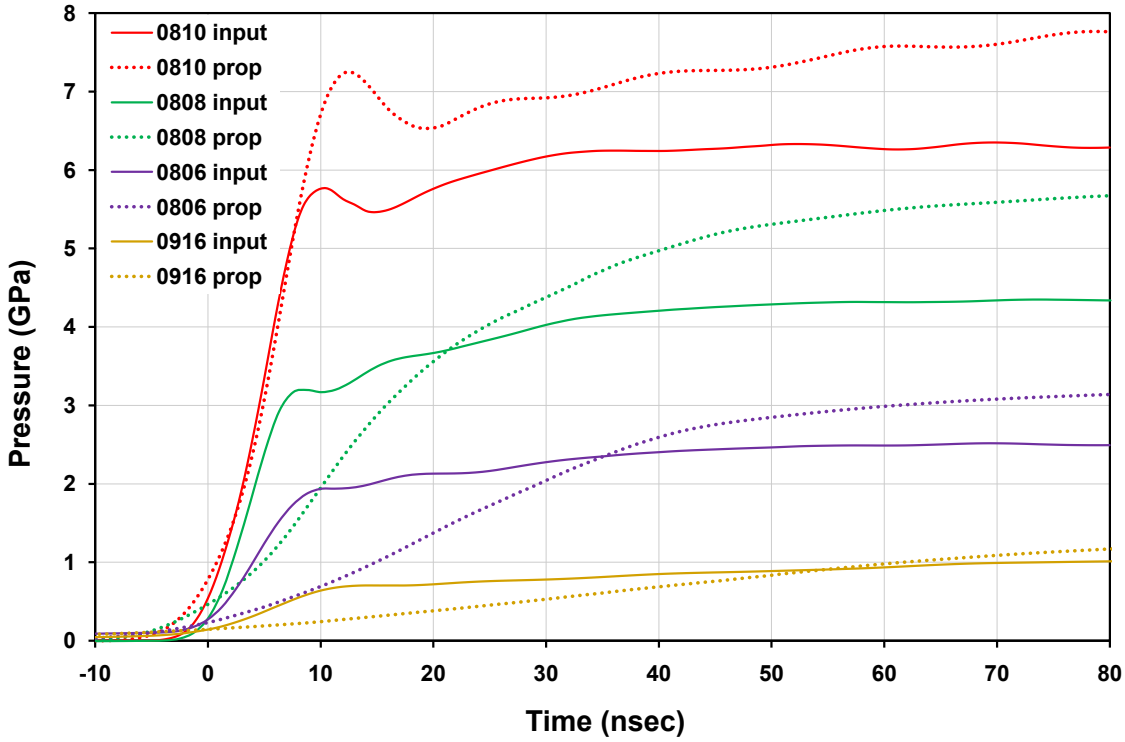

Figure 4.6: Input (1^{st} gauge) and propagated (2^{nd} gauge) PVDF pressure traces for ZrC/THV experiments.

A summary of the gas gun experimental conditions and measured/calculated parameters for each material type is shown in Table 4.6. Shock velocity (U_S) measurements were obtained from time-of-arrival calculations by finding the time at which the respective input and propagated stress trace had risen to 50% of the steady state value, less the time of travel through the gauge packages at pressure (where PVDF was modeled as Kel-F). The uncertainty in the travel time was the difference in the arrival times of the foot of the wave and the top of the wave. The large uncertainties in U_S (as much as $\pm 4\%$) are primarily driven by variation in the rise times (as shown in Figure 4.7). The pressure (P) reported in Table 4.6 was obtained from the input PVDF gauge (placed between the driver and the sample). In most experiments, the pressure indicated by the PVDF gauge was not stable behind the shock front, and so the pressure reported is the average of the stress behind the shock front and before the arrival of the release wave or the destruction of the gauge, while the plus/minus values correspond to the maximum and minimum pressure over the same time span, as shown in Figure 4.7. The measured shock velocity (U_S) vs pressure (P) data

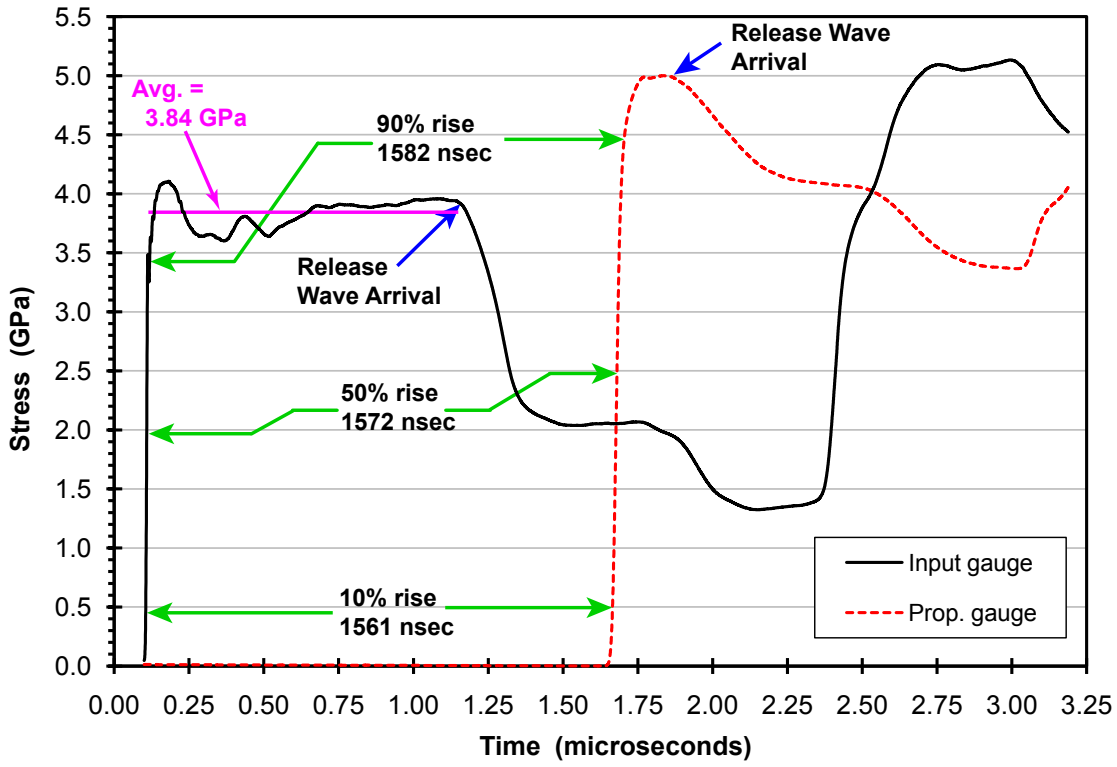

Figure 4.7: PVDF gauge traces for experiment 0754. Note the uneven shock state prior to release wave arrival, as well as the variation in shock travel time in a dispersive material due to taking the arrival time at 10%, 50%, and 90% rise.

is plotted in Figure 4.8. In four of the shots in Table 4.6 (0822,0821,0752, and 0810), the PVDF gauges did not survive long enough to establish a steady state pressure. For these four experiments, the pressure calculated from impedance matching is substituted. These data points are identified in the figure, along with the two experiments where the recorded pressure differed significantly from the pressure calculated using impedance matching (0803 and 0808). The last two columns in the table are calculated values of particle velocity (U_P) and pressure (P), obtained from the measured U_S values and the measured impact velocities using standard impedance matching techniques and the known Hugoniots of the impactor and driver materials (the PVDF gauges are used simply as time-of-arrival guages). Performing these transformations obviously involves invoking the jump conditions, which are not strictly valid for dispersive materials where steady-state equilibrium conditions may not be present. However, in order to convert between the various shock parameters to compare with model predictions, the jump conditions are hereafter applied. It should be noted that in all but two experiments (0803 and 0808), the agreement between the measured pressure and the calculated pressure is good. Although not conclusive, such agreement supports the validity of applying the jump conditions even though the input gauge obviously does not capture a steady-state waveform in the sample material. Similar conclusions were previously found with THV in Section 4.1.1.

The results for each of the composite types are plotted in U_S-U_P space, along with linear best fits, in Figure 4.9 using the measured U_S and calculated U_P values. No nonlinearities indicating phase transitions or reactions are evident in the data within the range investigated. The linear fits were then used to generate the quadratic fit lines in P-U_P space plotted in Figure 4.10.

Although the best-fit line for ZrC/THV in U_S-U_P space is not dramatically different from the line for pure THV (Figure 4.2), the composite does have a higher impedance as shown in P-U_P space in Figure 4.10. In fact, the impedance of all composites is similar, and higher than that of pure THV, except for the 1 μm Al_2O_3 composite. Since all of these composites consist of 25% by volume relatively rigid reinforcement particles and the remainder THV, the ZrC composite is expected to have the highest impedance compared to

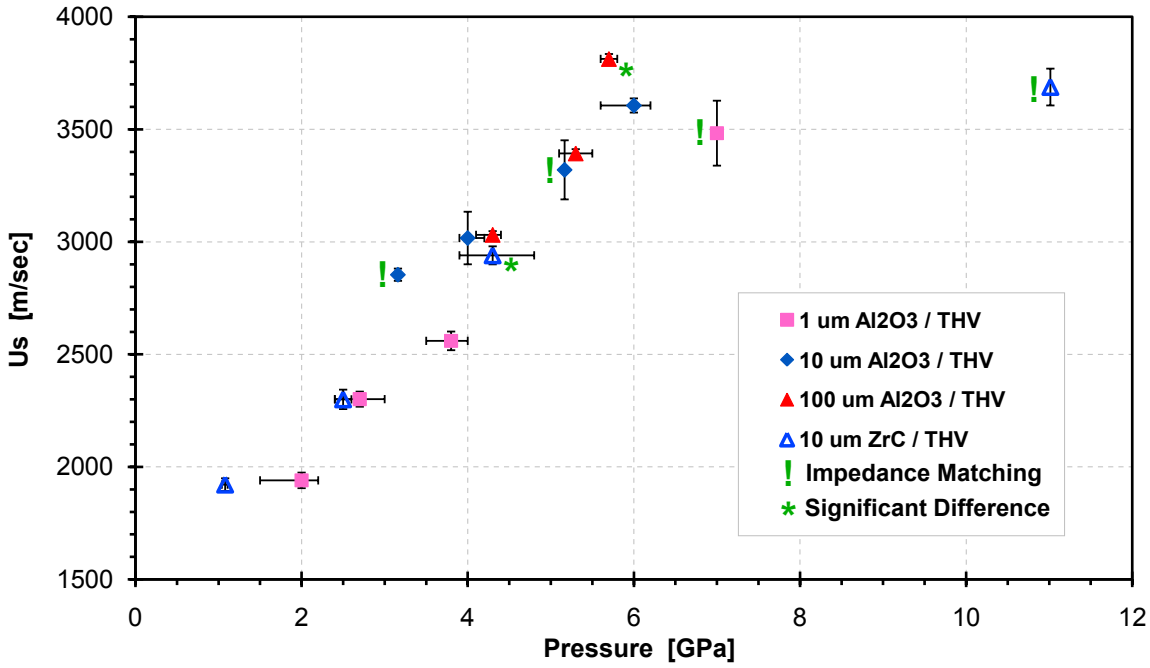

Figure 4.8: Pressure - Shock Speed data obtained from direct measurements. In four of the shots in Table 4.6 (0822,0821,0752, and 0810), the PVDF gauges did not survive long enough to establish a steady state pressure. For these four experiments, the pressure calculated from impedance matching is substituted. These data points are identified in the figure, along with the two experiments where the recorded pressure differed significantly from the pressure calculated using impedance matching (0803 and 0808).

Table 4.6: Gas Gun Experiments Performed on THV composites

Shot#	Material	Measured Values			Calculated Values[a]	
		Impact Vel.	Us	P	Up	P_{calc}
		m/sec	m/sec	GPa	m/sec	GPa
0755	1μm Al_2O_3/THV	538	1940±35	$2.0^{+.5}_{-.2}$	483	2.0
0757	1μm Al_2O_3/THV	656	2301±34	$2.7^{+.3}_{-.3}$	579	2.8
0754	1μm Al_2O_3/THV	786	2560±42	$3.8^{+.3}_{-.2}$	686	3.7
0822	1μm Al_2O_3/THV	1150	3483±144	–[b]	964	7.0
0821	10μm Al_2O_3/THV	542	2854±27	–[b]	455	3.2
0748	10μm Al_2O_3/THV	660	3017±117	$4.0^{+.2}_{-.1}$	550	4.0
0752	10μm Al_2O_3/THV	783	3320±131	–[b]	643	5.2
0746	10μm Al_2O_3/THV	894	3606±32	$6.0^{+.2}_{-.4}$	725	6.3
0802	100μm Al_2O_3/THV	635	3031±17	$4.3^{+.1}_{-.2}$	528	3.9
0759	100μm Al_2O_3/THV	806	3393±19	$5.3^{+.2}_{-.2}$	658	5.5
0803	100μm Al_2O_3/THV	1009	3813±22	$5.7^{+.1}_{-.1}$	809	7.6
0916	10μm ZrC/THV	235	1921±28	$1.08^{+.03}_{-.04}$	203	1.1
0806	10μm ZrC/THV	486	2300±43	$2.5^{+.1}_{-.1}$	412	2.7
0808	10μm ZrC/THV	862	2940±40	$4.3^{+.5}_{-.4}$	705	5.9
0810	10μm ZrC/THV	1046	3688±82	–[b]	1059	11.0

[a] U_P and Pressure were calculated from impact velocity and U_S using impedance matching.
[b] The PVDF gauges did not survive long enough to establish a steady state pressure.

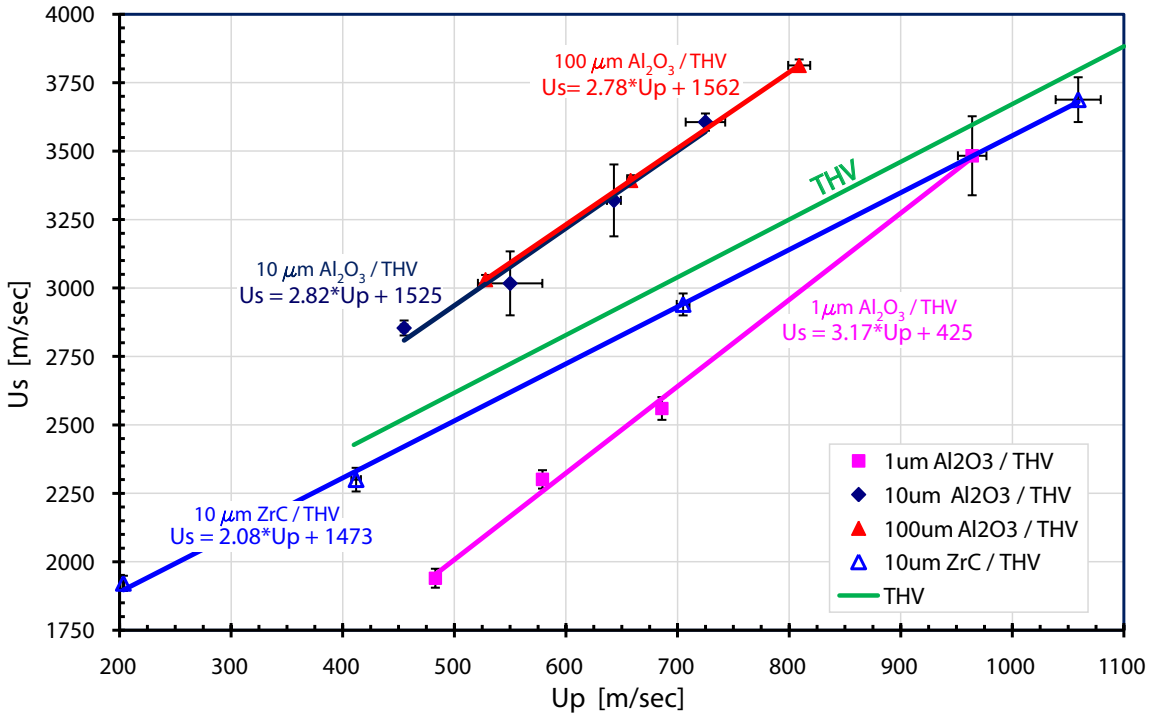

Figure 4.9: U_S-U_P data for THV composites, with linear fits and associated equations. The linear fit for THV is $U_S = 1562 + 2.11U_P$ (Section 4.1.1).

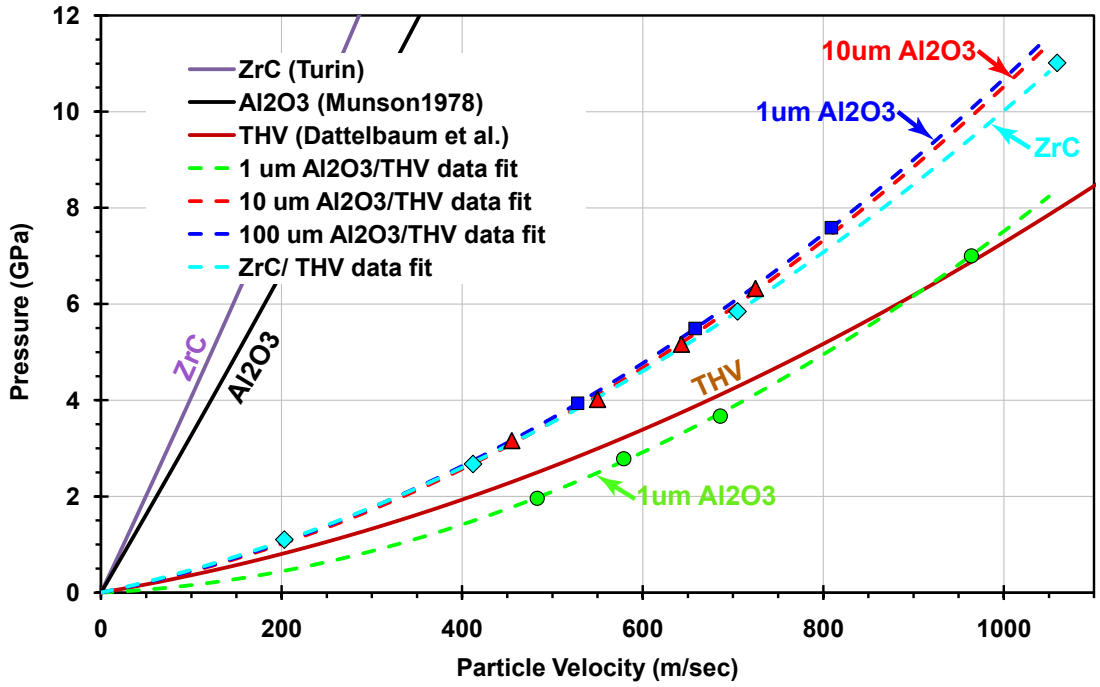

Figure 4.10: Pressure - Particle Velocity data for pure THV and THV composites. The dashed lines are calculated from linear fit data in Fig 4.9. The points are experimental data points from Table 4.6.

the other composites due to its higher density. Any difference in the impedance of the Al_2O_3 composites is expected to be due to differences in the particle size, morphology, or porosity (density). It can be seen that the 100 μm Al_2O_3 composite has a slightly lower porosity (1.4%) than the 10 μm material (2.6%), and has a slightly higher shock impedance. The 1 μm Al_2O_3 composite has 16% porosity, and consequently, a far lower shock impedance. Additionally, in the lower pressure regime (up to approx. 6 GPa) the impedance of the $1\mu m$ Al_2O_3/THV composite is below that for pure THV, indicating that in the pressure regime investigated, the inclusion of the 1 μm alumina (and 16% void space) weakens the composite material. The ZrC composite has 11% porosity, but because of the much higher density of ZrC, the overall composite has a shock impedance higher than that of pure THV and similar to that for the 10 and 100 μm Al_2O_3/THV composites.

4.2.2 Composite Rod-on-Anvil (Taylor) Impact Tests

Cylindrical specimens of each of the four ceramic particle/THV composites (1, 10, and 100 μm Al_2O_3 and 10 μm ZrC) were obtained for use in Taylor rod-on-anvil impact experiments to determine an averaged high-strain-rate yield strength. Table 4.7 lists the impact conditions and calculated yield strengths using the Hutchings analysis (Section 3.2.3) for specimens that did not fracture.

In Table 4.7, $\epsilon_{elastic}$ represents the observed elastic engineering strain, as measured by comparing the recovered specimen length l_{rec} to the length at maximum deformation l_{min} through the relation $\epsilon_{elastic} = (l_{rec} - l_{min})/l_0$, where l_0 is the initial length. The length at maximum deformation is determined from the high speed camera record, as shown previously in the case of pure THV in Figure 4.4. The critical velocity is the threshold velocity below which plastic strain does not occur, and the yield strength Y, and yield strain ϵ_y are calculated using the Hutchings analysis discussed previously in Section 3.2. The critical velocity is determined using the data shown in Figure 4.11.

As illustrated in the table, yield strength was mostly consistent within each material group ($\pm$4% with the exception of shot 08-79). The measured densities of the Taylor specimens varied by up to 2% over 4 or 5 samples, illustrating the heterogeneity and variation

Table 4.7: Taylor shots performed on ceramic particle/THV composites

Shot	Material	Density $[kg/m^3]$	Imp. V. $[m/sec]$	Crit. V. $[m/sec]$	σ_y [MPa]	ϵ_y	$\epsilon_{elastic}$
08-118	10μm Al_2O_3/THV	2410	109	54	146	.046	>.113[c]
08-119	10μm Al_2O_3/THV	2410	129	54	144[a]	.047[a]	>.150[c]
08-120	10μm Al_2O_3/THV	2430	102	54	156	.044	.104
08-121	10μm Al_2O_3/THV	2410	71	54	146	.046	.105
08-122	10μm Al_2O_3/THV	2430	71	54	146	.047	.082
08-79	100μm Al_2O_3/THV	2440	60	40	168	.022	.075
08-80	100μm Al_2O_3/THV	2410	85	40	130	.028	.070
08-81	100μm Al_2O_3/THV	2430	82	40	132	.028	.080
08-82	100μm Al_2O_3/THV	2450	104	40	127	.029	>.127[c]
08-128	10μm ZrC/THV	2790	81	49	156	.041	.075
08-129	10μm ZrC/THV	2830	96	49	154	.042	.083
08-130	10μm ZrC/THV	2820	104	49	_[b]	_[b]	_[b]
08-131	10μm ZrC/THV	2820	65	49	155	.041	.060

[a]Specimen fractured, but held together sufficiently for measurements.

[b]Specimen fractured severely, no measurements were possible.

[c]Camera image record ended before specimen recovery began- no maximum strain could be established from the image record.

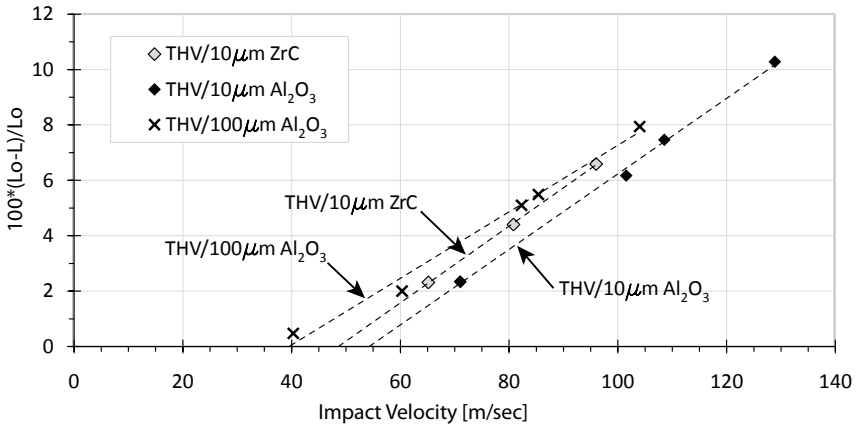

Figure 4.11: Critical Velocity determination for THV composites. The abscissa is the percent axial strain in the recovered specimen, as done in the work by Hutchings[143]. It can be seen that the critical velocities for 100μm Al_2O_3/THV, 10μm ZrC/THV, and 10μm Al_2O_3/THV are 39.7, 48.6, and 54.3 m/s, respectively.

within samples of the same material. The yield strain values given in the table can be compared with the maximum recovered strain observed. In an elastic-perfectly plastic sytem, the yield strain is the amount of elastic deformation the sample experiences during the deformation event. By comparing the minimum specimen length in the camera images l_{min} with the recovered specimen length l_{rec}, we can also determine the longitudinal elastic engineering strain through the equation $\epsilon_{elastic} = (l_{rec} - l_{min})/l_0$ by the methods discussed previously (see Figure 4.4). These data are listed in the final column of Table 4.7. Although the strain state is not constant in the sample, these data clearly show that some portions of the sample exhibit much higher elastic strains than the yield strain predicted by the Hutchings analysis. This is not suprising since the same effect was observed in similar tests on the matrix material, THV, as previously discussed.

Despite this similarity, the Taylor test data indicate that the composite materials behave very differently than the pure THV polymer discussed previously. In the pure polymer, a strain-rate softening effect was evident, where yield strength decreased and yield strain increased as impact velocity increased. However, no such trends exist in the 10 μm composite data. Instead, the yield strength is constant over the impact conditions investigated, and yield strain is constant as well. It is obvious that the inclusion of the particles has a profound effect on the mechanical properties of the material. However, it is also clear that the density of the particles is a minor effect at best. Comparing the yield strengths σ_y and yield strains ϵ_y for the 10 μm Al_2O_3 and ZrC composites, there is no significant difference in σ_y and a small difference in ϵ_y. The data for the 100 μm Al_2O_3 is noisier, and may even display a small amount of the strain rate softening and increased ductility observed in the THV polymer. It is unclear whether this is a real effect or simply due to experimental uncertainty. However, the yield strain for the 100 μm composite is significantly less than that for either of the 10 μm composites.

If the strain rate softening in the pure THV is due to a local heating effect, as speculated, perhaps the lack of the effect in the composite can be attributed to the ceramic particles acting as thermal sinks. There are several ways to critically evaluate this explanation, one of which is to see if heat generated in the THV regions can dissipate out of the THV by

conduction in the timescale of the experimental deformation. If we model the regions of pure THV as 0.5mm spheres, we can use the heat equation to estimate the temperature in a sphere of THV surrounded by an alumina sink, which is always at ambient temperature. The heat equation for an isotropic sphere with no internal heat generation is given in Equation (67) below[1], where α is the thermal diffusivity $\alpha = \frac{k}{\rho c_p}$, Θ is the normalized temperature $\Theta = \frac{T - T_{initial}}{|T_{final} - T_{initial}|}$, r is the radius of the point of interest within the THV particle, T is temperature, k is thermal conductivity ($\sim$0.35 $\frac{W}{mK}$), and c_p is isobaric specific heat ($\sim$1 $\frac{J}{gK}$).

$$\frac{1}{\alpha}\frac{\partial \Theta}{\partial t} = \frac{1}{r^2}\frac{\partial}{\partial r}\left(r^2 \frac{\partial \Theta}{\partial r}\right) \tag{67}$$

From camera records such as those shown in Figure 4.4, we know that the deformation is taking place in the first few hundred microseconds. If we solve Equation (67) for a 0.5 mm diameter sphere of THV in perfect thermal contact with an infinite sink of temperature T_{final}, we can see how the temperature of the THV sphere evolves. The initial and boundary conditions are given in Equation (68), where r_0 is the radius of the sphere (0.25 mm in this example).

$$\begin{aligned} \text{I.C.} &: \Theta(r,t) = 0 \text{ for } 0 \leq r \leq r_0 \text{ and } t < 0 \\ \text{B.C.} &: \Theta(r,t) = 1 \text{ for } r = r_0 \text{ and } t > 0 \\ \text{B.C.} &: \tfrac{\partial \Theta(r,t)}{\partial r} = 0 \text{ for } r = 0 \text{ and } t > 0 \end{aligned} \tag{68}$$

These conditions represent the best case for a thermal sink effect- any thermal interface resistance or heating of the surroundings as the sphere cools, and any heat conduction limitations from the alumina particles, will only lessen the effectiveness of the thermal sink. Thus, it represents the limiting case and provides insight into the limits of thermal conduction effects. The equations were solved using Matlab, and Figure 4.12 shows several plots of the temperature evolution of the THV sphere. Figure 4.12(a) shows the evolution

[1]The equation given in most texts (for example, see Eckert and Drake[150]) is slightly different from Equation (67). To reach the equation given in most texts, apply the product rule to the r-derivative. The form shown is necessary to solve the equation computationally using Matlab.

at a sufficiently long timescale that the center of the sphere reaches ∼90% of the final temperature. However, the time required (∼0.1 sec) is much longer than the timescales for deformation in the rod-on-anvil tests (∼1-100 microseconds). Figure 4.12(b) shows a more detailed surface for the first few milliseconds, and Figure 4.12(c) shows a 2D plot of normalized temperature vs. radial position, where each line represents a slice of the surface at a constant time. It is clear that at the times of interest (tens of microseconds), the influence of heat conduction from the sphere is limited to the outermost ∼5μm of material. Therefore, it is unlikely that any thermal sink can affect the bulk THV response. However, to the extent that the deformation is influenced by the THV within the mixed phase region and the surface "skin" of the large regions of pure THV, the thermal sink effect could reduce any thermal strain rate softening. We can also take a simple energy balance approach to evaluating this explanation. The composite is 75% by volume THV, which corresponds to ∼60% by mass THV and the remainder alumina. Using these mass fractions, along with the specific heat values ($c_{P,alumina} = .765\ \frac{J}{gK}$), we can show that, once equilibrium is reached, the change in temperature of the THV will equal approximately half the change in temperature of the alumina, again indicating that the thermal sink idea is unlikely to influence the response. However, it remains possible that the early-time mechanical response of the THV very near the alumina particles is being affected by the alumina heat sinks.

It is also possible that the lack of strain rate softening in the composites is due to an inertial confinement effect- i.e., when the higher density particle is present, inertial resistance could hinder the motion of the lower density matrix which would otherwise result in larger strains. However, for this argument to hold, the inertial confinement would have to exactly counterbalance the thermal heating argument given for the strain rate softening, otherwise, we would observe a strain-rate hardening effect. While possible, it is unlikely that two totally different mechanisms would negate each other over a range of strain rates. A more likely explanation is that the difference in mechanical response (the lack of strain rate softening in the composite) is due to the unavailability of the responsible mechanism in the composite. If we assume that the responsible mechanism is a local thermal softening, then the morphology of the composites, where the regions of THV are almost completely separated from one

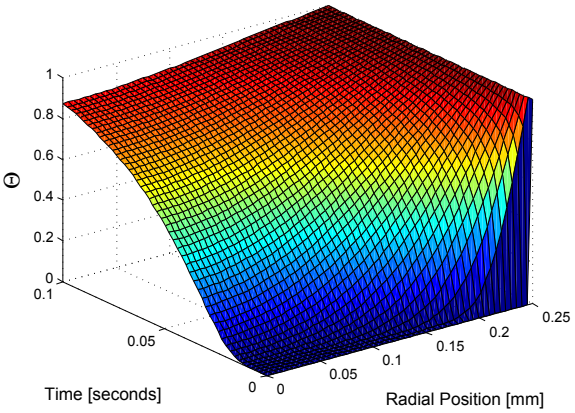

(a) To 100 msec.

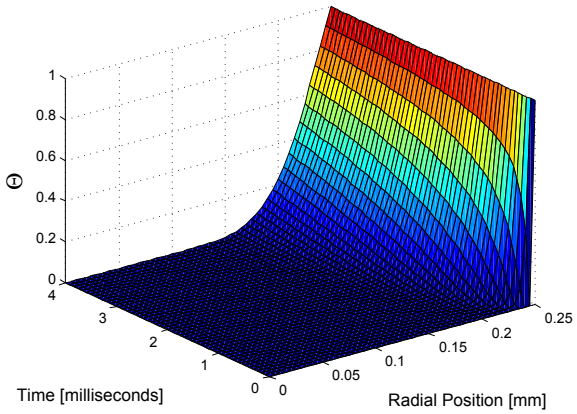

(b) To 4 msec.

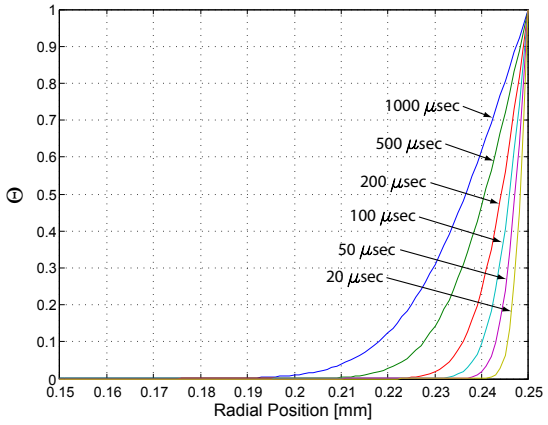

(c) Temp vs Radial Position for several times. Note the zoomed radial position axis.

Figure 4.12: Temperature evolution in a 0.5mm diameter THV sphere as a function of radial position and time. The sphere, initially at a constant temperature $\Theta = 0$, is subjected to a final temperature $\Theta = 1$ at the surface. This represents the limiting case for the kinetics of a "thermal sink" effect influencing material response.

another by regions containing very little THV, is suppressing the propagation of any local high strain regions, and so suppressing the strain rate softening observed in the pure THV specimens.

4.3 Characteristics of Measured Stress Wave Profiles

A significant advantage of using the nanosecond-resolved PVDF stress gauges discussed in Chapters 2 and 3 and employed in this work is that details can be resolved in the initial shape of the stress pulse, possibly revealing characteristics of the material response. The time required for the stress pulse to rise from ambient pressure (effectively zero) to essentially the steady-state shocked pressure is called the risetime. The effect of particle morphology on the risetime has been a topic of interest for understanding the shock response of porous and/or particulate materials, as well as particle-filled composites such as those examined in this study. This section will examine the trends observed in this study with respect to risetime and illustrate how they compare and contrast with observations made elsewhere in the literature.

Variation in risetimes for the input gauge and propagated gauges can be seen in the PVDF stress guage traces in Figure 4.6. The input gauge risetimes are largely a function of the response time of the gauges, which is primarily driven by the shock transit time across the PVDF film. Other potential causes of increased input gauge risetimes are tilt at impact, dispersion of the wave by the driver, air cushioning due to an inadequately evacuated experiment chamber, and poor (non-planar) experimental assembly. The propagated gauge risetime is of more interest because it indicates material response, such as that associated with void collapse in porous materials[80]. Heterogeneous and porous materials are each known to display dispersive behavior similar to that exhibited by the propagated stress waveforms in Figure 4.6. The only effect the condition of the input wave has on the steady-state wave induced in the material is on the amount of time required for the steady wave to develop (and retain its strength before attenuating).

Risetimes measured by fitting a line to the steepest portion of the stress profile and finding the intersection points of the line with zero pressure and steady-state line for the

Table 4.8: Stress wave risetimes for THV composite parallel plate impact experiments.

Shot#	Sample	t_{input} ns	t_{prop} ns	Bland Number
0755	1μm Al_2O_3/THV	17	–[a]	–
0757	1μm Al_2O_3/THV	8.5	41	69
0754	1μm Al_2O_3/THV	8	33	91
0822	1μm Al_2O_3/THV	–[a]	–[a]	–
0821	10μm Al_2O_3/THV	14	35[b]	13
0748	10μm Al_2O_3/THV	6	41[c]	8
0752	10μm Al_2O_3/THV	–[a]	18	19
0746	10μm Al_2O_3/THV	9	16	22
0802	100μm Al_2O_3/THV	20	23	13
0759	100μm Al_2O_3/THV	17	15	22
0803	100μm Al_2O_3/THV	12.5	14	26
0916	10μm ZrC/THV	18	100	2
0806	10μm ZrC/THV	11	45	5
0808	10μm ZrC/THV	9	30[c]	11
0810	10μm ZrC/THV	9	9	43

[a]Gauge did non survive long enough to establish a risetime.
[b]Pressure rise shifted shifted halfway through rise.
[c]Significant break in slope of pressure rise on propagated gauge.

various experiments performed in this work are listed in Table 4.8. The time between the two intersections is the risetime.

The ratio of sample thickness to the predicted steady-wave propagation distance predicted by Bland, as reported by Swegle and Grady[2] is also given in Table 4.8. The Bland number is derived assuming a linear shock EOS with a linear viscous dissipation term depending on the strain η. The Bland number is (d/δ), where δ is the distance required for a steady-wave to develop, and d is the sample thickness is calculated using Equation (69).

$$\delta = \frac{8}{3}\frac{C_0}{S\dot{\eta}} \tag{69}$$

If the Bland number is greater than 1, steady state conditions are expected. Strain rate is represented by $\dot{\eta}$, and is calculated using the propagated risetime and the volumetric strain. At first glance, the Bland numbers shown in Table 4.8 indicate that steady state

[2]Based on papers by Swegle and Grady [151] and also by Setchell and Anderson [122]. The Bland paper cited by those authors could not be obtained and verified ("D.R. Bland, J. Inst. Math. Appl. **1**, 56 (1964)"), but the two papers are consistent in their description of the citing except that the work of Setchell and Anderson stipulates that the relationship applies for the "peak" strain rate.

conditions exist. However, the number shown makes a number of assumptions. The first is the use of the C_0 and S values from the Hugoniot in Figure 4.9, which includes an inherent assumption of steady state behavior. The second is that the aforementioned method of determining rise times is valid. Because it was not clear whether the phenomenon of large risetimes (due to the slow increase in pressure after the initial jump) was a material response, a gauge response (see Section 5.1), due to experimental assembly, or due to the material heterogeneity, the intersection method used was the only method that could be applied consistently across all experiments. If the slow rise often observed in the PVDF traces is due to a material response, the rise times should be longer, decreasing the average strain rate (but not the max. strain rate). Any decrease in the strain rate would proportionally decrease the Bland number, and therefore decrease confidence that steady-state conditions were reached. Nevertheless, such an analysis does provide some additional confidence that the propagated waveforms observed represent measurements performed under steady-state conditions.

A correlation between risetime and shock pressure has been noted by several previous researchers[3]. Such analysis originated with the work of Swegle and Grady[151], who examined existing data for fully dense materials and noted a relationship between strain rate $\dot{\epsilon}$ (and therefore rise time) and pressure P of the form $\dot{\epsilon} = aP^n$, where a was a material parameter and $n \approx 4$. This empirical correlation has since been explained as a consequence of dislocation generation in metals by Armstrong et al.[153], but n is commonly called "shock viscosity" or "artificial viscosity" in the literature and is often treated as an empirical parameter employed to smear the shock front to facilitate use of numerical codes (to avoid infinite strain rates) or simply to match experimental data. Working with fully dense ALOX (described in Section 2.6), Setchell and Anderson[122] found a similar relationship with $n \approx 4$. Likewise, for fully dense, but periodically layered composites of polycarbonate and several metals, Zhuang et al. [154] found $n \approx 2$.

For the composite materials studied in this work, using the risetimes shown in Table 4.8, the exponents are much less than 4; they range between 1.0 for the 1 μm Al_2O_3 composite,

[3]There is also literature indicating that at high pressures, rise times are independent of pressure [152]

1.1 for the 10 and 100 μm Al_2O_3 composite, and 1.4 for the ZrC composite. Since the minimum risetime of a PVDF gauge is limited by the time for a wave to propagate through the gauge package, we can attempt to correct for this effect by subtracting the time for a stress wave to propagate through the PVDF gauge material (6-11 ns for the pressure range in this work). Even if the wave propagation time through the gauge packages are subtracted from the measured risetime, values of the exponent n only change to 1.2 to 1.8, which are still below the value of $n \approx 4$ reported for the fully dense materials by Swegle and Grady. Recently, Brown et al.[28], working with sand, and Vogler et al.[76], working with WC powders, have reported values of n in the range of 1-1.2. Both Brown and Vogler also examined the previous work of Anderson et al.[70] on rutile TiO_2 powder and found a value of $n = 1.0$. The few available studies indicate that the composite materials investigated in this work are behaving more as powders rather than as solids, even though the distention (or porosity) for the composites in this work is very low by pressed powder standards.

The shock front thickness (or shock width) has also been examined, and has been correlated to the particle size in powders by several authors[9]. The shock front thickness can be easily calculated by multiplying the wavespeed minus the particle velocity ($U_S - U_P$) by the risetime[9], although it has been described as simply the wavespeed U_S times the risetime[12]. In reality, the distinction is unlikely to make much difference, since results are usually given as broad ranges. For the present work, the shock front thickness was calculated from $(U_S - U_P) * t_r$, where t_r is the risetime reported in Table 4.8. In several previously reported studies, the front thickness has been found to be on a similar length scale as the particle size, and is usually reported normalized by particle size. Sheffield et al.[12], working with HMX and sugar, found that wave front thickness varied with particle size, and reported shock front thicknesses of six-eight particles for fine HMX particles and three-four particles in coarse HMX particles (with results in sugar that qualitatively agreed), although, as Vogler[76] notes, the risetimes for fine and coarse particles converged at higher stresses. Also, Nesterenko[9] has noted that such observations may be caused by the rate dependence of HMX's mechanical properties and the large difference in strain rates in the coarse and fine particles. Anderson et al.[70], working with rutile TiO_2, reported

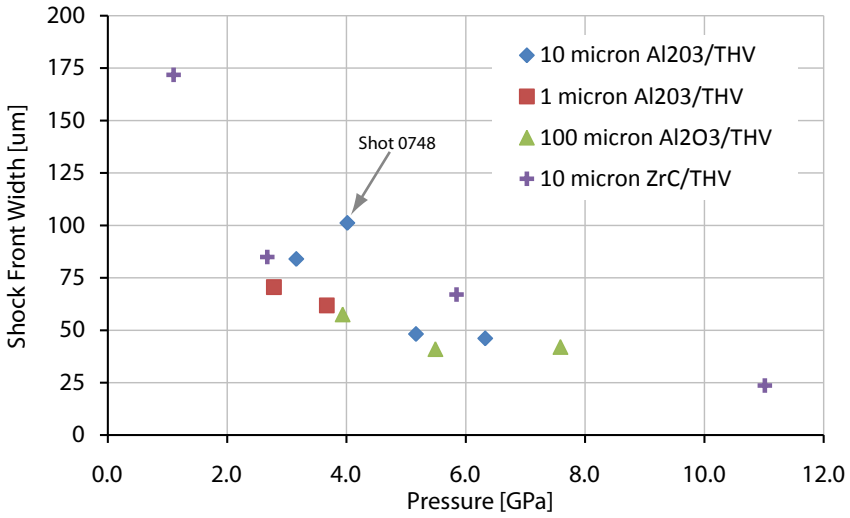

Figure 4.13: Shock front thickness of THV composites. Note the general trend of an inverse relation between thickness and pressure. The only outlier is shot 0748, as noted in Table 4.8, had an irregular pressure trace profile.

an inverse relationship between pressure and risetime, although the particle size range in their powders was so broad as to make reporting the front width in terms of the number of particles meaningless. Nesterenko[9] has devoted significant effort to discussing shock front width, and summarized the main features of the available data, stating that the shock front width depends on particle size, but not necessarily on porosity, is of the same order of magnitude as the particles size, and decreases with increasing pressure. The results of the present work follow some, but not all, of these accepted trends, as shown in Figure 4.13. It can be seen that there is a general trend of decreasing shock front thickness with increasing pressure. This is in agreement with previously discussed literature results. However, no evidence of a dependence on the particle size is revealed by the data shown in Figure 4.13. This is explained by recalling that the composites are actually composed of ceramic particles surrounded by large THV particles. Since the composites were not heated and mixed sufficiently to homogenize the particle/matrix distribution, the measured risetimes are likely influenced by the large ($\sim$ 500 μm) THV particles. It was also shown that the shock front thickness did not vary with porosity in the various composites studied in this work.

Table 4.9: Fischmiester - Arzt Fit Data

Powder	Avg. ρ_0 [% TMD]	σ_Y [MPa]
AEE	30.92	1598
Unibrite	43.55	952

4.4 Compaction of Alumina Powders

In order to better understand and explain the behavior of the ceramic-particle/THV composites, an effort was made to understand the densification of the constituent ceramic powders. In particular, the pressure at which the powders completely densify was of interest. Therefore, the static compaction behavior was determined, and a shock compaction experiment was performed in which the samples were recovered to quantify the amount of densification occurring during shock loading.

4.4.1 Static Compression of Alumina Powders

The AEE 1 μm and Unibrite 10 μm Al_2O_3 powders were quasi-statically pressed to 878 MPa using the apparatus and methods previously described in Section 3.1. The results for both powders are shown as plots of pressure versus % theoretical maximum density (TMD) in Figure 4.14.

It can be seen that the 1 μm AEE material is significantly stiffer than the 10 μm Unibrite Al_2O_3 powder. The Fischmeister-Arzt model (Section 2.4) was used to fit the loading portion of the data for each powder type and estimate the average values for the yield strength σ_y. The fitted strength values are shown in Table 4.9, along with the initial relative density.

SEM images of the post-pressed powders are shown in Figure 4.15. Several observations can be made by comparing these post-pressing images with the pre-pressed images in Figures 3.9 and 3.10. For the 1 μm powder, the powder still consists of agglomerates of $\sim$250 nm particles, but the particles are no longer fused together- the fused bridges between particles have been broken. The small features described previously as possible grain boundaries remained unchanged. For the 10 μm powder, many more fine particles were observed, and

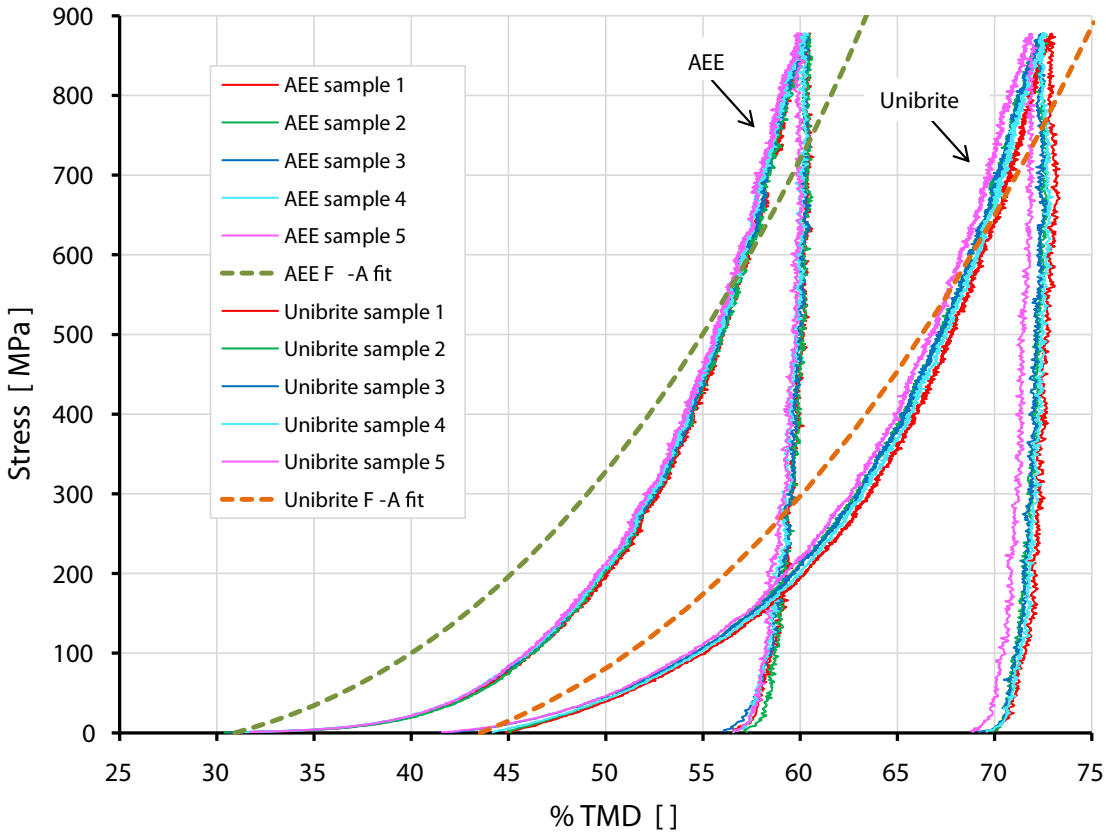

Figure 4.14: Static compression for 1 μm AEE and 10 μm Unibrite alumina powders, along with plots of the Fischmeister-Arzt model fit to the loading portion of each powder type (see Equation (58)). It is easily seen that the AEE powder is much stiffer than the Unibrite powder. It is also apparent that the repeatability of the AEE powder is higher. This is most likely caused by the experimental difficulties experienced with the Unibrite powder arising from its increased tendency to cling to the walls of the die body and pouring funnel, so that the precise mass delivered to the bottom of the die body was less precise.

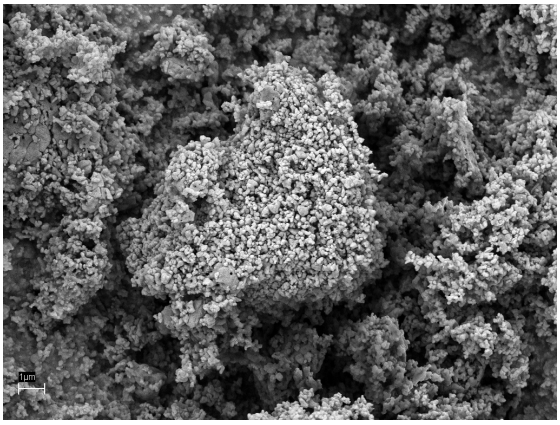

(a) 1 μm AEE Al_2O_3 powder at 5kx.

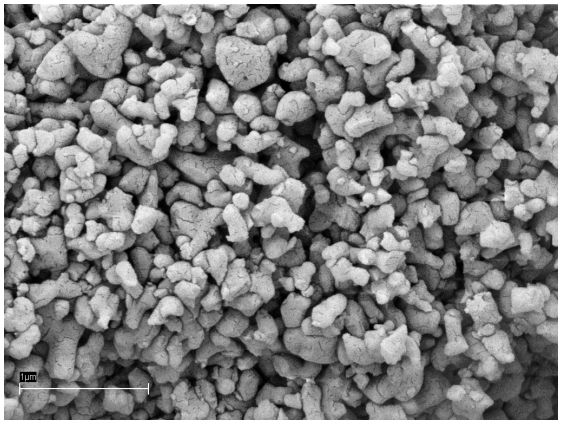

(b) 1 μm AEE Al_2O_3 powder at 25kx.

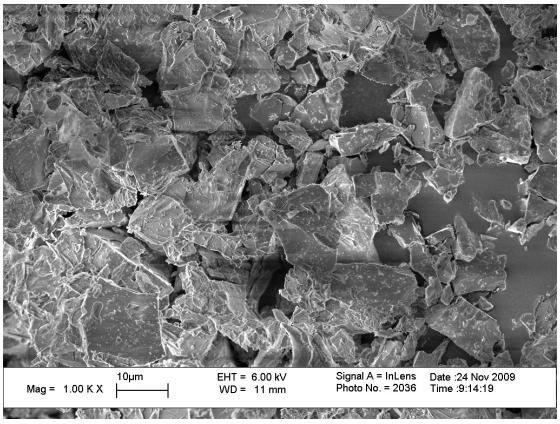

(c) 10 μm Unibrite Al_2O_3 powder at 1kx.

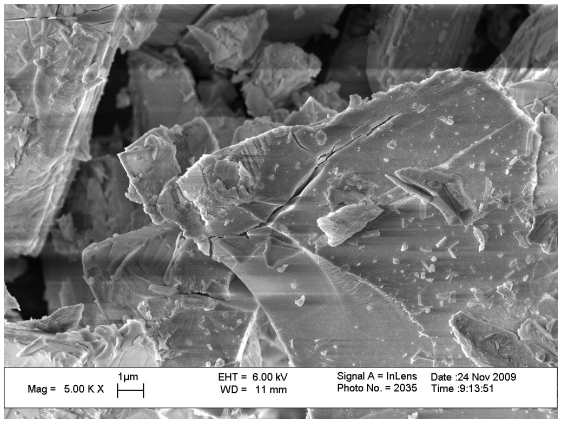

(d) 10 μm Unibrite Al_2O_3 powder at 5kx.

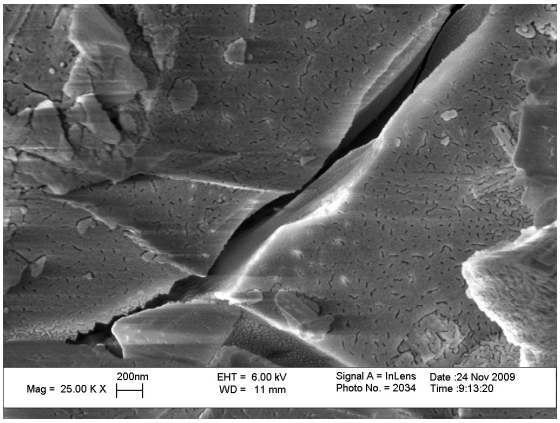

(e) 10 μm Unibrite Al_2O_3 powder at 25kx.

Figure 4.15: Alumina powders after pressing to 878 MPa.

the large particles also appear to show cracking. In the highest magnification image of the fractured particle, the small grain-boundary-like features can again be seen, and again appear unaffected by the static pressing operation.

4.4.2 Shock Compaction Recovery (3-capsule) Experiment

In addition to the static compression tests, a recovery experiment was performed on both of the Al_2O_3 powders, as well as on the 1 μm Al_2O_3/THV composite. The purpose was to determine the extent of powder densification during shock compression for the interpretation of the Hugoniot behavior of the composites.

The geometry of the 3-capsule recovery experiment was described in Section 3.2.2. The experiment was conducted at an impact velocity of 382 $\pm$1 m/s, yielding a calculated pressure of $\sim$6.8 GPa in the steel flier/driver. Of the three capsules, two of them contained alumina powder. Capsule I contained the 1 μm AEE Al_2O_3 powder, and Capsule II contained the 10 μm Unibrite Al_2O_3 powder. These powders were described previously in Section 3.1.3. The powders were pressed into the capsules to the initial densities listed in Table 4.10. The densities of the recovered specimens were measured by the wax immersion technique[155] since they readily absorbed water. The recovered compacts had barely sufficient mechanical integrity to handle without crumbling, and the samples completely crumbled during the removal of the wax coating after the density measurements due to- a clear indication of minimal interparticle bonding. The maximum pressure values given in the table were computed using CTH, which incorporated modeling the geometry of the sabot, flier, capsules, and fixturing using built-in values for the EOS and strength of the materials (the steel was modeled as 21-6-9 stainless because of the availability of strength models) and using the P-α model for the porous alumina as described in Section 4.5.1. Figure 4.16 illustrates the geometry used for the CTH simulations and the output obtained for each of the three capsules. Although the absolute values of the pressures obtained varied for the two aluminas because of their different initial porosities, the pressure profiles were similar.

The values of maximum pressure (P_{max}) in Table 4.10 are those that were reached and

Table 4.10: Initial and recovered densities of Al_2O_3 powders

Capsule	Material	Initial Density g/cm^3 (%TMD)	Recovered Density[a] g/cm^3 (%TMD)	P_{max} GPa
I	1 μm	2.23 $\pm$0.02 (56.5)	2.65 $\pm$0.1 (67.1)	6.5-8.5
II	10 μm	2.66 $\pm$0.02 (67.3)	2.92 (73.9)	6.5-7.5

[a]The shocked samples did not fuse or otherwise consolidate. Three intact pieces of the 1 μm material were recovered for density measurements. Only one piece of the 10 μm material had sufficient strength to handle. Therefore, the range given for the 1 μm material is for the three pieces, and the value for the 10 μm value is for a single sample.

maintained for more than a few nanoseconds, as predicted using CTH. As illustrated in Figure 4.16, the complex geometry causes some areas in the sample to experience higher peak pressures than others due to two-dimension effects.

The recovered samples from Capsules I and II were examined to determine the extent to which they were compacted. As illustrated by the microstructures shown in Figure 4.17, the 1 μm AEE powder did not completely densify. Although the fused-agglomerate structure appears to have been broken at the fused points, the structure is largely transformed from one of agglomerated and fused 200 nm particles to one of still agglomerated but less-fused 200 nm particles. This result is similar to that found in the statically-compacted powder shown in Figure 4.15(b). However, there appeared to be more fused links surviving the shock event to 7-8 GPa than the static pressing event to 0.9 GPa. Another observation was the intermittent appearance of a fused "glaze" over the particles. Finally, there was a lack of the small grain-boundary-like features previously identified on the virgin powders (see Figure 3.9(d)). Although similar features were observed in a few places, when they were found it was under a thick coating of the "glaze", and in many parts the features were absent.

The 10 μm (Unibrite) powder recovered from Capsule II was more predictable, and showed little observable change from the statically compressed powder. Although the particles were smaller than the virgin particles, it was not possible to quantitatively determine whether or not they were smaller than the statically compressed powder. Like the statically compressed powder, numerous fractures were visible, and the grain-boundary-like surface features were unaltered.

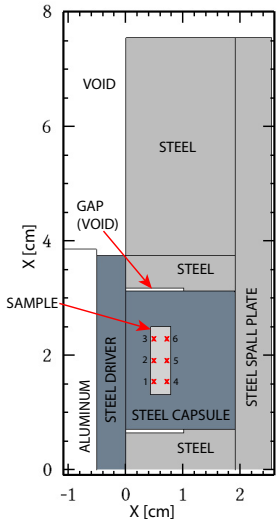

(a) CTH material position plot for one capsule in the 3-capsule recovery experiment. The positions of the six Lagrangian tracers in the sample are shown.

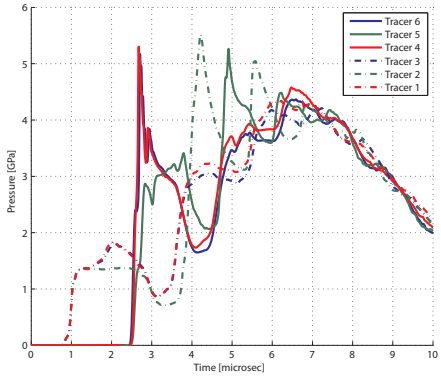

(b) Predicted pressure history for the six tracers for Capsule III (1 μm Al_2O_3/THV composite). Zero time corresponds to the time of impact.

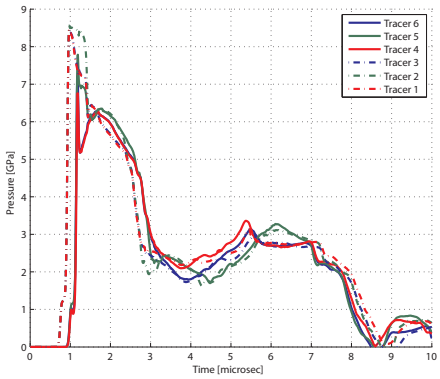

(c) Predicted pressure history for the six tracers for Capsule I (1 μm Al_2O_3 powder). Zero time corresponds to the time of impact.

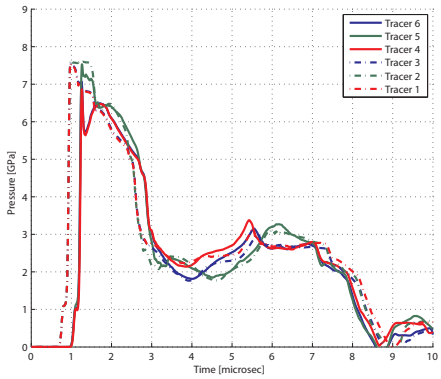

(d) Predicted pressure history for the six tracers for Capsule II (10 μm Al_2O_3 powder). Zero time corresponds to the time of impact.

Figure 4.16: CTH simulations for the 3 capsule experiment. All simulations used the geometry shown in a), where the aluminum and steel driver were initially moving at 382 m/s to the right. Note that the pressure for Capsule I is slightly greater than that for Capsule II- the model assumed complete crush-up of the porous alumina, so increased porosity leads to increased impedance. Also note that the porous alumina powders ring down due to their slightly higher impedance than the steel, whereas the composite rings up.

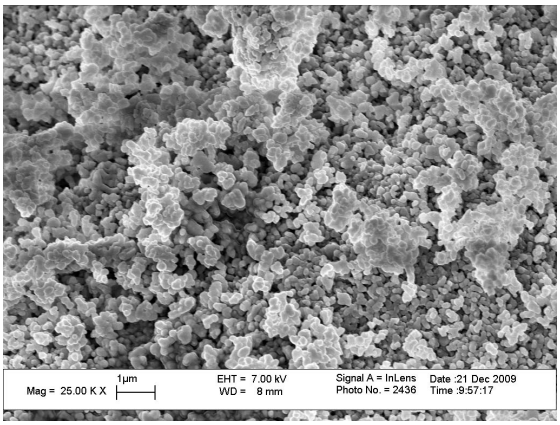

(a) 1 μm AEE Al_2O_3 powder at 25kx. Most, but not all particle fused-points are broken.

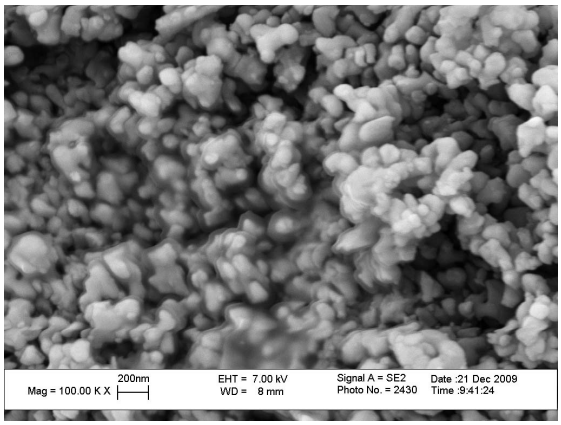

(b) 1 μm AEE Al_2O_3 powder at 100kx. Some regions showed new fused "glaze".

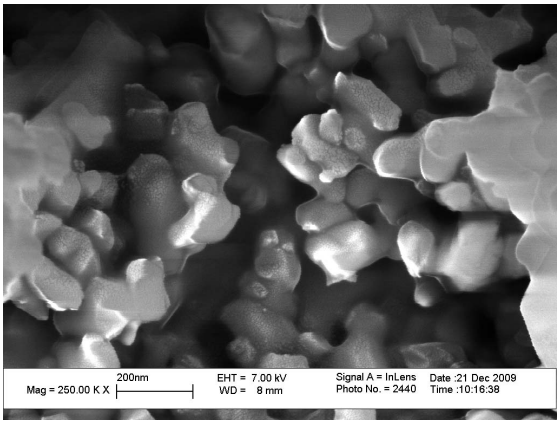

(c) 1 μm AEE Al_2O_3 powder at 250 kx. The grain boundary-like surface features previously identified were largely absent, but similar features are shown here.

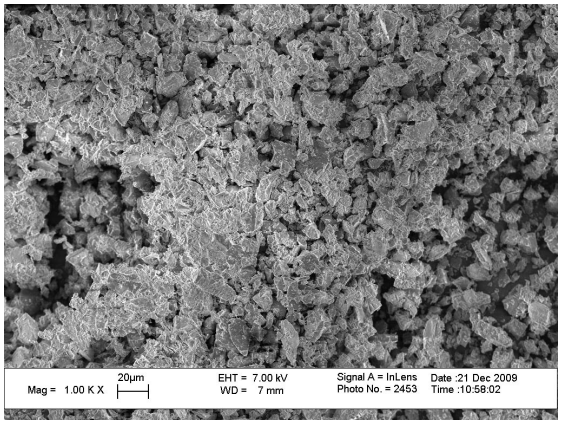

(d) 10 μm Unibrite Al_2O_3 powder at 1kx.

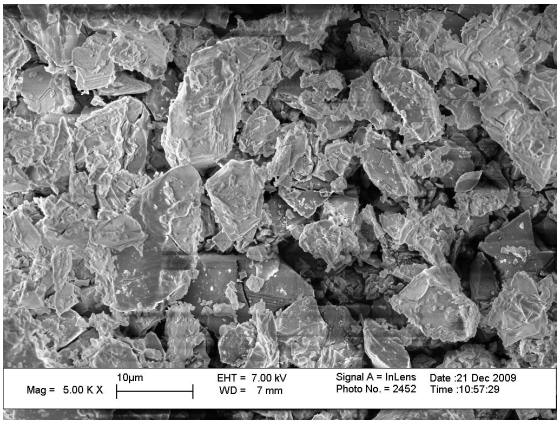

(e) 10 μm Unibrite Al_2O_3 powder at 5kx.

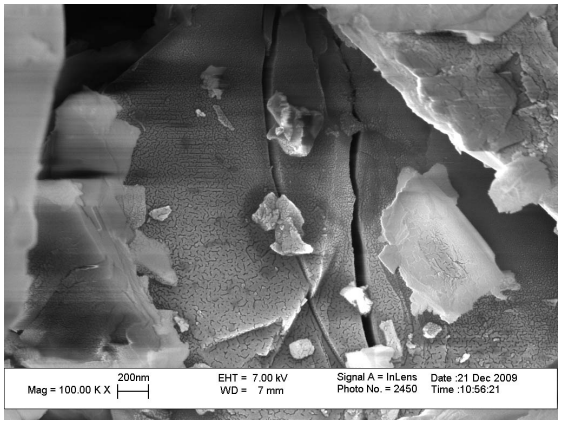

(f) 10 μm Unibrite Al_2O_3 powder at 100kx.

Figure 4.17: 1 and 10 μm Al_2O_3 powder recovered from 3 capsule experiment

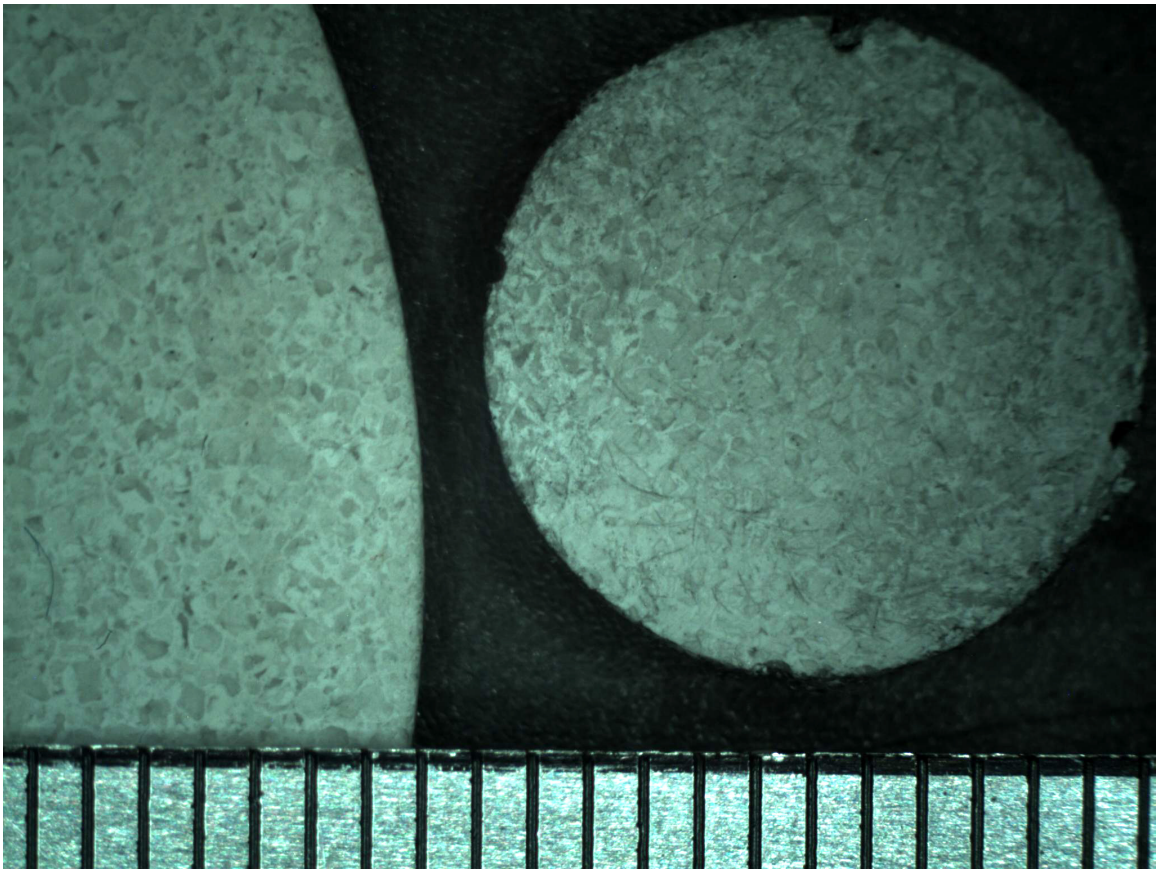

Figure 4.18: Image of unshocked (left) vs shocked and recovered (right) 1 um Al_2O_3/THV composite. The scale bar ticks at the bottom are millimeters. The disc on the right is the recovered "pill", and the larger disc on the left is the original disc from which the specimen was cut.

Capsule III was the 1 μm Al_2O_3/THV composite described previously. The recovered steel capsule was machined away to leave an intact pill-shaped specimen. Except for small amounts that adhered to the capsule wall, the specimen appeared intact. Pre-experimental mass was 0.973g, and the recovered mass was 0.958g, indicating minimal material loss. The density of the sample was determined using the Archimedean water-immersion method and found to be 2.344 g/cm^3, or 94% TMD. This was considerably denser than the initial value of 84% TMD. The recovered material looked very similar to the initial material, as shown in Figure 4.18.

SEM images of the recovered specimen shown in Figure 4.19 reveal that the THV does not flow sufficiently to infiltrate the porous Al_2O_3 particles. Additionally, the "glaze"

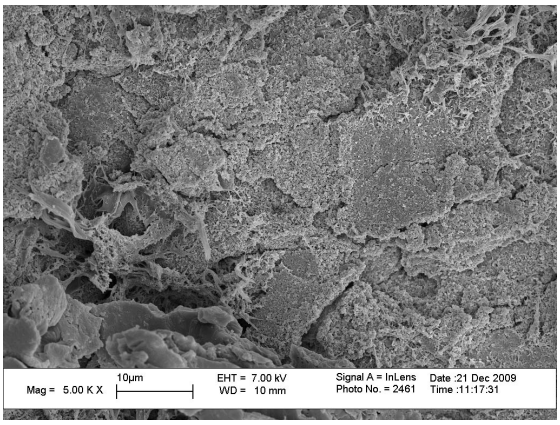

(a) 1 μm Al_2O_3/THV composite powder at 5kx.

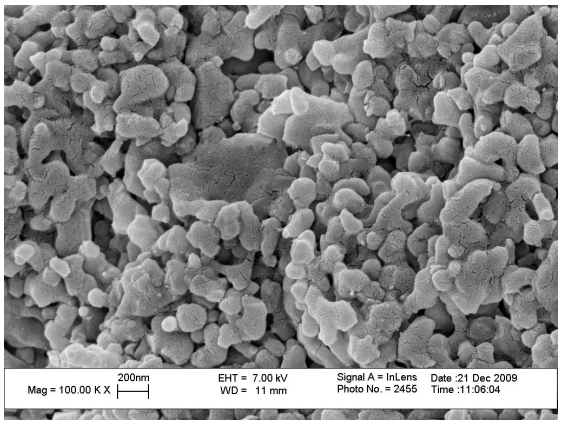

(b) 1 μm Al_2O_3/THV composite powder at 5kx. Note familiar grain-boundary-like features, lack of glaze, and lack of polymer infiltration.

Figure 4.19: 1 μm Al_2O_3/THV composite recovered from 3 capsule experiment

observed in Capsule I was not observed on the alumina in Capsule III.

4.5 Microstructure Based Computational Simulations of Densification

Microstructure based computational simulations were used in this work to predict the shock compression behavior of the ceramic particle/THV composites using the P-α model, and to evaluate whether or not the ceramic particles fully crush up (completely densify) during the shock event. For both purposes, the CTH Eulerian hydrocode package[156] was used.

4.5.1 Predicting Shock Compaction using the P-alpha Model

In order to predict the shock compression response of the particle filled composites using the P-α model, some assumptions must be made about the porosity distribution. Namely, since the P-α model cannot handle discreet porosity, the porosity must be incorporated into a continuum, creating a homogeneous, but porous, phase. Hence, for the P-α simulations performed in this work, the porosity was assumed to be in the alumina phase, as evidenced by the microstructural observations discussed previously. The micrograph shown in Figure 4.20(a) is a 3.2x2.6 μm section of the 1 μm Al_2O_3 composite. Using a technique similar to that employed by Eakins[124], the micrograph was used to create the test image shown in Figure 4.20(b) by tracing the areas of pure THV, and then slightly adjusting them so that

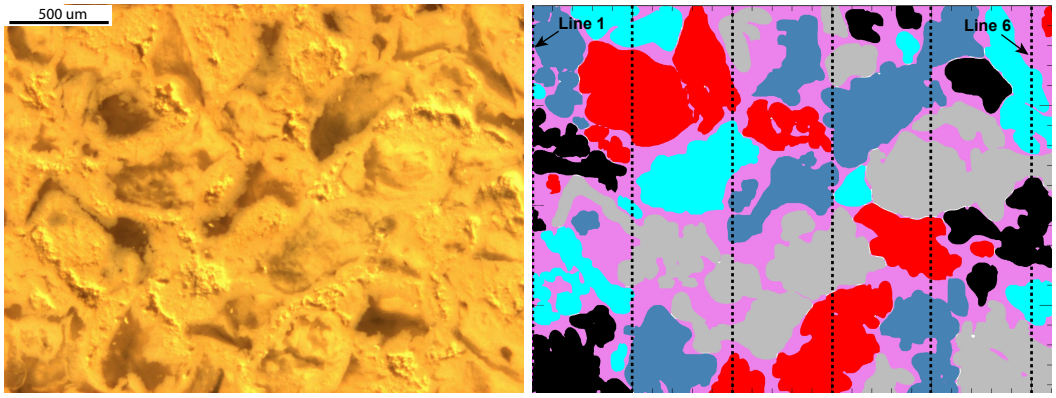

(a) Optical micrograph of 1 μm Al_2O_3/THV composite. The small scale bar at the top is 250 μm, and the whole image is 3.207 x 2.604 μm. The dark areas are regions of pure, transparent, THV. The regions that appear rough are where a large THV particle pulled out. This image is very similar to Figure 3.5 c.

(b) CTH material position plot. The continuous pink area is porous alumina and the other colors are solid THV. The small white spots along some of the boundaries are artifacts of the visualization routine- no void space existed in the model. A constant velocity boundary was applied on the left, and 6 vertical lines of 10 tracers each were placed in the sample to track the movement of the resulting pressure wave. Each tracer line is separated by 0.5 mm from the next line.

Figure 4.20: Optical and CTH images for P-α Model.

the area fraction of the THV in the test image was representative of the overall volume fraction of THV in the sample. For the 1 μm Al_2O_3 composite shown, since the material is ~15.9% porous, and the solid volume fraction of alumina is 25%, the volume fraction and density of the alumina when all porosity is assigned to it is 32.9% and 2.27 g/cm^3 respectively.

The crush strength used for this P-α simulation was taken from the Fischmeister-Arzt fit to the static compression data for the AEE alumina powder ($2.97\sigma_Y$). The strength of the THV was approximated by modeling it as Lexan^{TM}using CTH's built-in Johnson-Cook strength parameters. The equation of state for alumina and THV were approximated by the tabular data for alumina built into CTH, and the viscoelastic EOS data built into CTH for Kel-F^{TM}, respectively.

In the P-α simulation, the sample space (shown in Figure 4.20(b)) was subjected to a constant velocity boundary condition on the left side, effectively setting the U_P. The lateral sides were set to symmetrical boundary conditions. To evaluate the pressure, 6 lines consisting of 10 "tracers" each were set in the material, as shown in Figure 4.20(b). Each

tracer is a Lagrangian position tracker. The pressure of the 10 tracers on each line were averaged together, yielding 6 "averaged" pressure traces. Shock wave arrival times were assigned for each averaged pressure trace when the pressure reached 90% of its maximum value, and then the shock speed was determined using the distance between the tracer lines and the wave arrival times.

The results of the P-alpha simulations are shown in Figures 4.21 and 4.22. In Figure 4.21, a spatial plot of pressure at 700 nsec for the U_P=500 m/s boundary condition case is shown, along with outlines of the particles shown in Figure 4.20(b) and dotted lines showing the width of the shock front. In Figure 4.22, each trace represents the average pressure of the line of tracers previously described and shown in Figure 4.20(b). Figure 4.22(a) is for the case where the $U_P = 500$ m/s boundary condition was imposed. For this case, arrival times were taken at the point where the pressure exceeded 1.9 GPa. Since the spacing between the lines is known, U_S is determined for each tracer line pair and averaged. The rise time at the 4^{th} line of tracers, near 700 nsec, is also shown for comparison with the spatial depiction of shock front width in Figure 4.21. The 1000 m/s case is shown in Figure 4.22(b), and the analysis is very similar. The values of U_S corresponding to U_P values of 500 and 1000 m/s were 2139 m/s and 3010 m/s, respectively. Considering the uncertainty in the crush strength P_c used in these simulations, these data are in reasonable agreement with the experimental data for the 1 μm Al_2O_3/THV composite shown in Figure 4.9. The low pressure point ($U_P = 500$, $U_S = 2139$ m/s) agrees very well, while the high pressure point ($U_P = 1000$, $U_S = 3010$ m/s) lies significantly below the experimental data, implying that the initial crush-up is reasonably well simulated, while the higher pressure crush-up behavior is not.

4.5.2 Ceramic Particle Densification - Explicit Porosity Simulations

The second purpose of computational modeling in this work was to evaluate whether or not the ceramic particles embedded in the matrix fully crush up (completely densify) during the shock event. Again, the CTH hydrocode[156] was used. The test geometries were constructed in a similar manner to the P-α simulation geometry discussed above, except

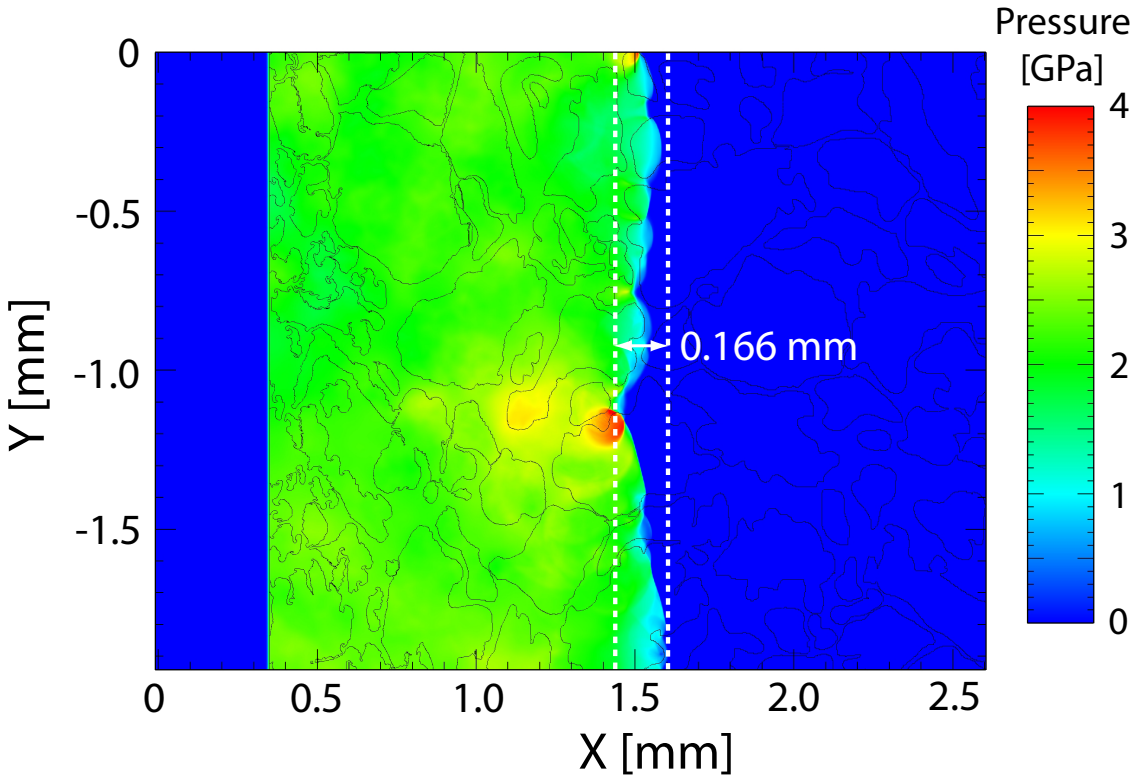

Figure 4.21: Spatial pressure plot illustrating non planar shock front resulting from material heterogeneity for the U_P=500 m/s case of the P-α CTH simulations described previously. The elapsed time since "impact" is 700 nsec. It can be seen that the simulated shock front is ∼0.166 mm wide.

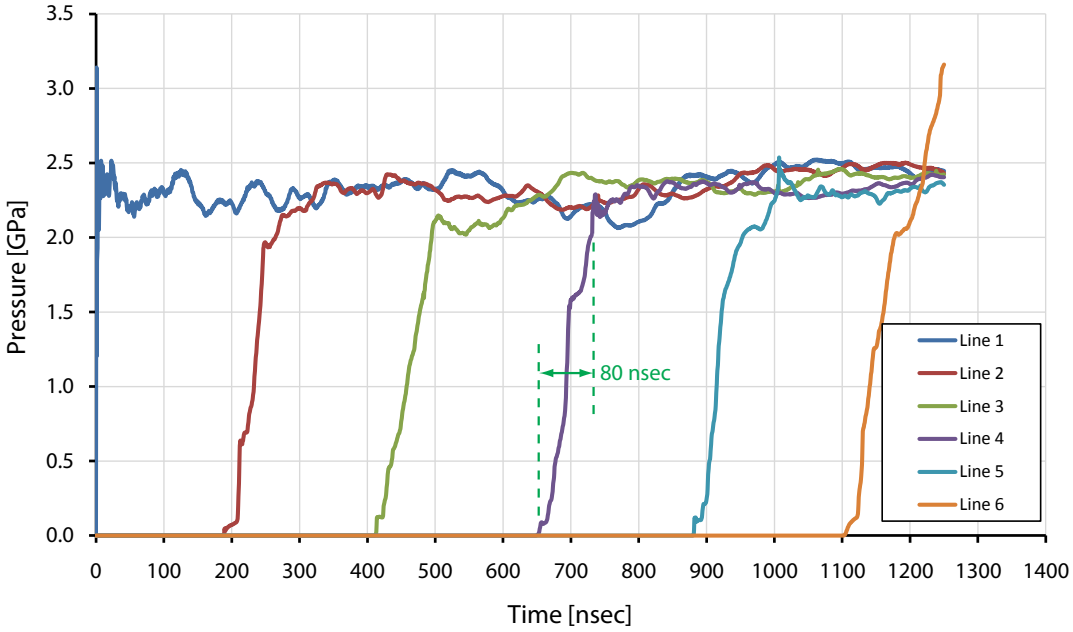

(a) 500 m/s case. The higher pressure on Line 6 is due to the boundary condition at the right side of the sample and the resulting reflection, but the arrival time of Line 6 at 2 GPa is unaffected. The traces appear to have risetimes of ∼50 nsec due to the heterogeneity of the sample and the resulting phenomena where some tracers in a line see the pressure wave before others. When averaged, this leads to a smearing effect. A risetime of 80 nsec is shown for the 4th tracer line (near 700 nsec). From this rise time, and the shock front width shown in Figure 4.21, a shock front speed of 2075 m/s is calculated. This is in good agreement with the overall average of 2139 m/s.

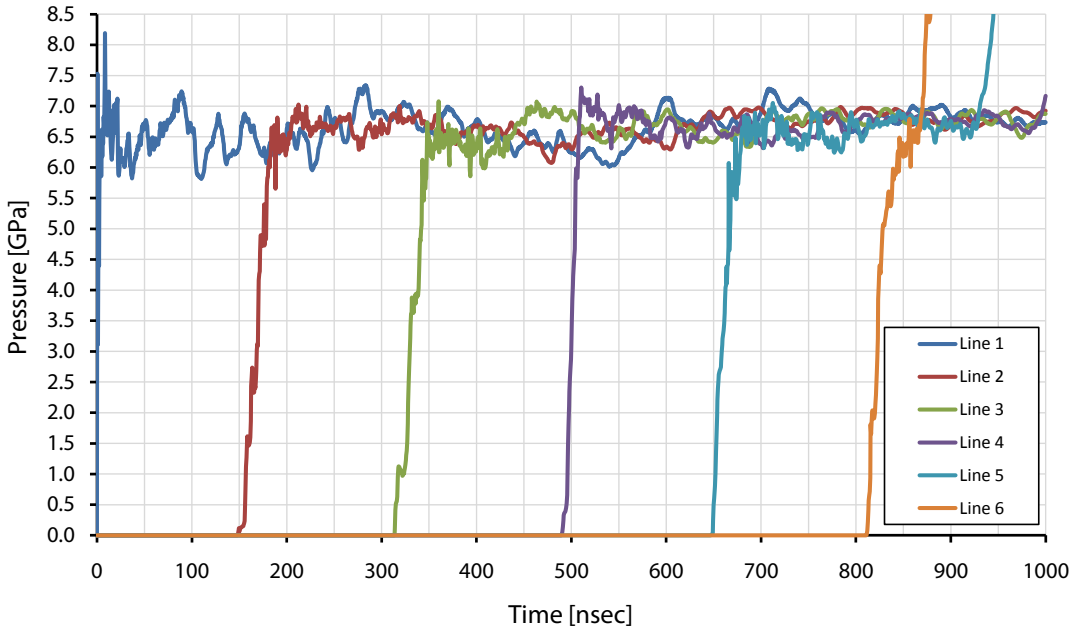

(b) 1000 m/s case. Analysis was similar to the 500 m/s. Arrival times were taken at 5.5 GPa.

Figure 4.22: Pressure vs. time for averaged CTH tracers in P-α simulations.

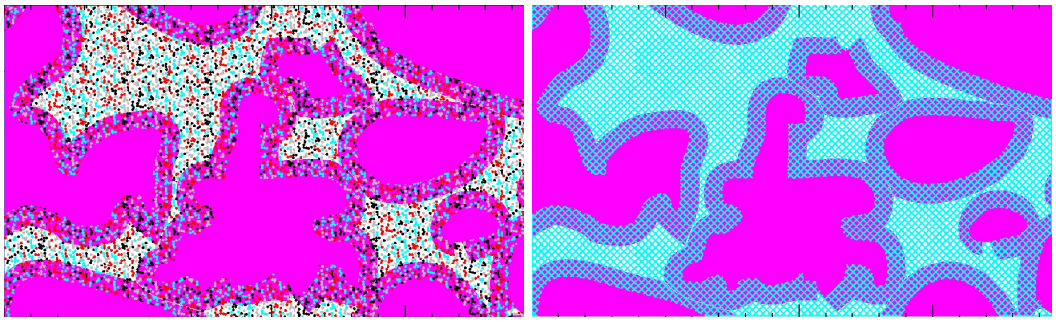

(a) CTH material position plot for scenario 1-alumina is represented by small (∼1.5 μm) balls.

(b) CTH material position plot for scenario 2-alumina is represented by a continuous, porous grid.

Figure 4.23: CTH images for alumina crush-up. In both images, the THV is represented by magenta and void space is represented by whitespace. Alumina is represented either by the cyan, red, black, and grey balls or by the cyan grid.

that instead of using just a micrograph, alumina particle geometry was created using a pc-based graphics program, overlaid with a micrograph, and then imported into the CTH input file. Since the purpose of the simulations is to determine whether or not crush-up occurs, the porosity cannot be incorporated into the continuum, as done in the P-α simulations. Instead, it must be modeled explicitly.

The alumina has been shown (Figure 3.9) to have complex 3-D porosity due to its fused-agglomerate morphology, but computational resource limitations required reducing the structure to 2-D. Therefore, two different 2D morphologies were modeled, as shown in Figure 4.23. Both geometries are created from the same micrograph. In Figure 4.23(a), the alumina has been represented by small, discrete, cylinders approximately 1.5 μm in diameter, with a finite-element grid mesh size such that each element was 0.1 x 0.1 μm. In Figure 4.23(b), the alumina has been represented by a continuous, porous alumina grid. These two morphologies, the cylinders and the grid, were chosen because of the difficulty in simulating a 3-D network of fused spheres (see Figure 3.4) in 2-D. The two morphologies each represent different 2-D approximations of the 3-D network. Again, in both cases, the traced microstructure was tuned to accurately represent the overall bulk composition, so that the area fractions for THV, alumina, and void were respectively 63%, 21%, and 16%.

In the explicit porosity simulations, as in the P-α simulations, the strength and EOS of

the THV were again approximated by Lexan^{TM}and Kel-F^{TM}using CTH's built-in parameters. However, in the explicit porosity simulations, both the equation of state and strength of alumina was modeled using the Johnson-Holmquist II Ceramic model[157].

For both morphologies, the sample space was subjected to a constant velocity boundary condition on the left side, effectively setting the U_P. Several particle velocities were investigated in an effort to find the threshold at which complete crush-up was predicted. The lateral sides were set to symmetrical boundary conditions. After shock passage, the simulated geometry was inspected for remnant porosity.

Simulations were performed with U_P values from 500 m/s down to 200 m/s. Even at the lowest value of U_P (200 m/s), the simulations depicted complete crush-up of the alumina for both microstructures, as shown in Figure 4.24. This is in spite of the fact that at $U_P = 200m/s$, the pressure is only 550 $\pm$100 MPa. From the static compression results, we know that the alumina was $\approx$ 43 % porous at 550 MPa. This very poor agreement casts doubt upon the ability of the simulations to accurately predict the crush strength of the alumina. This lack of applicability is not entirely suprising, as ceramic powder crush-up and Hugoniot behavior remains an active and unsettled area of research[157].

4.6 ALOX Hugoniot Results

The alumina-epoxy composite (ALOX) described previously in Chapter 3 was also investigated. The purpose of this was twofold. Because ALOX is by far the most investigated ceramic-particle/polymer composite in the field of shock compression, literature data from several investigators and several particle sizes is available. As previously discussed, Setchell et al.[123] have even examined the effect of particle shape. In order to contribute to the objective of this work of understanding how hard particles interact with a soft matrix in shock compression, an experiment was performed on ALOX to further investigate the effect of particle shape in a more homogeneous system, where the effect of porosity could be eliminated and the particles could be evenly distributed throughout the matrix. The second reason for the examination of the ALOX composite was to evaluate the various analytical mixture models introduced in Section 2.2 using historical data from a number of researchers

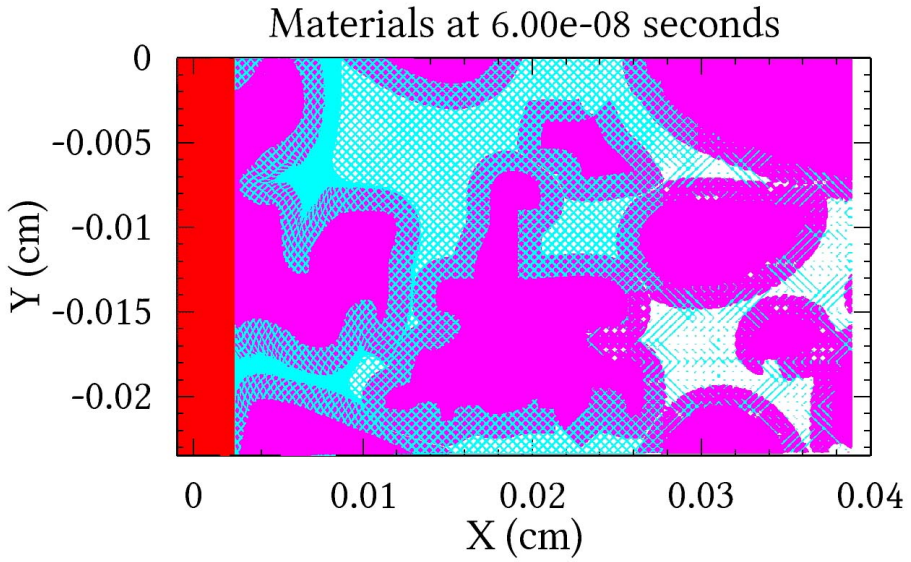

(a) Porous grid morphology.

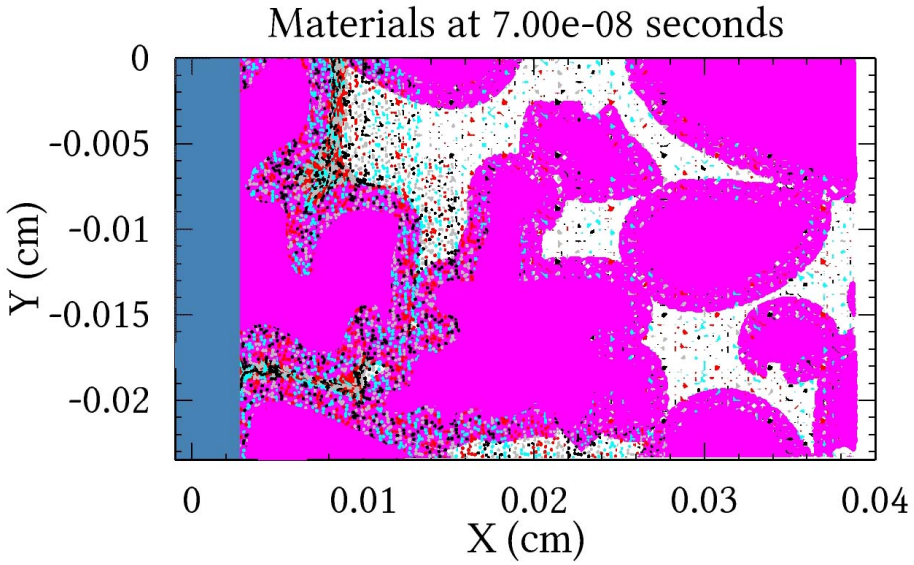

(b) Discreet balls morphology.

Figure 4.24: Explicity-modeled porosity CTH crush-up results. In both cases, due to computational resources, the simulation was only run until it became clear that the alumina was densifying. The fully densified alumina can be seen on the left, and the adaptive-mesh refining can be seen preceeding the shock front. Both images are from 400 m/s simulations, and are virutally identical to the images from 200 m/s and 300 m/s simulations.

and laboratories. This second objective will be discussed later.

In order to fulfill the first goal, a symmetric gas-gun impact experiment was performed using the method described previously with a 2.97 mm thick ALOX flier plate impacting a target assembly consisting of three ALOX discs (all discs were cut from the cast cylinder described in Section 3.1.5) cemented together using low-viscosity epoxy. A PVDF stress gauge (Section 2.3.2) was embedded between the driver (1.35 mm thick) and sample (2.97 mm thick) discs to monitor the input stress profile, and between the sample and backer (7.30 mm thick) to monitor the propagated stress profile. A piece of 25 μm thick etched FEP-Teflon^{TM}film was inserted on either side of each PVDF gauge to protect the gauge and so prolong the gauge life sufficiently to record release wave profiles.

The symmetric impact experiment was conducted at a velocity of 569 ± 1 m/s, yielding a particle velocity (U_P) in the ALOX of 284.5 m/s. The recorded stress wave profiles from the input and propagated PVDF stress gauges are shown in Figure 4.25. The PVDF stress gauges reveal a sharp jump in stress to about 1.8 GPa before gradually rising to a peak value of about 2.25 GPa before the release wave arrives. The familiar "lazy S", or sigmoidal rise profile is evident. The profiles for the input and propagated gauges are similar, indicating a steady-state condition. The shock speed based on the travel times through the sample thickness for 10%, 50%, and 90% rise are also shown in the figure, and are essentially identical (all are within 0.1%). The shock transit times were corrected for the travel time through the gauges and Teflon^{TM}film. The corrected release wave velocity is calculated from the points shown in Figure 4.25, yielding a value of $U_R = 5685$ m/s.

The initial portion of the recorded stress wave profiles are also shown on an expanded time scale in Figure 4.26 with the propagated gauge profile shifted to coincide with the input profile. Again, the overall risetimes for the input and propagated gauge are similar. As shown in the figure, the initial portion of the rise (up to $\sim$0.15 GPa), especially on the input gauge, is so gradual that an exact arrival time is difficult to define. This may have been due to some tilt in the impact, although it is unclear why a similarly long initial rise is not observed on the propagated response.

The rise times shown in Figure 4.26 are markedly longer than those observed by Setchell

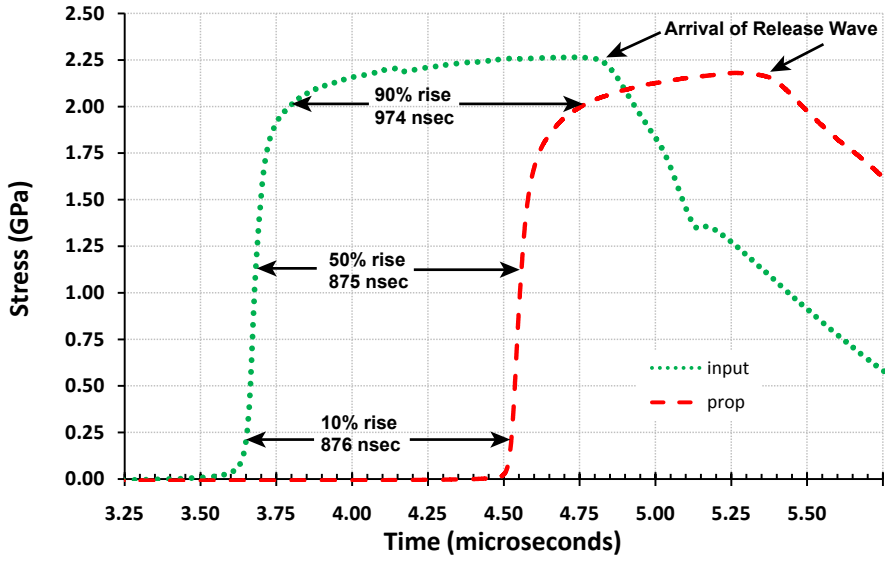

Figure 4.25: PVDF traces for ALOX symmetric impact experiment. As expected from prior work on the steady-state viscous response of ALOX, the travel time at 90% rise is significantly longer. The additional time is a function of sample thickness and is due to viscoelastic dispersion rather than geometric dispersion due to the inclusion of Al_2O_3 particles[131].

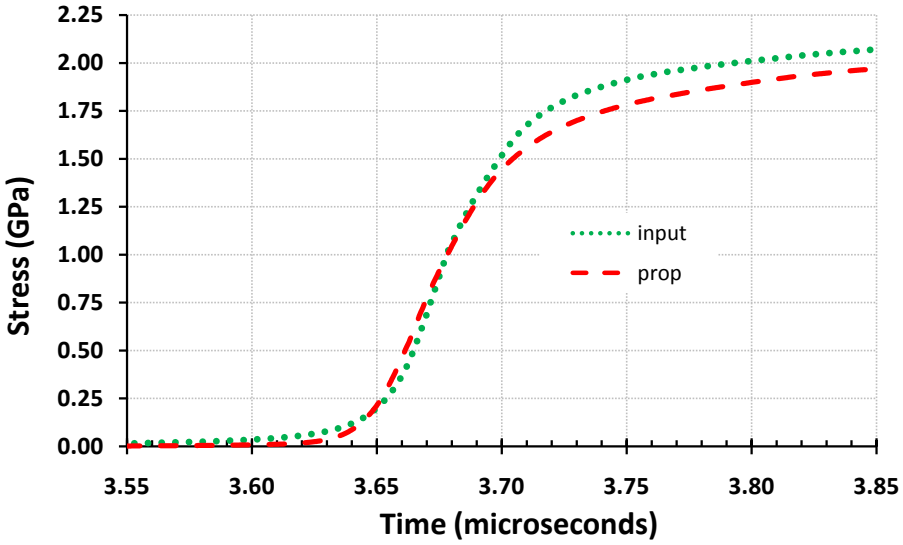

Figure 4.26: The same profiles shown in Figure 4.25, but with the propagated waveform shifted by -875 nsec and shown on an expanded time scale.

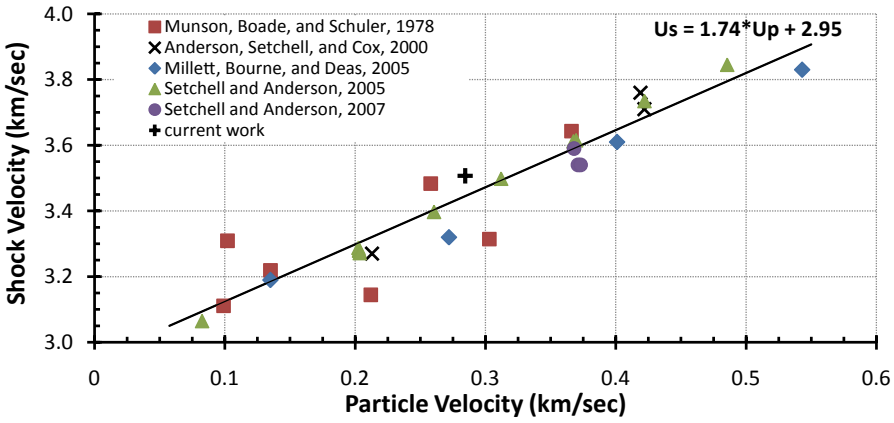

Figure 4.27: Comparison of Hugoniot results in the current work to ALOX data from the literature with 43% Al_2O_3 by volume. The equation and line represent a linear fit to all data shown.

and Anderson[123] under similar impact conditions. Although it is difficult to assign a time of first deviation, the rise times shown are on the order of ~50 nsec to reach 50% of the equilibrium value, which is significantly longer than the 14 nsec rise reported by Setchell and Anderson for ALOX made with irregular, blocky Al_2O_3 particles. This longer rise time is in keeping with the theory that the higher the aspect ratio of the particles, the more viscous effects in the matrix disperse the shock pulse. Despite the longer rise time, the Hugoniot data point fits well with prior work from literature as shown in Figure 4.27. As expected for polymers and polymer-matrix composites, the extrapolated sound speed is above the value of C_B calculated from ultrasound measurements at ambient pressure[17]. The measured Lagrangian release wave velocity is shown plotted with release wave speeds obtained from the literature in Figure 4.28. As seen in the figure, the data fits very well with previous results, indicating that particle shape does not influence sound speed at pressure, even with high-aspect ratio particles. Both of these results, including the longer rise times and the unaffected release wave velocity, corroborate Setchell and Anderson's work.

4.7 Correlation of Hugoniot Results with Analytical Predictions

A number of previously described analytical models (see Section 2.2) were used to predict the Hugoniot of the composites tested in the current work, and these predictions were compared with the experimental data. Pressure - volume ($P - V$) space was chosen to display the

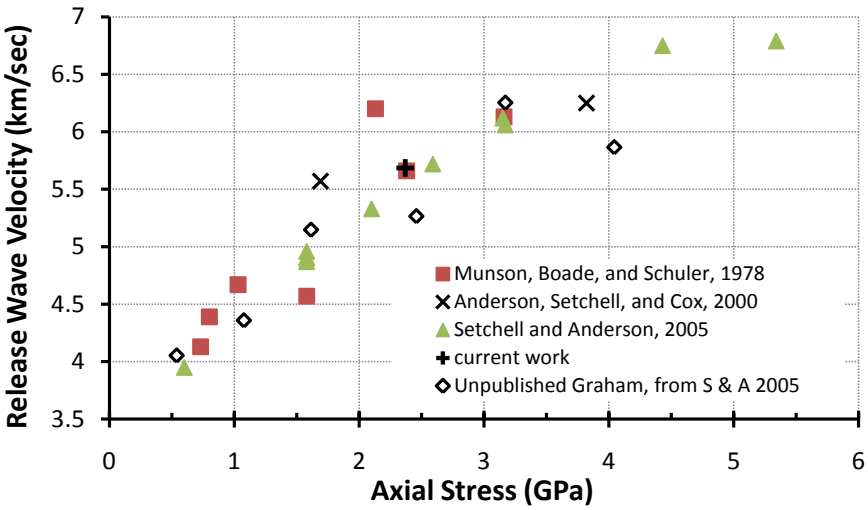

Figure 4.28: Comparison of ALOX Lagrangian release wave speeds in the current work to data from the literature.

correlation data because it provides the most intuitive representation. Most of the models were developed and validated for metallic mixtures. The ALOX experiment, along with data from the literature on ALOX, provides a validation of these models on a nonporous composite where the matrix is a soft polymer and the reinforcement is a stiff ceramic. In order to employ the models, material properties for the constituents must be known. The material properties (for both ALOX and the THV composites) used for implementing the models are given in Table 4.11.

The Hugoniot of monoclinic zirconia is available in the data of Mashimo et al.[159],

Table 4.11: Material Properties used for Model Implementation

Material	Density (kg/m^3)	C_0^a (m/s)	S^a	γ_0
Al_2O_3	3960	8140[119]	1.28[119]	1.54[72]
ZrC[74]	6730	5940	1.049	1.42[158]
ZrO_2(monoclinic)^b	5800	5069	1.08	1.65
THV[110]	2000	1600	2.04	1.22
epoxy^c	1190	2660	1.57	1.13

[a]Coefficients for linear EOS (See Equation (10))

[b]Coefficients for linear EOS obtained from the data of Mashimo et al.[159] below 75 GPa. Grüneisen coefficient obtained from applying Equation (13) to thermodynamic constants obtained from [160, 161, 162]

[c]Numerous data exists in the literature for epoxy. Values shown are averaged from literature values.[17, 47, 102, 104]. Grüneisen coefficient taken from the CTH EOS database.

which reveals a shock EOS below 75 GPa of $U_S = 1.08\,U_P + 5069$ $[m/s]$.

If McQueen's ROM method is applied to ALOX, the predicted Hugoniot is a reasonable approximation to the experimental data, as shown in Figure 4.29. A modified version of the Krueger-Vreeland method was also applied, where the component elastic pressures were created using zero K isotherms rather than Murnaghan EOS fits and all of the thermal energy generated was assigned to the epoxy matrix (a reasonable approximation since most of the deformation takes place within the epoxy). The additivity method predicts a response virtually identical to the Krueger-Vreeland method and is not shown. In both cases shown, the prediction is fair, but the predicted pressures are systematically below the experimental data. This can be explained by recalling the difference in pressure and stress, and by considering that the weaker phase (epoxy) is likely to exhibit a much higher shear strength due to the high fraction of ceramic particles restricting polymer network deformation. Since the experimental points measure stress in the longitudinal direction σ_x, if the composite exhibits an increased shear stress τ due to the inclusion of the particles, the measured stress σ_x will exceed the predicted pressure according to Equation (2): $\sigma_x = P + \frac{4}{3}\tau$. Since the data points are only ~250 MPa above the predicted line, it is reasonable to speculate that the deviation is due to this effect. This is similar to the argument made by Millett and Bourne[115] working with sugar crystals dispersed in HTPB discussed in Section 2.6.

The porous THV composite Hugoniot results described in Section 4.2.1 are much more complex than the non-porous, relatively homogeneous ALOX. However, the solid mixture methods seem to predict the Hugoniots reasonably well. Although a fully dense THV composite was not tested, the 100 μm Al_2O_3/THV composite is only 1.4% porous (Table 3.2) and so can serve as an approximation of a fully dense composite. Three mixture prediction methods were applied to the 100 μm Al_2O_3/THV composite, as shown in Figure 4.30. The data points taken from Table 4.6 for the composite are shown, along with the predicted solid Hugoniot using McQueen's model, the Dremin model, and the Baer model (see Section 2.2.1). From the figure, McQueen's model and the Dremin model predict virtually identical Hugoniots- indicating that the thermal pressure is insignificant for this material at these pressures. It is also clear that the McQueen and Dremin model more

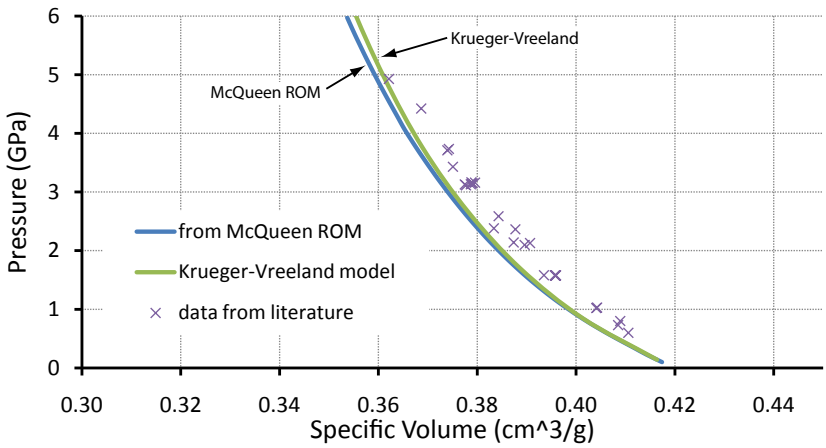

Figure 4.29: ALOX data vs. Prediction using McQueen's ROM method and the modified Krueger-Vreeland nonporous model. The data is the same data plotted in Figure 4.27. Note that the prediction is only fair, and the volumes are underpredicted.

closely predict the data than the Baer model. These trends, indicating that the McQueen and Dremin model predictions are nearly indistinguishable, and are closer to the data than the Baer model, hold for the other composites as well. Therefore, due to its more widespread use, the McQueen ROM model was used as the nonporous model in the remainder of this work, although the simpler Dremin model could be substituted with no significant change in the figures or conclusions.

The effect of porosity on the Hugoniots was also predicted for the each of the composites. Again, trends were consistent across the materials. The Hugoniot of the most porous material, the 1 μm Al_2O_3/THV composite with 15.9% porosity, was obviously expected to be most affected by the porosity. Several models predicting the effects of porosity were applied, including the additivity method, the Mie-Grüneisen (MG) method, the Wu-Jing method, the Simons and Legner model, the Baer 3-phase model, and the Kruger-Vreeland model (see Section 2.2.2 for references and background). All models were implemented using MATLAB^{TM}. The results of these models are shown in Figure 4.31, along with the experimental data for the 1 μm Al_2O_3/THV composite and the solid prediction of McQueen's ROM method (the same curve as shown in Figure 4.30). It can be seen that the Hugoniot predicted by the MG method, the Wu-Jing model, and the additivity method are

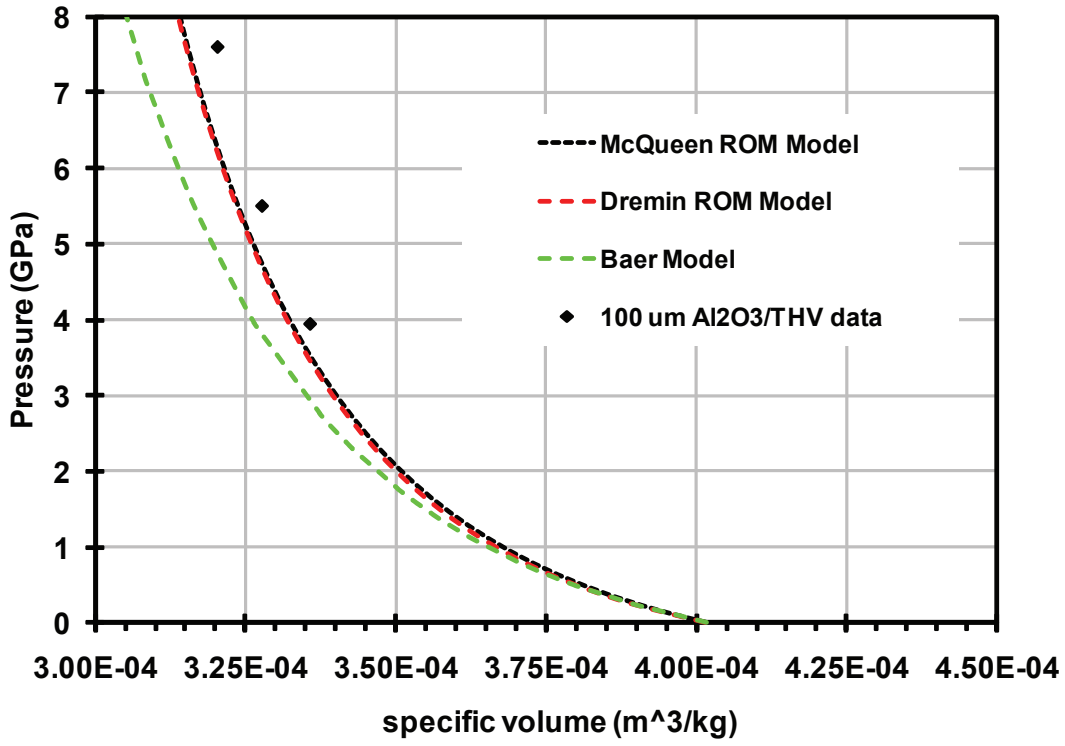

Figure 4.30: Near Dense alumina-THV vs. Solid Prediction. The predicted Hugoniots of the Al_2O_3/THV composites using the McQueen, Dremin, and Baer models, along with the data for the most fully-dense Al_2O_3/THV composite (the 100 μm).

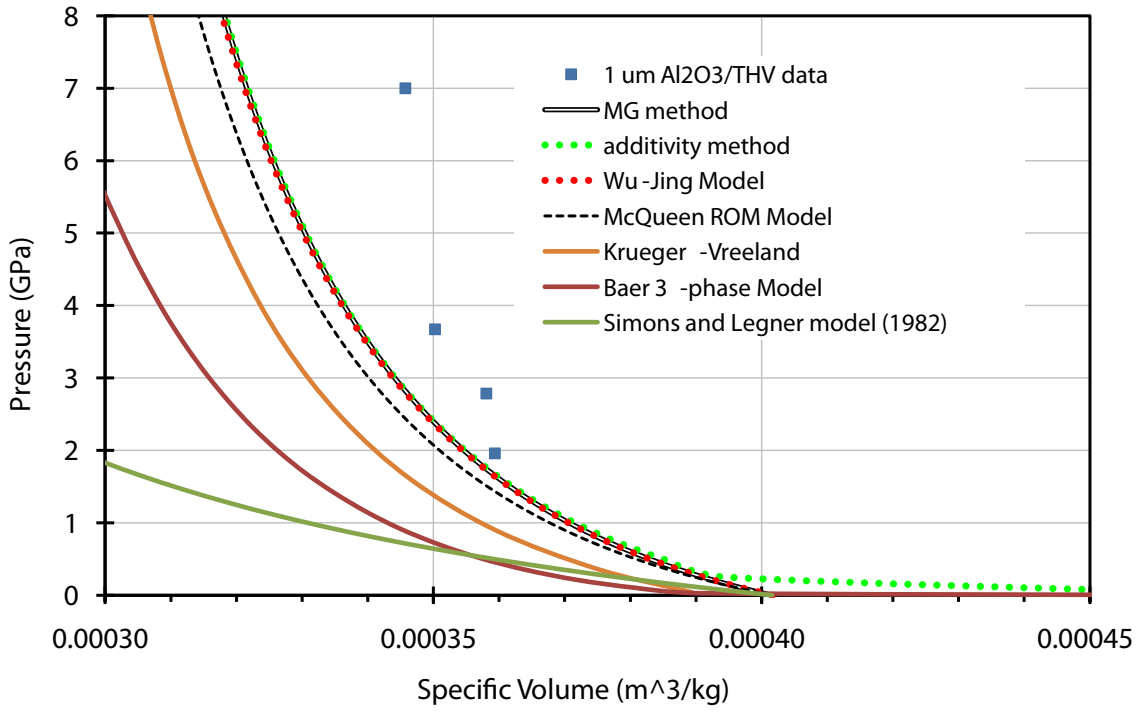

Figure 4.31: Predictions of the Hugoniot for the 1 μm Al_2O_3/THV composite. The material is 15.9% porous.

virtually identical. The Baer, Simons and Legner, and Krueger-Vreeland are quite different, and are very poor fits to the experimental data. As in the solid material models, because several of the methods yield equivalent results at relatively low pressures and porosities, the most well-known of the group, the Mie-Grüneisen method, will be used as the porous model.

The solid and porous predicted Hugoniots for each of the THV composites, along with the experimental data, are shown in Figure 4.32. As justified above, only the McQueen ROM (for the solid material predicted Hugoniot) and the Mie-Grüneisen (for the porous material predicted Hugoniot) are shown. One trend exists in all four plots, namely, that the shocked volume of the composite is underpredicted. However, generalization beyond that is more difficult. For all the alumina/THV composites, the experimental data seems to start off very close to the predicted curve, and then steadily depart, but for the ZrC/THV composite, it seems to be offset from the beginning, and remain offset by approximately

the same amount through the range of data, especially if the ceramic particles are modeled as ZrC. It was previously shown in Section 3.1.2 that a substantial amount of ZrO_2 is present along with the ZrC. The volumetric ratio of ZrC to ZrO_2 was estimated to be 1.25, corresponding to 55.6% of the powder being ZrC and 44.4% ZrO_2. Therefore, McQueen's ROM routine was employed to predict the Hugoniot of the mixture of ZrC, ZrO_2, and THV by assuming that the ZrC powder was already contaminated when it was weighed and mixed with the THV (leading to mass fractions of .3031, .2103, and .4865 respectively, with a porosity of 8.5%). This prediction is also shown in Figure 4.32(a), and is closer to the experimental data, but still is offset by about 1-2 GPa throughout the predicted range.

Again, the recent investigation of Setchell et al.[123] found particle size to have little effect on the Hugoniot of an alumina-epoxy composite. In the present work, any effect of particle size is overshadowed by the confounding effect of porosity and by different powder morphologies. Additionally, it remains unknown whether the heterogeneous composites in the present work, with all ceramic particles in contact, display the same shock response as a homogeneous composite with hard particles uniformly distributed in a soft matrix.

The consistent trend- that volume is underpredicted for porous material- can be qualitatively explained by considering that the alumina may not be fully compacting at the pressures achieved. Since the P-alpha model was developed for situations in which powders are not fully compacted, it can be applied in the present case.

4.8 Correlation of Hugoniot Results with Computational Simulations

Of the comparisons between the experimental Hugoniot results and predictions just presented, the predictions for 1 μm Al_2O_3/THV are the least accurate. Since the static compression results as well as the recovery experiment on the 1 μm Al_2O_3 powder indicates a very stiff material with remnant porosity even at high pressures, it may be possible that the poor agreement between the experimental data and the model predictions are simply due to incomplete crush-up of the powder. Furthermore, although it was previously shown that the P-α model did not predict the high pressure behavior of the 1 μm Al_2O_3/THV

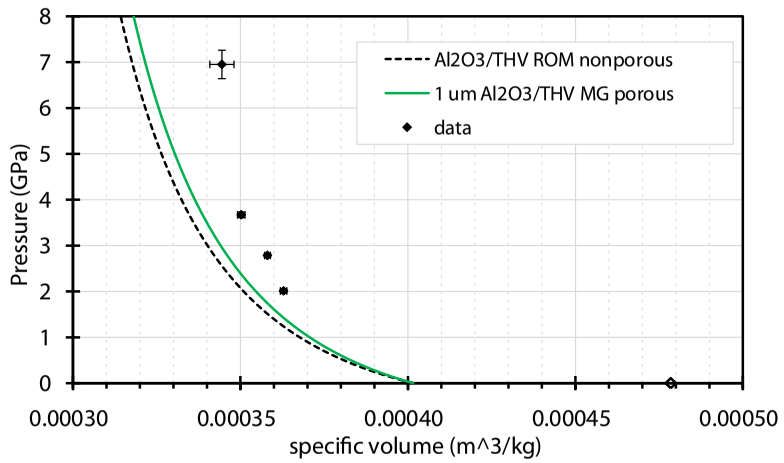

(a) 1 μm Al_2O_3/THV

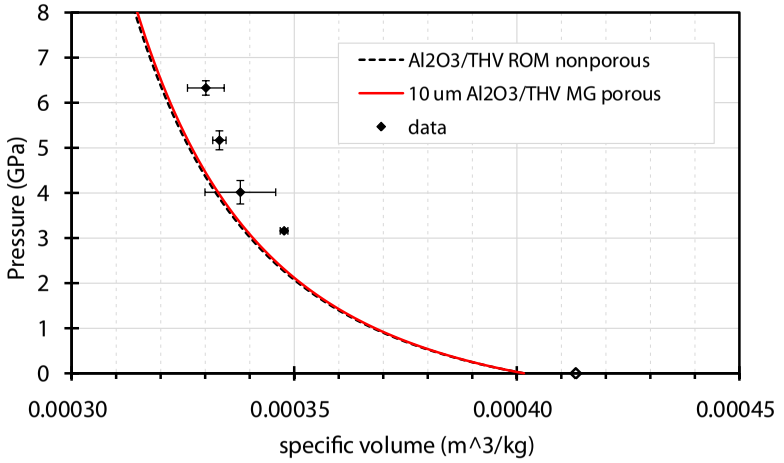

(b) 10 μm Al_2O_3/THV

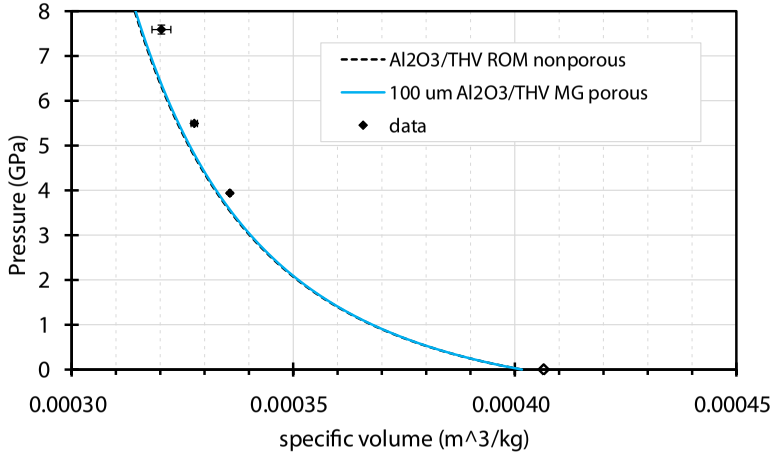

(c) 100 μm Al_2O_3/THV

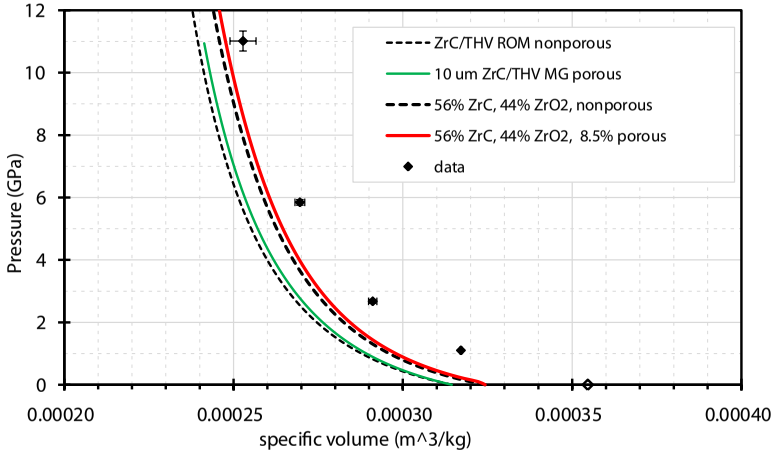

(d) 10 μm ZrC/THV

Figure 4.32: Solid and porous predictions of the Hugoniots for the THV composites. The black dashed lines are predictions based on nonporous material and McQueen's ROM method, and the solid colored lines are porous predictions using the MG EOS. The initial specific volume is shown by a hollow diamond on the abscissa. The figure for the "ZrC/THV" composite includes predictions for ZrC/THV and a mixture of ZrC and ZrO_2/THV, each with the respective porosities to match the measured density.

composite very well, it is worthwhile to investigate whether or not such a model could possibly predict the experimental data, especially since the Fischmeister-Arzt model used to determine the consolidation pressure does not fit the static data on the alumina powders very well as the density approached the solid density (Figure 4.14). Therefore, the 1 μm Al_3O_3/THV results presented in the preceding section are examined to see if an explanation based on incomplete crush-up is possible. Since the P-α model allows for an arbitrary function $\alpha(P)$ relating porosity to pressure, the P-α model was chosen to see whether or not such an explanation was possible. The P-α model was implemented, using MATLAB, to calculate the Hugoniot of the 1 μm Al_3O_3/THV when the porosity was distributed various ways between the alumina and the THV and when the crush pressure P_{Con}, as well as the form of $\alpha(P)$, was varied. To check the validity of the MATLAB simulation, the case where the porosity was completely contained within the alumina was also modeled in CTH, as described in Section 4.5. Figure 4.33(a) depicts, for the case of all porosity in the alumina, the Hugoniots of porous alumina, solid THV, and the 1 μm Al_3O_3/THV composite, together with the 1 μm Al_3O_3/THV experimental data and the results of the CTH simulations given in Section 4.5.1, converted from $U_S - U_P$ to $P - V$ space. Figure 4.33(b) depicts the same system, except that all the porosity is contained within the THV.

Although the plots in Figure 4.33 depict specific cases of P_c (or P_{Con}), n (the exponent in $\alpha(P)$), and porosity distribution, a range of values for these parameters was examined before it became clear that the P-α model could not adequately describe the data without resorting to physically unrealistic forms of $\alpha(P)$. This realization follows from the observation that in order for a $P-\alpha$ model with the form of $\alpha(P)$ given by Equation (53) to describe the data, the porous Hugoniot must continuously approach the crushed-up Hugoniot once the crush-up process begins (once the model parameter P_e is exceeded). It can be seen that this is not the case for any of the Al_2O_3/THV composites, especially the 1 μm Al_2O_3 composite. This concept can also be illustrated by examining Figure 4.34, which is very similar to Figure 4.33, except that several Hugoniots are shown for alumina and for the composite, each corresponding to a residual porosity in the alumina. The data points should begin on a higher porosity composite line and move to lower porosity composite lines, since additional

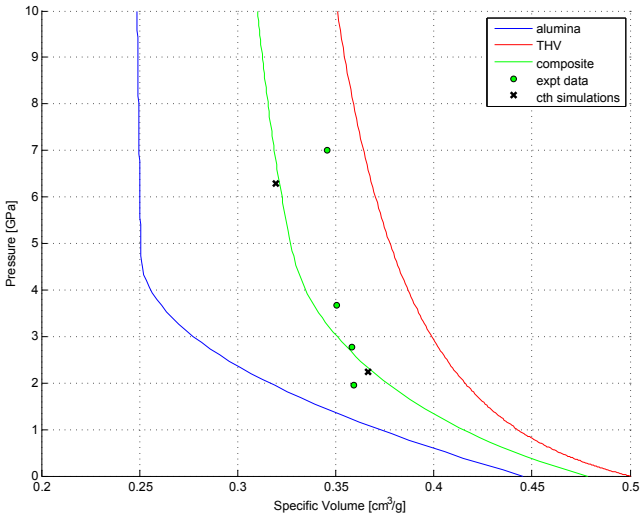

(a) All porosity assigned to alumina. Note that the CTH P-α simulation results agree quite well with the relatively simple MATLAB P-α calculations. The crush strength P_c of the alumina was taken from the Fischmeister-Arzt fit (Equation(58)) to the static compression data (Section 4.4) and was equal to $2.97 * 1.598 = 4.75\ GPa$.

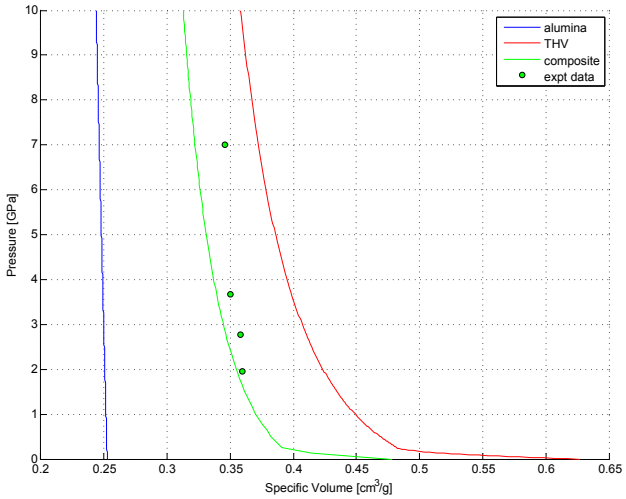

(b) All porosity assigned to THV. The crush strength P_c of the THV was assumed to be 250 MPa.

Figure 4.33: P - V calculations for 1 μm Al_3O_3/THV composite using the P-α model. In both calculations shown, the exponent n in the equation for α (Equation (53)) was 2, and $P_e = 0$. Although a range of exponents, crush strengths, and porosity distributions was examined, no reasonable value set was found that could adequately fit the experimental data (shown on both plots).

pressure must decrease the distention. However, it is clear that the data points move to progressively more porous composite lines in the figure. In the framework of the P-α model, or any other porous ROM model, this can only be explained by having a component compress and densify normally at first, but then the porosity must increase as pressure increases. Again, this is quite implausible. In highly porous materials, porosity can cause the densified volume to increase as pressure increases, but the densified volume cannot first decrease, and then increase, with pressure, as seen here. By this line of reasoning, the results of the recovery experiment, where the 1 μm alumina was found to densify to 2.65 g/cm^3 (67.1% TMD) at 7-8 GPa (Table 4.10), also cannot explain the experimental results.

The results of the recovery experiment on the 10 μm Al_2O_3 powder were not incorporated into the discussion on the 10 μm Al_2O_3/THV composite because the same trend applies: for both the 10 and 100 μm composites, the data gets progressively farther from the predicted values. Although in those cases, having a few percent remnant porosity in the alumina can shift the predicted curve to agree with a data point, the porosity must be increased.

One possible explanation for this anomalous behavior is that a chemical reaction is taking place. For the alumina/THV composite material, the higher porosity of the 1 μm composite is known to lead to hot spots that can serve as reaction initiators. In addition, the morphology of the 1 μm Al_2O_3 powder is such that the surface area is extremely high. These factors combine to provide an explanation for the behavior of the Al_2O_3 composites based on the possibility of an exothermic, shock induced reaction, which will be discussed in the next section.

In the ZrC composite, the predicted Hugoniot is offset from the experimental data and remains offset throughout the pressure range investigated. Unlike the Al_2O_3 composites, the predicted ZrC composite actually approaches the experimental data slightly as pressure increases. Although the predictions for the ZrC/THV system are somewhat suspect because of the uncertainty concerning the makeup of the composite, the results could also be explained by a shock-induced reaction initiated at low pressures.

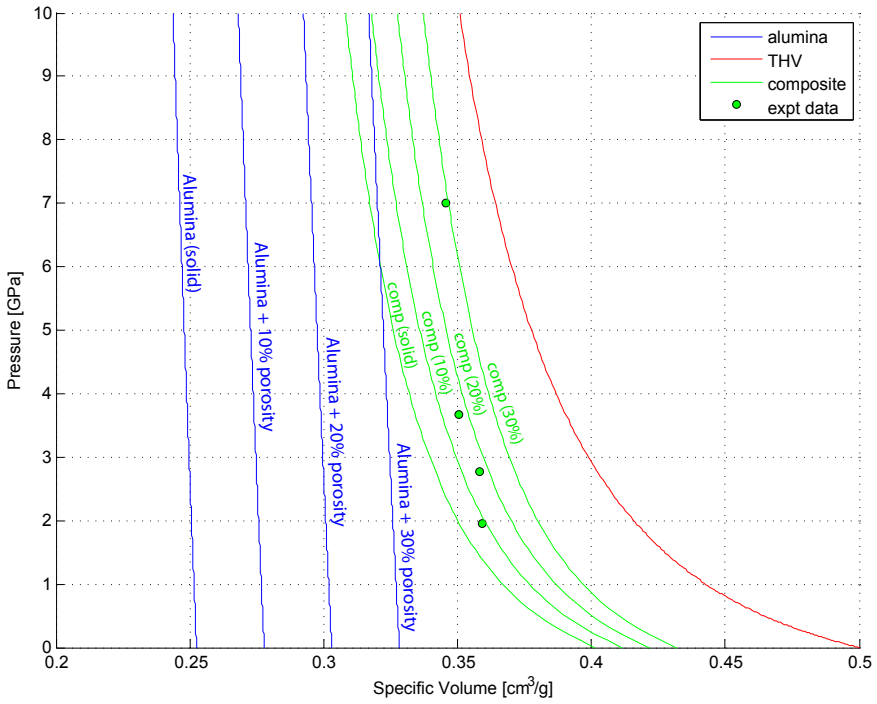

Figure 4.34: ROM plots showing the effect of increasing porosity of one component of a ROM composite model with experimental data overlaid. The Hugoniot for alumina is shown, along with curves that have been offset by 10, 20, and 30% volume to approximate the Hugoniots of porous alumina that is incompletely crushed-up. Corresponding composite curves are also shown that use the appropriate alumina curve with the solid THV curve shown. Experimental data points for the 1 μm Al_3O_3/THV are also shown. Note that at low pressure, the data lies near the 10% porous composite curve, while at high pressure, the data lies near the 30% porous composite curve. The conclusion is the same, regardless of how the porosity is distributed between components or of the form of $\alpha(P)$ (as long as α decreases with increasing P).

4.9 Possibility of Shock-Induced Reaction Influencing Shock Response

In the preceding section, a shock induced chemical reaction was cited as a possibility that could explain the deviation of the model predictions from the measured Hugoniot results, especially for the 1 μm Al_2O_3/THV and the ZrC/THV composites. In this section, this possibility will be explored further.

4.9.1 Alumina-THV Composite

Pyrolysis of fluorocarbon polymers and the wide assortment of resulting gaseous fluorocarbons is well known due to the use of PTFE in cookware and the associated public health concerns when overheated. Also, the shock-physics literature contains several references to the reactive aluminum/PTFE system, and the creation of some reactive fluorocarbon gas in the absence of air is easily inferred from the work of Mock and Holt[163] and Raftenberg et al.[164], and is explicitly discussed in the work of Lee et al.[165], who indicates that the polymer largely depolymerizes to the monomer. Turi[166] reported that 96% (by mole) of the volatile products of thermally degraded PTFE are indeed the monomer, tetrafluoroethylene (TFE), and further indicated that although a temperature of 580°C is necessary for the depolymerization to be thermodynamically favorable, a large amount of depolymerization will occur "well below" 580°C. Morris et al.[148] recovered sealed capsules of shocked PTFE and reported that 95% of the gas in the capsules was TFE, with the remained higher order perfluorocarbons. The decomposition is more complex in the presence of oxygen [167], but since the experiments in this work were performed under vacuum, it will be assumed that oxygen is not present. TFE, in turn, readily decomposes into carbon and carbon tetrafluoride and is quite reactive [168]. Insufficient data is found in the literature for the other monomer components of THV (hexafluoropropylene and vinylidene fluoride).

There are several difficulties in determining whether or not a reaction of THV and Al_2O_3 is thermodynamically favorable. One is determining full thermodynamic data for the polymer. Although standard entropy of formation is tabulated for many compounds of interest here, it is notably lacking for polymers. Another is the difficulty of deciding which products will form. Although the equilibrium compound of aluminum and fluorine

is the solid AlF_3, AlF, AlF_2, as well as gaseous AlF_3 can also form. In addition, it has been noted that $AlOF_2$ will occur when oxygen is available [169]. Further complications arising from the vinylidene-fluoride monomer and its hydrogen content are the likelihood of producing HF gas [169] and other hydrogenated compounds. Finally, thermodynamic data as basic as the enthalpy of formation are scarce for fluoropolymers, and although one source was found for PTFE [170], none were found for poly(VF) or poly(HFP). Collectively, these factors make it difficult to predict the likelihood of a reaction by the standard technique of calculating the free energy as a function of temperature. The literature is also sparse concerning the ability of fluorine compounds to reduce metal oxides. However, Lee [165] suggests that metal oxides do not react in mixtures with PTFE and Kel-F, although that work is not completely consistent (the body of the work indicates that metal oxides do not react with fluorine or fluorinated compounds, but the second sentence of the abstract indicates they can). Nevertheless, despite the inability to determine exactly which reactions are taking place, we can make some general assumptions as a starting point.

Although the precise reactants and products are not known, we know the initial materials and can assume that the products will be stable AlF_3. The following four reactions are of interest:

$$1.5F_2 + Al \rightarrow AlF_3(s) \qquad \Delta H_f^\circ = -1510\ kJ/mol\ [171] \tag{70}$$

$$C + 0.5O_2 \rightarrow CO \qquad \Delta H_f^\circ = -110.5\ kJ/mol\ [171] \tag{71}$$

$$2Al + 1.5O_2 \rightarrow Al_2O_3 \qquad \Delta H_f^\circ = -1676\ kJ/mol\ [171] \tag{72}$$

$$2C + 2F_2 \rightarrow C_2F_4(g) \qquad \Delta H_f^\circ = -659\ kJ/mol\ [172] \tag{73}$$

If these equations are summed and balanced appropriately, we get the following equation:

$$1.5(C_2F_4)(g) + Al_2O_3 \rightarrow 2AlF_3(s) + 3CO \qquad \Delta H_f^\circ = -687\ kJ/mol \tag{74}$$

The free energy of this equation, assuming ideal behavior at standard pressure, can be calculated from the standard enthalpy of formation (ΔH_f°) data and the standard entropy (ΔS°) data tabulated in the reference given for ΔH_f°. The standard Gibbs free energy of

formation (ΔG_f°) of this reaction is $\Delta G_f^\circ = -687 - 0.2246\,T$ $[kJ/mol]$. This reaction is thermodynamically favorable at all temperatures since the products have a higher entropy than the reactants. However, there are a number of assumptions built into this reaction. In Equation (73), the gas (TFE) is used rather than the polymer(PTFE). This is because no value for ΔS° could be found for the polymer PTFE. Since, as previously discussed, PTFE is known to degrade primarily into the monomer at elevated temperatures, it seemed reasonable to assume that a similar decomposition would take place at elevated pressure. From the data of Mock and Holt [163], some decomposition is evidently taking place. If the PTFE analogue to Equation (73) shown in Equation (75)

$$C + F_2 \rightarrow (CF_2)_{polymer} \qquad \Delta H_f^\circ = -419\ kJ/mol\ [170] \tag{75}$$

is used to obtain

$$3(CF_2)_{polymer} + Al_2O_3 \rightarrow 2AlF_3(s) + 3CO \qquad \Delta H_f^\circ = -419\ kJ/mol \tag{76}$$

the reaction is still favorable even if the polymer entropy is assumed to be just as high as the monomer gas entropy, which is an obviously conservative assumption. The ΔG_f° of this reaction (assuming $S_{PTFE}^\circ = S_{TFE}^\circ$) is $\Delta G_f^\circ = -419 - 0.2246\,T$ $[kJ/mol]$. Either way, the reaction is favorable at atmospheric pressure, as long as we assume that the stable solid phase of AlF_3 is formed. The addition of some free oxygen in the reactants allows the formation of CO_2, but since the experiments in this work were performed in a vacuum of $\sim$1/10,000 atm (100 mtorr), and the fraction of oxygen is about 0.21, the partial pressure of O_2 can be assumed to be negligible. By far the largest source of uncertainty about this reaction is the effect of pressure. A quick inspection of Equation (74) reveals that increasing pressure is likely to favor the reverse reaction. However, thermodynamic data is not available for the fluorinated compounds at anything approaching the pressures of interest. Since the thermodynamic data necessary to understand the effect of pressure on chemical potential is only available up to a few tens of atmospheres [172, 173], no defensible extrapolation can be made. The best we can do is say that a reaction such as that of Equation (74) or (76) cannot be ruled out.

However, recovered specimens can be examined to look for evidence of reaction. In the three-capsule recovery experiment described previously, one of the capsule contained the 1 μm Al_2O_3/THV composite. In that experiment, the composite sample was "shocked" to $\sim$4 GPa, although that pressure was not reached as a single shock, but instead by several recompression waves as the low-impedance composite rings up within the steel capsule over several microseconds from an initial shock of $\sim$1.4 GPa (see Figure 4.16(b)). As previously discussed, the mass loss was negligible and the appearance of the recovered specimen was very similar to that of the unshocked material (Figure 4.18). In addition, XRD analysis performed on the recovered specimen is shown in Figure 4.35, and appears to be identical to the as-received XRD trace except for small peaks at $2\Theta = 24.84°$ and 29.33°. These peak positions do not correspond to aluminum fluoride or aluminum oxide-fluoride, and most likely represent contamination introduced during the removal of the sample from the steel capsule. The results indicate that a shock-induced reaction did not occur in the recovered material. However, since the loading in the recovery experiment was "stepped", rather than a shock, to 4 GPa, relatively little shock-induced heat was generated in the material and so the temperature would have been lower than the 370°C expected in a shock to 4 GPa from ambient conditions.

Since pressure at slightly elevated temperature did not induce a reaction, the effect of high temperature was investigated. A sample of the 1 μm Al_2O_3/THV composite was placed in a tube furnace and heated at 3°C/min in a flowing argon atmosphere to 600°C and held there for 2.5 hours. At the end of the run, the composite was collected and analyzed via XRD. The temperature selected was above the decomposition temperature of the THV matrix, and so the composite was charred. The charred pieces were powdered in a mortal and pestle and the remains were examined using XRD to look for evidence of a reaction. The resulting trace is shown in Figure 4.35. It can be seen from the figure that the specimen recovered from the furnace remains unreacted Al_2O_3. The mass of the sample after the furnace run was 40.3% of the original mass. In addition to the furnace run, Differential Scanning Calorimetry (DSC) and Thermo-Gravimetric Analysis (TGA) were performed on the 1 μm Al_2O_3/THV composite. The TGA was performed on a Netzsch STA 449c

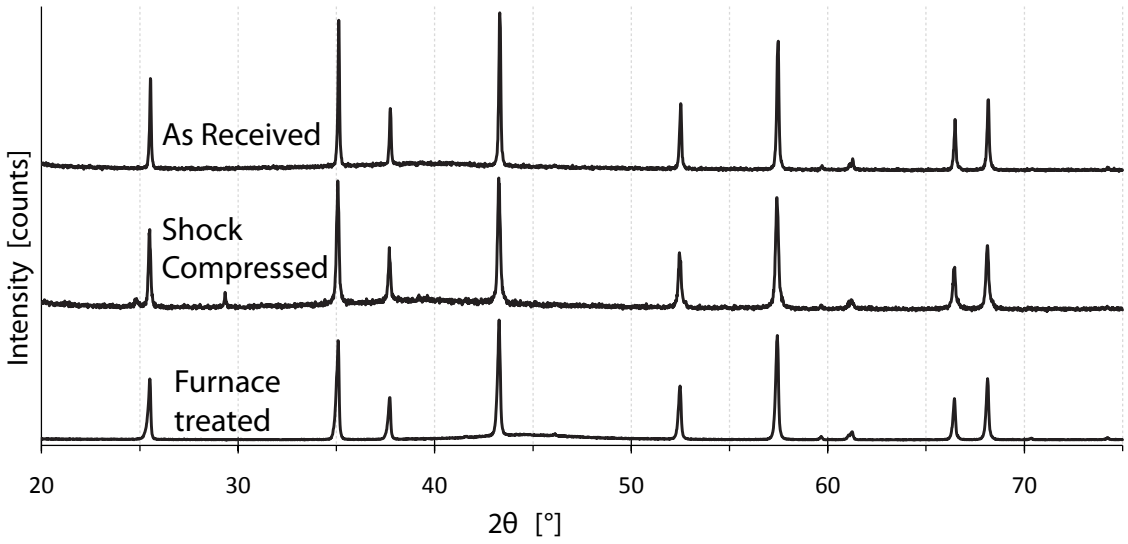

Figure 4.35: XRD of 1 μm Al_2O_3 composites from recovery experiment and furnace run. The "As Received" material is the original material received from ATK, and is the same trace shown previously in Figure 3.7. The "Recovered" material is the material recovered from capsule III of the recovery experiment. "Furnace" material is the composite sample recovered from the furnace, where it was subjected to a temperature ramp to 600°C and held isothermally for 2.5 hours in flowing argon. Acquired using Cu Kα_1 radiation.

at 5°C/min to a maximum temperature of 600°C and the DSC was performed on a TA Instruments DSC100 at 20°C/min to a maximum temperature of 550°C. Both tests were performed in a nitrogen atmosphere at ambient pressure. Figure 4.36 shows a representative DSC and TGA trace for the 1 μm Al_2O_3/THV composite as well as corresponding traces for pure THV for comparison. The DSC trace becomes erratic at ∼455°C due to the onset of degradation of the THV. However, no exotherm inicating a reaction is observed. The TGA trace shows degradation beginning at 400°C and mass steadily decreasing until degradation is complete at about 510°C.

The residual masses from the furnace experiment and the TGA experiment agree exactly; both show 40.3% of the initial mass remaining. This provides additional evidence that no reaction is taking place, since each gram of Al_2O_3 that reacts forms 1.65 grams of AlF_3. Since the mass fraction of Al_2O_3 in the composite is 39.8%, and the residual ash from THV is 1.25% of the initial mass of THV, the residual mass of 40.3% is easily attributed to the alumina and residual ash. Any reaction should cause an increase in recovered mass.

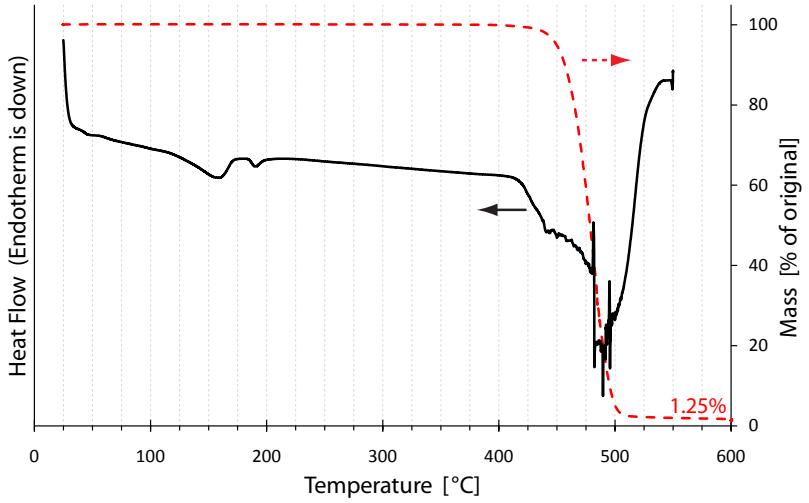

(a) Pure THV

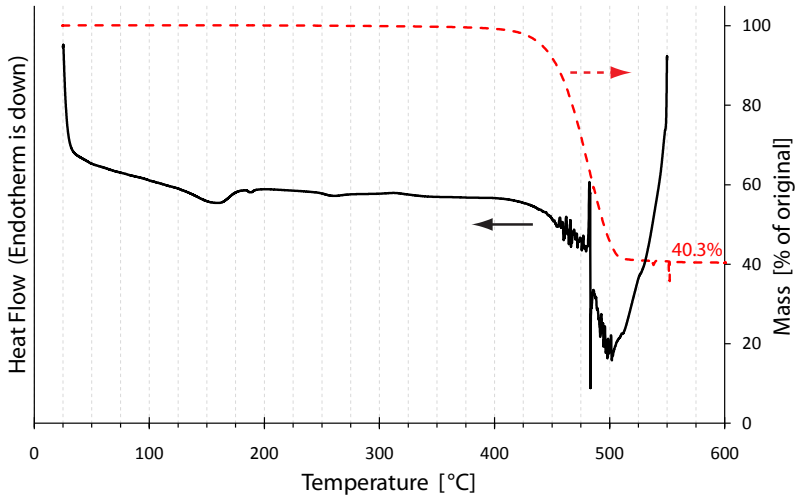

(b) 1μm Al_2O_3/THV composite

Figure 4.36: DSC and TGA results on THV and 1μm Al_2O_3/THV composite. The composite results are very similar to the pure THV results, suggesting no reaction is occurring. The decomposition of the polymer and the resulting mass decrease causes the noise in the DSC signal. Once the mass begins to decrease, the ordinate axis of the DSC trace is no longer to scale. However, it can be seen that no exotherm is present. In both cases, the DSC trace returns to the zero (starting) point as the run ends. This is an experimental artifact, not an exotherm in the material.

4.9.2 ZrC-THV Composite

For the ZrC/THV composite, there is some literature on reactions of ZrC or ZrO_2 with fluorine gas which show that both ZrC [174] and ZrO_2[175] react to form ZrF_4 at moderately elevated temperatures of a few hundred degrees C. However, there is no literature on the reaction of ZrC or ZrO_2 with TFE. It can be shown that the reaction of TFE with ZrO_2 and the reaction of TFE with ZrC to form ZrF_4 are both thermodynamically favorable, leaving open the possibility of the reaction represented by Equation (77) or (78), which can be built from reactions (79)-(80) and (73) or (75).

$$C_2F_4 + ZrC \rightarrow ZrF_4 + 3C \qquad \Delta H_f^\circ = -1045\ kJ/mol \tag{77}$$

$$2(CF_2)_{polymer} + ZrC \rightarrow ZrF_4 + 3C \qquad \Delta H_f^\circ = -867\ kJ/mol \tag{78}$$

$$Zr + 2F_2 \rightarrow ZrF_4 \qquad \Delta H_f^\circ = -1911\ kJ/mol\ [171] \tag{79}$$

$$Zr + C \rightarrow ZrC \qquad \Delta H_f^\circ = -207\ kJ/mol\ [171] \tag{80}$$

In order to search for this (or another) reaction, DSC and TGA were also performed on the ZrC/THV composite. The parameters and tools used for both tests were identical to those described previously for the alumina/THV composite, and the results are shown in Figure 4.37. It is immediately noticeable from the ZrC/THV composite DSC trace that there are two exotherms centered at 501 and 539°C. However, as Shimada[129] has shown that ZrC exhibits an exotherm at ∼550°C even in the presence of low amounts of oxygen, 99.5% pure ZrC powder was obtained from Alfa Aesar and was also run in the DSC as a control to ensure that the reaction was indeed occurring between ZrC and THV, rather than ZrC and residual oxygen. The DSC trace for ZrC is also shown in Figure 4.37. A comparison of the DSC traces for the ZrC powder and the ZrC/THV composite reveals that the exotherms visible in the ZrC/THV composite are due to the reaction of THV and ZrC.

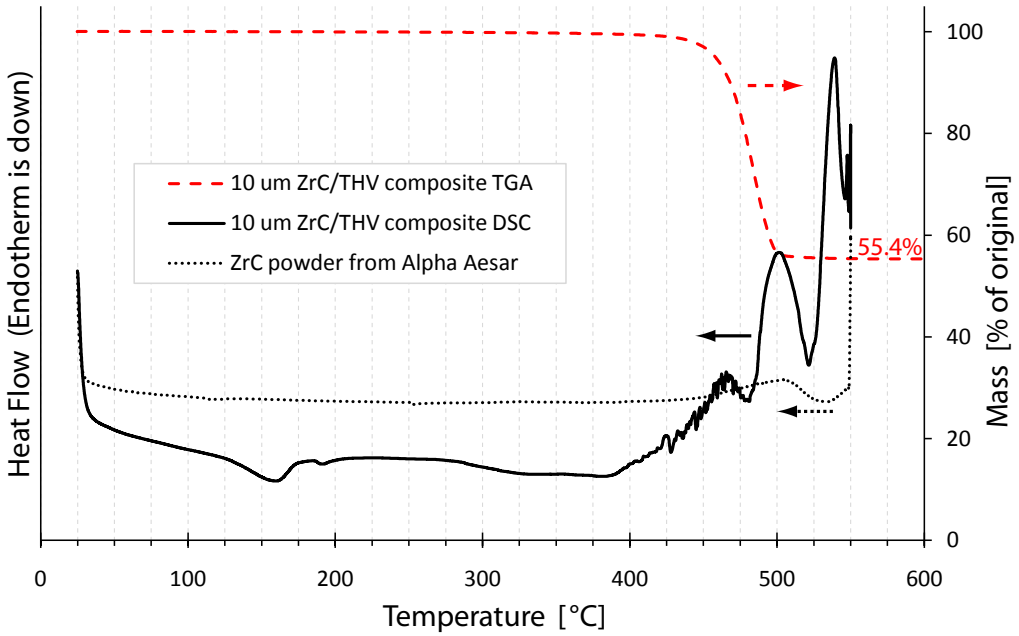

Figure 4.37: DSC and TGA results on THV and 10μm ZrC/THV composite. Note the difference between the DSC traces for the ZrC powder and the ZrC/THV composite.

The TGA results shown in the figure indicate that the residual mass of the ZrC/THV composite was 55.4%. If the composite was 25% ZrC and the remainder THV, the ZrC would be 52.8% by mass. If the poweder was actually not pure ZrC when it was mixed, but instead was some mixture of ZrC, ZrO_2 and C, the mass fraction would still be 52.8%, since the mixing was presumably done by using the literature values for the density of ZrC and THV and weighing an appropriate amount of the respective powder. The residual ash from the decomposed THV can only account for an additional 0.6% residual mass. Therefore, the higher residual mass indicates a reaction of some kind with the THV is occuring, in agreement with the DSC results discussed previously.

The ZrC/THV composite was also heated in the tube furnace so that a sufficient sample could be obtained for XRD analysis. The recovered sample retained 58.0±0.2% of the original mass. The retained mass after the furnace run is significantly higher than the retained mass in the TGA experiment (55.4%). The reason for this is unknown, but could be partly due to the heterogeneity of the sample and the small sample size used in the TGA (49.506 mg), i.e., the TGA sample may have contained a larger fraction of polymer

than the overall composite. The difference could also be due to a modified reaction or some secondary reaction product removing more mass in the TGA, since the TGA run was done in flowing nitrogen while the furnace run was done in flowing argon (although this seems unlikely). However, in both cases the retained mass is significantly above 52.8%, indicating that a reaction is occuring. XRD was performed on the sample heated in the furnace, and is shown in Figure 4.38. The ZrC peaks and the unassigned peaks are no longer present, and have been replaced by peaks mostly corresponding to a non-stoichiometric zirconium-fluoride-oxide compound with orthorhombic structure reported by Papiernik et al.[176]. Unfortunately, no other information about the compound is available in the literature. Four new unassigned impurity peaks are also present, but are relatively small.

Although the data presented in this section indicates the possibility of a reaction in a shocked sample, especially in the ZrC/THV composite, it by no means guarantees it. As mentioned previously, the effect of pressure on the reaction thermodynamics is unknown and cannot be easily investigated. Also, even if we assume that the reaction will occur due to the passage of a shock wave, it is unclear whether the reaction would be "shock induced" and proceed quickly enough to occur within the shock pulse, and so manifest itself in the measured shock parameters, or would only be "shock assisted" and begin to react after unloading from the high pressure state, leaving no indication of reaction on shock parameters (see Section 2.2.3).

4.9.3 Incorporating the Reactions into the Models

Previously in this chapter, several different models were applied in an attempt to explain the observed Hugoniot results of the various THV composites, and it was shown that the predictions do not agree with the observed response. Several simulations and experiments investigating the crush-up response of the particles and investigations of the possibility of reaction were also presented in an attempt to understand the Hugoniot results. This section will further discuss those topics and will build a framework for explaining the observed composite Hugoniot results.

For the 10 and 100 μm Al_2O_3/THV composites, the observed Hugoniots are relatively

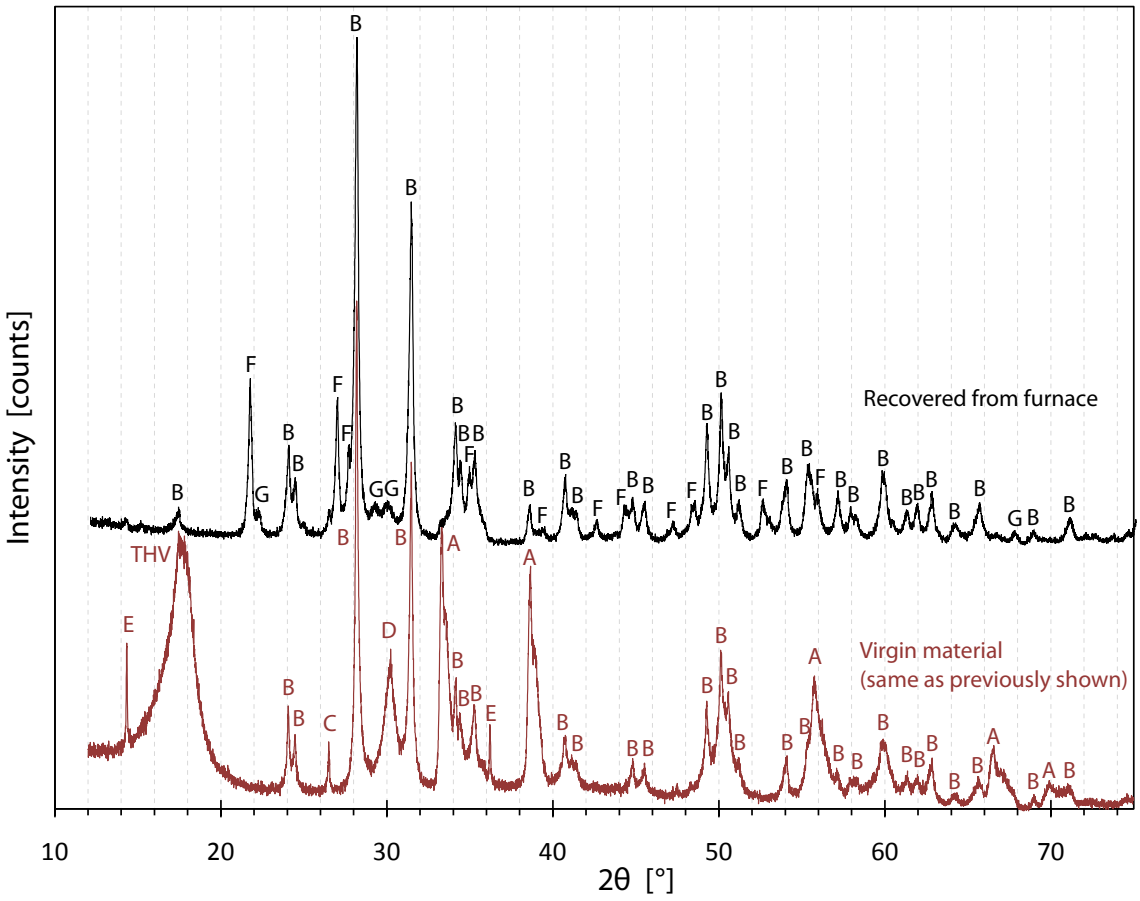

Figure 4.38: XRD of 10 μm ZrC composite recovered from furnace run to 600°C. The lower trace labeled "Virgin material" is the same trace previously shown and discussed in Figure 3.8, and the upper trace is the material recovered from the tube furnace. Comparing the two traces reveals several conclusions. The peaks corresponding to the ZrO_2, labeled "B", remained virtually unaltered. As expected, the THV peak is absent. Also absent are all of the peaks corresponding to ZrC (labeled "A" in the lower trace). In addition, all four of the original impurity peaks ("C","D", and both "E"s) from the virgin material are absent. Numerous new peaks are present, most of which can be explained by a non-stoichiometric zirconium-oxide-fluoride compound labeled "F". Four new unassigned peaks labeled "G" are present.

close to the predicted behavior. The slight differences in how well the results match the predictions are not due to an effect of particle size on strength, as shown by the Taylor test results of Section 4.2. Instead, they are due to differences in porosity. This leads to the conclusion that, at least in this system, the particle size does not affect the high-strain rate strength or the Hugoniot. However, for the 1 μm Al_2O_3/THV composite, the results did not match predictions. Although it was shown that the powder does not fully densify, even at the upper limit of pressure investigated in this work (∼8 GPa), it was also shown that the results cannot be explained by this remnant porosity. Although a reaction is thermodynamically possible and might explain the shock compression results, from the recovery experiment as well as from thermal testing it does not appear that a reaction is taking place.

It is interesting to note that Dai et al.[29] found somewhat similar results with nano-iron powder compaction (∼25 nm diameter) where the powders initially densified, but then began to distend as shock pressure increased further, as shown in Figure 4.39. They speculated that the phenomenon was due to either the internal energy imparted to the material by the high initial surface area as the surface area was decreased during compaction, or due to a nano-particle size effect on the Grüneisen parameter. While the phenomenon observed in the current work does not completely match that depicted in Figure 4.39, it's possible that it is a less pronounced manifestation of the same effect, since the particles comprising the alumina in the 1 μm Al_2O_3/THV composite in this study are nanoscale (∼250 nm), albeit an order of magnitude larger in diameter than the iron particles in the Dai et al.[29] study. The smaller effect could also be due to dilution- in the Dai et al. study, the sample was 100% nanoiron powder, whereas in the current study, the sample is initially only 25% nanopowder by volume.

For the ZrC/THV composites, which actually contained ZrC, ZrO_2, some other contaminants, and THV, a major challenge is to determine the initial composite composition. Because the THV proved difficult to dissolve and could not be separated by mechanical means or by burning it away without reacting the ZrC, estimates were employed to determine the initial composition based on XRD traces. The predictions are therefore expected

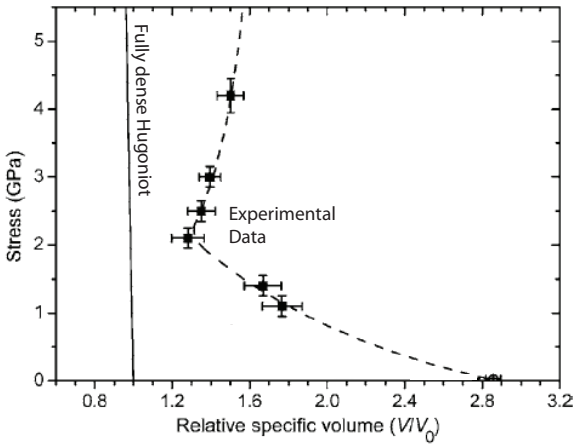

Figure 4.39: Densification follow by distention data for 35% TMD iron powder. Note that the material initially densifies, but then appears to distend above 2 GPa. From Dai et al.[29]

to be less than perfect. In addition, clear evidence of an exothermic reaction was observed by heating the ZrC/THV composite above 500°C in which the ZrC transformed to a nonstoichiometric zirconium-oxide-fluoride (ZOF), but the ZrO_2 remained unaltered. Unfortunately, no Hugoniot data is available for ZOF, but it will likely behave similarly to ZrO_2 (a mixture of ZrO_2 and ZrF_4 would likely be even better, but no Hugoniot data is available for zirconium fluoride either). Therefore, we can assume that the ZrC is converted into ZrO_2 and compare the predicted Hugoniot with the experimental results. The mixture is treated as a reactive system, and since no ZrC was detected in the XRD data for the heated sample, it was assumed that all ZrC reacts with THV according to Equation (78). Since the heat of formation of this reaction is 867 kJ/mol of ZrC reacted, and the composite is 30.3% ZrC by mass, the available energy due to reaction is 2545 kJ per kg of composite (the ZrC is the limiting reagent). If we assume that all ZrC reacts, that the mass of TFE required is removed from the THV and otherwise leaves the THV unaltered, and that the carbon in the products acts as graphite (Hugoniot data from Marsh[47]), we can construct a "product" Hugoniot composed of 19.2% THV, 10.5% C(graphite), and 70.3% ZrO_2 (by mass). This product Hugoniot is shown in Figure 4.40, along with the starting material Hugoniot. The figure also shows the results of applying the Ballotechnic model (see Section 2.2.3) to these products with a reaction energy of 2.545 MJ/kg. The figure is otherwise

similar to that shown previously in Figure 4.32(d), except that the ZrC/THV predictions have been removed, and the P-α model (with P_{Con} estimated to best fit the data) has been applied to the reactant Hugoniot. From Figure 4.40, it would be possible to explain the data as follows: The first two data points are offset from the reactant Hugoniot simply due to the crush-up behavior of the ZrC/ZrO_2 particles in the as-yet unreacted composite. The third and fourth data points (near 6 and 11 GPa) begin to diverge from the predicted curve due to some reaction of the ZrC and fluoropolymer. It would be possible to estimate a percent reaction at each pressure from the relative distance (at constant pressure) between the reactants curve and the curve predicted by the Ballotechnic model. However, such an analysis is unwarranted due to the number of rough estimations built into the analysis. These estimates include the composition of the original system, the Hugoniot behavior of ZOF, the assumed reaction, the Hugoniot behavior of the carbon, and the crush-up behavior of the particles in the composite. Additionally, the reaction scenario presented here should be reflected in the U_S-U_P Hugoniot as either a sharp break (for a clear reaction threshold) or as a nonlinearity in the region of partial reaction. From the data in Figure 4.9, neither of these signatures is present.

4.10 Influence of the Grüneisen Coefficient on Model Prediction

An alternative explanation of the Hugoniot behavior of all the THV composites investigated in this work lies in the possibility of a higher Grüneisen coefficient γ for THV. There is some evidence that the values for γ calculated for polymers using Equation (12b) are too low by an order of magnitude. The argument seems to have originated with Wada[177] and is based on the idea that γ is influenced primarily by anharmonic (assymetical) potentials between atoms in the structure, rather than harmonic (symmetrical) potentials. In metals and ceramics, the interactions between atoms are dominated in every direction by primary bonds, which tend to be strong and harmonic. Since each direction is composed of primary bonds, which are relatively harmonic, γ is only due to these harmonic bonds, and tends to be low ($\sim$1-2). However, in polymers, atomic interactions are due to primary bonds only along the covalently-bonded backbone chain, and secondary (or Van der Waals) bonds in directions

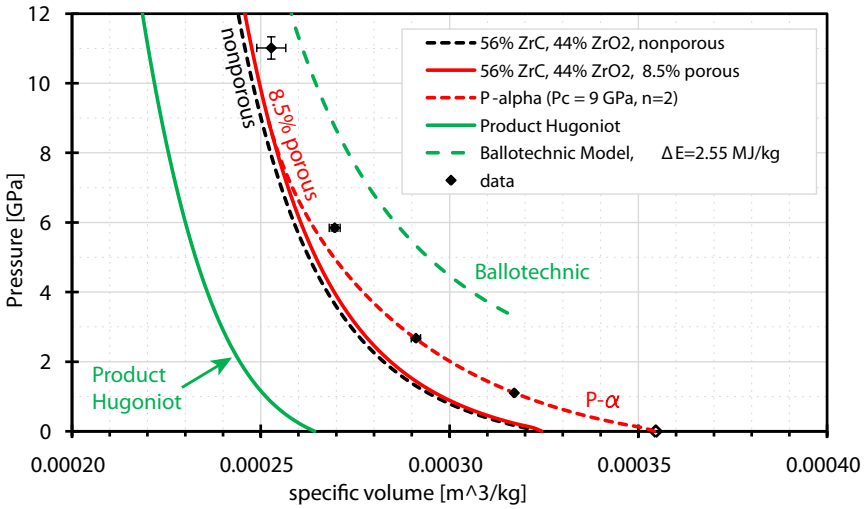

Figure 4.40: Prediction of ZrC composite Hugoniot if treated as a reactive system with all ZrC reacting according to equation (78). This figure is similar to Figure 4.32(d), except that the ZrC/THV predictions have been removed, and product Hugoniot is added, along with the predictions of the Ballotechnic reactive-mixture model. Again, the initial specific volume is shown by a hollow diamond on the abscissa.

perpendicular to the chain. Therefore, the *intra*chain forces are much stronger and more harmonic, whereas the *inter*chain forces are weaker and anharmonic. Since γ is due to anharmonic potentials, it follows that secondary, interchain interactions will dominate γ.

Recall that the commonly used method of calculating γ given by Equation (12b) (repeated here) is based on the observed isochoric specific heat C_V and is derived from the Grüneisen Equation (Equation (13)).

$$\gamma = V\frac{3\alpha\beta_T}{C_V} \tag{81}$$

The observed C_V will take into account contributions from the intrachain vibrations in addition to the intrachain vibrations that dominate anharmonic responses such as the Grüneisen coefficient. Therefore, the analogous expression of γ for polymers should be written as:

$$\gamma \approx V\frac{3\alpha\beta_T}{C_{V,inter}} \tag{82}$$

where $C_{V,inter}$ corresponds to the portion of the specific heat due to interchain vibrations.

Since $C_{V,inter}$ is necessarily smaller than the C_V observed through standard (calorimetric) experiments, γ measured using Equation (82) will be larger than γ measured using standard techniques and Equation (13). Barker[178] further develops this idea, explaining that the Grüneisen Equation, and hence the common formulation of γ, assumes that all oscillators are identical, which is a reasonable assumption for metals and ceramics, but a poor one for polymers. He goes on to show that predictions of γ based on interatomic potentials are consistent with Wada's[177] ideas and results. Warfield[179] developed a method for determining γ based on the pressure dependence of the bulk modulus, measured γ for a number of polymers, and found excellent agreement with the data Wada[177] obtained using the pressure dependence of the sound speed. He introduced a notation, calling γ_T the thermodynamic γ measured using conventional calorimetric methods, and γ_L the lattice γ due to only the anharmonicity of the atomic system, and found that $\gamma_L/\gamma_T \approx 5$ -20. Notably, γ_L values are reported for PTFE and PVDF of 8 and 6.4, respectively, although the predominant phase or percent crystallinity is not specified. According to Warfield[179], the data did not seem to obey rules corresponding to easily identifiable characteristics such as % crystallinity, and so it is very much an estimation to assign a γ_L for THV from the data for the two monomer components.

It is unclear whether these higher values of γ are applicable at the pressures investigated in this work. Undoubtedly, γ will decrease with pressure, but the question is whether it will initially decrease at a faster rate than predicted by $\gamma/V = \gamma_0/V_0$ as the interchain distance strains more than the intrachain distance (making the interchain bonds approach the harmonicity of the intrachain bonds). From the dilatometry data of Dattelbaum et al.[111] on THV 500 from ambient pressure to 200 MPa, Warfield's method can be applied to find γ. The calculated values are found to range from 20 at ambient pressure to 5.5 at 200 MPa, whereas if γ_0 is taken as 20 and $\gamma = (\gamma_0/V_0)V$ is applied, γ only changes from 20 at ambient pressure to 18.9 at 200 MPa, indicating that the bond behavior does indeed become more harmonic as shock pressures are approached. However, it remains unknown whether $\gamma_L \rightarrow \gamma_T$ as P is increased, and if so, how it approaches. Even such a fundamental assumption as γ monotonically decreasing with pressure (a widely held belief) has been

challenged by Morris et al.[148] working with PTFE, who found that γ_T was too low (by a factor of $\sim$3) even at pressures of several tens of GPa. They did not, however, challenge the validity of γ_T as the proper initial value of γ, and so concluded that γ must increase. They explained the increase as a consequence of optic phonon modes becoming increasingly activated at higher temperatures. Unfortunately, it is unclear whether they were unaware of the aforementioned arguments of Wada[177] and so did not consider them, or found some fault with them and so did not employ them.

Despite these uncertainties, it is worth investigating the effect of a larger Grüneisen coefficient on the predicted results for the data presented in this work. If $\gamma(V)$ were known to a higher pressure, it would be straightforward to implement the experimentally-obtained form of $\gamma(V)$ into Equation (33). If we take a simpler approach and assume $\gamma_{0,THV} = 6$ (reasonable from both the analysis of Dattelbaum et al.'s data[111] and the data reported by Warfield[179]), we can recreate the predictions for the Al_2O_3/THV composites shown previously in Figure 4.32, which was created with γ_0=1.3 for all composites. The nonporous curves do not change, but the porous curves, calculated using Equation (33), are functions of γ and shift accordingly. The higher γ_0 values were calculated from the mass-weighted component γ_0 values, and were found to be 4.2 for the Al_2O_3/THV composites and 3.7 for the ZrC/ZrO_2/THV composite. The new predictions incorporating the revised values of γ_0 are shown in Figure 4.41. The prediction for the ZrC composite also includes a P-α prediction using the same parameters as used in Figure 4.40.

Comparing Figure 4.41 with Figure 4.32, it is apparent that raising the Grüneisen coefficient has a substantial impact on the predicted behavior for the more porous composites. For the least porous materials (the 10 and 100 μm Al_2O_3/THV composites), the effect is minimal because the porosity is so low. Nevertheless, the new predictions (γ_0=3.7) are closer to the data points than the previous predictions (γ_0=1.3), and it remains plausible that the slight underprediction is due to the particles decreasing the mobility of the polymer or interlocking with one another and therefore increasing the effective shear strength enough to slightly stiffen the Hugoniot. For the 1 μm Al_2O_3/THV composites, the higher γ makes a very substantial difference in the predicted porous Hugoniot. Whereas the original, low

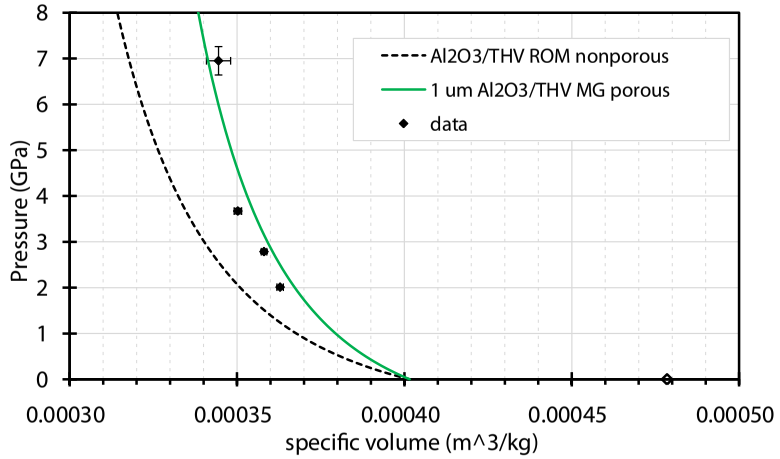

(a) 1 μm Al_2O_3/THV

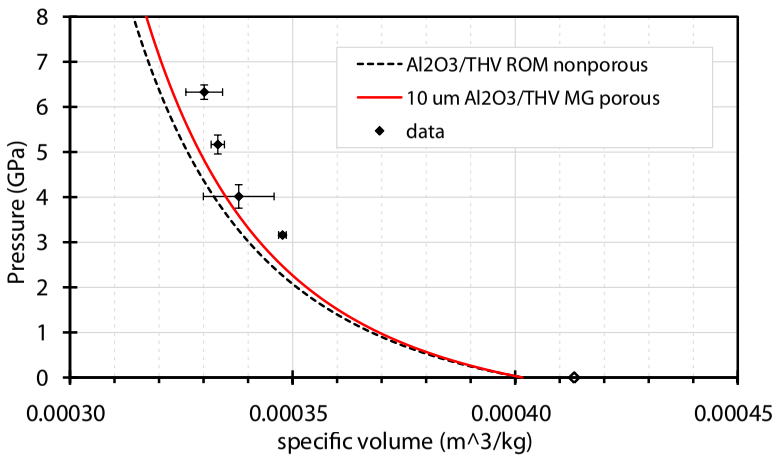

(b) 10 μm Al_2O_3/THV

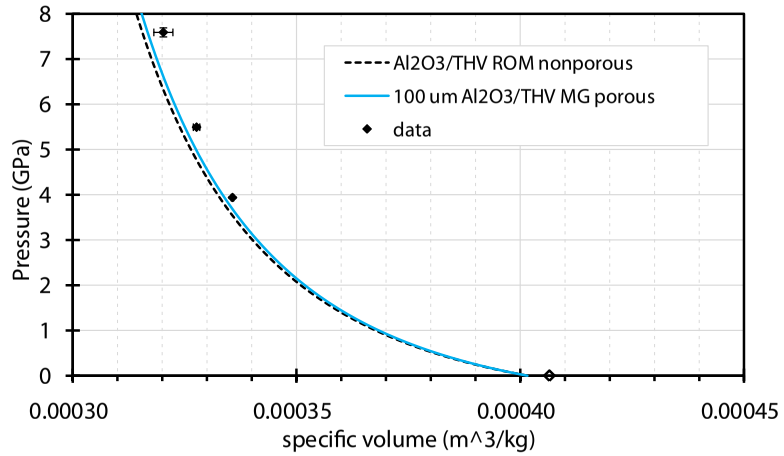

(c) 100 μm Al_2O_3/THV

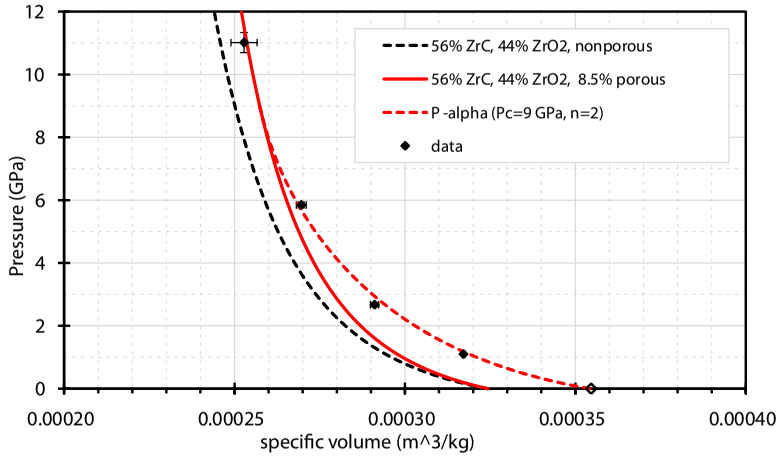

(d) 10 μm ZrC/THV

Figure 4.41: All THV Composites vs. Predictions from Porous Models with Higher Grüneisen Coefficients. The black dashed lines are nonporous predictions based on McQueen's ROM method (identical to those shown in Figure 4.32, and solid colored lines are porous predictions using the MG EOS with higher γ values. The figure for the ZrC/ZrO_2/THV composite includes the crush-up behavior predicted by the P-α model.

γ predictions significantly underestimated the response, the new predictions approximate it much better. The original predictions differed sufficiently from the data that the only plausible explanation for the discrepancy was based on an unexplained stiffening behavior observed previously in nanopowders. However, the new predictions approximate the experimental data well enough that it is tempting to explain the discrepancy as due simply to the high heterogeneity of the samples. For the ZrC/ZrO_2/THV composite, the difference between the old and new predictions are similarly striking, especially when crush-up behavior is estimated. In fact, like the case for the 1 μm Al_2O_3/THV composite, it appears that the higher γ makes another explanation available to explain the experimental data. Rather than an explanation based on a reaction and the associated expansion, the possibility of a higher γ makes an explanation based only on established powder compaction models plausible.

4.11 Summary of Shock Compression of THV-Ceramic Powder Composites

The shock compression response of THV and several composites composed of THV and ceramic particles has been investigated in this work, along with the strength at strain rates of $\sim 10^4$. The measured Hugoniot did not correlate well with the predictions of mixture-prediction models from the literature. Much work was done to investigate the reason for the poor correlation. The investigation involved experiments and numerical modeling to validate compaction model assumptions, as well as theoretical considerations such as whether an explanation based on partial crush-up or shock-induced reaction was possible. Arguments proposing that the Grüneisen coefficient for polymers should be higher than the thermodynamic average value given by Equation (13) were presented. Several explanations were put forth, as discussed in this chapter, each of which can potentially explain some portion of the observed response.

Any attempt to generalize the results, even across only the four composites investigated here, is difficult and leads to as many questions as answers. For example, it is tempting to say that the present work presents evidence of a higher Grüneisen coefficient for polymers than the thermodynamic/calorimetric value typically quoted in the literature, and it might seem that the data from all four composites support this conclusion. However, if we accept

that explanation, then we would not expect the 10 and 100 μm Al_2O_3/THV composites predictions to remain slightly below the experimental data, while the prediction for the 1 μm Al_2O_3/THV composite is not. This is especially puzzling considering the explanations considered for the slight underprediction; namely, that the particles are increasing the effective shear stress either by reducing chain mobility (a particle-matrix interaction) or by particle-to-particle interlocking. If reduced mobility is the cause, the 1 μm Al_2O_3 composite should exhibit a larger effect, and if particle interlocking is the cause, the 100 μm composite should exhibit the larger effect, which is also refuted by the data. In addition, the Taylor anvil-on-rod tests indicate essentially no difference in the yield strength between those two materials, although the stress state in the Taylor test is far more complex than in the Hugoniot state. If we accept the higher value for γ, then we must recognize that the shock temperatures in the ZrC/ZrO_2/THV composite will surpass the temperature needed to induce a reaction in the material at a pressure of only 5 GPa (temperature rise in a shock wave will be discussed in the following chapter), and at the localized hotspots the necessary pressure would be even less. Although the effect of pressure in addition to temperature on the ZrC reaction kinetics is admittedly unknown, we would still expect the Hugoniot point at 11 GPa (shock temperature $\sim$950°C) to exhibit some degree of reaction, and so be at a higher volume than was observed. If we do not accept the high γ value based explanation, the alternative is an unsatisfying combination of explanations specific to each case; that is, unexplained nano-scale related behavior for the 1 μm composite (possibly related to relatively high surface energy contributions as interfaces are eliminated), rather large (up to $\sim$1 GPa) increased effective yield strengths in the 10 and 100 μm composites due to decreased polymer chain mobility, and for the ZrC/ZrO_2/THV a reaction model based upon multiple compounding assumptions concerning the composition of the initial and reacted materials, and whose U_S-U_P Hugoniot does not show obvious evidence of reaction. The results of the recovery experiment revealing residual porosities after shock passage (and therefore a small clue in the crush-up response) shed little additional light on the issue of generalizing the results. While it is clear that the 1 μm Al_2O_3 powder is much stiffer than the 10 μm Al_2O_3 powder, and is still remarkably porous (26%) even after being subjected

to an ∼8 GPa shock, it was shown that incomplete crush-up cannot explain the results. Although it was not explicitly shown, the same arguments also apply for the 10 μm Al_2O_3 composite.

It should be noted that the results of this investigation do not unequivocally support any one explanation for the shock comporession behavior, and due to the complexity of the system, there are undoubtedly other explanations for the phenomena discussed in this chapter that have not been considered. Despite the complications and uncertainties discussed above, we can make a few conclusions for the shock compression response of the composites. First, the strength of the composites is unaffected by the size of the particles, and within the uncertainty caused by the porosity, the Hugoniots are also unaffected. Second, the predictions for polymer-ceramic powder composites systematically underestimate the stiffness of the composites, and using conventional Grüneisen coefficients to account for any porosity only increases the underprediction. The results also indicate the possibility of a reaction fueled by a depolymerizing fluoropolymer (although not necessary a shock induced reaction), and suggest that the traditional method of finding the Grüneisen coefficient for polymers is poorly suited to materials with such anisotropic bonding.

CHAPTER V

ANOMALOUS RESPONSE OF PVDF STRESS GAUGES

This chapter will focus on observations briefly mentioned in the previous chapter concerning the difference in the recorded shock wave profiles measured by the two different time-resolved measurement techniques used in this study. The disagreement between the PVDF stress gauge profiles and the VISAR particle velocity traces is related to the discussion in the previous chapter not only because the ensuing discussion complements the Hugoniot response of the composites, but because both discussions suggest the possibility of an alternative form of the Grüneisen coefficient $\gamma(V)$ for polymers.

5.1 Comparison of Shock Wave Profiles from VISAR and PVDF

Earlier, in the presentation of the parallel-plate experimental results on THV (section 4.1), it was mentioned that the propagated PVDF stress trace and the VISAR traces do not reveal the same characteristic shape of the stress wave pulse. Figure 4.1 showed the propagated PVDF trace sharply rising to about 80% of the final value, then slowly approaching the final stress over a period of about 1 μsec. The VISAR trace, however, sharply rose to the final value and was steady. In fact, in all experiments where a sufficiently long PVDF trace was obtained, the PVDF stress traces continued to indicate a rise in pressure for $\sim$1 μsec after the arrival of the pressure pulse. One possible explanation for this phenomenon in the PVDF gauge traces is simply that the observed response is due to the electrical response of the circuitry used to monitor and record the output of the PVDF gauges.

The electrical recording circuit used is based on the system developed at Sandia National Labs in the late 1980's and early 1990's. Several reports are available in the literature characterizing the electrical response of the gauges, as well as the gauge/CVR/cabling system[180, 58]. Charest and Lynch[180] reported a time constant of 10 nsec for their PVDF gauge system by treating the circuit as a simple RC circuit described by Equation (83), where Q is charge (analagous to pressure in our case), Q_0 is the steady state charge

(or pressure), t is time, R is the impedance of the transmission lines (50Ω), and C_g is the combined capacitance of the gauges element, gauge transmission lines, and CVR (200 pF in the analysis of Charest and Lynch[180]).

$$Q(t) = Q_0 \left[1 - exp\left(\frac{-t}{RC_g}\right)\right] \tag{83}$$

However, the analysis by Charest and Lynch incorporated a coaxial cable between the gauge and CVR. Eliminating the capacitance of the cable from their calculations yields a time constant of 5 nsec. This value is roughly consistent with the fastest risetimes we have recorded with our system (≈10 nsec, keeping in mind that three time constants must elapse for an exponential system to reach 95% of the equilirium level). This time constant is far too small to explain the slow rise observed in Figure 4.1. Additionally, the structure of the observed profiles cannot be explained by a simple electrical response, because the initial rise is very short (10-20 nsec), which requires a time constant on the order of 5 nsec, but the final rise is very slow, requiring a time constant of 100-150 nsec. If a physical reason for the circuit displaying such a two-stage response exists, it is unknown to the author.

Another possible explanation for this phenomenon in the PVDF gauge traces is based on shock induced polarization of the THV sample. Shock induced electrical polarization of polymers has been documented[147] and is a known concern with PVDF gauges because of the potential for capacitive coupling of the sample with the gauges[181]. Therefore, several attempts were made to shield the PVDF gauges from such interference by inserting a grounded conductor between the sample and the PVDF gauges. One such attempt was shot 0827 on pure THV, which replicated shot 0725 except for the addition of the grounded Cu foils. Input and propagated PVDF stress gauge traces, as well as the VISAR particle velocity trace, for shot 0827 are shown in Figure 5.1. This experiment was at a higher impact velocity than experiment 0723 (see Figure 4.1), but was otherwise similar. As seen in Figure 5.1, even with the grounded conductor shielding, both PVDF gauges continue to rise after the initial arrival of the pressure pulse, but the VISAR trace jumps to a steady particle velocity very quickly and remains constant at ∼670 m/s until the arrival of the reshocking wave. Once again, this particle velocity is in very good agreement with

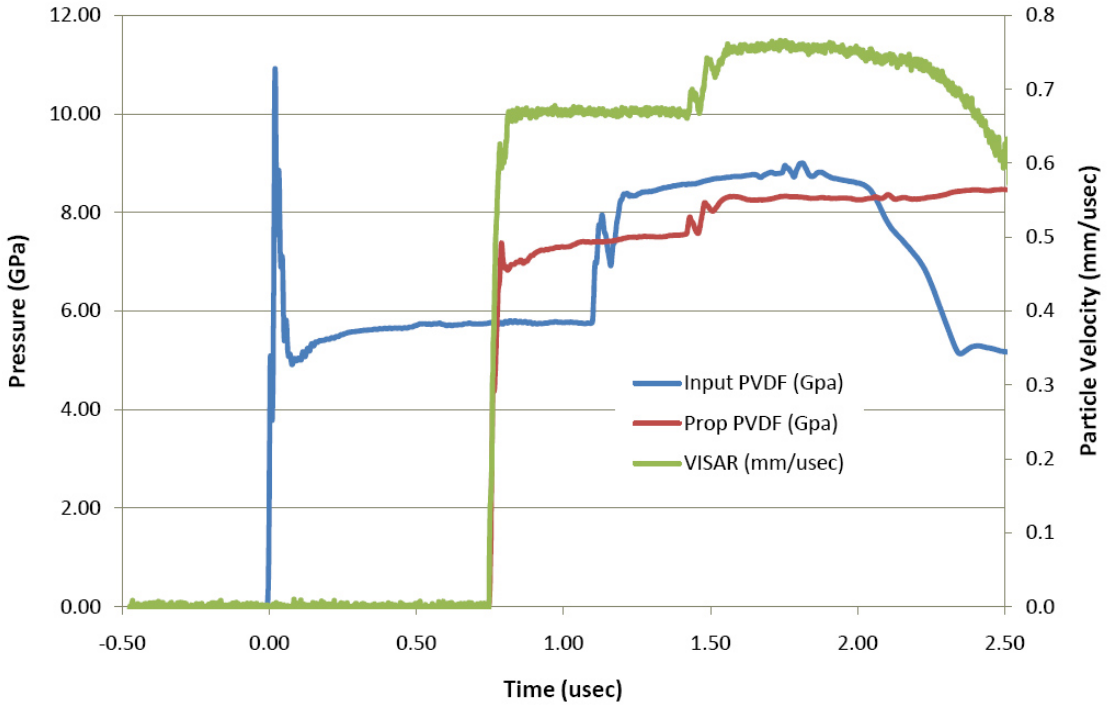

Figure 5.1: Pressure traces and VISAR trace for experiment 0827. The large pressure spike on the first PVDF gauge is due to the presence of the Cu foil. Reshocking waves are visible in all traces, and release waves are visible in the first PVDF and the VISAR trace. The second PVDF gauge was destroyed before the arrival of the release wave. Note the steady rise of the PVDF traces and the sharp rise and steady value of the VISAR trace.

impedance matching calculations. This experiment demonstrates that electrical polarization of THV is not affecting the PVDF electrical response, and so is not responsible for the phenomena.

It has also been suggested that this phenomena might be due to lateral strains in the PVDF gauge. This suggestion arises from considerations about the signs of the various piezoelectric coefficients. In piezoelectric materials the polarization vector P is related to the piezoelectric strain coefficient tensor d and the stress tensor σ by $P_i = d_{ijk}\sigma_{jk}$. By convention for a polymer film, direction **1** is parallel to the draw direction, direction **3** is perpendicular to the film surface, and direction **2** is perpendicular to **1** and **3**. For PVDF stress gauges, the polarization of interest is in the **3** direction, and since the film is biaxially stretched, the **1** and **2** directions are equivalent. In the biaxially stretched film used for the PVDF gauges, the piezoelectric strain coefficients are $d_{311} = d_{322} = 6\ pC/N$ and $d_{333} = -22$

pC/N[182]. The orthorhombic 2mm symmetry eliminates the six remaining d_{3jk} coupling P_3 to shear stress. Since d_{311} and d_{322} are positive and d_{333} is negative, it is obvious that tensile stresses or strains in the **1** and **2** direction have the same effect on P_3 as compressive stresses or strains in the **3** direction. Assuming that d_{311} and d_{322} decrease with pressure in a similar manner as d_{333}, we can easily estimate that in order for the transverse strains in the biaxial film to raise the total polarization in the **3** direction by 20%, the strains in the **1** and **2** directions (ϵ_1 and ϵ_2) must be 37% of the strain in the **3** direction (ϵ_3).

Since the measurements in this work were obtained using parallel-plate impact geometries at times well before the arrival of release waves from the edge of the plates, the only location where lateral strains can develop is in the only part of the assembly that lacks cylindrical symmetry- the gauge package. Because the gauge package consists of a narrow piece of PVDF film surrounded by epoxy (see Figure 5.2 for a more detailed gauge package illustration), and because PVDF has a slightly higher impedance than epoxy, the PVDF will flow slightly outward (radially) into the epoxy during a shock event, causing positive lateral strains in the PVDF.

In order to evaluate whether the positive lateral strains would be sufficient to explain the slow-rise phenomenon, CTH was used to model a 2-D PVDF gauge package in a typical experimental setup. The model consisted of a copper driver (initially at a particle velocity of 375 m/s and pressure of 15 GPa) attached to a gauge package and backed by THV polymer[110]. The gauge package consisted of a 25 μm PTFE film, a 25 μm PVDF film encapsulated by epoxy, and another 25 μm PTFE film. The mesh was a uniform, square mesh with 1 cell per μm. The boundary conditions were set to create cylindrical symmetry about x=0. The initial material layout is shown in Figure 5.3. To capture the highest plausible lateral strain, the materials were modeled without strength.

Results from CTH simulations shown in Figure 5.4 illustrate lateral strains (from all but tracer #1 which is not shown due to erratic behavior) rising to about 0.0001 as the lateral release wave from the PVDF/epoxy interface propagates past each tracer to the center of the PVDF gauge over a time period of $\sim$0.5 μsec. Although the timing is encouraging, the equilibrium pressure in the PVDF gauge in the model is 3.8 GPa, which corresponds to

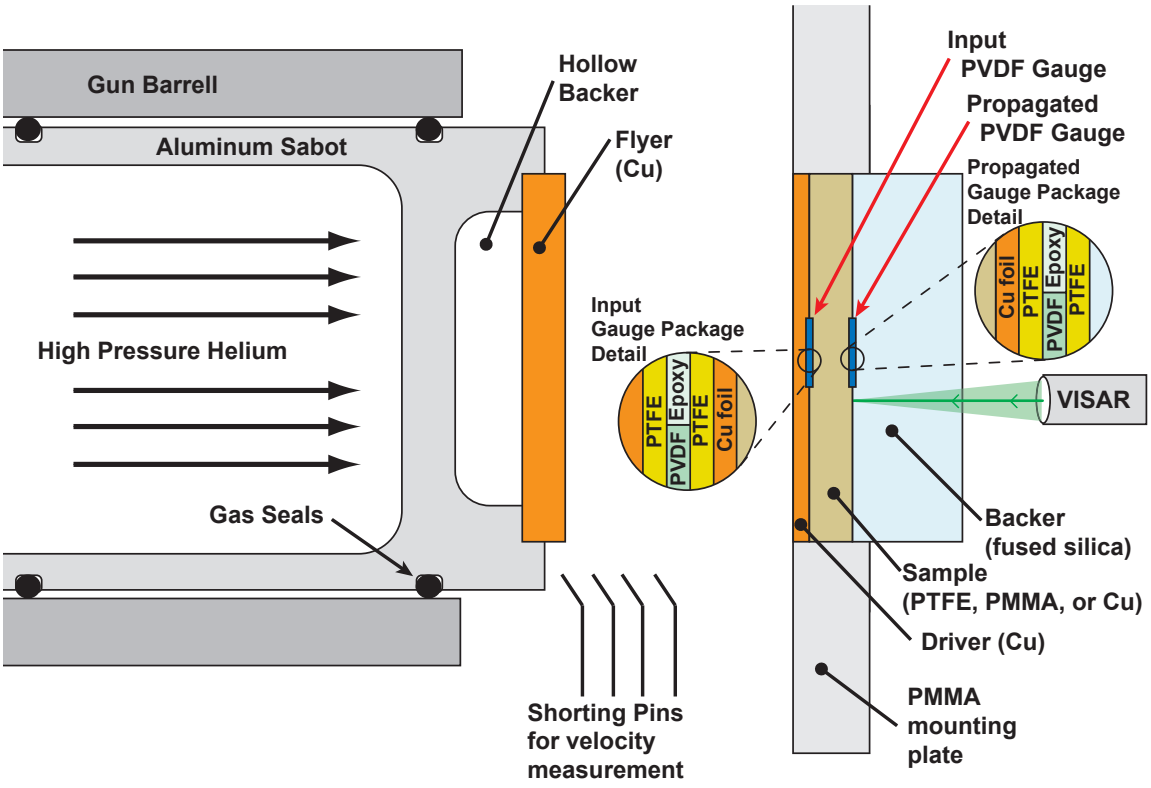

Figure 5.2: Experimental Parallel-Plate Setup for Cu, PMMA, and PTFE experiments.

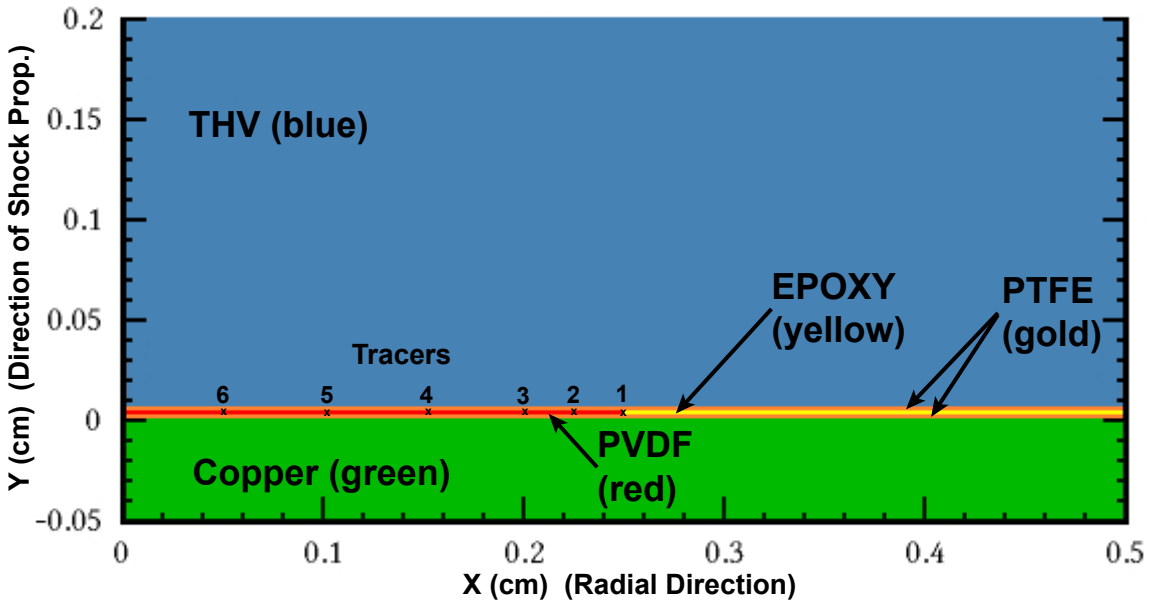

Figure 5.3: Initial geometry of 2D simulation of input gauge in a typical experiment. The copper is initially at a particle velocity and pressure of 375 m/s and 15 GPa, and the remaining materials are stationary and at zero pressure. Position tracers were placed along the middle of the PVDF gauge to track strain. The center of the PVDF gauge is at $X = 0$. Since the PVDF is higher impedance than the epoxy, the PVDF will move slightly to the right when the shock wave, traveling upward, reaches the gauge package.

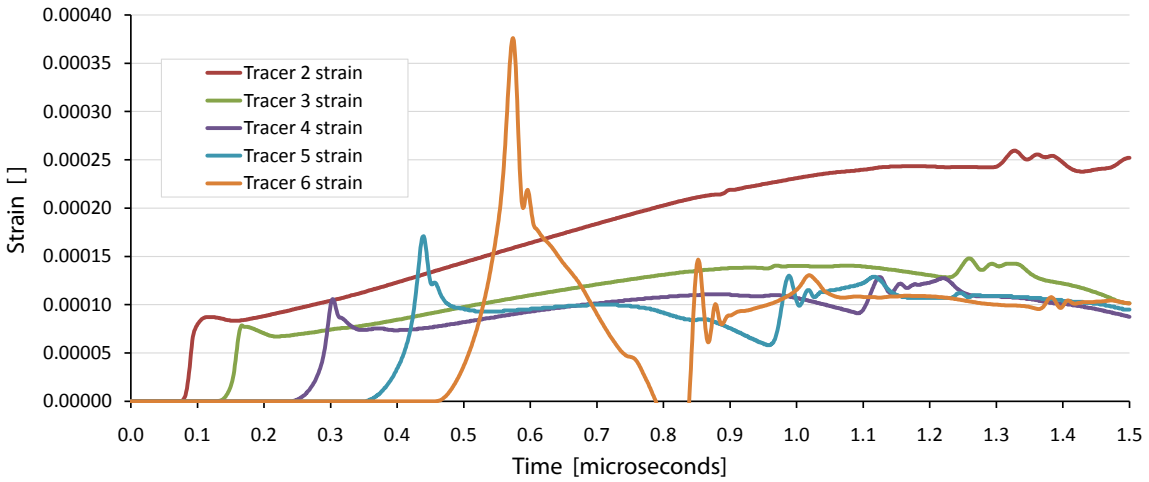

Figure 5.4: Modeling results showing predicted lateral strains in PVDF gauge package as a function of time.

$\epsilon_3 = 0.22$. Therefore, in order for the lateral strains to explain a 20% rise, we must have $\epsilon_1 = \epsilon_2 = 0.08$, two and a half orders of magnitude greater than the strains predicted by the hydrocode. Even if we recognize that the piezoelectric coefficient relates polarization to stress, rather than strain, and recogize that elastic modulus in the **3** direction (E_3) will be lower than E_1 and E_2 due to the backbone chain alignment along **1** and **2**, the resulting correction cannot account for such a discrepancy.

In an effort to further investigate whether this phenomena was a material response or a gauge artifact, three parallel-plate impact experiments using VISAR and PVDF, in addition to those already discussed on THV, were performed. The shock response of the materials chosen, PMMA, PTFE, and copper, have been thoroughly investigated. As in the previously discussed parallel-plate impact experiments, the VISAR laser was reflected off a Cu foil placed in the sample/backer interface (except in the case of the copper sample, where the laser was reflected directly off the rear surface), which allowed a comparison between the particle velocity trace from VISAR and the pressure trace from PVDF at the same interface. The experimental configuration was almost identical to that previously discussed and shown in Figure 3.15, except that for the two experiments on polymeric materials (PMMA and PTFE), grounded 25 μm Cu foils were added to each gauge package on either side of the sample, as shown in Figure 5.2 to guard against shock-induced electrical polarization in the sample and to provide a VISAR reflective surface. The PMMA and virgin PTFE were obtained form SABIC (formerly GE plastics), and OFHC copper was purchased from a commercial supplier. A summary of the gas gun experiments and measured/calculated parameters is given in Table 5.1.

From the data in the table, it can be seen that the pressure measured using VISAR P_{visar} was a few percent below the expected pressure P_{exp}, and the pressure measured by the PVDF gauges P_{pvdf} was a few percent above the predicted pressure. Figure 5.5 shows the propagated PVDF traces and the VISAR traces for all three experiments. For clarity, the three sets of traces are arbitrarily offset in time, and the PMMA trace is offset vertically (by 1 GPa or 100 m/s). Once again, it can easily be seen that the PVDF gauges continue to indicate a pressure rise for $\sim$1 μsec, whereas the VISAR trace shows a fast rise to peak

Table 5.1: Parallel-Plate Experiments Performed on Standard Materials with VISAR instrumentation

Material	Impact Vel.	Up[a]	P^b_{visar}	P^c_{pvdf}	U_S	P^d_{exp}
PTFE	444	239	2.90	3.1	2257	3.01
PMMA	519	235	2.85	3.1	3223	2.94
Cu	336	235	2.85	3.0	4108	2.96

[a] U_P measured from VISAR using fused silica window corrections.
[b] Calculated pressure from measured U_P and fused silica material properties below 20 GPa [47]
[c] Measured steady-state pressure from propagated PVDF gauge.
[d] Expected pressure using the impact velocity, impedance matching, and known material properties for PTFE, PMMA, and copper ([2]).

particle velocity and remains stable until the arrival of the recompression or release wave. The VISAR traces for the two polymers show a spike due to the presence of the Cu foil. The effect is muted in the PVDF traces because of the PTFE film separating the foil and the PVDF gauge. A small spike is visible in the Cu VISAR trace because of the relatively low impedance of the gauge package in relation to the sample and backer.

Although a viscoelastic response in PMMA is expected, it will be small because the shock wave has been propagating for only ∼800 nsec and is hidden behind the spike due to the Cu foil. The PTFE sample used in this work is 59% crystalline (as determined from density measurements), which has previously not been reported to show a viscous response in shock loading[183]. Likewise, no viscous response is observed in the present work, although the spike due to the Cu foil masks any material response for the first 100 nsec, and, as in the PMMA, the wave propagation time in the PTFE (1184 nsec) was likely insufficient for such a response to become pronounced. OFHC Copper is a well behaved standard and is known to be non-dispersive. The steadily-increasing PVDF profile obtained for Cu shown in Figure 5.5, together with the steady-state VISAR profile, is strong evidence that the gradual rise observed in the PVDF traces is a gauge response rather than a material response.

One possible explanation for the PVDF gauge response (the slight increase in indicated pressure during the application of a constant stress) is based on a pressure-induced α to β phase transition in the PVDF. As previously discussed, the β phase is favored at high pressure, and molten PVDF will crystallize to the β phase at pressures greater than about 0.1 MPa. Also as previously discussed, the β phase is the piezoelectric phase, and so any

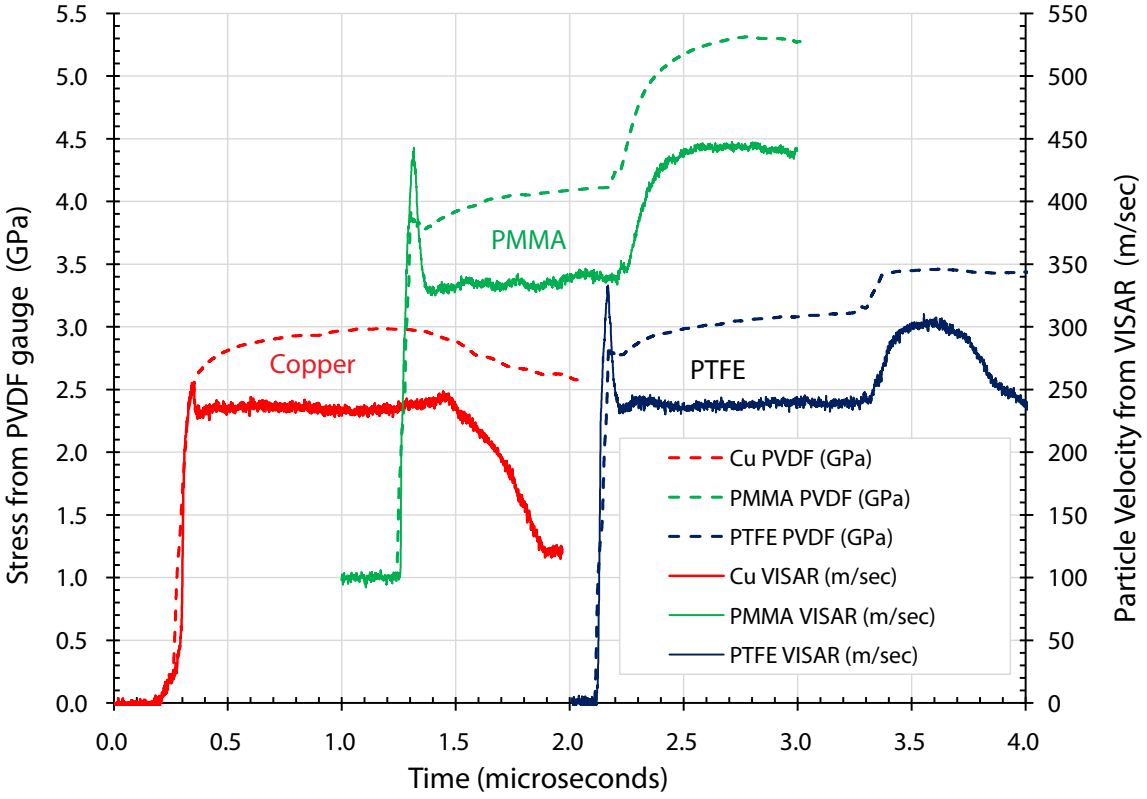

Figure 5.5: Propagated PVDF stress traces and VISAR traces for Cu, PMMA, and PTFE experiments. For clarity, the traces are offset horizontally, and the PMMA trace is offset vertically. The propagated PVDF gauge and VISAR probe both sampled the interface between the sample and the fused silica backer. The initial pressure spikes on the PVDF traces for the PMMA and PTFE experiments is due to the presence of the Cu foil. Reshocking waves are visible in the PMMA and PTFE traces, and release waves are visible in the Copper and PTFE traces. Note the steady rise of the PVDF traces and the sharp rise and steady value of the VISAR trace (disregarding the pressure spikes). The slight oscillations in the VISAR trace is due to configuring the VISAR to a fringe constant of 171 m/sec so that only about 1.5 fringes were recorded.

increase in the % β phase (assuming the newly created phase aligns with the already extant β domains) in the gauge will result in an increase in the piezoelctric response of the gauge material. The increase in piezoelectric response will be manifested in the PVDF gauges as an increase in recorded pressure as the additional β phase forms.

In order to test the hypothesis, experiments were performed using a diamond anvil cell (DAC) at the University of Hawaii while monitoring the relative amounts of α and β phases with Raman spectroscopy so that spectra can be taken in real time as the sample is subjected to elevated pressure. Raman spectroscopy has been shown to be an effective tool to differentiate between α and β PVDF by examining the relative strengths of the Raman band at 794 cm^{-1} (characteristic of α phase) and 839 cm^{-1} (characteristic of β phase)[184, 185]. Poled PVDF film specimens representative of the active element of the PVDF gauges (but without the sputtered electodes) were obtained from Dr. François Bauer at Piezotech, SAS, in France. Results from the Raman spectroscopy test at a range of pressures from ambient to 10.8 GPa are shown in Figure 5.6, along with the ratio of the intensities of the characteristic peaks as a function of pressure. It can be seen from the figure that the relative fraction of β phase does not increase as pressure increases, indicated that no room-temperature phase transition is occurring at pressures up to $\sim$10.8 GPa.

Graham[186] has suggested an alternative explanation for the PVDF gauge behavior based on an electromechanically-coupled relaxation, similar to the analysis performed by Chen et al.[187] for thick piezoelectric gauges. In the calibration for the PVDF stress gauge discussed in Section 2.3, it is assumed that charge density is a function of stress alone, and independent of stress history or boundary conditions. However, in reality the mechanical response is coupled to the boundary conditions through the electrostrictive and piezoelectric response, and to the loading rate and stress history through viscoelasticity (both volumetric and shear). Although it seems plausible that a viscous relaxation or, as Graham suggests, some hysteresis in the coupled response is causing the effect in PVDF, the analysis is a complex one, involving numerous material properties not readily found in the literature, and so is mentioned here for completeness but is not pursued.

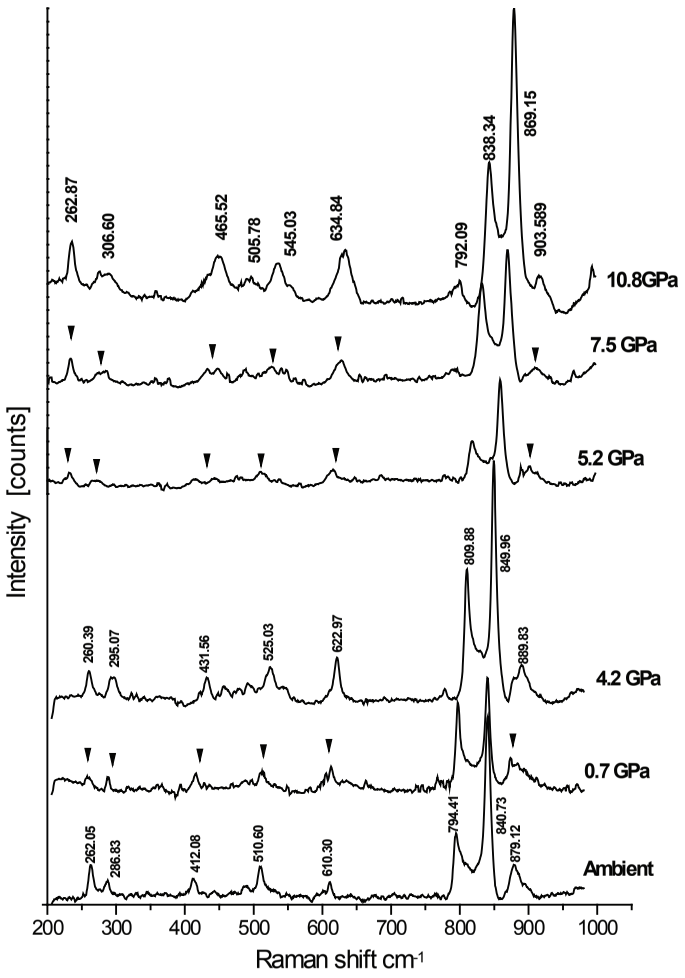

(a) Raman spectra of poled PVDF at pressures from ambient to 10 GPa.

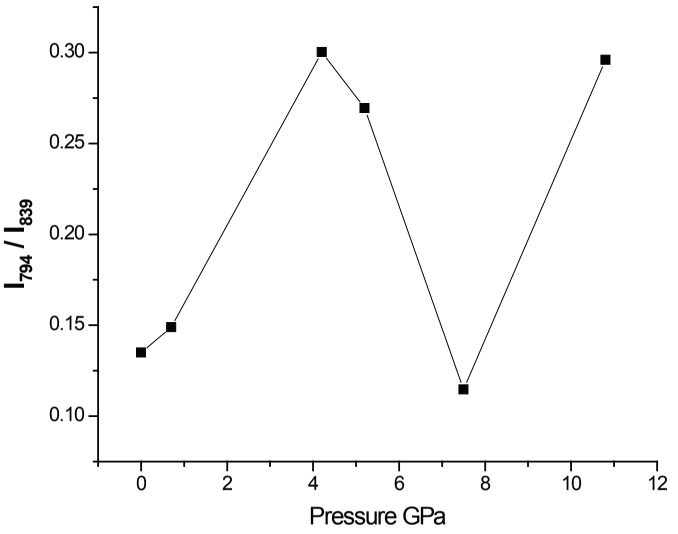

(b) Ratio of the intensity of the 794 cm^{-1} peak to that of the 839 cm^{-1} peak. Although the scale of the ordinate makes the change appear significant, these data points all represent a ratio of 0.2 within the experimental.

Figure 5.6: Raman Spectroscopy Results on PVDF as a Function of Pressure. The samples appears to be mostly β phase, as expected. However, the relative fraction of β phase does not increase as pressure increases.

5.2 Effect of Temperature and the Grüneisen Coefficient

It was shown in the previous section that the stress wave profiles recorded by the VISAR probe and the PVDF gauge are distinctly different, despite probing virtually identical locations in the specimens. It was also shown that the difference is due to a the response of the PVDF gauge, rather than a viscous response of the sample material. Although a pressure-induced phase transformation would explain the results, static high pressure experiments at ambient temperature with Raman spectroscopy indicate that no transformation is taking place at up to 10 GPa, well beyond the shock pressures at which the phenomenon was observed. However, the failure of the static high pressure experiments to reveal a phase transition could be due to the dependence of the glass transition temperature T_g on pressure. The pressure dependence of phase transition thresholds in polymers is well known, and it has been shown in the case of PVDF that both melt temperature T_m and T_g are particularly strong functions of pressure. The results of Samara's [188] investigation of T_m up to 450 MPa, and Scheinbeim et al.'s[189] investigation of T_g up to 700 MPa is shown in Figure 5.7, along with the temperature rise associated with a shock wave.

In the figure, three dashed lines are shown for the shock temperature. All are calculated from Equation (84), which is derived by Meyers[2], and where T is the temperature during the duration of a shock and T_0 is the initial temperature, taken to be 25°C. The pressure P in the integrand is a function of V, and is evaluated using Equation (85), which is derived from the jump conditions and the linear shock EOS discussed previously. The initial specific volume V_0, as well as the shock EOS constants C_0 and S are taken from the data of Marsh[47] in the pressure range below 35 GPa. The integral is solved numerically.

$$T = T_0 \, exp\left[\frac{\gamma_0}{V_0}(V_0 - V)\right] + \frac{V_0 - V}{2C_\nu}P + \frac{exp[(-\gamma_0/V_0)V]}{2C_\nu}\int_{V_0}^{V} P \, exp[(\gamma_0/V_0)V]\left[2 - \frac{\gamma_0}{V_0}(V_0 - V)\right]dV \tag{84}$$

$$P = \frac{C_0^2(V_0 - V)}{[V_0 - S(V_0 - V)]^2} \tag{85}$$

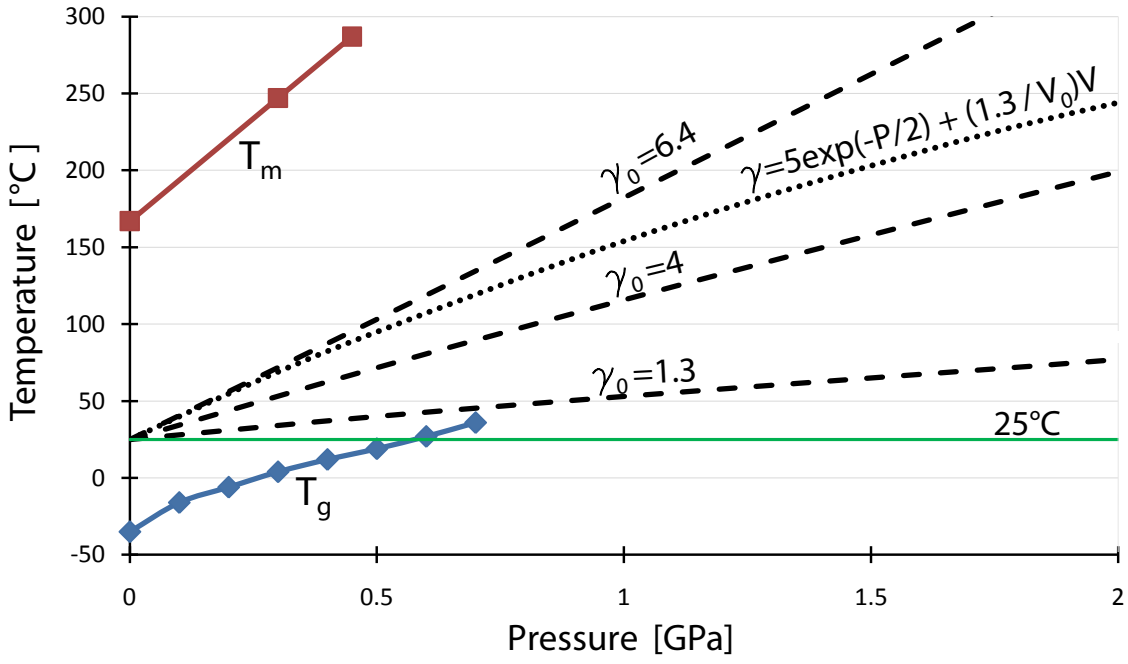

Figure 5.7: Pressure dependence of thermal transitions in PVDF. Data points for melting temperature T_m and glass transition temperature T_g taken from Samara[188] and Scheinbeim[189], respectively.

The three dashed lines are calculated for different values of the ambient Grüneisen coefficient γ_0, and it is clear that shock temperature is a strong function of γ. As previously discussed, there is some evidence that the value for γ calculated for polymers using Equation (12b) are too low by an order of magnitude[179, 177, 178]. In the case of PVDF, Warfield[179] reports γ_0=6.4, and although he points out that the value can vary significantly with both crystal structure and degree of crystallinity, no additional details about either of those characteristics for the PVDF material are presented. Tanaka et al.[190] investigate PVDF using Wada's method[177] of calculating γ from the pressure dependence of the sound speed, and differentiate between α and β phase. They report values for each phase as a function of pressure that agree overall with the single value reported by Warfield[179]. Therefore, the first value plotted in Figure 5.7 is γ_0=1.3, and is calculated using Equation (12b) and thermodynamic values from the literature. The second line is plotted with γ_0=4, because this is approximately the value of γ for which $(dT/dP)_{shock}$ equals dT_g/dP at upper limit of Scheinbeim et al.'s data[189]. The third line is plotted for γ_0=6.4, the value

reported by Warfield[179] and corroborated by Tanaka et al.[190] using different techniques.

In each of the three dashed lines, γ is a function of pressure through the relation $\gamma = (\gamma_0/V_0)V$ where $V = V(P)$. As previously discussed in the context of THV, such a dependence causes γ to decrease far slower than measured values. Therefore, the figure also shows a dotted line calculated using an exponential decay form of γ, allowing the higher initial γ values to decay quickly and then approach the traditional value measured through calorimetric methods. The form of γ chosen is given in Equation (86). In the equation, the exponential term can be thought of as representing the rate at which the interchain bonds quickly become more harmonic as they are compressed, and the second term is the "traditional" formulation of γ, where the γ_0 value is the lower, thermodynamic average value obtained from Equation (81). In the equation, **A** and **B** correspond to fitted parameters that, respectively, govern the initial value of γ and the rate at which the high initial value decays to the traditional value. For PVDF, **A** and **B** were found to be approximately 5 and 2, respectively.

$$\gamma = A\exp(-P/B) + (\gamma_0/V_0)V \tag{86}$$

Since Equation (84) is derived assuming $\gamma/V = \gamma_0/V_0$, it cannot be used for the new form of $\gamma(V)$. Instead, the following differential equation (from which Equation (84) is derived[6]) is solved numerically, where only the specific heat must be constant.

$$\frac{\partial T}{\partial V} + \frac{\gamma}{V}T = \frac{P + (V_0 - V)\frac{\partial P}{\partial V}}{2C_\nu} \tag{87}$$

From the figure, the T_g exceeds room temperature at about 600 MPa, and will exceed the shock temperature T_s at about 750 MPa if the conventional Grüneisen parameter γ_0 of 1.3 is used. However, if Warfield's value[179] of 6.4 is used, the polymer will remain above its T_g regardless of the shock pressure. Note that even at γ_0=6.4, the shock temperature will not exceed the melt temperature of the polymer, and so is still consistent with the observations and work of Samara[188], i.e., the higher γ_0 will still not cause the polymer to melt and so lose the crystalline structure necessary for piezoelectricity. If we employ

Equation (86) and assume that γ begins at 6.3 and decays to the thermodynamic value of $(1.3/V_0)V$, we can see that the polymer will still remain above T_g until at least several GPa, beyond which extrapolating the T_g data is unwarranted at best.

The above discussion illustrates that since the polymer at room temperature becomes a glass at ∼500 MPa, any pressure-induced phase transformation was prevented in the room temperature DAC Raman spectroscopy study. Since shock compression introduces not only high pressure, but also high temperature, shocked PVDF remains above T_g regardless of the shock intensity, thereby allowing any phase transformation to proceed. Therefore, the possibility of a shock-induced phase transformation cannot be ruled out just on the basis of the room-temperature diamond anvil cell Raman spectroscopy studies presented earlier. To conclude, a phase transformation can possibly explain the observed anomalous response of PVDF gauges, and such a phase transition is enabled by reconsidering the Grüneisen parameter for polymeric materials such as PVDF.

5.3 Summary of the Anomalous Response of PVDF Gauges

This chapter presented a comparison of shock wave profiles collected using both PVDF and VISAR gauges where the gauges probed essentially the same location within the target assembly (the sample/backer interface). Despite probing the same interface, the two gauges recorded distinctly different stress wave structures. It was shown that the VISAR gauges record a sharp rise and a flat-top stress pulse, while the PVDF gauges record a sharp rise followed by a decaying rise to an equilibrium stress. Some viscoelastic materials are known to develop similar structured waveforms as shock waves propagate through them, but through experiments on standard materials, this work showed that the observed structure is an anomalous gauge response rather than a material response. This anomalous gauge response has been noted in the literature, and several explanations have been put forth, including electromechanically-coupled relaxation, shock-induced polarization, lateral strains, and a shock-induced phase transformation. With the exception of the relaxation, each of these explanations were examined, and it was shown that neither shock induced polarization, nor lateral strains can explain the response. It was also shown that a pressure-induced phase

transformation is not present, and that a shock-induced phase transformation is unlikely if we use the traditional, "thermodynamic average" Grüneisen parameter. However, it has been argued in the polymer physics literature that the Grüneisen parameter for polymers is initially higher than the thermodynamic average value, and it was shown that implementing a higher value, even if we allow it to decay to the traditional value over the first few GPa, allows for the possibility of a shock-induced phase transition.

CHAPTER VI

SUMMARY OF RESULTS AND CONCLUSIONS

The results of this work investigating the shock response of 25% by volume of either 1, 10, or 100 μm Al_2O_3 or 10 μm ZrC particles in a THV matrix can be briefly summarized as follows:

- The shock compression response of THV, as well as the strength at strain rates on the order of $\sim 10^4$ are investigated. The Hugoniot results did not show evidence of a reaction or decomposition, and the U_S-U_P Hugoniot response is observed to be similar to that reported for other fluoropolymers in the literature.

- The shock response and high-strain-rate strength of the composites composed of ceramic particles in a THV matrix are investigated. The Hugoniots displayed some unexpected trends and, in general, did not match the predictions of a number of analytical models. The trends observed in the stress wave profiles obtained in the course of the Hugoniot experiments were compared with trends reported in the literature for similar materials.

- Two of the alumina powders employed in the composites were investigated using static and dynamic methods to understand the compaction/compression response. The dynamic response was also modeled using hydrocode simulations.

- In order to build confidence in the ability of analytical models used in the literature to predict the shock response of a polymer composite, an experiment on a homogenous ceramic powder/polymer composite was performed. Several of the models gave acceptable results, and so these models were applied to the more complex THV composites. Correlating the model predictions and the experimental data lead to questions concerning the inertness of the composites and the validity of the assumed form of the Grüneisen coefficient.

- Possible reactions between the ceramic particles and the THV matrix were investigated. Although no reaction was discovered between Al_2O_3 and THV, evidence of a reaction was found between ZrC and THV. Consideration of the reaction was found to improve the

correlation between the predictive models and the observed response.

- The proper form of the Grüneisen coefficient γ for polymers was discussed, and a new dependence of γ on volume was proposed based on literature data. The new form of γ improved the correlation between the predictive models and the observed response, and also aided in explaining possible reasons for the anomalous response of the PVDF stress gauge used in the study.

The results in this work on ALOX and on the less-porous 10 and 100 μm Al_2O_3/THV composites show that the Hugoniot of nonporous composites made of polymers and ceramic particles can be reasonably predicted by several analytical models from the literature, although for all composites, the Hugoniot stiffness is underpredicted. As the porosity of the composites increases, the underprediction increases. Although there are several possible explanations for the observed response, it is most satisfyingly explained by reconsidering how the Grüneisen coefficient γ is evaluated for polymers. By considering that γ is a measure of the anharmonicity of the system, it follows that the most anharmonic bonds primarily determine γ. Such considerations have been analyzed by previous researchers, and lead to much higher values of γ for polymers. Increasing γ has a strong effect on the Hugoniot of a porous material, and leads to significant improvements in the agreement between the experimental and predicted shock Hugoniot for all of the Al_2O_3/THV composites.

For the 10 μm "ZrC/THV" composite, a major challenge in predicting the shock results is identifying the starting components. It was shown that the composite is actually composed of ZrC, monoclinic ZrO_2, THV, and some other unknown contaminants. Even with this compositional uncertainty, predictions for the composite Hugoniot agree quite well with experimental results, provided the higher γ was used and the crush-up behavior of the particles is accounted for. This work also presents evidence of a thermally-induced reaction in the ZrC/THV composite, and presents an alternative explanation for the observed Hugoniot based on an exothermic, shock-induced reaction model. Waveforms of the porous, heterogeneous polymer composites follow previously noted trends of decreasing risetime with increasing pressure, and show that the relationship between risetime and pressure, and therefore the wave dispersion characteristics, follows trends more closely associated with

powders than with solids.

As part of the investigation into the shock-wave risetimes of the composites, this work investigated the inherent risetime of the PVDF gauges used to record the pressure wave profile, using comparisons with experiments done with VISAR particle velocity gauges. A clear discrepancy in the gauge records after the initial shock wave front has passed was observed. It has been proposed in the past that this discrepancy is due to a pressure-induced phase transformation in the PVDF gauge material, but no such phase transition is observed to occur at room temperature. However, a significant question raised by this work is that of an appropriate form of the Grüneisen coefficient for polymeric materials. Although the exact form of $\gamma(V)$ is unclear, it is reasonable to assume an exponentially-decaying form of $\gamma(V)$ where at low temperatures γ is an order of magnitude higher than the traditional values, and at high pressures, the traditional (lower) values are approached as the bonding becomes less anharmonic. When such an exponentially decaying form of $\gamma(V)$ is applied to the PVDF gauge material, it is shown that a pressure-induced phase transformation can be prevented in static high pressure experiments at room temperature, while still occurring in the shock compressed material. Although this work does not prove the existence of a shock-induced phase transformation in PVDF, it is the first time the arguments made in the polymer-physics literature concerning a higher $\gamma(V)$ for polymers has been applied to the shock-physics field, and it is hoped that this work will lead to further inquiry into $\gamma(V)$.

This work examined ceramic-particle-filled polymer composite materials that are substantially more complex than most materials tested in the literature, in that the composites are highly heterogeneous and contain particulate components which themselves display incompletely understood shock compression behavior. It is challenging to draw conclusions from a set of composite materials in which each material varies in several ways from the others. As a result, elements of this research have exposed further gaps in our current understanding of the shock compression response of ceramic-polymer composites:

1) There is no widely accepted model to account for the shock compression of ceramic particles that accounts for variations in particle size and morphology. Reliable models need to be developed to predict the compaction behavior of ceramic powders in order to

subsequently model the shock-compression response of complex ceramic particle-containing composites. The compaction behavior of ceramic particles is highly dependent on particle shape, and less so on size, which in turn radically influences the shock compression response of ceramic particle / polymer composites, especially when the ceramic particles are in contact with one another, rather than isolated in the polymer matrix.

2) The response of the polymer composites illustrates that questions surrounding the proper Grüneisen coefficient (γ) for polymeric materials must be addressed in order to predict the shock response of porous polymeric composites.

CHAPTER VII

FUTURE WORK

This research was complicated by the manufacturing approach taken. In particular, the non-uniform particle distribution within each composite, and the varying porosity across the various composite formulations must be eliminated (assuming, of course, that the goal was not to produce a non-uniform distribution). This is especially important considering that a composite with all particles in contact will behave very differently than one in which each particle is isolated in a soft matrix material. The porosity must also be precisely controlled, even in inert materials, since the porosity has a large effect on the amount of energy deposited into the material during shock loading, which in turn affects the measured shock response. In energetic materials, it is even more crucial to control the porosity, as the hot spots caused by the localized deformation have a large effect on the ignition behavior.

These considerations are of paramount importance for planning future investigations into the shock properties of particle reinforced ceramics. Beyond these general considerations, recommended future work includes:

1. Conducting experiments to investigate the proper form of the Grüneisen coefficient (γ) for polymers. These experiments could include:

   (a) shock/reshock experiments, where a primary, as well as a recentered, Hugoniot is obtained. The two Hugoniots can be related using the Grüneisen coefficient.

   (b) shock compression experiments where the temperature during the shock pulse is measured, as temperature rise during the shock wave is highly dependent on the Grüneisen coefficient.

   (c) shock compression and release experiments where the sound speed at pressure is measured. The Grüneisen coefficient relates the Hugoniot and the isentrope, and sound speed at pressure is a measure of the initial slope of the isentrope.

2. Development of a model to predict the shock compaction/compression behavior of ceramics, taking into account the dependence of compaction on morphology and particle size. The model could be anything from an analytical, empirically based engineering model applied to the macroscopic volume of powder, to a physically-based strength and fracture model to be implemented computationally at the microscale.

3. Characterization of the reaction thermodynamics and kinetics of fluorinated monomer compounds with commonly used filler particles. Ideally, the characterization would include the effect of high pressure and/or temperature.

REFERENCES

[1] Ames, R. G. In *Materials Research Society Symposium Proceedings, 2005, Section H*, 0896–H03–08, (2006). 1, 2

[2] Meyers, M. *Dynamic Behavior of Materials.* John Wiley and Sons, Inc., New York, (1994). 3, 18, 166, 170

[3] Graham, R., Anderson, M., Horie, Y., You, S.-K., and Holman, G. *Shock Waves* **3**(2), 79–82 (1993). 3, 32

[4] Kinslow, R., editor. *High Velocity Impact Phenomena.* Academic Press, New York, (1970). 3

[5] Asay, J. and Shahinpoor, M., editors. *High Pressure Shock Compression of Solids.* Springer-Verlag, N.Y., (1993). See chapter 4 by T.J. Ahrens. 3

[6] Davison, L. *Fundamentals of Shock Wave Propagation in Solids.* Springer-Verlag, Berlin, (2008). 3, 5, 11, 13, 14, 172

[7] Drumheller, D. *Introduction to Wave Propagation in Nonlinear Fluids and Solids.* Cambridge University Press, New York, (1998). 3

[8] Zel'dovich, Y. and Raizer, Y. *Physics of Shock Waves and High-Temperature Hydrodynamic Phenomena.* Dover, Mineola, NY, (2002). Originally published in English in two volumes in 1966 and 1967 by Academic Press Inc., New York. 3

[9] Nesterenko, V. *Dynamics of Heterogeneous Materials.* Springer-Verlag, New York, (2001). 3, 107, 108

[10] Horie, Y. *Journal de physique, IV* **110**, 3–7 (2003). 3

[11] Kolsky, H. *Stress Waves in Solids.* Dover, N.Y., (1963). 5

[12] Sheffield, S., Gustavsen, R., and Anderson, M. *Shock Loading of Porous High Explosives.* Springer-Verlag, New York, (1997). Chapter 2 of High-Pressure Shock Compression of Solids IV, edited by Davison, Horie, and Shahinpoor. 6, 107

[13] Gourdin, W. *Progress in Materials Science* **30**, 39–80 (1986). 6, 43

[14] Champion, A. *Journal of Applied Physics* **42**(13), 5546–5550 (1971). 9

[15] Chapman, D., Tsembelis, K., and Proud, W. In *Shock Compression of Condensed Matter - 2005,* Furnish, M., Elert, M., Russell, T., and White, C., editors, 1445–1448, (2006). 11

[16] Batsanov, S. *Effects of Explosions on Materials.* Springer-Verlag, N.Y., (1994). 12, 20

[17] Carter, W. J. and Marsh, S. P. Technical report, (1995). Los Alamos Report LA-13006-MS, UC-910. 12, 47, 86, 127, 128

[18] Ruoff, A. L. *Journal of Applied Physics* **38**, 4976–4980 (1967). 12

[19] Steinberg, D. *The Journal of Physics and Chemistry of Solids* **43**, 1173–1175 (1982). 12

[20] Cooper, P. *Explosives Engineering.* VCH, New York, (1996). 15, 17

[21] Alekseev, Y., Al'tshuler, L., and Krupnikova, V. *Jounal of Applied Mechanics and Technical Physics* **12**, 624–627 (1971). 20

[22] McQueen, G., Marsh, S., Taylor, J., Fritz, J., and Carter, W. *The Equation of State of Solids from Shock Wave Studies, High Velocity Impact Phenomena*, 230. Academic, New York (1970). 20

[23] Jordan, J. Master's thesis, Georgia Institute of Technology, (1999). 21

[24] Baer, M., Hall, C., Gustavsen, R., Hooks, D., and Sheffield, S. *Journal of Applied Physics* **101**, 034906 (2007). 21

[25] Jordan, J., Dattelbaum, D., Ferrant, L., Sutherland, G., Baer, M., Richards, W., Sheffield, S., Dick, R., and Thadhani, N. In *Shock Compression of Condensed Matter - 2009,* Elert, M., Buttler, W., Furnish, M., Anderson, W., and Proud, W., editors, 1253–1256, (2009). 21, 26

[26] Wallis, G. B. *One-dimensional two-phase flow.* McGraw-Hill, New York, (1969). 21

[27] Grady, D., Winfree, N., Kerley, G., Wilson, L., and Kuhns, L. *Journal de Physique* **10**, 9.15–9.20 (2000). 22

[28] Brown, J., Vogler, T., Grady, D., reinhart, W., Chhabildas, L., and Thornhill, T. In *Shock Compression of Condensed Matter - 2007,* Elert, M., Furnish, M., Chau, R., Holmes, N., and Nguyen, J., editors, 1363–1366, (2007). 23, 30, 107

[29] Dai, C., Eakins, D., and Thadhani, N. *Journal of Applied Physics* **103**, 093503 (2008). 24, 25, 77, 149, 150

[30] Deal, W. *Journal of Applied Physics* **28**, 782–784 (1957). 24

[31] Wu, Q. and Jing, F. *Journal of Applied Physics* **80**, 4343–4349 (1996). 25

[32] Simons, G. A. and Legner, H. H. *Journal of Applied Physics* **53**, 943–947 (1982). 26

[33] Krueger, B. R. and Vreeland, T. *Journal of Applied Physics* **69**, 710–716 (1991). 27

[34] Murnaghan, F. *Proceedings of the National Academy of Sciences of the United States of America* **30**(9), 244–247 (1944). 29

[35] Herrmann, W. *Journal of Applied Physics* **40**, 2490–2499 (1969). 29, 30

[36] Carroll, M. and Holt, A. *Journal of Applied Physics* **43**, 759–761 (1972). 30

[37] Borg, J., Chapman, D., Tsembelis, K., and Proud, W. *Journal of Applied Physics* **98**, 073509 (2005). 30, 42

[38] Thadhani, N. *Journal of Applied Physics* **76**, 2129–2138 (1994). 31

[39] Bennett, L. and Horie, Y. *Shock Waves* **4**, 127–136 (1994). 32

[40] Barker, L. and Hollenbach, R. *The Review of Scientific Instruments* **36**, 1617–1620 (1965). 33

[41] Taniguchi, T., Yasuo, H., Kondo, K., and Sawaoka, A. *Journal of Applied Physics* **66**, 1662–1666 (1989). 33, 42

[42] Strand, O., Goosman, D., Martinez, C., Whitworth, T., and Kuhlow, W. *Review of Scientific Instruments* **77**, 083108 (2006). 33

[43] Barker, L. and Hollenbach, R. *J Appl Phys* **43**, 4669–4675 (1972). 34, 35, 76

[44] Kepler, R. and Anderson, R. *Advances in Physics* **41**, 1–57 (1992). 34

[45] Scheinbeim, J., Nakafuku, C., Newman, B., and Pae, K. *J. Appl. Phys.* **50**, 4399–4405 (1979). 35

[46] Ohigashi, H. and Hattori, T. *Japanese Journal of Applied Physics* **28**, 1612–1615 (1989). 35

[47] Marsh, S. P., editor. *LASL Shock Hugoniot Data.* University of California Press, Berkeley and Los Angeles, CA (1980). 35, 83, 128, 150, 166, 170

[48] Wackerbarth, D., Anderson, M., and Graham, R. Technical report, (1992). Sandia Report SAND92-0046. 35

[49] Bauer, F. *IEEE Transaction on Ultrasonics, Ferroelectrics, and Frequency Control* **47**, 1448–1454 (2000). 35, 75

[50] Newnham, R. E. *properties of materials.* Oxford Univ. Press, N.Y., (2005). See chapter 12. 35

[51] Bauer, F. In *High-Pressure Science and Technology - 1993*, 1727–1730, (1994). 35, 36

[52] Bauer, F. US Patent 4,611,260, (1986). 35

[53] Bauer, F. In *Shock Waves in Condensed Matter - 1985,* Gupta, Y., editor, 483–496. Plenum, (1986). 35

[54] Graham, R., Lee, L., and Bauer, F. In *Shock Waves in Condensed Matter - 1987,* Schmidt, S. and Holmes, N., editors, 619–622, (1988). 35, 75

[55] Anderson, M. and Wackerbarth, D. Technical report, (1988). Sandia Report SAND88-2327, UC-13. 35

[56] Fogelson, D., Lee, L., Gilbert, D., Conley, W., Graham, R., Reed, R., and Bauer, F. In *Shock Waves in Condensed Matter - 1987,* Schmidt, S. and Holmes, N., editors, 615–619, (1988). 36

[57] Lee, L., Hyndman, D., Reed, R., and Bauer, F. In *Shock Compression of Condensed Matter - 1989,* Schmidt, S., Johnson, J., and Davison, L., editors, 821–824, (1990). 36

[58] Kotulski, J., Anderson, M., Brock, B., Gomez, J., Graham, R., and Vittitoe, C. In *High Pressure Science and Technology - 1993,* Schmidt, S., Shaner, J., Samara, G., and Ross, M., editors, 1739–1742, (1994). 36, 159

[59] Samara, G. and Bauer, F. In *Shock Waves in Condensed Matter - 1987,* Schmidt, S. and Holmes, N., editors, 611–614, (1988). 36

[60] Ferranti, L. *Mechanochemical Reactions and Strengthening in Epoxy-Cast Aluminum Iron-Oxide Mixtures.* PhD thesis, Georgia Institute of Technology, (2007). 37, 49

[61] Lemar, E., forbes, J., Tasker, D., and Bur, A. In *Shock Waves in Condensed Matter - 1985*, 503–508, (1986). 36

[62] Lynch, C. and Charest, J. In *Shock Waves in Condensed Matter - 1991*, 901–904, (1992). 36, 75

[63] Graham, R., Anderson, M., Bauer, F., and Setchell, R. In *Shock Waves in Condensed Matter - 1991,* Schmidt, S., Dick, R., Forbes, J., and Tasker, D., editors, 883–886, (1992). 36, 76

[64] Borissenok, V., Simakov, V., Kuropatkin, V., Bragunets, V., Volgin, V., Romaev, V., Tukmakov, V., Kruchinin, V., Lebedeva, A., Goncharova, D., and Zhernokletov, M. *Instruments and Experimental Techniques* **51**(4), 593–601 (2008). Original Russian text in *Pribory i Tekhnika Eksperimenta*, 2008, No.4, pp. 113-121. 36

[65] Setchell, R. E. In *Shock Waves in Condensed Matter - 1987*, 623–626, (1988). 36, 38

[66] Anderson, M. and Graham, R. Unpublished Presentation made at Institut de Saint-Louis (ISL) for the Ferroelectric Polymer Shock and Dynamic Sensor Workshop, (1994). 38

[67] Moulard, H. and Bauer, F. In *Shock Waves in Condensed Matter - 1995*, 1073–1076, (1996). 38

[68] Anderson, M., Graham, R., and Wackerbarth, D. In *Shock Compression of Condensed Matter - 1989,* Schmidt, S., Johnson, J., and Davison, L., editors, 805–808, (1990). 38

[69] Grady, D. Technical report, (1991). Sandia Report SAND91-0147, UC-704. 39, 40, 41

[70] Anderson, M., Graham, R., and Holman, G. In *High Pressure Science and Technology - 1993*, 1111–1114, (1994). 41, 43, 107

[71] Erlich, D. and Curran, D. *Characterization of the Dynamic Behavior of Porous Solids-Part 6. Dynamic Response of Porous Ceramics - Experiments.* SRI International, Menlo Park, CA (1976). 42

[72] Bourne, N., Millett, J., Chen, M., McCauley, J., and Dandekar, D. *J. Appl. Phys* **102** (2008). 42, 128

[73] Resnyansky, A. and Bourne, N. *Journal of Applied Physics* **95**, 1760–1769 (2004). 42

[74] Trunin, R. *Experimental Data on Shock Compression and Adiabatic Expansion of Condensed Matter*. Russion Federal Nuclear Center - VNIIEF, Sarov, (2001). 42, 128

[75] Malaise, F., Chevalier, J., Bertron, I., and Malka, F. *Journal de Physique IV* **134**, 929–934 (2006). 42

[76] Vogler, T., Lee, M., and Grady, D. *Int. J. of Solids and Structures* **44**, 636–658 (2007). 42, 43, 107

[77] Borg, J.P. Vogler, T. *Int. J. of Solids and Structures* **45**, 1676–1696 (2008). 43

[78] Millett, J., Bourne, N., and Dandekar, D. *Journal of Applied Physics* **96**, 3727–3732 (2004). 43

[79] Mashimo, T., Nagayama, K., and Sawaoka, A. *Journal of Applied Physics* **54**, 5043–5048 (1983). 43

[80] Tong, W. and Ravichandran, G. *Recent Developments in Modeling Shock Compression of Porous Materials*. Springer-Verlag, New York, (1997). Chapter 7 of High-Pressure Shock Compression of Solids IV, edited by Davison, Horie, and Shahinpoor. 43, 104

[81] Linde, R., Seaman, L., and Schmidt, D. *Journal of Applied Physics* **43**, 3367–3375 (1971). 43

[82] Akashi, T., Lotrich, V., Sawaoka, A., and Beauchamp, E. *Journal of the American Ceramic Society* **68**, C322–C324 (1985). 44

[83] Akashi, T. and Sawaoka, A. *Journal of Materials Science* **22**, 3276–3286 (1987). 44

[84] Akashi, T. and Sawaoka, A. *Journal of Materials Science* **22**, 1127–1134 (1987). 44

[85] Akashi, T. and Sawaoka, A. *Journal of Materials Science* **22**, 1031–1036 (1987). 44

[86] Sawaoka, A., Takamatsu, M., and Akashi, T. *Advanced Materials* **6**, 346–354 (1994). 44

[87] Sawaoka, A., Soga, s., and Kondo, K. *Journal of Materials Science Letters* **1**, 347–348 (1982). 44

[88] Sawaoka, A., Kondo, K., and Akashi, T. Technical report, Tokyo Institute of Technology, (1979). Number 4. 44

[89] Bergmann, O. and Barrington, J. *Journal of the American Ceramic Society* **49**, 502–507 (1966). 44

[90] Meyers, M., Benson, D., and Shang, S. In *High Pressure Science and Technology - 1993*, 1239–1242, (1994). 44

[91] Meyers, M., Benson, D., and Olevsky, E. *Acta Materiala* **47**, 2089–2108 (1999). 44, 45

[92] Fischmeister, H. and Arzt, E. *Powder Metallurgy* **26**, 82–88 (1983). 45, 46

[93] Arzt, E. *Acta Metallurgica* **30**, 1883–1890 (1982). 45

[94] Sawaoka, A. *Shock waves in materials science.* Springer-Verlag, Tokyo, (1993). Chapter 7. 45

[95] Carroll, M. and Holt, A. *Journal of Applied Physics* **43**, 1626–1636 (1972). 46

[96] Kondo, K., Soga, S., Sawaoka, A., and Araki, M. *Journal of Materials Science* **20**, 1033–1048 (1985). 46

[97] Barker, L. and Hollenbach, R. *J Appl Phys* **41**, 4208–4226 (1970). 48, 83

[98] Schuler, K. *J. Mech. Phys. Solids* **18**, 277–293 (1970). 48

[99] Schuler, K., Nunziato, J., and Walsh, E. *Int. J. Solids Structures* **9**, 1237–1281 (1973). 48

[100] Sheffield, S. and Alcon, R. In *Shock Waves in Condensed Matter - 1991*, 909–912, (1992). 48

[101] Barker, L. *Journal of Composite Materials* **5**, 140–162 (1970). 49

[102] Munson, D. and May, R. *J. Appl. Physics* **43**, 962–971 (1971). 49, 128

[103] Millett, J. and Bourne, N. K. *Journal of Applied Physics* **88**, 7037–7040 (2000). 49

[104] Barnes, N., Bourne, N., and Millett, J. In *Shock Compression of Condensed Matter - 2001,* Furnish, M., Thadhani, N., and Horie, Y., editors, 135–138, (2002). 49, 128

[105] Millett, J., Bourne, N. K., and Barnes, N. *J. Appl. Phys* **92**, 6590–6594 (2002). 49, 52, 71

[106] Bourne, N. and Gray, G. *J. Appl. Phys* **98** (2005). 50, 51

[107] Bourne, N., Millett, J., Chen, M., McCauley, J., and Dandekar, D. *J. Appl. Physics* **102** (2008). 50, 64

[108] Robbins, D., Sheffield, S., and Alcon, R. In *Shock Compression of Condensed Matter - 2003*, 675–678, (2004). 50, 86

[109] Duchesne, D., Kaspar, H., Chen, L. P., Hintzer, K., Molnar, A., Mayer, L., and Lohr, G. US Patent # 6489420, (Dec. 3 2002). 50

[110] Dattelbaum, N., Sheffield, S., Stahl, D., Weinberg, M., Neel, C., and Thadhani, N. *Journal of Applied Physics* **104**, 113525 (2008). 50, 57, 58, 85, 86, 128, 162

[111] Dattelbaum, D., Velisavljevic, N., Emmons, E., Stahl, D., Sheffield, S., Weinberg, M., Brown, E. N., Rae, P. J., and Orler, E. Unpublished report, (2007). 51, 64, 89, 153, 154

[112] Bourne, N. and Millett, J. *Metallurgical and Materials Transactions A* **39A**, 266–271 (2008). 51

[113] Millett, J., Bourne, N., and Gray, G. *Journal of Applied Physics* **96**, 5500–5504 (2004). 51, 86

[114] Gustavsen, R. and Sheffield, S. In *High-Pressure Science and Technology - 1993,* Schmidt, S., Shaner, J., Samara, G., and Ross, M., editors, 1393–1396, (1994). 51

[115] Millett, J. and Bourne, N. *Journal of Physics D: Applied Physics* **37**, 2613–2617 (2004). 52, 129

[116] Millett, J., Bourne, N. K., Akhavan, J., and Milne, A. *Journal of Applied Physics* **97**, 043524 (2005). 52

[117] Lundergan, C. and Drumheller, D. *Journal of Applied Physics* **42**(2), 669–675 (1971). 52

[118] Munson, D. and Schuler, K. *J. Comp Matls* **5**, 286–304 (1971). 52, 71

[119] Munson, D., Boade, R., and Schuler, K. *J. Appl. Physics* **49**, 4797–4807 (1978). 52, 128

[120] Millett, J., Deas, D., Bourne, N. K., and Montgomery, S. *Journal of Applied Physics* **102** (2007). 52, 71

[121] Millett, J., Bourne, N. K., and Deas, D. *Journal of Physics D: Applied Physics* **38**, 930–934 (2005). 52, 71

[122] Setchell, R. and Anderson, M. *J. Appl. Phys* **97** (2005). 52, 71, 91, 105, 106

[123] Setchell, R., Anderson, M., and Montgomery, S. *J. Appl. Phys* **101** (2007). 53, 71, 74, 123, 127, 133

[124] Eakins, D. E. *Role of Heterogeneity in the Chemical and Mechanical Shock-Response of Nickel and Aluminum Powder Mixtures.* PhD thesis, Georgia Institute of Technology, (2007). 54, 117

[125] Personal communication with Kyle Mychajlonka at ATK. 57

[126] Emmons, E., Velisavljevic, N., Schoonover, J., and Dattelbaum, D. *Applied Spectroscopy* **62**(2), 142–148 (2008). 57, 58

[127] Cheng, D., Wang, S., and Ye, H. *Journal of Alloys and Compounds* **377**, 221–224 (2004). 64

[128] Rama Rao, G. A. and Venugopal, V. *Journal of Alloys and Compounds* **206**, 237–242 (1994). 64

[129] Shimada, S. *Solid State Ionics* **149**, 319–326 (2002). 64, 145

[130] Underwood, E. E. *Quantitative Stereology.* Addison-wesley, Reading, MA, (1981). See chapter 2.3. 71

[131] Sutherland, H. J. *Journal of Comp Matls* **13**, 35–48 (1979). 71, 74, 126

[132] Varadan, V., Ma, Y., and Varadan, V. *Pure and Applied Geophysics* **131**, 577–603 (1989). 74

[133] Fused silica obtained from Mark Optics, composed of Corning 7980 fused silica. 74

[134] Wackerbarth, D. E. *PlotData Graph Plot Software User Manual: Version 2.* Sandia Natl Labs, (2003). Export Controlled Software. 76

[135] Wackerbarth, D. Personal Communication, (2009). 76

[136] Anderson, M. Personal Communication, (2009). 76

[137] Buttler, W. T., Lamoreaux, S. K., Omenetto, F. G., and Torgerson, J. R. Technical report, (2004). Los Alamos Report LA-UR-04-6453. 76

[138] Dolan, D. H. Technical report, (2006). Sandia Report SAND2006-1950. 76

[139] Taylor, J. *An Introduction to Error Analysis- The Study of Uncertainties in Physical Measurements.* University Science Books, Sausalito, CA, (1997). 77

[140] Mitchell, A. and Nellis, W. *Journal of Applied Physics* **52**, 3363–3374 (1981). 77

[141] Fredenburg, D. A., Thadhani, N. N., and Vogler, T. J. *Materials Science and Engineering A* (submitted in Dec. 2009). 78

[142] Taylor, G. I. *Proc. Roy. Soc. London* **A-194**, 289–299 (1948). 79

[143] Hutchings, I. *J Mech. Phys. Solids* **26**, 289–301 (1979). 79, 99

[144] House, J., Lewis, J., Gillis, P., and Wilson, L. *International Journal of Impact Engineering* **16**(2), 189–200 (1995). 79

[145] House, J., Aref, B., Foster, J., and Gillis, P. *Journal of Strain Analysis* **34**(5), 337–345 (1999). 79

[146] Eakins, D. and Thadhani, N. *J Appl Phys* **100**(7), 073503 (2006). 79

[147] Graham, R. *Solids Under High-Pressure Shock Compression.* Springer-Verlag, New York, (1993). 81, 90, 160

[148] Morris, C., Fritz, J., and McQueen, R. *Journal of Chemical Physics* **80**, 5203–5218 (1984). 86, 139, 154

[149] Dattelbaum, D., Robbins, D., Sheffield, S., Orler, E., Gustavsen, R., Alcon, R., Lloyd, J., and Chavez, P. In *Shock Compression of Condensed Matter - 2005,* Furnish, M., Elert, M., Russell, T., and White, C., editors, 69–72, (2006). 86

[150] Eckert, E. and Drake Jr., R. *Analysis of Heat and Mass Transfer.* McGraw-Hill, New York, (1972). 101

[151] Swegle, J. and Grady, D. *Journal of Applied Physics* **58**, 692–701 (1985). 105, 106

[152] Holman, G., Graham, R., and Anderson, M. In *High Pressure Science and Technology - 1993*, 1119–1122, (1994). 106

[153] Armstrong, R., Arnold, W., and Zerilli, F. *Metallurgical and Materials Transactions A* **38A**, 2605–2610 (2007). 106

[154] Zhuang, S., Ravichandran, G., and Grady, D. *Journal of the Mechanics and Physics of Solids* **51**, 245–265 (2003). 106

[155] American Society for Testing and Materials (ASTM). *Standard Test Method for Bulk Density and Volume of Solid Refractories by Wax Immersion*, (1999). ASTM Designation C 914-95. 112

[156] Bell, R., Baer, M., Brannon, R., Crawford, D., Erlick, M., Hertel, E., Schmitt, R., Silling, S., and Taylor, P. *CTH Users Manual and Input Instructions*. New Mexico, (2006). 117, 119

[157] Holmquist, T. and Johnson, G. *Journal of Applied Physics* **104**, 013533 (2008). 123

[158] Lawson, A., Butt, D., Richardson, J., and Li, J. *Philosophical Magazine* **87**, 2507–2519 (2007). 128

[159] Mashimo, T., Nagayama, K., and Sawaoka, A. *Physics and Chemistry of Minerals* **9**, 237–247 (1983). 128

[160] Munro, R. *Journal of Research of the National Institute of Standards and Technology* **109**, 497–503 (2004). 128

[161] Patil, R. and Subbarao, E. *Journal of Applied Crystallography* **2**, 281–288 (1969). 128

[162] Luo, X., Zhou, W., Ushakov, S., Navrotsky, A., and Demkov, A. *Physical Review B* **80**, 134119 (2009). 128

[163] Mock, W. J. and Holt, W. In *Shock Compression of Condensed Matter - 2005*, 1097–1100, (2006). 139, 141

[164] Raftenberg, M., Mock, W., and Kirby, G. *International Journal of Impact Engineering* **35**, 1735–1744 (2008). 139

[165] Lee, I., Reed, R., Brady, V., and Finnegan, S. *Journal of Thermal Analysis* **49**, 1699–1705 (1997). 139, 140

[166] Turi, E. A. *Thermal Characterization of Polymeric Materials*. Academic Press, San Diego, CA, (1997). 139

[167] Jun, H., Kim, K., Park, K., and Woo, S. *Korean Journal of Chemical Engineering* **12**, 183–187 (1995). 139

[168] Epsch, R., Goldmann, G., Killich, A., Lohr, G., and Staudt, H. *Chemical Engineering & Technology* **25**, 277–282 (2002). 139

[169] Reed, R., Zentner, B., Marrs, C., and Mason, B. In *Proceedings of the 15th International Pyrotechnics Seminar*, 815–841, (1990). 140

[170] Wood, J., Badachhape, R., Lagow, R., and Margrave, J. *The Journal of Physical Chemistry* **73**, 3139–3142 (1969). 140, 141

[171] Kubaschewski, O., Alcock, C., and Spencer, P. *Materials Thermochemistry*. Pergamon Press, Oxford, England, (1993). 140, 145

[172] Lide, D. R. *CRC Handbook of Chemistry and Physics, 83rd Edition*. CRC Press, Boca Raton, FL, (2002). 140, 141

[173] Kleimenov, N., Borisov, A., and Markevich, A. *Russian Journal of Physical Chemistry* **54**, 183–185 (1980). 141

[174] Kuriakose, A. and Margrave, J. L. *The Journal of Physical Chemistry* **68**, 290–295 (1964). 145

[175] Haendler, H., Bartram, S., Becker, R., Bernard, W., and Bukata, S. *Journal of the American Chemical Society* **76**, 2177–2178 (1954). 145

[176] Papiernik, R., Frit, B., and Gaudreau, B. *Revue de Chimie minérale* **23**, 400 (1986). In French with English abstract. 147

[177] Wada, Y., Itani, A., Nishi, T., and Nagai, S. *Journal of Polymer Science: Part A-2* **7**, 201–208 (1967). 151, 153, 154, 171

[178] Barker Jr., R. *Journal of Applied Physics* **38**, 4234–4242 (1967). 153, 171

[179] Warfield, R. *Die Makromolekulare Chemie* **175**, 3285–3297 (1974). 153, 154, 171, 172

[180] Charest, J. and Lynch, C. In *Shock Compression of Condensed Matter - 1989,* Schmidt, S., Johnson, J., and Davison, L., editors, 797–800, (1990). 159, 160

[181] Anderson, M. U., Chhabildas, L. C., and Reinhart, W. D. In *Shock Waves in Condensed Matter - 1997*, 841–844, (1998). 160

[182] Bauer, F. Personal Communication, (2009). 162

[183] Bourne, N. and Gray, G. *Journal of Applied Physics* **93**, 8966–8969 (2003). 166

[184] Yang, Y., Wu, G., Ramalingam, S., Hsu, S., Kleiner, L., and Tang, F. *Macromolecules* **40**, 9658–9663 (2007). 168

[185] Constantino, C., Job, A., Simoes, R., Giacometti, J., Zucolotto, V., Oliveira Jr., O., Gozzi, G., and Chinaglia, D. *Applied Spectroscopy* **59**(3), 275–279 (2005). 168

[186] Graham, R. Personal Communication, (2009). 168

[187] Chen, P., Davison, L., and McCarthy, M. *Journal of Applied Physics* **47**, 4759–4764 (1976). 168

[188] Samara, G. *Journal of Polymer Science, Part B: Polymer Physics* **27**, 39–51 (1989). 170, 171, 172

[189] Scheinbeim, J., Chung, K., Pae, K., and Newman, B. *Journal of Applied Physics* **51**, 5106–5110 (1980). 170, 171

[190] Tanaka, H., Takayama, K., Okamoto, T., and Takemura, T. *Polymer Journal* **14**, 719–727 (1982). 171, 172